ISAS - INTERNATIONAL SCHOOL
FOR ADVANCED STUDIES

Modelling the SED Evolution of Dusty Galaxies and Applications

Thesis submitted for the degree of

"Doctor Philosophiæ"

CANDIDATE

Laura Silva

SUPERVISORS

Prof. Luigi Danese

Dr. Gian Luigi Granato

October 1999

SISSA - SCUOLA INTERNAZIONALE SUPERIORE DI STUDI AVANZATI

TRIESTE
Via Beirut 2-4

TRIESTE

SISSA ISAS

SCUOLA INTERNAZIONALE SUPERIORE DI STUDI AVANZATI
INTERNATIONAL SCHOOL FOR ADVANCED STUDIES

Modelling the SED Evolution of Dusty Galaxies and Applications

Thesis submitted for the degree of
"Doctor Philosophiæ"

CANDIDATE

Laura Silva

SUPERVISORS

Prof. Luigi Danese
Dr. Gian Luigi Granato

October 1999

To my parents

Contents

Chapter 1

Introduction

Dust in the local universe

Infrared observations of the local universe performed in the last decade or so have clearly demonstrated that dust is one of the most important components of the interstellar medium, containing a large fraction of heavy elements ejected from stars. It has been recognized that dust is an active factor in galaxy evolution (e.g. Dorschner & Henning 1995). It modifies the physical and chemical conditions of the interstellar medium (ISM), in particular it prevents stellar radiation from penetrating dense clouds, that remain cool; molecules formed at the grain surfaces or in the gas are therefore enriched in these clouds; the low temperatures reached within clouds favours the occurence of gravitational instabilities. Therefore dust is a fundamental component for the occurence of star formation, the most basic process of galactic evolution.

The ubiquity of dust and its radiative effects on stellar radition heavily affect our view of galaxies: it absorbs and scatters photons, mostly at wavelengths $\lesssim 1$ μm and returns to the radiation field the subtracted energy in the form of infrared (IR) photons. The resulting spectral energy distribution (SED) of galaxies is often substantially changed and in many relevant cases radically modified.

The first all-sky survey at far-IR (FIR) wavelengths, carried out by IRAS, revealed the stength of this effect for the local universe. The majority of galaxies detected by IRAS ranged from normal spirals, emitting about 1/3 of their bolometric luminosity in the IR, to the a new class of IR-bright objects, the luminous (L $\geq 10^{11} L_{\odot}$, LIRG) and ultraluminous (L $\geq 10^{12} L_{\odot}$, ULIRG) IR galaxies (e.g. Sanders & Mirabel 1996) with bolometric luminosities dominated by the IR spectral region. In particular, an important empirical trend emerging from these observations was that at increasing luminosities, from normal spirals to LIRG and ULIRG, most of the energy is emitted in the IR due to dust reprocessing. Among the LIRG mostly interacting/merging galaxies undergoing strong starbursts are found, while nearly all ULIRG appear to be advanced mergers powered by both starbursts and AGN (even though about 20-30% of the energy radiated by local ULIRG is estimated to be powered by AGN activity, Genzel et al. 1998, Lutz et al. 1998).

Therefore, observations show that dust reprocessing of the optical–UV stellar photons into the infrared regime is particularly severe in galaxies undergoing massive episodes of star formation and, in particular, that the fraction of energy emitted in

the IR increases as a function of the strength of the star formation activity. Indeed the SED of normal star–forming disk–like galaxies is affected by dust, mainly associated with the diffuse ISM and with the envelopes of evolved asymptotic giant branch stars, while for starbursts most of the IR luminosity comes from the central ($\lesssim$ 1kpc) molecular-rich regions wherein the starburst is embedded. Even local quiescent elliptical galaxies exhibit infrared emission and visual dust obscuration, arising in part from dust grains continuosly formed in dusty outflows from AGB stars, as well as molecular line emission.

In fact, this correlation between the amount of dust reprocessing and star formation could be expected due to the role, mentioned above, played by dust in allowing the formation of dense molecular clouds and of star formation within them.

A global estimate of the energy balance in the local universe, as provided by IRAS observations (Soifer & Neugebauer 1991), is that about 30% of starlight is dust–reprocessed into the region from 8 to 1000 μm. This is the integrated contribution of moderately to extremely dusty galaxies, with the latter providing about 6% of the total IR luminosity. However deep IRAS surveys, probing to $z \sim 0.3$, show a significant evolution of the IR-bright galaxy population in number counts (e.g. Bertin et al. 1997, Kim & Sanders 1998), that are indeed confirmed by the deeper observations described below.

Dust in the high-z universe

Great efforts have been recently devoted to investigate also the high-z universe in the IR (e.g. ISO, SCUBA, IRIM, DIRBE and FIRAS on COBE). These new long wavelengths inspections of the distant universe are unvealing substantial populations of high-z galaxies, missed by optical studies because of dust obscuration, pointing to a stronger role of dust at $z > 0$ than locally:

- Deep ISO surveys have been performed in the mid-IR, at 6.7 and 15μm (Oliver et al. 1997, Flores et al. 1999) and in the far-IR, at 175μm (Kawara et al. 1998, Puget et al. 1999). Strong IR sources have been revealed, with surface densities implying strong evolution from $z \lesssim 0.3$ (IRAS), and interpreted as the high-z counterparts of the local LIRG discovered by IRAS (Rowan-Robinson et al. 1997, Elbaz et al. 1999).

- A new population of sub-mm sources has been discovered at high redshift ($z \gtrsim 1$) using SCUBA. The luminosities, if powered by star formation in dust-enshrouded galaxies, imply very large star formation rates ($\sim 10^2 - 10^3$ $M_\odot yr^{-1}$), and a total star formation density comparable to what is inferred from the UV luminosities of the Lyman-break galaxies (Smail et al. 1997, Hughes et al. 1998, Lilly et al. 1999). Also, some extremely red objects (ERO) have been detected in the submm, (Dey et al 1999, Smail et al. 1999) revealing this new class of objects is made of extremely extincted starbutsts.

- The millimeter lines and continuum emission detected from high-z QSO (e.g. Omont et al. 1996) has been attributed to dust heated by a starburst in the host galaxies, although the AGN activity is simultaneously present.

- The population of star forming galaxies at $z \sim 2-4$ detected through the strong Lyman-break features has been discovered to be heavily extincted in the rest-frame UV, so that the star formation rates in these objects are $\sim 3-10$ times higher than would be inferred by ignoring dust (Pettini et al. 1998, Steidel et al. 1999).

- The COBE satellite discovered a cosmic far-IR/submm background with energy density comparable to that in the UV and optical background (Puget et al. 1996, Fixsen et al. 1998, Hauser et al. 1998, Schlegel et al. 1998). Since the background provides information on the integrated emission from extragactic source, this implies that a large fraction of all the energy radiated by stars over the history of the universe is hidden from optical observations because reprocessed by dust in the far-IR/submm .

Implications for galaxy formation and evolution

These new discoveries have strong implications for understanding galaxy formation and evolution. Indeed, by combining observations in the UV, optical, IR and sub-mm, we can now start to reconstruct the history of star formation in galaxies over the epochs when the bulk of the stars have formed (e.g. Madau et al. 1996, Steidel et al. 1999, Hughes et al. 1998).

Initial studies from optical surveys suggested that the cosmic star fomation rate (SFR) peaked at $z \sim 1-1.5$ (Madau et al. 1996) and decreased at higher redshifts. The new observations demonstrate a large fraction of the cosmic SFR has been lost by optical searches because of dust reprocessing: the strong evolution required to match the faint IR-submm population, as well as the cosmic IR background, argues for a stronger role of dust-enshrouded starbursts in the past than at $z \sim 0$, as initially suggested by IRAS. Keeping into account also the optically hidden star formation, the cosmic SFR may be roughly constant above $z = 1$ (e.g. Rowan-Robinson et al. 1997, Dwek et al. 1998).

Actually, the contribution from dust-enshrouded AGNs to the IR-submm counts and background is currently uncertain, but they are estimated not to dominate, accounting for $\sim 10-20\%$ of the background light (Granato et al. 1997, Almaini et al. 1999). This is close to the value estimated in the local universe (see first section).

A relatevely late formation epoch ($z \lesssim 1$) of the bulk of galaxies observed today is predicted by models based on the paradigm of structure formation through hierarchical clustering, i.e. bottom-up scenarios of galaxy formation (White & Frenk 1991), in which dust effects were not considered. These models were in agreement with the observational evidence of strong evolution of optical galaxies below $z = 1$ and of a star formation activity peaking at $z \sim 1$. In these models massive galaxies at high redshifts do not exist, since galaxy formation is a continuous process.

Also the opposite scenario is pursued, envisaging instead a unique hig-z epoch for galaxy formation with a one-to-one correspondance between local and high-z galaxies. The main driver for these opposite theories is concerned with explaining the properties of early-type galaxies. Indeed, due to the old and almost coeval ages of the stellar populations in these systems, and to the lack of remaining fuel to entertain new star

formation, these galaxies are expected to have rapidly formed the bulk of their stars at early epochs ($z \gtrsim 2$). Therefore optical searches for primeval galaxies (e.g. through strong Lyα emission lines, Djorgovski & Thompson 1992) were expected to detect this luminous starburst phase of proto-spheroids. The failure to detect it was exactly interpreted as either the non-existence of primeval galaxies or that this first episode of massive star–formation was optically hidden due to dust reprocessing, since the ISM might have been metal enriched on a very short timescale, the lifetime of the first generation of massive stars (Franceschini et al. 1994 and references therein). In this case primeval galaxies are expected to be found in IR surveys. In fact, the IR-submm background was predicted by Franceschini et al. (1994) under the assumption that the main phases of energy production by stellar nucleosynthesis were obscured by dust, particularly in elliptical galaxies.

This two opposite theories may be not mutually exclusive: in order to match observations at different wavelengths, they will probably have to converge someway. Indeed a strong evolution of optical galaxies below $z = 1$ is observed, where mainly interacting/merging systems are found suggesting this kind of evolution may have played a major role, that should be accounted for in molithic scenarii. On the other hand the IR-submm universe argues for a strong dust reprocessing in massive starbursting objects already at high redshifts, indicating part of the star formation predicted by hierarchical models is shifted to higher-z larger objects .

Theory: spectral synthesis models

The importance of dust effects for building a complete picture of galaxy formation seems now well established: in order to understand the history of star formation in the universe from observational data, one must have a unified picture that covers all wavelengths from the far-UV to the sub-mm, but especially the UV and the far-IR, since young stellar populations emit most of their radiation in the rest-frame UV, and the part of this that is absorbed by dust is re-radiated mostly in the rest-frame far-IR, so that luminosities in these two wavelength ranges are the best tracers of the SFR at different redshifts.

Up to a few years ago, the importance of dust, and therefore its inclusion in spectral synthesis models, was generally under-appreciated, especially for the study of high redshift galaxies, for several reasons. One of these was a real underestimate based on the scarce number of LIRG and ULIRG in the local universe, providing only a low fraction (0.06, see end of first section) of the total IR luminosity: the detection by IRAS of these objects was not supposed to change our understanding of the history of star formation because of the marginal proportion of stars born in these galaxies. Another reason is that the inclusion of dust effects into spectrophotometric codes leads to many difficulties. While the integrated photometric properties of an hypothetical dust–free galaxy are geometry independent, dust introduces a strong dependence on the distribution of both stars and ISM. Moreover the optical properties of dust grains and their dependence on environmental conditions have not yet been fully explored and understood. The ensuing uncertainty may only be parametrized to some extent. The effects of scattering, absorption and emission of grains, which may not be in radiative equilibrium with the radiation field, complicate the solution of the integro–differential transfer equation in a

complex geometry.

Therefore in many papers dealing with the spectrophotometric evolution of galaxies the radiative processes occurring in a dusty ISM are not included (e.g. Bruzual & Charlot 1993 and Leitherer & Heckman 1995, Leitherer et al. 1999, the former the most adopted one to interpret data on different galaxy types; the latter two appositely built for starburst galaxies). Indeed their codes are commonly used together with some prescription to approximate the effects of dust in the ISM.

In other cases the effects of dust on galaxy luminosities at different wavelengths have been included at various levels of sophistication, but always with a number of simplifying assumptions, e.g. often extinction is considered but thermal reradiation is not, or scattering is neglected, or not all the relevant dusty environments are considered, or optically thin emission is assumed, or an unrealistic geometry is adopted. Guiderdoni & Rocca-Volmerange (1987) were the first to include dust absorption in a model of this type, based on a 1D slab model for the star and dust distribution; Lançon & Rocca–Volmerange (1996) and Fioc & Rocca–Volmerange (1997) models include dust extinction but not emission. Models that include in a consistent framework the chemical and spectro photometric evolution of galaxies with both dust extinction of starlight and IR reemission are those from Mazzei et al. (1992), the first to try this kind of comprehensive modeling, and Devriendt et al. (1999). In both models the same approach of estimating the global amount of absorbed stellar energy is used; the latter empirically adjust the IR SED according to the observed average IRAS colors of galaxies. Therefore a fit to observed SEDs is essentially a rescaling of model spectra, that lack the predictive power that in principle should have a physical, eventhough more complex, model.

Those works facing a complete computation of the radiative transfer through a dusty medium, do not include it in the more general framework of galaxy evolution, but are instead interested either in the interpretation of single objects (e.g. Krügel & Siebenmorgen 1994) or in understanding the effects of dust geometry on the extinction of the emerging spectrum (e.g. Bruzual, Magris, & Calvet 1988; Witt, Thronson, & Capuano 1992; Cimatti et al. 1997; Wise & Silva 1996; Bianchi, Ferrara, & Giovanardi 1996; Gordon, Calzetti, & Witt 1997, Ferrara et al. 1999).

Given the large amount of data accumulated both on dust properties itself and on its role in modifying our view of the universe, a more realistic and complete computation of the spectrophotometric galaxy models including dust is required since, as we have seen, neglecting the complexity of the dust effects can lead to erroneous estimates of many interesting quantities such as the SFR. Also, the estimate of the age of a galaxy through the fit of its broadband SED is hampered by the degeneracy between the colors of an old galaxy and those of an extinguished young galaxy, further complicating the well known age–metallicity degeneracy.

We have therefore developed chemo–spectrophotometric self–consistent galactic models including dust (Silva et al. 1998, Chap. 2) and applied them in different contexts in order to interpret galaxies from their SED (Chaps. 4 to 6). Three different dusty environments are considered in order to properly understand the UV to submm properties of galaxies: (i) dust in interstellar HI clouds heated by the general interstellar radiation field (ISRF) of galaxies (the 'cirrus' component), (ii) dust associated with star forming molecular clouds and H II regions and (iii) circumstellar dusty shells produced

by the windy final stages of stellar evolution. Indeed these environments have different importance in different galactic systems and at various evolutionary stages. The dust model is comprehensive of normal big grains, small thermally fluctuating grains and polycyclic aromatic hydrocarbons (PAH) molecules; for each grain family, the appropriate computation of absorption and reemission is performed. The models are suited to simulate galaxies of any Hubble type, in different evolutionary stages, since we include the possibility of different geometrical distributions both for stars and gas. The complete radiative transfer equation is numerically solved whenever necessary.

The many parameters and uncertainties introduced by the presence of dust can be constrained only by consistently reproducing the spectrophotometric properties of galaxies from the UV to the submm, i.e. taking into account extinction at short wavelengths and the consequent thermal emission in the IR regime. This allows us to retrieve information from all the available and incoming data on galaxies, covering the UV to submm spectral range, provided by both space and ground-based telescopes.

Organization of the thesis

In **Chap. 2** our spectrophotometric model, GRASIL, is described in details. Since the first input to provide to GRASIL is the star formation history of the model galaxy, we describe our chemical code, that will then be used in different applications throughout the thesis. Then we present our adopted dust model, i.e. our choice for chemical and physical properties of dust grains, their optical efficiencies and size distribution. This is fixed according to the observations of extinction and emission for the diffuse ISM in our galaxy. Then, once we set the geometrical distribution of stars and dust, the radiative transfer of stellar radiation through the galaxy is solved, assuming the ISM is subdivided into a dense component, i.e. molecular clouds wherein stars are born, and a diffuse (cirrus) one, mostly associated with older stars. The preliminary inclusion of nebular emission and the radio emission are also described. Further computational details are in **App. A**.

Chap. 3 describes our library of single stellar populations (SSP). It provides the spectra for the generations of stars making up a galaxy model. In particular, we include the spectral effects of AGB dusty envelopes already in this spectral library. The method for this inclusion as well as the comparison with observations of late-type stars are presented. We discuss the possible breaking of the age-metallicity degenaracy intrinsic in integrated spectra of stellar populations, by considering optical and near/mid-IR flux ratios.

As a first application of our model, we consider in **Chap. 4** local starbursts, normal spirals and ellipticals. We show the capability of our model to provide quantitative estimates of the properties of galaxies with different star formation activity and extinction by reproducing their SED. Also one high-z galaxy is addressed here, HR10 at z=1.44.

In **Chap. 5** we apply our model to study a sample of K-selected early-type galaxies in the HDF, for which UBVIJHK data are available. These galaxies show no signatures of dust, so that their modeling require only stellar spectral synthesis. We find the SED indicate a fairly wide range of ages (1.5 to 3 Gyrs) for the stellar populations in these

objects, corresponding to a rather protracted star formation activity. In particular, we argue the absence of sample objects at $z > 1.3$ could be due to dust enshrouded starbursts occurring during the first few Gyrs of the galaxy lifetime.
The preliminary results of the same kind of study, for a sample of K-selected late-type galaxies in the HDF are in **App. B**. In this case we find a strong age-extinction degeneracy affects the analysis of the optical-near-IR SED available for the sample galaxies. We stress the importance of having a full coverage of the SED for galaxies undergoing star formation in order to be able to retrieve information.

In **Chap. 6** we apply GRASIL as the observational interface to semi-analytical models of galaxy formation. The latter provide the main inputs for GRASIL, i.e. star formation and metallicity enrichment histories, and most geometrical parameters - scalelengths of star distributions in the bulge and disk components. We compute a synthetic catalogue of local galaxies, distinguished in normal and stabursts, that we compare with observations: SEDs, extinction properties, luminosity functions in different bands. We find a global good agreement.

Some preliminarly results are also shown for high-z galaxy catalogues, compared with number counts and the cosmic background in different bands: the only real, and stimulating problem encountered is in the submm number counts, lower by an order of magnitue as compared to observations. A possible explanation is that star formation is distributed in too many low luminosity objects.

Chapter 2

SED models for galaxies with dust reprocessing

Summary. We[1] present models of spectrophotometric evolution of galaxies in which the effects of a dusty interstellar medium have been included with particular care. The computations are performed with our code GRASIL. The input ingredients for the spectral synthesis are the evolutions of the star formation rate (SFR), the gas fraction and the metallicity. We describe our chemical evolution code providing these inputs. The stellar population synthesis is then performed with a grid of integrated spectra of simple stellar populations (SSP) of different ages and metallicities, in which the effects of dusty envelopes around asymptotic giant branch (AGB) stars are included. The residual fraction of gas in the galaxy is divided into two phases: the star forming molecular clouds and the diffuse medium. The relative amount is a model parameter. The molecular gas is subdivided into clouds of given masses and radii (i.e. optical depths): it is supposed that each SSP is born within a cloud and progressively escapes it. The emitted spectrum of the star forming molecular clouds is computed with a radiative transfer code. The diffuse dust emission (cirrus) is derived by describing the galaxy as an axially symmetric system, in which the local dust emissivity is consistently calculated as a function of the local field intensity due to the stellar component. Effects of very small grains, subject to temperature fluctuations, as well as polycyclic aromatic hydrocarbons (PAH) are included. We are working to include in GRASIL the nebular emission lines. A preliminar investigation seems to require a third component in the ISM with optical depth intermediate between molecular clous and diffuse medium, where IR lines should form. The radio emission is predicted as a function of the supernova rate (SNR) provided by the chemical code.

[1]This Chapter is mainly based on the paper *Silva L., Granato G.L., Bressan A. & Danese L., 1998, ApJ, 509, 103* (Silva et al. 1998).

2.1 Introduction

We compute the spectrophotometric galaxy models with our code GRASIL. The executable of the code is available at *http://grana.pd.astro.it.* This is a "light" version of GRASIL, because some of the parameters are already fixed to typical values in order to simplify the usage, but we plan to make available more complete versions. In this chapter we describe how GRASIL works.

We divide the problem of estimating the SED of a galaxy at age t_G, including dust effects, in two steps: (1) the history of the star formation rate $\Psi(t)$, of the initial mass function (IMF), of the metallicity $Z(t)$ and of the residual gas fraction $g(t)$ is determined and then (2) the integrated SED of the galaxy is predicted taking into account all the stars and the gas present at t_G.

Step (1) includes a number of possible choices for the star formation history, which can be easily interfaced to our spectrophotometric code in order to describe the corresponding evolution of the SED. In this way our model may constitute an observational interface to any code predicting galaxy star forming evolution. In Sec. 2.2 our chemical evolution model is described. It predicts galaxy SFR evolution in the framework of the monolithic galaxy evolution scenario. This approach is surely accettable to quantify current properties (i.e. estimates of SFR, masses, age of bursting stellar populations) of nearby galaxies, indeed it provides, for instance, the inputs for the fits to the observed SED of local star forming galaxies presented in Chap. 4. In the following chapters we consider the cosmological evolution of galaxies through two complementary approaches based on the hierarchical merging and the monolithic galaxy formation scenarii.

When the effects of dust are neglected, step (2) simply involves a sum of the spectra of all stars. In Sec. 2.3, the spectral synthesis of starlight spectrum is briefly described. It is performed through the evolutionary population synthesis technique, which is based on a library of SSP spectra. Our library, including dusty envelopes around AGB stars, is then presented in details in Chap. 3. To take into account the effects of dust first we have to define a model for dust composition (Sec. 2.4) in order to fix the way dust extingushes the optical–UV starlight and thermally reemits it in the IR. Then we assume a specific geometry for the distribution of gas and stars in the galaxy model, and compute the radiative transfer through the galaxy of the radiation emitted by stars and dust (Sec. 2.5).

We have further extended the wavelength coverage of our model to the radio domain, where the SED is predicted as a function of the type II supernova rate (Sec. 2.6). In Sec. 2.7 the introduction of the nebular emission lines in our model is described, a piece of work still in a preliminary phase.

Details on model computation are in App. A.

2.2 Chemical code

The chemical evolution, providing a star formation history, is a preliminary step for our spectrophotometric model. The computations are performed, when required, with our new chemical code. It can be downloaded at *http://grana.pd.astro.it.* We report here its main aspects.

The code describes one–zone (no dipendence on space, only on time) open models including the infall of primordial gas, according to the standard equations of galactic chemical evolution, which we outline below.

In order to simulate the chemical evolution of galaxies, we have to express the time derivative of total gas mass $M_g(t)$ and of the mass of gas in the form of element i, $M_{g,i}(t) = X_i(t)M_g(t)$, in terms of computable quantities at time t, i.e. as a function of the previous history of the galaxy, keeping into account all the processes intervening in the evolution:

$$\dot{M}_{g,i} = \dot{M}_{g,i}\Big|_{\rm SF} + \dot{M}_{g,i}\Big|_{\rm FB} + \dot{M}_{g,i}\Big|_{\rm Inf} \tag{2.1}$$

where the 3 terms on the right hand side represent, respectively, the depletion of gas due to the formation of new stars, the feedback to the ISM due to the final stages and death of stars, and the infall of primordial gas forming the galaxy.

The rate of gas depletion due to star formation can be written as:

$$\dot{M}_{g,i}\Big|_{\rm SF} = -X_i(t)\,\Psi(t) = -M_{g,i}(t)\frac{\Psi(t)}{M_g(t)} \tag{2.2}$$

where $\Psi(t)$ is the SFR, which we write as the sum of two terms, a Schmidt–type one and, when needed, an analitycal one, explicit function of time (e.g. constant or exponential, used for instance to add a burst of star formation over a quiet evolution):

$$\Psi(t) = \nu\, M_g(t)^k + f(t) \quad M_\odot\, yr^{-1} \tag{2.3}$$

The stellar mass return to the ISM is computed under the assumption that it takes place entirely at the stars death. With this (good) approximation, the mass of gas in the form of element i given back to the ISM by all stars died before time t is:

$$M_{g,i}(t)|_{\rm FB} = \int_0^t dt' \int_{\mathcal{M}(t-t',Z(t'))}^{\infty} dm\, \Psi(t')\, \Phi(m) R_i(m, Z(t')) \tag{2.4}$$

where $\mathcal{M}(t, Z)$ is the mass of the star of metallicity Z and lifetime t, $\Phi(m)$ is the IMF (see below) and $R_i(m, Z)$ the mass fraction in the form of element i ejected by the star of mass m and metallicity Z (we adopt stellar ejecta from Portinari et al. 1998). The time derivative of this integral yields the rate of stellar feedback to the ISM:

$$\dot{M}_{g,i}(t)\Big|_{\rm FB} = -\int_0^t \frac{\partial \mathcal{M}(t-t', Z(t'))}{\partial t} \Psi(t')\, \left[\Phi\left(m\right) R_i\left(m, Z(t')\right)\right]_{m=\mathcal{M}(t-t',Z(t'))}\, dt' \tag{2.5}$$

The IMF is a power–law, $\Phi(m) \propto m^{-x}$ in different mass intervals, normalized to unitary total mass. Of course, since the purpose is the spectral synthesis, we adopt those IMF for which our SSP library has been computed (see Sec. 2.3).

An equation analogous to the latter one holds for the type II supernova rate, i.e. the death rate of stars more massive than $M_{up} = 5 - 8 M_\odot$ (depending on stellar models having or not overshooting):

$$SNR(t) = -\int_0^t \frac{\partial \mathcal{M}(t-t', Z(t'))}{\partial t} \Psi(t')\, \left[\Phi\left(m\right)/m\right]_{m=max(M_{up},\mathcal{M}(t-t',Z(t')))}\, dt' \tag{2.6}$$

In practice, since only stars born during the last few 10^7 yr contribute to the above integral (the lifetime of the star with initial mass M_{up}), it is convinient to integrate

from $t - \tau(M_{up}, Z(t))$. This is a good approximation since stellar lifetimes are weak functions of Z and the timescales involved are short.

We do not include type Ia supernovae. This is justified for our purposes: we are not interested at this stage in the delailed chemical evolution of galaxies, just on the global metal content and its evolutionary rate, since they provide a hint to the amount of dust in the ISM and its variation in time (but we are working to improve this point in order to predict the detailed evolution of heavy elements making up dust grains). Moreover the SNR is computed only to estimate the radio emission from galaxies (Sec. 2.6), not the energetics of the ISM ruling for instance the star formation efficiency and the onset of galactic winds (see below).

We assume, as has been usually done, that the gas accretes into galaxies at an exponential rate:

$$\dot{M}_{g,i}\Big|_{\rm Inf} = X_{i,\rm Inf}\, A_{\rm Inf}\, \exp(-t/\tau_{inf}) \tag{2.7}$$

normalized in order to accrete a mass of gas $M_{\rm Inf}$ at time $t_{\rm Inf}$. $X_{i,\rm Inf}$ is the mass fraction of element i in the infalling gas.

We allow for the possibility of interrupting the star formation activity and the infall at a time t_{wind}. In models for the chemical evolution of galaxies (see Matteucci 1996), this break is introduced to reproduce the chemical and spectrophotometric properties of elliptical galaxies. The computation is usually performed igniting galactic winds when the amount of thermal energy from supernova explosions and stellar winds into the ISM overhelms the gravitational binding energy of the gas. Actually this requires a complicated treatment for a very simple and unrealistic scheme, i.e. the sudden break, all over the galaxy, of every activity. The many uncertain factors required for this computation (i.e. amount and distribution of dark matter, interactions of supernovae and stellar winds with ISM) are introduced as parameters to set in order to find the value of t_{wind} reproducing the observations.

Therefore we set t_{wind} directly as a parameter (Mihara & Takahara 1994, Matteucci 1996), with the typical values that fit the observed properties of elliptical galaxies. At that time the galaxy is supposed to be totally depleted of gas, and possibly replenished due to stellar feedback: a fraction f_{wind} of the stellar mass from dying stars remains within the galaxy while $1 - f_{wind}$ continues to be lost. We introduced this further parameter in order to reproduce the amount of dust and IR emission observed in local giant ellipticals (see Sec. 4.4), that (with the ejecta we have adopted) require $f_{wind} \sim 10^{-3}$.

2.3 Synthesis of starlight spectrum

The library of isochrones for the SSP, the building–blocks of galaxy models, is based on the Padova stellar models (Bertelli et al. 1994), with a major difference, consisting in the computation of the effects of dusty envelopes around AGB stars (see Chap. 3). The SSPs span a wide range in age, from 1 Myr to 18 Gyr, and in metallicity, $Z = 0.004, 0.008, 0.02, 0.05, 0.1$, (keeping the relative proportion of the metals equal to the solar partition) to realistically reproduce the mix of age and composition of the stellar content of galaxies.

Stellar flux library	Kurucz (1992)stellar atmosphere models
M Giant spectra	Straizys & Sviderskiene (1972)
	Lançon & Rocca-Volmerange (1992)
	Fluks et al. (1994)
Metallicity Z	$0.02Z_{\odot}$ - $5Z_{\odot}$
IMF	Salpeter (1955); Kennicutt (1983)
Age	10^6 yr - 18 Gyr
$BC_{V_{\odot}}$	-0.08
$M_{bol\odot}$	4.72
Initial stars mass	0.15 $M_{\odot}$ - 120 $M_{\odot}$

Table 2.1: Inputs to the Single Stellar Population models.

At present our SSP spectral library has been computed for two IMF ($\Phi(m) \propto m^{-x}$ in mass):

Salpeter (1955): $x = 1.35$ from 0.15 to 120 $M_{\odot}$;

Kennicutt (1983): $x = 0.4$ from 0.15 to 1 $M_{\odot}$; $x = 1.5$ from 1 to 120 $M_{\odot}$

A summary of the inputs used for the SSP models is reported in Table 2.1.

The spectral synthesis technique, for the starlight alone, consists in summing up the spectra of each stellar generation, provided by the SSP of the appropriate age and metallicity, weighted by the SFR at time of the stars birth (e.g. Bressan et al. 1994):

$$F_{\lambda}(t_G) = \int_0^{t_G} SSP_{\lambda}(t_G - t, Z(t)) \times \Psi(t)\, dt \tag{2.8}$$

Instead, to keep dust into account, we have to specify a dust model and a geometry, and then to solve the transfer equation for the radiation in presence of dust in the different phases of the ISM. This gives rise to substantial complications which are addressed in the following sections.

2.4 The dust model for the ISM

The effects of dust on radiative transfer depend on the physical and chemical properties of grains as well as on the geometrical arrangement dust–stars (described in Sec. 2.5.1). It is expected and observationally well established that these properties are functions of the particular environment in which grains happen to live. Several populations may be distinguished (see Dorschner & Henning 1995 for a review): (i) stellar outflow dust (further subdivided into the two chemical subgroups of carbon rich and oxygen rich dust); (ii) dust in the diffuse ISM; (iii) dust in molecular clouds and dust around YSOs. As for stellar outflow dust, see Chap. 3. Here we discuss our choices for the latter two dusty components of the model galaxy.

Although a lot of efforts have been devoted to derive a so called *standard* model for dust in the diffuse ISM, its precise composition remains controversial. Significant clues can be derived from observations. The prominent features observed in its spectrum

at 9.7 and 18 μm indicate the presence of silicate grains. By converse, the origin of the 2175 Å feature is somewhat debated, though graphite still stands as the most attractive solution (see e.g. Mathis 1990). The emission bands in the 3-13 μm region indicate the presence of PAHs (Puget, Léger, & Boulanger 1985), which together with small thermally fluctuating grains contribute also to produce the warm mid–IR cirrus emission. Therefore we included these components in our diffuse dust model. We adopted the same mixture even for MCs, for which the information are scanty, only decreasing the fraction of PAH molecules (see below).

2.4.1 Big and small grains

The optical properties of silicate and graphite grains have been computed by Laor & Draine (1993) for spherical shapes using Mie theory, the Rayleigh–Gans approximation and geometric optics. In particular we used the cross sections of graphite and silicate grains computed by B.T. Draine for 81 grain sizes from 0.001 to 10 μm in logarithmic steps $\Delta \log a = 0.05$, and made available via anonymous ftp at *astro.princeton.edu*. The absorption and scattering efficiencies (defined as $Q = C/(\pi a^2)$ where C is the cross section) for dust grains of different radii are reported Fig. 2.1.

In order to get the overall radiative properties of the dust mixture, the abundance and the size distribution of grains must be specified. We started from the distribution proposed by Draine & Lee (1984, henceforth DL), which is tuned on the optical–UV extinction law of the galactic diffuse ISM. On the other hand DL pointed out that their model displays significant discrepancies with extinction data above 2 μm, and that these discrepancies are not surprising, since observations at longer λ tend to sample lines of sight through denser clouds, where grain population may differ from that present in more diffuse regions.

A more severe limitation of DL model is that the mid–IR cirrus emission at wavelengths $\lambda \leq 60$ μm is not reproduced (Fig. 2.5, below), because grains are always large enough to maintain a low temperature thermal equilibrium in the general ISRF. This emission requires reprocessing of the field by particles, very small grains and/or PAH molecules, reaching temperatures higher than those attained with equilibrium heating (e.g. Puget et al. 1985; Draine & Anderson 1985; Dwek et al. 1997). This requirement can be matched by decreasing the lower limit of the graphite grain distribution. Since these grains must be more numerous than the simple extrapolation of the DL power law, a break to a steeper power law is introduced below a_b. These adjustments to the DL model enhance the MIR cirrus emission, but tend to degrade the agreement with the observed extinction law in the optical–UV region. However a reasonable compromise can be found. For graphite grains we adopted the following size distribution:

$$\frac{dn_i}{da} = \begin{cases} A_i\, n_H\, a^{\beta_1} & \text{if } a_b < a < a_{\max}\,, \\ A_i\, n_H\, a_b^{\beta_1-\beta_2} a^{\beta_2} & \text{if } a_{\min} < a < a_b\,, \end{cases} \tag{2.9}$$

with $a_{\min} = 8$ Å, $a_{\max} = 0.25$ μm, $a_b = 50$ Å, $\beta_1 = -3.5$, $\beta_2 = -4.0$ and $A_g = 10^{-25.22}$ cm$^{2.5}$/H. This last value is set in order to mantain the same volume of graphite grains as in the DL model. As for silicate grains, we maintained the same size distribution as DL, a single power law with $a_{\min} = 50$ Å, $a_{\max} = 0.25$ μm, $\beta = -3.5$ and $A_s = 10^{-25.11}$ cm$^{2.5}$/H.

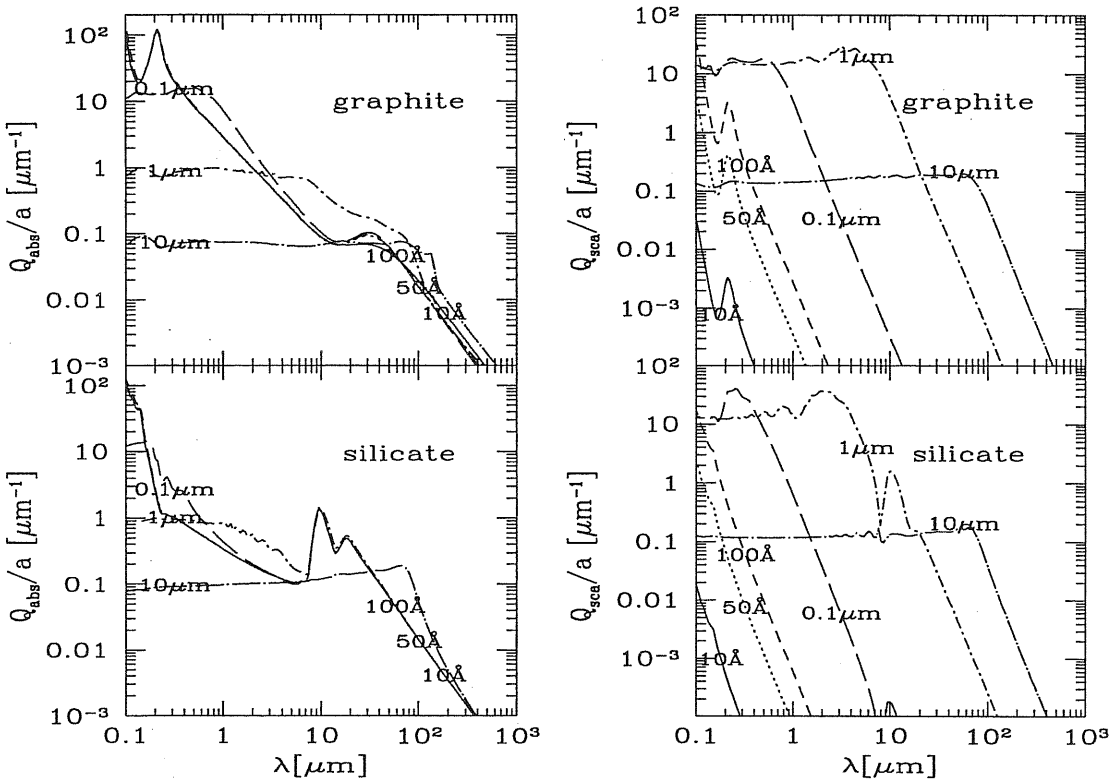

Figure 2.1: Adopted absorption and scattering efficiencies computed by B.T. Draine for graphite and silicate dust grains of different radii (10, 50, 100 Å, 0.1, 1 and 10μm). The ratio Q/a is plotted to reduce the number of decades required for the ordinate. For $a \lesssim 0.1\mu$m Q_{abs}/a ($\propto$ absorption cross section per unit mass) is independent of a. The 2175 Å feature of graphite appears for $a \lesssim 300$ Å. The silicate feature at 9.7μm is present in grains with $a \lesssim 1\mu$m.

With this choice of the dust parameters for graphite, the number of small fluctuating grains with radius $a < a_b$ is enhanced by a factor $\sqrt{a_b/a} \sim 2$ relative to the DL law extrapolated below a_b, and so is their corresponding cirrus emission (see Fig. 2.4).

In the code the size distributions have been discretized in N=20 logarithmic bins following the prescriptions given by Draine & Malhotra (1993). The dust mixture cross section (for extinction, absorption or scattering) is

$$\sigma_\lambda = \int_{a_{min}}^{a_{max}} \pi a^2 Q(a,\lambda) \frac{1}{n_H} \frac{dn}{da} da \quad cm^2 \tag{2.10}$$

(n_H [cm^{-3}] is the gas number density, Q stands for either Q_{abs} or $Q_{ext} = Q_{abs} + Q_{sca}$). The discretization over the N bins results in a sum over the dust grain radii with suitable

weights w_i:

$$\sigma_\lambda = \sum_{i=1}^{N} w_i Q(a_i, \lambda) \quad cm^2 \tag{2.11}$$

$$w_i = \pi a_i^{-1} \int_{b_{i-1}}^{b_i} a^3 \frac{1}{n_H} \frac{dn}{da} da \sim \pi a_i^2 n_i / n_H \quad cm^2 \tag{2.12}$$

where $b_i = \sqrt{a_i a_{i+1}}$.

Other quantities of interest (optical depth τ_λ, extinction or absorption coefficient α_λ, cross section per unit dust mass k_λ, albedo ω_λ) are defined as follows:

$$\begin{aligned} \tau_\lambda &= \sigma_\lambda \int_l n_H \, dl = \sigma_\lambda \, N_H \\ \alpha_\lambda &= \sigma_\lambda \, n_H \quad cm^{-1} \\ k_\lambda &= \frac{\sigma_\lambda}{m_H \, \delta} \quad cm^2 \, g^{-1} \\ \omega_\lambda &= \frac{\sigma_\lambda^{sca}}{\sigma_\lambda^{ext}} \end{aligned} \tag{2.13}$$

where N_H [cm^{-2}] is the gas number column density and δ is the dust to gas ratio (see below).

Once the bathing radiation field is specified, the emissivity of grains with radius $a > a_{flu}$ is computed assuming that they achieve thermal equilibrium, so that all grains of a given composition and radius emit as gray bodies at a single temperature:

$$j_\lambda^{big} = \int_{a_{flu}}^{a_{max}} \pi a^2 Q_{abs}(a, \lambda) B_\lambda(T(a)) \frac{dn}{da} da = \sum_{i, a_i > a_{flu}} w_i Q_{abs}(a_i, \lambda) B_\lambda(T(a_i)) \, n_H \quad \frac{erg}{cm^3 \, s \, st \, \text{Å}} \tag{2.14}$$

$T(a)$, the equilibrium temperature for grain a, is given by the energy balance between absorption from the radiation field J_λ and emission:

$$\int Q_{abs}(a, \lambda) \, J_\lambda \, d\lambda = \int Q_{abs}(a, \lambda) \, B_\lambda(T(a)) \, d\lambda \tag{2.15}$$

We set $a_{flu} = 100$ Å. The maximum grains size for which fluctuations are important depends on the intensity and shape of the radiation field, but 100 Å is a safe value whatever the radiation field properties are (see Siebenmorgen et al. 1992).

Below a_{flu} a temperature distribution $P(T)$ for each size bin and composition is computed following Guhathakurta & Draine (1989) and Siebenmorgen et al. (1992), and then the emissivity is obtained by integrating over this distribution:

$$j_\lambda^{small} = \int_{a_{min}}^{a_{flu}} \pi a^2 Q_{abs}(a, \lambda) \left(\int_{T_{min}}^{T_{max}} B_\lambda(T(a)) \, P(T(a)) \, dT \right) \frac{dn}{da} da = \sum_{i, a_i < a_{flu}} w_i Q_{abs}(a_i, \lambda) \, n_H \int_{T_{min}}^{T_{max}} B_\lambda(T(a_i)) P(T(a_i)) dT \quad \frac{erg}{cm^3 \, s \, st \, \text{Å}} \tag{2.16}$$

The method to compute $P(T)$ is described in App. A.1.

2.4.2 PAH

To model the observed IR emission occurring in bands at 3.3, 6.2, 7.7, 8.6 and 11.3 μm we include also a population of planar PAH. The optical–UV absorption cross–section σ_{PAH} is reported in Fig. 2.2. This has been obtained by averaging the cross sections of 6 different PAH mixtures measured by Léger et al. (1989) above 1200 Å, and smoothly joining the resulting mean curve to the coronene cross section below this limit. The same cross section is used to take into account the effects of PAH on the extinction curve, assuming a vanishing albedo (Fig. 2.5). Désert, Boulanger, & Puget (1990) have proposed an analytical description of σ_{PAH} derived from the observed interstellar extinction curve in the 1200–3300 Å range, under the assumption that these particles dominate its extreme UV rise. On the other hand the EUV rise can be ascribed to small grains. Actually using DL optical efficiencies, the EUV part of the extinction curve is produced by small grains. Our σ_{PAH} rests on laboratory measurements and predicts, in the local interstellar radiation field, a PAH absorption and subsequent IR emission lower by a factor ~ 0.5 with respect to the Désert et al. (1990) analytical approximation.

In order to compute the IR emission of PAH, their heat capacity $C_{PAH}(T)$ must be specified. A numerically convenient and accurate enough representation of the estimate given by Léger, d'Hendecourt, & De Fourneau (1989) is:

$$\frac{C_{PAH}(T)}{C_{max}} = \begin{cases} 9.25 \times 10^{-4} T & \text{if } T < 800 \text{ K}, \\ 2 \times 10^{-4} T + .58 & \text{if } 800 \leq T < 2100 \text{ K}, \\ 1 & \text{if } T \geq 2100 \text{ K}, \end{cases} \tag{2.17}$$

where $C_{max} = 3[N_t - 2]k$ and $N_t = N_C + N_H$ is the total number of atoms (carbon and hydrogen) in the molecule. We adopt a population of PAHs with a distribution $dn/dN_C \propto N_C^{-2.25}$ from $N_C = 20$ to $N_C = 280$. Smaller molecules are easily destroyed by UV photons (Omont 1986). This distribution is quite similar to those adopted by other authors (Dwek et al. 1997, Désert et al. 1990). Astrophysical PAH are thought to be partially *dehydrogenated*: probably due to the large UV flux in the emission regions, some of the CH bonds, responsible for the 3.3, 8.6 and 11.3 μm bands, are broken. The number of H atoms in a molecule is thus written as $N_H = x_H N_{s,H}$, where $N_{s,H}$ is the number of hydrogen sites and x_H is the H coverage. The relationship between $N_{s,H}$ and N_C depends on the arrangements of hexagonal cycles in the molecule. The ratio $N_C/N_{s,H}$ is rather constant around 2 for laboratory PAH molecules, for which $N_C \lesssim 50$. However, the structure of typical interstellar PAHs is likely closer to that of *catacondensed* PAH (Omont 1986), which are the most compact and stable ones and have the general formula $C_{6p^2}H_{6p}$, i.e. $N_{s,H} = (6\,N_C)^{0.5}$. For these quasi–circular molecules, usually assumed to represent the gross features of interstellar PAHs, the radius is given by $a = 0.9\sqrt{N_C}$ Å if $N_C >> 1$. With the above relationship between $N_{s,H}$ and N_C the typical flux ratios observed in the ISM between CH and CC bands (Mattila et al. 1996) is fairly well reproduced by our PAH model setting $x_H = 0.2$.

PAH emissivity was then computed following substantially the guidelines given by Xu & De Zotti (1989)[2]. The adopted abundances of PAH molecules in the diffuse ISM

[2] Apart two imprecisions in their equations: the factor 2 before σ_{PAH} in their equation (13) is wrong since their cross section already takes into account the two molecule surfaces. On the other hand the

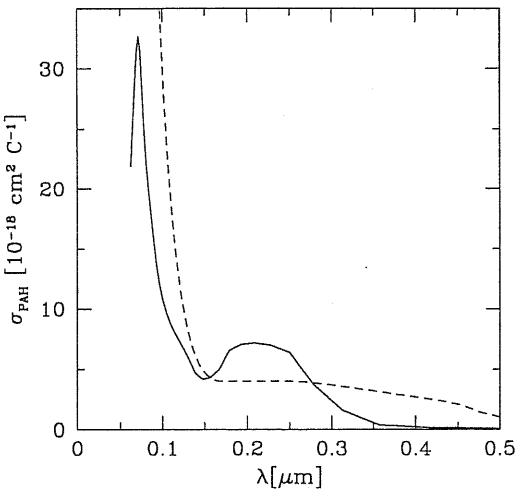

Figure 2.2: Solid line: cross–section of PAH per carbon atom, derived from laboratory measurements taken from Léger et al. (1989); dashed line: the analytical law assumed by Désert et al. (1990) for molecule with $N_C = 50$ C–atoms (N_C controls the cut–off above 0.3 μm).

and in the MCs implies that 18 and 1.8 ppM of C are locked in this component respectively. Indeed there are indications showing that in denser environments and/or in stronger UV radiation field the relative number of small particles is significantly diminished (Puget & Léger 1989; Kim & Martin 1996 and references therein). In particular Xu & De Zotti (1989) concluded that PAH molecules are less abundant by a factor ~ 10 in our galaxy star forming regions than in the diffuse gas. Details on the computations are in App. A.2.

Our computations of PAH emissivity allow us to estimate the amount of energy carried by the PAH emission bands. But in many astrophysical applications (e.g. estimate of SFR from MIR dust emission, galaxy counts in the near and mid IR) it is important to know the profiles of the bands within which this energy is distributed. Since a theoretical treatment of astrophysical PAH is still rather uncertain, we have adopted, when needed, the observed PAH profiles for the Ophiuchus molecular cloud by Boulanger et al. (1998) (examples are in Sec. 4.2). They find that the PAH bands are best fitted by Lorentz profiles, characterized by wide wings accounting a large fraction of the continuum between the features.

2.4.3 Overall properties and comparison with observations

The extinction curve and the albedo for our dust model are shown in Fig. 2.3, with the single contributions from graphite, silicate and PAH. The latter component gives

integration over solid angle yields a factor 4π before $I_{\nu'}$ in the same equation, which in conclusion should be multiplied by a factor 2 on the rhs

a negligible contibution to the UV rise, which is instead dominated by small graphite grains. As an example, the dependence on the choice of a_{max} is also shown on the right, where a_{max} is set to 0.4μm for graphite instead of 0.25μm. The dust model emissivity in the local interstellar radiation field (Mathis, Mezger, & Panagia 1983) is shown in Fig. 2.4, together with the contribution from graphite (also a few single grains) and silicate. This is then compared with the IR emission that would be obtained if the DL slope would be kept the same also for small fluctuating grains.

In Fig. 2.5 our dust model is compared with data: it reproduces reasonably well both the extinction from IR to UV and the whole cirrus emission. The model predicts an extinction below a few observational estimates at $\lambda \gtrsim 300\mu$m by a factor ~ 10. To account for this, Rowan–Robinson (1986, 1992) introduced *ad hoc* grain optical properties in his discretized models, tuned to reproduce observations of late–type stars (see Sec. 3.2). We avoid in general this approach (but see Sec. 4.2) mainly because these data have large uncertainties (DL), as it is apparent from their scatter. Moreover they refer to dusty environments for many respects different from the diffuse dust, which is instead the dominant contributor to the emission at $\lambda \gtrsim 100$ μm in our galaxy models. Also it has been suggested that the silicate grain absorption in the sub–mm wavelength range may decline less steeply than λ^{-2} (Agladze et al. 1996). The adopted mixture, even taking into account the contribution of PAH emission features, tends to underpredict the MIR cirrus emission, in particular the shorter λ data. A larger quantity of small grains and/or PAH molecules would improve the match with DIRBE observations, but would also produce a large disagreement with observed UV–extinction (Dwek et al. 1997). We prefer to adopt a compromise more balanced toward the extinction law, since in our models and in most interesting cases the MIR emission is in general dominated by warm dust in MCs rather than thermally fluctuating grains in the cirrus, whilst a good specification of the extinction properties is crucial. Moreover, DIRBE cirrus data at short wavelength could be affected by significant systematic effects (Dwek et al. 1997).

2.4.4 Dust–to–gas and Abundances

The mass of dust enclosed in grains of composition i and the dust–to–gas mass ratio are given by:

$$m_i = \int_{a_{min}}^{a_{max}} \frac{4\pi a^3 \rho_i}{3 n_H} \frac{dn_i}{da} da \quad g \quad , \quad \delta = \frac{\sum_i m_i}{m_H}$$

where ρ_i is the grain mass density, 2.26 and 3.3 gcm^{-3} for graphite and silicate respectively. The total (i.e. cirrus + MCs) dust content of a galaxy ISM depends on the residual gas and on δ. The residual gas mass is provided at each time step by the chemical evolution model. Determinations of δ in our Galaxy ISM and in nearby objects range typically from 1/100 to 1/400. Where the model is compared to galaxies in the local universe (Chap. 4), we simply set $\delta = 1/110$, the value of DL model. However the code is thought to interpret data on objects in very different evolutionary stages, thus we need in general a recipe to scale δ when the chemical conditions in the ISM where very different. We adopt the simplest assumption $\delta \propto Z$, with the proportionality constant adjusted to have $\delta = 1/110$ for $Z = Z_\odot$. This relation is the one found by Dwek (1998) with a comprehensive model for the evolution of the composition and

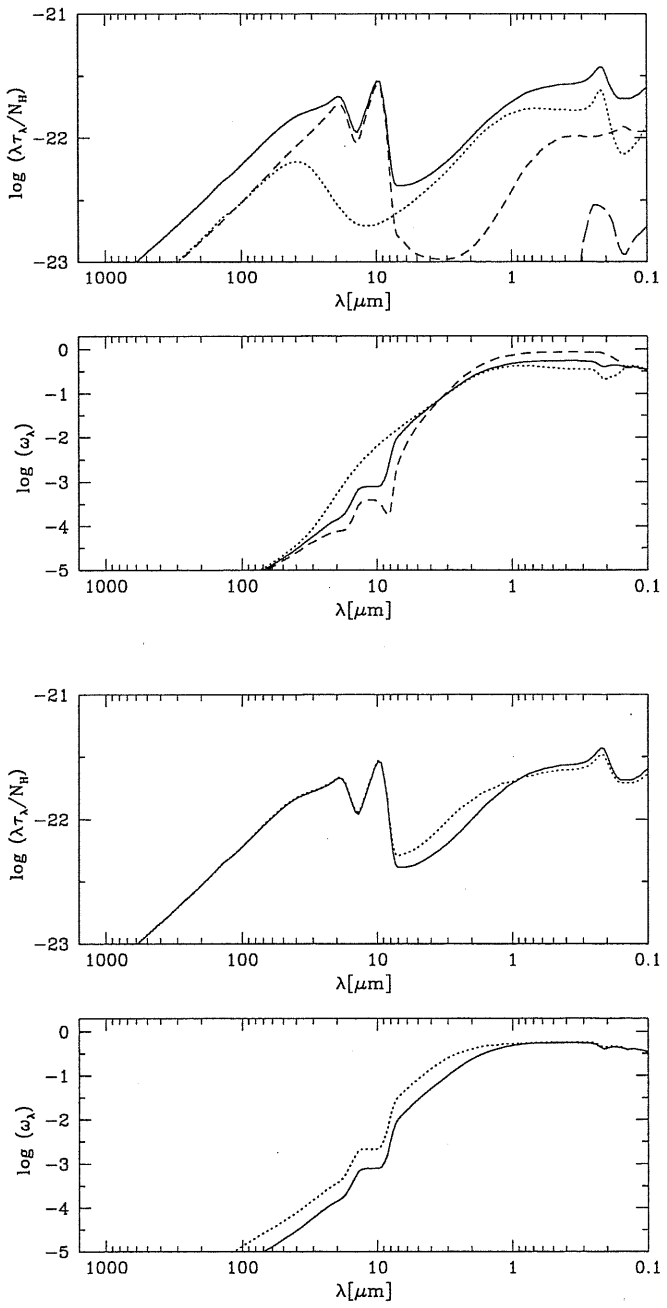

Figure 2.3: *Above:* Extinction curve and albedo for our dust model. Dotted: graphite; dashed: silicate; long-dashed: PAH. *Below:* Dependence on the choice of dust parameters: dotted line is with $a_{max} = 0.4\mu$m for graphite grains, continuous with the chosen value of 0.25μm

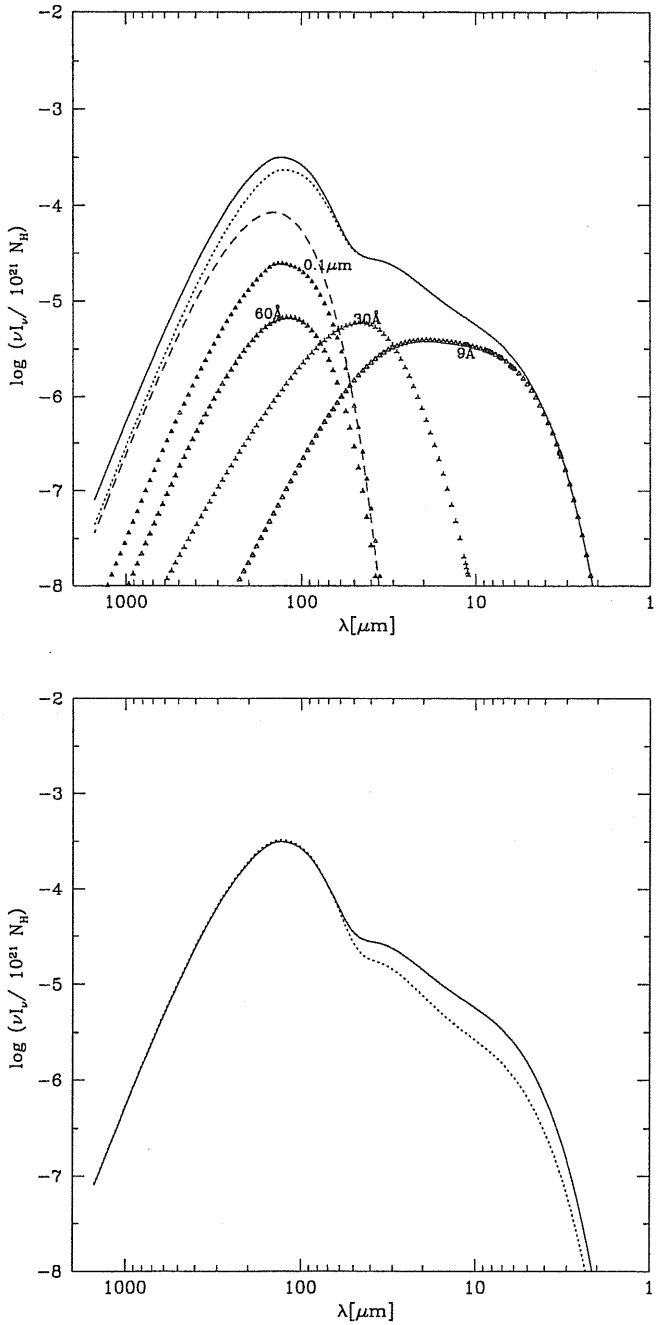

Figure 2.4: *Above:* Cirrus emission (erg s^{-1} cm^{-2} st^{-1} N_H^{-1}) for our dust model (without PAH). The contribution from graphite (dotted) and silicate (dashed) are shown, as well as from some single graphite grains, whose radii are indicated. *Below:* The Galaxy cirrus emission for our dust model (continuous) is compared with the one (dotted) that would be obtained with $a_{min} = 8$ Å for graphite grains keeping the same slope of -3.5. The two curves differ by a factor ~ 2 correspondig to the enhanced number of small fluctuating grains (see Sec. 2.4.1).

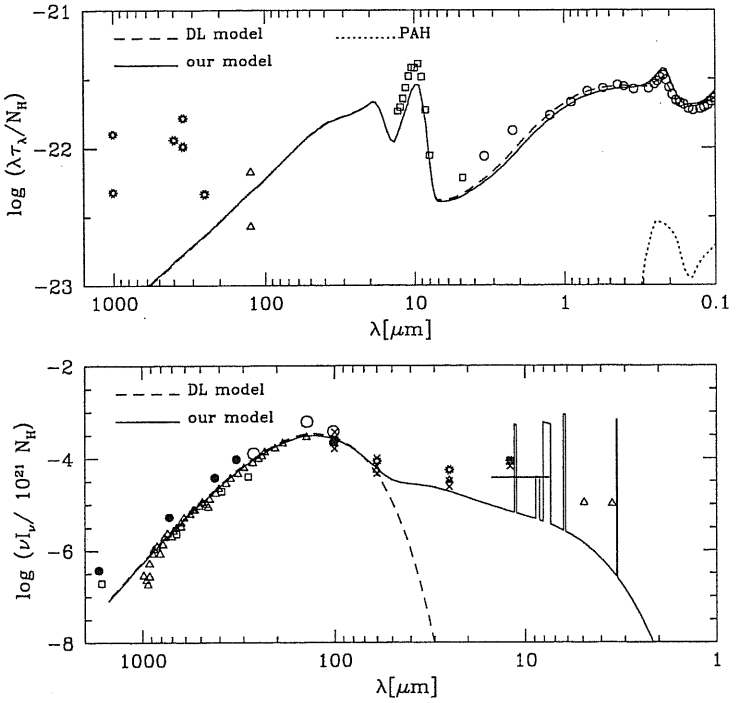

Figure 2.5: *Upper panel:* the extinction curves of the dust model we adopt for diffuse and molecular gas, and that by Draine & Lee (1984) are compared with available data. *Lower panel:* the predicted emissivity of grains (erg s^{-1} cm^{-2} st^{-1} N_H^{-1}) in the local interstellar radiation field (Mathis, Mezger, & Panagia 1983) compared with observations toward the galactic pole. The orizontal line around 12μm marks the flux level obtained by convolving our expected SED with the 12μm IRAS passband. Triangles in the lower panel are data from Dwek et al. (1997), for references to other observations see Rowan–Robinson (1992, 1986)

abundances of the elements and the dust in the Galaxy.

The number of atoms of a given type in dust grains per million H atoms (ppM hereafter) is given by $\frac{m_i}{A m_H}$, where A is the atomic mass, 12 for graphite grains and 169 for silicate grains [assuming an olivine–type silicate composition of $(Mg_{1.1}Fe_{0.9}Si)O_4$]. As a result, in DL as well as our model, 282 ppM of C and 32.6 ppM of Si (a comparable number for Mg and Fe atoms and 4 times as many O atoms) are locked in dust grains.

These values must be compared with the correspondig cosmic abundances. Recently evidence has been accumulated that the abundances of heavy elements in the ISM are less than their solar values.

The model carbon abundance is 55 % of the solar abundance which was adopted by DL as cosmic reference, but $\sim$ 80 % of the more recent estimate in the solar system $\simeq$ 355 ppM quoted by Grevesse & Noels (1993). In young star photospheres carbon is found to be only $\simeq 200-250$ ppM (e.g. Snow & Witt 1995, 1996; Gies & Lambert 1992).

This, if really representative of the ISM abundance, would put restrictions difficult to meet by carbon–based dust models (Sofia, Cardelli, & Savage 1994; Cardelli et al. 1996; Mathis 1996), especially when taking into account that about 140 ppM seem to be in gas phase (Cardelli et al. 1996), leaving for dust only about 1/3 of the C required by the DL model. This has given rise to the so–called *carbon crisis* (Kim & Martin 1996).

Moreover the ISM abundances of other heavy elements seem to be depleted by $\sim 60 - 80$ % compared to their solar values (see the review by Mathis 1996). Therefore the crisis is not restricted to carbon but applies to Mg, Si and Fe as well. In fact the dust model uses up almost all the available solar abundances of these elements (respectively 38, 36 and 32 ppM, while 17 % of solar O is in silicate dust – Grevesse & Noels 1993).

Possible ways out have been suggested: for instance big grains could be porous, likely because they are built up by sticking of smaller ones (Mathis & Whiffen 1989; Mathis 1996, 1998), or dust could be to some extent prevented to be incorporated into stars during their formation (Snow & Witt 1996). Also, the use of more complex size distributions than a simple power law, an elongated grain shape and, for carbonaceous grains, the introduction in a form other than graphitic (amorphous carbon, possibly hydrogenated, or composite grains), tend to alleviate the abundances requirements (Mathis 1996; Kim & Martin, 1996).

Since these problems are still far from being clarified and our major concern is to obtain a good description of the absorption and emission properties of dust, we maintain by now a DL–type model, with only the minimum modifications required to obtain an acceptable overall match of the extinction curve from the UV to the far–IR and of the galactic cirrus emission. It is worth noticing that in the future this goal should be achieved with a more efficient use of the available cosmic abundances.

2.5 The radiative transfer in dusty media

As already pointed out, the dust effects on SEDs depend on the relative distribution of stars and dust. The assumed geometry and galaxy components are sketched in Fig. 2.6. We take into account three components:

- star forming molecular clouds complexes, hereafter MCs, comprising dusty gas in a dense phase, H II regions and very young stars embedded in it (young stellar objects YSO);
- stars already escaped from these dense clouds (henceforth *free stars*);
- diffuse gas (cirrus).

Once we set the distribution of gas and stars (Sec. 2.5.1), we ascribe a fraction f_{mc} of the model gas mass $M_{\rm gas}$ at age t_G to MCs, subdivided into clouds of given mass and radius (i.e. optical depth). The remaining is in the diffuse phase. The energy source inside MCs is due to newly born stellar generations, which gradually escape as they get older. The computation for this dense phase of the ISM is in Sec. 2.5.2. The starlight from older generations and the emission from MCs are the energy source for the diffuse dust (Sec. 2.5.3): the volume emissivities j^*_λ and j^{mc}_λ (erg cm^{-3} s^{-1} st^{-1} Å^{-1}) of the galaxy at each point determine the local radiation field heating the diffuse dust in all

δ	dust-to-gas mass ratio; can be fixed or $\propto Z$ (Sec. 2.4.4)
f_{mc}	fraction of gas in MCs (Sec. 2.5.2)
m_{mc}, r_{mc}	mass and radius of MCs;
	they define $\tau_{mc} \propto \delta\, m_{mc}/r_{mc}^2$ (Sec. 2.5.2)
t_0	escape time of young stars from MCs (Sec. 2.5.2)
T_s	sublimation temperature for dust inside MCs (Sec. 2.5.2)
$r_c^{*,c,mc}$	core radii of King profiles for stars and dust (Eq. 2.20)
$R_d^{*,c,mc}$	scalelengths of exponential disks for stars and dust (Eq. 2.18)
$z_d^{*,c,mc}$	scaleheights of exponential disks for stars and dust (Eq. 2.18)

Table 2.2: Input parameters of GRASIL. Note that the actual number of the scale parameters for disks is 2, since in general we simply set R_d and z_d to the same values for all the components (e.g. Chaps. 4 and 6). Moreover there is 1 true fitting parameter for the emission from MCs, their optical depth τ_{mc}. This means that identical SED from MCs are produced keeping constant the ratio $\delta m_{mc}/r_{mc}^2$. The sublimation temperature for graphite and silicate dust grains inside MCs affects their short wavelength ($\lesssim 10\mu$m) emission from clouds; this parameter is needed because of the simplified geometry of a central point source inside MCs. In general we find that a fixed value of 400 K is able to reproduce the MIR spectra of galaxies. See text for details.

other volume elements, thus the local dust emission j_λ^c. The galaxy volume integral yields the observed flux.

The input parameters of GRASIL are summarized in in Table 2.2. These computations require a proper setting of the grids of radial and angular arrays. These details are in App. A.3.

2.5.1 Geometry

In Silva et al. (1998) we considered either spheroidal or disk dominated systems. In order to describe galaxies of all morphological types we have introduced more recently a general geometry consisting in a composite disk + bulge system. In any case we assume azimuthal symmetry as well as planar symmetry with respect to the equatorial plane (Fig. 2.6). This was firstly required to provide a proper observational interface to the semi–analitycal models of galaxy formation described in Chap. 6.

Distributions

We work in spherical coordinates (r, θ, ϕ). The densities of the three components ρ_{mc}, ρ_*, and ρ_c respectively, depend on r and θ through analytical laws. In the following, unless otherwise explicitly stated, ρ_{mc} and ρ_* have identical spatial dependence. In order to describe disks, we use a double exponential of the distance from the polar axis $R = r\sin\theta$ and from the equatorial plane $z = r\cos\theta$:

$$\rho_D = \rho_o \exp(-R/R_d) \exp(-|z|/z_d)\,. \tag{2.18}$$

In the code the scale lengths R_d and z_d can be independently set for the three components. In general we simply adopt identical values for them i.e. there are two adjustable

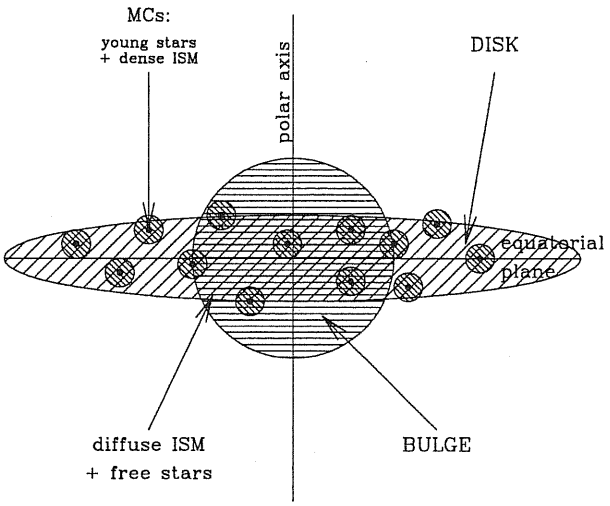

Figure 2.6: Scheme of the components included in our model computations and their adopted geometry.

parameters for disks: $R_d^* = R_d^{mc} = R_d^c$ and $z_d^* = z_d^{mc} = z_d^c$ (as for instance in the models in Chaps. 4 and 6). Observations within our Galaxy suggest $z_d^\star \sim 0.35$ kpc. As a reference the e-folding scale length is related to the absolute magnitude by

$$\log_{10}(R_d/\mathrm{kpc}) \sim -0.2 M_B - 3.45\,, \tag{2.19}$$

(Im et al. 1995).

In the case of spheroidal systems we adopt for both stars and dust (only for stars in the case of bulges) spherical symmetric distributions with King profile:

$$\rho_B = \rho_o (1 + (r/r_c)^2)^{-\gamma}\,, \tag{2.20}$$

extended up to the tidal radius r_t (see below). As for the stellar component we simply set $\gamma = 3/2$. It has been suggested that the core radius r_c correlates with the luminosity (Bingelli, Sandage, & Tarenghi 1984):

$$\log_{10}\left(\frac{r_c}{\mathrm{kpc}}\right) \sim \begin{cases} -0.3\,(M_B + 22.45) & \text{if } M_B \leq -20\,, \\ -0.1\,(M_B + 27.34) & \text{if } M_B > -20\,. \end{cases} \tag{2.21}$$

The distribution of dust in spheroidal systems is poorly known, but it has been suggested that $\rho_{\mathrm{dust}} \propto \rho_{\mathrm{stars}}^n$ with $n \simeq 1/2 \div 1/3$ (Froehlich 1982; Witt et al. 1992; Wise & Silva 1996), i.e. $\gamma \simeq 0.5 \div 0.75$. In other words the dust distribution seems to be less concentrated than that of stars. In particular an additional cool component located in the outer parts has been invoked to explain IRAS observations (Tsai & Mathews 1996).

Galaxy radius

The model galaxy is assumed to extend to a radius R_{gal} fixed according to the distribution of gas and stars.

Since the mass within the exponential profile converges at ∞, we truncate disks at $R_{gal} = 6R_d$, where R_d is the largest among the scale-lengths of three components. Since more than 98% of the mass is included within these radii, adoption of larger cut off radii would not produce any significant difference.

Spheroidal systems are assumed to extend up to the tidal radius $R_{gal} = r_t = 10^{2.2} r_c$ (r_c is the core radius of the stellar component). This truncation radius is required in King models since $M(r)$, the mass contained within r, diverges as $r \to \infty$. Anyway our results are not very sensitive to its precise choice, thus we simply adopted the standard value.

For composite systems, we fix the radius to the largest value we get for the two components.

2.5.2 Radiation transfer in MCs and emerging spectra

In the Galaxy virtually all the star formation activity resides in molecular clouds. Maps of CO and other tracers, show that MCs are non-uniform, highly structured objects, containing density-enhanced regions, the cores, wherein star formation actually occurs. This implies the clustering of young stars at different locations inside giant molecular clouds, as confirmed by infrared imaging. The first evolutionary stages are hidden at optical wavelengths and a significant fraction, if not all, of the energy of young stellar objects is reprocessed by dust and radiated in the IR, only a minor fraction being reradiated as recombination lines. The powerful stellar winds and outflows, and the ionizing flux from massive stars, all contribute to the destruction of the molecular clouds in a time scale comparable to the lifetime of OB stars, $\sim 10^6 - 10^7$ yr. Thus stars gradually get rid of their parent gas and become visible at optical wavelengths. The typical dust densities in these objects are so high that even IR photons are self absorbed, thus to compute the emitted SED the radiative transfer equation must be solved.

The complex evolution depicted above is simulated as follows. A fraction f_{mc} of the model gas mass $M_{\rm gas}$ at t_G is ascribed to the dense phase under discussion in this section. Recent estimates in our Galaxy suggest that half of the hydrogen mass is molecular H_2, mainly in clouds with diameters $\gtrsim$ 10 pc. The molecular gas $M_{mc} = f_{mc}\, M_{\rm gas}$ is then sub-divided into spherical clouds of assigned mass and radius, m_{mc} and r_{mc}, which may range in the typical observed intervals $\sim 10^5 - 10^6\ M_\odot$ and $\sim 10 - 50$ pc respectively. It is then supposed that each generation of stars, represented in our scheme by a SSP, is born within the cloud and progressively escapes it. This is mimicked by linearly decreasing the fraction f of SSP energy radiated inside the cloud with its age t:

$$f = \begin{cases} 1 & \text{if } t \le t_o\,, \\ 2 - t/t_o & \text{if } t_o < t \le 2\,t_o\,, \\ 0 & \text{if } t > 2\,t_o\,. \end{cases} \tag{2.22}$$

The model parameter t_o introduced by this relation sets the fraction of starlight that can

escape the starbursting region. The starlight locked up inside the cloud is approximated as a single central source.

The cloud optical depth, the real parameter setting the shape of the cloud spectrum, is fixed by the cloud mass and radius and by the dust-to-gas ratio ($\tau_{mc} \propto \delta\, m_{mc}/r_{mc}^2$). The emerging spectrum is obtained by solving the radiative transfer through the cloud with the code described by Granato & Danese (1994).

We summarize here only its main features. The transfer of radiation originating from a central source in an axisymmetric dust distribution is solved with the lambda–iteration method: at each iteration the local temperature of dust grains is computed from the condition of thermal equilibrium with the radiation field estimated at the previous iteration. The convergence is speeded up with respect to this simple scheme following the prescriptions given by Collison & Fix (1991). Moreover, in the present case (as for the AGB envelopes in Chap. 3), the computing times are reduced by about two orders of magnitude taking advantage of the spherical symmetry of the clouds. This code has been widely used in a different context, namely models of dusty tori around AGNs (see Granato et al. 1997 and references therein). Thus it is well tested in the more complex situation where spherical symmetry breaks down.

The distribution of stars in real GMCs implies a dust temperature distribution with many hot spots and cooler regions randomly distributed. A complete discussion of the effects of different approximations in this complex geometrical situation, including the single central source adopted here, can be found in Krügel & Siebenmorgen (1994, see in particular their Fig. 1a). An obvious drawback of our approach is an overestimate of the amount of very hot dust around the source, with respect to the more realistic approximation in which the stars are split in many sources at different locations. On the other hand the approximation of a central point source is not much different from the IR spectrum predicted by a full treatment with hot spots, if the emission from the whole cloud is considered (Krügel & Siebenmorgen 1994).

Since the treatment of many hot spots in the cloud would introduce many other geometrical parameters and would slow down considerably our code due to the loss of symmetry, we simply treat the maximum temperature T_s of the grains at the inner edge as a parameter, summarizing in some way the geometrical parameters which would result in a lower 'true' maximum temperature: lowering the grain 'sublimation' temperature produces a lower average temperature with a less opaque cloud. This brings the overall spectrum very close to that predicted with a proper treatment of the hot spots. It is anyway interesting to note that Gordon et al. (1997) found that their *shell geometry*, similar to that adopted here, is suited to explain the observed optical and UV properties of starburst galaxies, while the *dusty geometry*, in which dust and stars share the same spatial distribution, is not, even allowing for clumpiness.

For typical values of the relevant parameters our model predicts IR spectra of star forming regions peaking around 40–60 μm (in a νL_ν plot), depending on the optical depth, with a rather steep decrease at longer wavelengths. We found that this behavior reproduces quite well the typical range of IR spectra of galactic YSOs, H II, and star forming regions (e.g. Rowan–Robinson 1979; Ward-Thompson & Robson 1990; Men'shchikov & Henning 1996). For instance in Fig. 2.7 the observed SED of W49A, a huge star–forming region composed of H II regions and giant molecular clouds, is compared with the spectrum of the MC component we use in the fit of the overall SED of

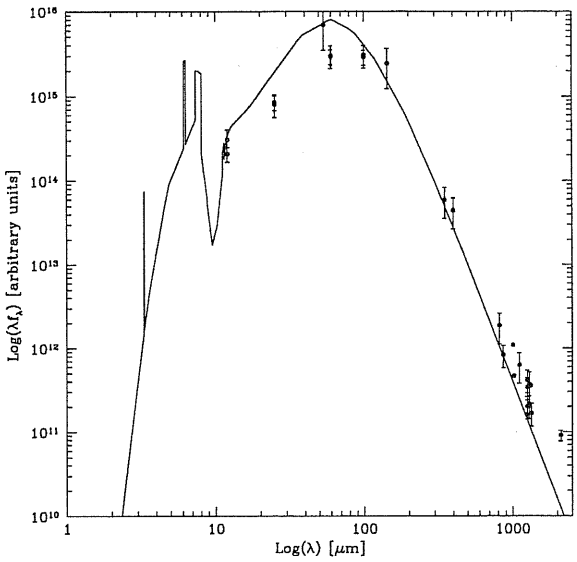

Figure 2.7: The observed SED of W49A (Ward-Thompson & Robson 1990), a huge star–forming region composed of H II regions and GMCs, is compared with the spectrum of the MC component we use in the fit of the overall SED of Arp 220.

Arp 220. Indeed we think that this ultraluminous infrared galaxy is a good benchmark for our MCs model, having an IR spectrum dominated by this component (see Sec. 4.2).

2.5.3 Propagation in the diffuse ISM and cirrus emission

Before escaping the galaxy the light arising from stellar populations and from molecular clouds interacts with the diffuse dust component.

We adopt a simplified treatment of radiative transfer in the diffuse gas which ignores dust self–absorption and approximates the effects of optical–UV scattering by means of an effective optical depth, given by the geometrical mean of the absorption and scattering efficiencies $\tau_{eff}^2 = \tau_a(\tau_a + \tau_s)$ (Rybicky & Lightman 1979, p. 36). Indeed the relatively low opacity of dust in the IR regime, where the dust emission occurs, implies that in most cases of interest the diffuse ISM is transparent to its own photons (see below).

The galaxy is subdivided into small volume elements V_i. The local (angle averaged) radiation field in the i–th element due to the extinguished emissions of free stars and MCs from all the other elements is computed from:

$$J_{\lambda,i} = \sum_k \frac{V_k \left(j^{mc}_{\lambda,k} + j^{*}_{\lambda,k}\right) \exp\left(-\tau_{eff,\lambda}(i,k)\right)}{r^2(i,k)} \quad \frac{erg}{cm^2\ s\ st\ \text{Å}}\,, \tag{2.23}$$

where $\tau_{eff,\lambda}(i,k)$ and $r(i,k)$ are the effective optical thickness and the distance between the elements i and k respectively ($r(i,k)$ is a volume average of the square of the distance from i to all points within volume k, see App. A). Then the local dust emissivity j^c_λ is calculated as described in Sec. 2.4 (Eqs. 2.14 and 2.16).

Therefore the volume emissivity of the galaxy at each point is the sum of three terms:

$$j_\lambda = j_\lambda^{mc} + j_\lambda^{*} + j_\lambda^{c} \quad \frac{erg}{cm^3\, s\, st\, \text{Å}}. \tag{2.24}$$

Finally the specific flux measured by an external observer in a given direction θ is derived as a sum over the galaxy of the extinguished emissivity of free stars, MCs, and diffuse dust:

$$F_\lambda(\theta) = 4\pi \sum_k V_k\, j_{\lambda,k}\, \exp\left(-\tau_{eff,\lambda}(k,\theta)\right) \quad \frac{erg}{s\, \text{Å}}, \tag{2.25}$$

where $\tau_{eff,\lambda}(k,\theta)$ is the optical thickness from the element k to the outskirts of the galaxy along the direction θ (this is the equation corresponding to eq. 2.8 when only stars are considered).

Deviations from the energy balance between dust emission and absorption, which mainly depend on the number of volume elements in which the galaxy is subdivided, are kept within $< 2 - 5\%$.

Our approximation for combined scattering and absorption processes is rigorously applicable only to an infinite homogeneous medium and isotropic scattering. However we checked this approximation by comparing our results with those obtained by Witt et al. (1992) and by Ferrara et al. (1999) by means of Montecarlo radiative transfer codes. The comparisons between the attenuation curves are in Figs. 2.8 and 2.9 respectively. We find an excellent agreement in the former case, referring to systems with spherical symmetry. The latter models are instead for composite systems. The cases depicted in Fig. 2.9 are for pure disks and only the diffuse phase for the ISM (see the caption of the figure). We find an almost perfect agreement for edge-on disks while we overestimate (always by less than $\sim 20 - 25\%$ and $\sim 10\%$ in the V band) the attenuation for diminishing inclination angles. Therefore our approximation for scattering with the effective optical depth defined above, results a good one for our purposes, and even more considering the uncertainties in the "true" dust scattering phase functions. Moreover in our clumpy medium the optical-UV extinction is in most cases strongly dominated by MCs, where we have a better treatment of scattering than in the diffuse phase.

2.6 Modelling radio emission

We have further extended the range of wavelengths covered by our model computing the radio emission due to the SF activity. Above ~ 1 mm dust emission is overwhelmed by radio emission that, for normal galaxies, is due to synchrotron radiation from relativistic electrons accelerated in supernova remnants, and to a lesser extent, to free–free emission from HII regions (see the review by Condon 1992). We have adopted the simple recipe given by Condon & Yin (1990), relating the nonthermal radio emission from galaxies to the type II supernova rate:

$$L_{NTh}(\nu) = 1.3\, 10^{23}\, \nu_{Ghz}^{-\alpha}\, SNR_{yr^{-1}} \quad \frac{W}{Hz} \tag{2.26}$$

where $\alpha = 0.8$ is the synchrotron spectral index. $L_{NTh}(\nu)$ is calibrated according to the total radio energy per supernova in the Galaxy, as given by the ratio between the observed total nonthermal luminosity (they adopt $L_{NTh} = 6.1\, 10^{21}$ W Hz^{-1} at 408

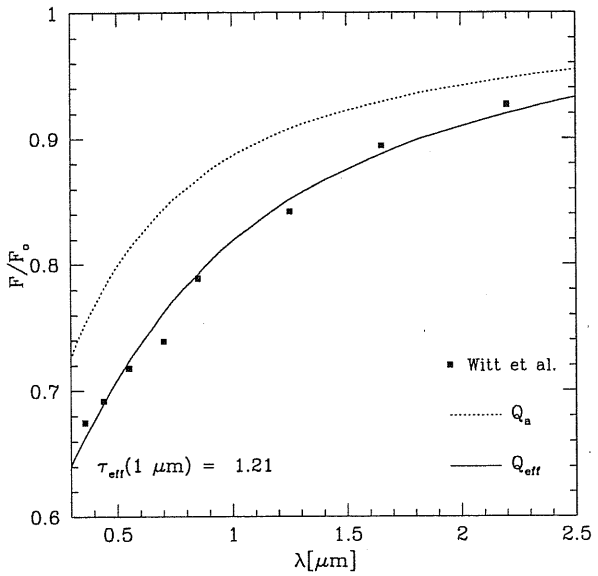

Figure 2.8: F/F_o, the attenuation curve, is the ratio between the dust extinguished flux and that expected if dust were not present. The points have been computed by Witt et al. (1992) with a Montecarlo radiative transfer code including anisotropic scattering, the dashed line represents the result of our code taking into account only absorption, whilst the solid line includes scattering with the effective optical depth $\tau^2_{eff} = \tau_a(\tau_a + \tau_s)$. The adopted geometry is that defined by Witt et al. as *elliptical galaxy*. We find that our approximation is fairly good in most "real–world" geometrical arrangements

MHz) and the type II SNR. They adopt the Tammann (1982) value. With the new estimates for the galactic type II SNR by Tammann et al. (1994) and Cappellaro et al. (1997) the constant of calibration is a factor ~ 1.1 to 1.6 higher. Moreover M_{up}, the minimum mass of stars exploding as type II SN, introduces a factor ~ 2 (for $M_{up} = 5$ or 8) of uncertainty in the amount of radio emission through the corresponding value computed for the SNR (Eq. 2.6).

The thermal component of the radio emission is taken into account exploiting the radio–IR correlation holding for local star–forming galaxies and regions, separately for the thermal and non–thermal component. Condon & Yin (1990) estimate $\log(L_{60\mu m}/L_{Th}) \sim 3.12$ at 2.7 Ghz in galactic HII regions and star forming galaxies. This same ratio at 1.4 Ghz (where the nonthermal radio component dominates) is observed to be 2.15 for infrared–selected galaxies. Assuming a spectral index of 0.1 for the free–free spectrum, the radio–IR ratios yield:

$$\frac{L_{NTh}(\nu)}{L_{Th}(\nu)} = 10.9\,\nu_{Ghz}^{0.1-\alpha} \tag{2.27}$$

Therefore the reproduction of the radio emission of galaxies provides an estimate of the SFR (of massive stars) to be compared with the one powering the IR emission from MCs (and estimated keeping into account the constraints set by the overall spectrum from the UV to the submm). This check is not based on the IR–radio correlation, even

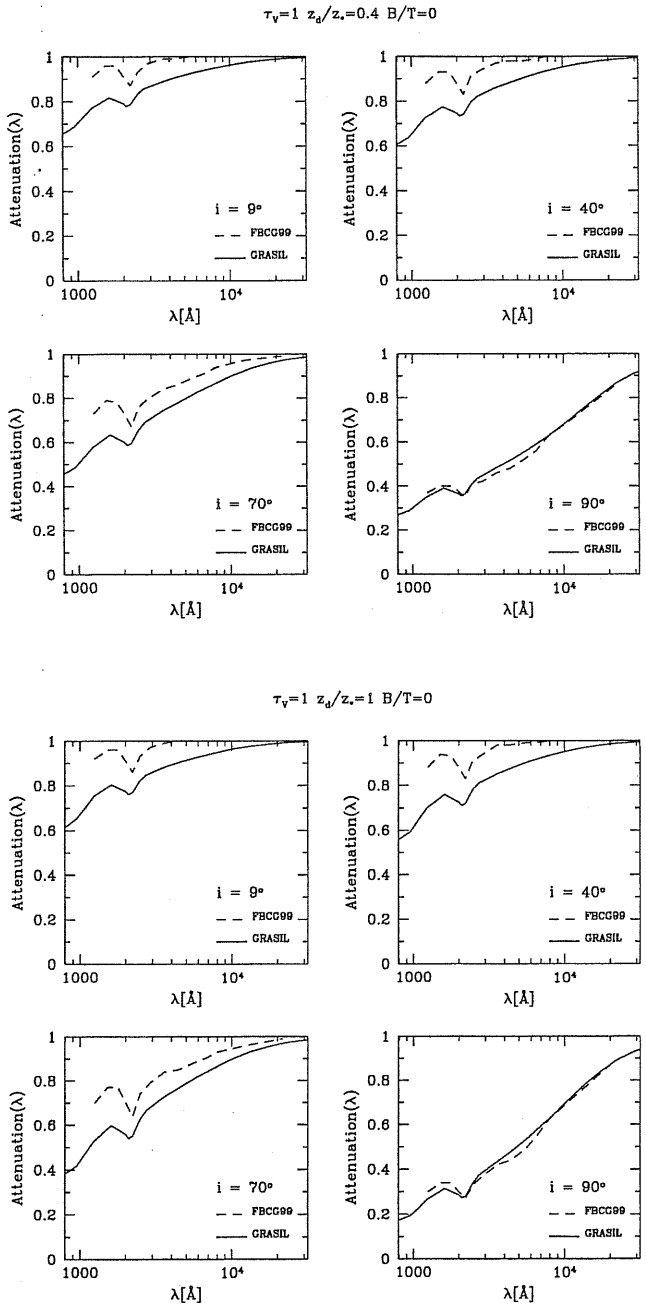

Figure 2.9: Comparison between the attenuation curves computed by Ferrara et al. (1999, FBCG99) and ours (GRASIL) for pure disks (the easiest choice to best reproduce the same conditions for the two models) with only the diffuse phase of the ISM, the one for which the FBCG99 models are computed. The plots shown are for $\tau_V = 1$ (but the result is general), 3 values of the ratio z_d^c/z_d^* (the disk scale-heights for diffuse dust and stars) and different inclinations. The agreement is almost perfect for edge-on disks while we overestimate the attenuation for diminishing inclination angles. The differences are never higher than $\sim 20 - 25\%$, increase for smaller λ and are always $\sim 10\%$ in the V band. See text.

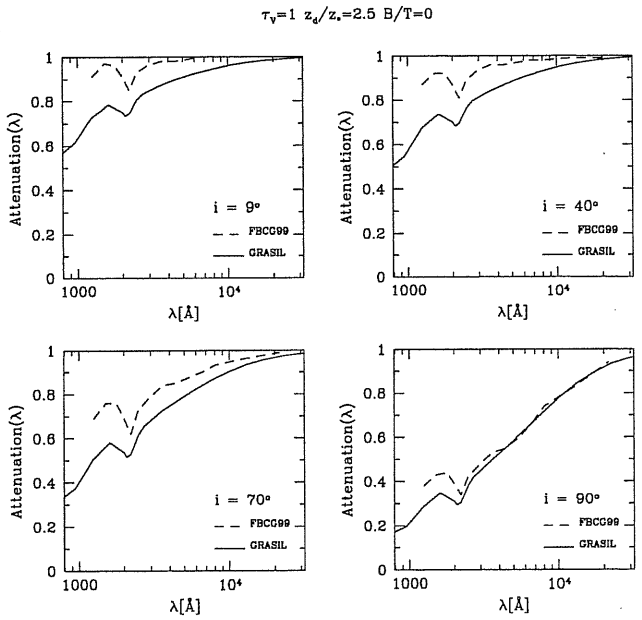

Figure 2.9: *Continued*

if the latter is reproduced with the adopted relations (e.g. see the fits to the SED of local galaxies in Chap. 4). Instead, the assumptions of these relations are that a fixed ratio between the two radio components holds, and that SN remnants in galaxies share the same global properties determining the same average energy per SN event.

2.7 Modelling nebular emission

We are at present working to include in GRASIL nebular emission from ionized HII regions and diffuse gas (Panuzzo et al. 1999).

The self-consistent inclusion of emission from ionized gas together with dust reprocessing is a necessary step forward to interpret star forming galaxies from their spectra. Indeed, while the energy balance of galaxies is essentially set by dust reprocessing, emission lines are direct probes of the physical and chemical conditions of the ISM, as well as of the main source of energy in galaxies (starburst or AGN). Then, since lines are mostly powered by young stars, they provide a further constraint on the SFR estimated from the IR emission by dust. Moreover, high-resolution spectral and broadband data are already or will soon be available for nearby and high-z galaxies, requiring this kind of complex modelling in order to be properly exploited to investigate on galaxies properties.

Here only a summary of the method to include nebular emission is presented (see Panuzzo et al. (1999) for details). With the code CLOUDY we computed grids of models for HII regions ionized by spectra from our SSP library. The input parameters of the grids are the following: gas density n_H and metallicity, and radius r of the HII region. In order to interpolate on the grid of nebular spectra, the latter are then parametrized,

for given n_H and r, as a function of the number of ionizing photons for H, He and O, i.e. $Q(H)$, $Q(He)$ and $Q(O)$ (s^{-1}; indeed $Q(H)$ is linked to the intensity of the ionizing radiation field and the ratios $Q(He,O)/Q(H)$ provide a measure of its 'hardness'). Therefore we associate to each stellar generation in the model galaxy the line spectrum pertaining to its spectral and environmental properties. The ensuing radiative transfer through the dusty media is then performed as already described in the previous sections.

A preliminary investigation of staburst spectral lines with this model (examples are in Chap. 4) seems to require the introduction of a third component in the ISM, with an optical depth intermediate between MCs and diffuse medium. Indeed we find that the high optical thickness of MCs, wherein all the youngest stars are embedded, allows only IR lines to emerge. The UV photons from older stars, already out from the parental clouds, are not enough to reproduce the observed UV–optical–NIR lines. The latter are reproduced with clouds with optical depths lower by a factor $\sim 10-20$ ($A_V \sim 3$) than normal MCs, involving a fraction $\sim 0.1-0.2$ of youngest stars.

Therefore the dust+lines model is a 3 component one: (1) starburst MCs, with dense ISM and youngest stars, providing IR nebular emission; (2) normal MCs, with intermediate density ISM and a a small fraction of young stars, interpreted as stars near the edge of MCs or associated with the quiescent star formation rather than the starburst one. This component provides the optical and NIR lines; (3) diffuse ISM, with older stars and providing optical, MIR nebular continuum and faint optical, NIR lines.

Chapter 3

SSP spectral library with AGB dusty envelopes

Summary. We[1] present our spectral library of single stellar populations (SSP), the building blocks of galaxy models. We first investigate the spectrophotometric properties of the asymptotic giant branch (AGB) stars in order to include their contribution to the integrated IR emission in SSP. To this aim, adopting analytical and empirical relations to describe the evolution of AGB stars in the HR diagram, their mass–loss rate and wind terminal velocity, we are able to model the effects of the dusty envelope around these stars. We then compute isochrones at different age and initial metal content. We compare our models with infrared colors of M giants and Mira stars and with IRAS PSC data. The former data are fairly well reproduced. The isochrones of different metallicity follow a single path in the IRAS two color diagram, fixed by the composition and optical properties of the dust mixture: the bulk of the data is delimited by the curves corresponding to a mixture of silicate grains and one of carbonaceous grains. In the new isochrones the mass–loss rate, which establishes the duration of the AGB phase, also determines the spectral properties of the stars. The contribution of these stars to the integrated light of the population is thus obtained in a consistent way. We find that the emission in the mid–IR is about one order of magnitude larger when dust is taken into account in an intermediate age population. The dependence of the integrated colors on the metallicity and age is discussed, with particular emphasis on the problem of the age–metallicity degeneracy. We show that, contrary to the case of optical or near–IR colors, the adoption of suitable passbands in the mid–IR allows a fair separation of the two effects. We suggest intermediate redshift elliptical galaxies (and/or post starburst galaxies) as possible targets of this method.

[1]This Chapter is based on the paper *Bressan A., Granato G.L., & Silva L., 1998, A&A, 332, 135* (Bressan et al. 1998).

3.1 Introduction

Effects of dust in the envelopes of Mira and OH/IR stars are usually neglected in the spectrophotometric synthesis of a composite population, on the notion that the contribution of dust enshrouded stars to the integrated bolometric light is negligible. This can be justified in very old systems, not in intermediate age ones, where AGB stars are the brightest tracers. In these stars, the light absorbed by dust at optical wavelengths is thermally reemitted in a broad region from a few to a few hundred microns, where it overwhelms the stellar component. In addition, molecular lines and often maser emission are observed.

Dust and molecular emission from Mira and OH/IR stars are interpreted as a signature of an expanding circumstellar envelope, where gas particles reach the escape velocity giving rise to significant mass loss (Salpeter 1974a,b, Goldreich & Scoville 1976, Elitzur et al. 1976). In fact it is believed they are undergoing their final nuclear evolutionary phase where low and intermediate mass stars lose the whole envelope and turn toward the fate of a white dwarf.

The process responsible of the observed huge mass loss is still unknown but there are both observational and theoretical evidences that large amplitude pulsations coupled with radiation pressure on dust grains play a major role: (1) a tight correlation between mass–loss rate and period of pulsation (see Habing 1996 for a thorough review) has been observed. On the other hand, hydrodynamic models show that large amplitude pulsations may levitate matter out to a radius where radiation pressure on dust accelerates the gas beyond the escape velocity (Bowen & Willson 1991); (2) luminosity functions of AGB stars in the Large Magellanic Cloud (LMC) indicate that the mass loss along this phase is far larger than that predicted by the usual Reimers law which successfully describes the evolution along the red giant branch in old systems. A super–wind phase (Fusi-Pecci & Renzini 1976) is often invoked to account for the paucity of bright AGB stars. A mass–loss rate exponentially increasing with time, naturally evolving into a super–wind phenomenon, is obtained both by the hydrodynamic models of Bowen & Willson (1991) and by the semiempirical treatment of Vassiliadis & Wood (1993–VW).

Moreover only mass–loss rates that include a super–wind phase can account for the relation between the initial stellar and final white dwarf mass (e.g. Weidemann 1987).

In spite of the link between mass–loss rate and IR emission in these objects very few attempts have been made to provide a coherent picture of the photometric evolution of an AGB star toward its final fate. In particular existing isochrones do not account for the effects of dust around AGB stars and are inadequate to study the photometric properties of star clusters and galaxies when these stars contribute a significant fraction of the light. Therefore we constructed a set of theoretical models which account for the effects of the circumstellar envelope and obtained a new set of isochrones suited for the analysis of the IR and mid–IR data.

Our approach is different from that adopted in several previous works. Usually a physically sound model is constructed and fitted to observations to obtain the model parameters: mass–loss rate, effective temperature, grain composition and so on. The ensemble of fits to specific objects then allows to parametrize the mass–loss rate as a function of the period of the stars, a relation that has been widely adopted in model computations.

Here we proceed along the opposite direction. We express the mass–loss rate, dust–to–gas ratio and outflow velocity of AGB stars envelopes (the main parameters driving the spectral properties of the envelopes) as a function of the basic stellar parameters (mass, luminosity, radius and metallicity) from semi–empirical relations (VW). Then for any given star we compute the radiative transfer of the photosferic spectrum through the envelope pertaining to that star.

Sec. 3.2 describes the envelope model. A relation between the optical depth of the envelope τ at 1μm (hereafter τ_1) and the envelope parameters mass–loss rate and expansion velocity is obtained. This is the parameter driving the spectral properties of the envelope. Then the radiative transfer equation through a spherically symmetric stationary flow of matter provides the dust-modified stellar spectrum. The reliability of the model is tested by comparing it to data.

Sec. 3.3 describes the construction of the isochrones in the HR diagram. Relations providing the mass–loss rate and the expansion velocity of the envelope as a function of the stellar parameters are adapted from Vassiliadis & Wood (1993) with some minor modifications suggested by the comparison of our envelope model with existing observations of stars in the Magellanic Clouds and in our galaxy: in both the super–wind mass–loss rate and the velocity period relation we include a dependence on the metallicity.

In Sec. 3.4 we describe the spectrophotometric properties of the isochrones. For the evolutionary phases before the AGB, the method is identical to the one adopted by Bressan et al. (1994). Along the AGB the suitable envelope model is applied to the otherwise unaffected stellar spectrum to compute the dust-modified one. In this way we are able to obtain consistent isochrones and corresponding integrated spectra in the mid IR. We compare our isochrones with the IRAS two color diagram to test the reliability of our sequence of envelope models. We briefly discuss the difficulty of a monoparametric sequence of envelopes with varying optical depth τ_1 to interpret the latter data, already encountered by other authors (Bedijn 1987, Ivezic & Elitzur 1995). The comparison with near IR colors of a sample of M giants and Miras shows that the inclusion of the dust constitutes a significant improvement with respect to previous models.

Sec. 3.5 is devoted to the spectrophotometric integrated properties of SSP, and in particular to the problem of age–metallicity degeneracy of optical and near-IR colors. We show that extending the colors to the mid–IR may solve the degeneracy at least in intermediate age systems. Therefore possible targets could be intermediate redshift elliptical or post–starburst galaxies with stellar populations of few Gyr old, and where the mid–IR dust emission is not dominated by star formation.

3.2 The dust envelope model

Envelope structure

Radiative transfer in dusty shells around "windy" stars has been previously considered by many authors (see Habing, 1996 and references therein). The most advanced approaches couple the radiative transfer and the hydrodynamic equations of motion for the two interacting fluids of the wind, the gas and the dust (Habing et al. 1994; Ivezic & Elitzur 1995). This is necessary to achieve a fully consistent solution, because the

radiation pressure on dust grains is widely believed to be the main driver of the high $\dot{M}$ observed in OH/IR stars.

However our interest here is to "correct" the stellar spectra predicted by standard evolutionary tracks by including the effects of dusty envelopes associated with AGB mass-loss. We need therefore a recipe, consistent with available observations, to associate the fundamental parameters of the star, in particular its luminosity L, radius R, mass M and metallicity Z, with the parameters of its dusty shell which are most relevant in determining its spectral effects. In Sec. 3.3.1 we collect semi-empirical relations allowing to determine the outflow velocity $v_{\rm exp}$ and the mass loss rate $\dot{M}$ as a function of these parameters. Thus here we assume that $v_{\rm exp}$ and $\dot{M}$ of the model star are known, and we will show how the corresponding spectral properties of the dust envelope are derived.

We adopt spherical symmetry and, in a first order picture, an outflow velocity $v_{\rm exp}$ independent of radius. Thus for a given $\dot{M}$, the dust density outside the sublimation radius r_{in} wherein the grains are supposed to form suddenly, scales as r^{-2}:

$$\rho_d(r) = \frac{\dot{M}\delta}{4\pi v_{\rm exp}} \frac{1}{r^2} \tag{3.1}$$

where δ is the dust–to–gas mass ratio. The envelope extends out to a radius $r_{out} = 1000\, r_{in}$. Our results are fairly independent of reasonable changes of the ratio r_{out}/r_{in}.

The dust-to-gas mass fraction δ can be expressed as a function of $v_{\rm exp}$ and L as follows. It is widely believed that the high mass loss rates in the AGB phase are driven by the transfer of momentum of photons to the dust grains and then to the gas (see Sec. 3.3.1). Therefore a close relationship between the dust abundance and the velocity of the flow is expected. The problem has been studied carefully by Habing et al. (1994), who confirmed that the terminal velocity of the gas flow $v_{\rm exp}$ depends rather strongly on δ. On the other hand they found also that the flow reaches quickly a velocity close to $v_{\rm exp}$, in keeping with our previous assumption, and that the difference between the dust and the gas velocity is positive and decreases with increasing $\dot{M}$. At the high mass loss rates mostly relevant for this work the two velocities are within 10 %, and the results by Habing et al. can be well approximated by the simple equation

$$\left(\frac{v_{\rm exp}}{21\,{\rm km/s}}\right) \simeq \left(\frac{L}{10^4 L_\odot}\right)^{0.35} \left(\frac{\delta}{10^{-2}}\right)^{0.5} \tag{3.2}$$

which can be inverted to yield

$$\delta \simeq 0.015\, v_{\rm exp}^2[{\rm km/s}] \left(\frac{L}{L_\odot}\right)^{-0.7} \tag{3.3}$$

Equations 3.1 and 3.3 yield the dust density at each position in the dusty shell, as a function of stellar parameters. Dust grains absorb and scatter the stellar radiation, with an efficiency much greater in the optical-UV regime than in the IR, and reradiate the absorbed energy at IR wavelengths. At the high mass loss rates achieved in the super-wind phase, the involved densities imply that the dust emission is self-absorbed, and therefore to compute the emitted spectrum the radiative transfer problem must be

solved. We use the numerical code by Granato & Danese (1994) (see Sec. 2.5.2 for a summary of its main features).

For the geometry adopted above, the effects of the envelope on the photospheric spectrum of the stars are fully determined by its optical thickness, which given the extinction law (i.e. the dust composition, see below) we parametrize with its 1 μm value τ_1. Integrating Eq. 3.1 from r_{in} to r_{out} we get

$$\tau_1 = \frac{\dot{M}\,\delta\,k_1}{4\pi\,v_{\rm exp}}\frac{1}{r_{in}} \tag{3.4}$$

where the term $1/r_{out}$ has been neglected with respect to $1/r_{in}$ and k_1 is the dust opacity at 1 μm. On the other hand the dust sublimation radius is (Granato & Danese 1994)

$$r_{in} = b\,L^{1/2} \tag{3.5}$$

where the factor b depends mainly on the dust composition (through its melting temperature $\sim$ 1000 K for silicates and $\sim$ 1500 K for graphite), the size distribution and only weakly on the shape of the stellar spectrum. Typical values of b are 2–3$\times10^{12}$ for silicates mixture and 1–2$\times10^{12}$ for carbonaceous mixture. Using this equation and Eq. 3.3 into Eq. 3.4 we get

$$\tau_1 = \alpha\frac{\dot{M}\,v_{\rm exp}}{L^{1.2}} \tag{3.6}$$

where v_{exp} is in km/s, $\dot{M}$ in $M_\odot$/yr and L in $L_\odot$. The quantity α, which incorporates the dependence upon k_1 and b, is affected only weakly by the spectrum of the illuminating star. For hot stars emitting mainly in optical UV regime, where the optical properties of dust do not show orders of magnitude variations with the wavelength, the latter dependence would be quite negligible for practical purposes. By converse in our case (cold AGB stars) the situation is a bit less simple. We checked however with the code that adopting $\alpha = 2.32 \times 10^9$ for the silicates mixture and $\alpha = 9.85 \times 10^9$ for the carbonaceous mixture, the errors in τ_1 estimated from Eq. 3.6 are kept within 5 % for stars with $T_{\rm eff}$ in the range 2500-4000. This is a fair approximation because models with τ_1 differing by less than 5-10 % produce almost identical spectra.

In summary Eq. 3.6 allows us to predict the modifications imprinted by the envelope on the photospheric star spectrum, by means of a suitable radiative transfer code and once relations for $\dot{M}$ and $v_{\rm exp}$ as a function of the fundamental stellar parameters are given. This latter point will be addressed in Sec. 3.3.

Grain mixture for the envelope

For the dust in the envelopes of AGB stars, we adopt the six-grain (three silicates plus three carbonaceous grains) dust model defined by Rowan-Robinson (1986). Specifically, when dealing with OH/IR stars we use the three silicate grains of the model (mixture A), while for carbon stars the three carbonaceous grains (mixture B). The characteristics of the dust grains, type, dimension, density, mass fraction and sublimation temperature are displayed in Table 3.1.

We adopt this dust model for AGB envelopes, different from the one we use for the ISM (see Sec. 2.4), since it is tuned to reproduce the IR spectra of these stars,

Table 3.1: Parameters of the adopted grain mixture.

Type	a [μm]	D [gr/cm^3]	X	T_s [K]
	Mixture A			
Amorph. Sil. ..	0.1	2.50	0.781	1000
Silicate	0.03	2.50	0.189	1000
Silicate	0.01	2.50	0.030	1000
	Mixture B			
Amorph. Carb.	0.1	2.26	0.398	1500
Graphite	0.03	2.26	0.258	1500
Graphite	0.01	2.26	0.344	1500

Table 3.2: Model parameters adopted to fit the energy distribution of star AFGL230 and OH 39.7+1.5. The dust mass–loss rate $\dot{M}_d$ ($M_\odot$/yr) has been computed assuming $v_{\rm exp}$ = 15 km/s; r_{in} is in cm and $\rho_{d\ in}$, the corresponding dust density is in g/cm^3.

τ_1	Log(L/L$_\odot$)	Te	r_{in}	$\rho_{d\ in}$	$\dot{M}_d$
		AFGL230			
29.4	4.715	2500	7.1E+14	5.9E-18	8.9E-07
		OH 39.7+1.5			
15.0	4.715	2500	7.1E+14	3.0E-18	4.5E-07

while the DL model is based on observations the ISM. The FIR DL dust opacities have $Q_{abs} \propto \lambda^{-2}$, while data of late–type stars show a dust emissivity $\propto \lambda^{-1}$, a behaviour that is expected for a disordered material, like amorphous carbon and silicate (see e.g. Marengo et al. 1997).

Comparison with other envelope models

We compared our envelope models to the fits provided by other authors to OH/IR stars spectra such as Justtanont & Tielens (1992) and Bedijn (1987). We found a quite good agreement in the fitting parameters (Figs. 3.1, 3.2 and Table 3.2 respectively) even if these authors have often introduced ad-hoc modifications in the optical properties of dust, variable from object to object, with the aim of giving a better description of the strengths and shapes of the 10 and 18 μm silicate features. We stress once again that our purpose is instead to have a good description of the average properties of grains in circumstellar shells.

Envelopes with density enhancement

We have also tested the effects of the presence of an expanding ΔM_a = 0.02 $M_\odot$ shell of matter superimposed to the standard r^{-2} law. However these effects will not be taken into account in our SSP models and are only meant to illustrate uncertainties brought about by transient phenomena (see Fig. 3.3). Adopting a gaussian profile for the density enhancement due to the annulus alone, centered at $r_a < r_{out}$ and with characteristic

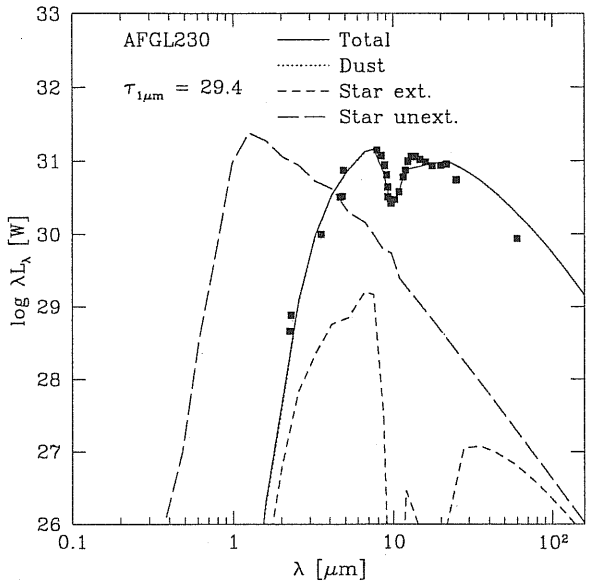

Figure 3.1: A fit to the star AFGL230 (data from Justtanont & Tielens 1992). The parameters of the fit are shown in Table 3.2. Continuous line: emerging spectrum; dotted line, coinciding with the continuous line in this case: dust emission; long dashed line: original photospheric spectrum (T_{eff}=2500 K); short dashed line: extinguished photospheric spectrum.

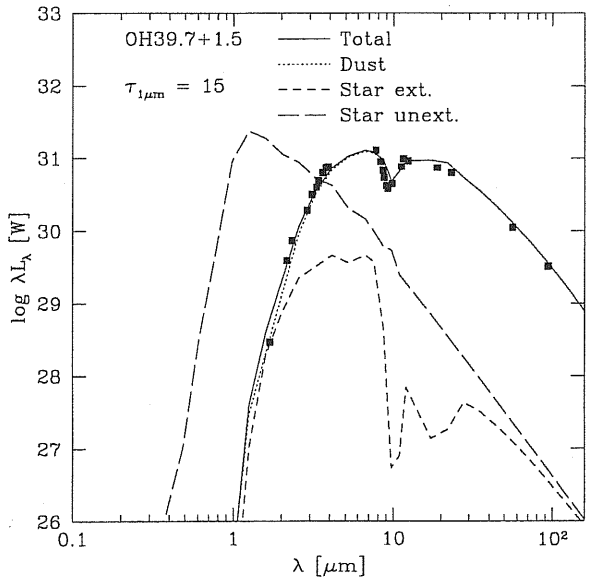

Figure 3.2: The same as in Fig. 3.1 but for OH 39.7+1.5 (data from Bedijn 1987).

width Δr_a, the total dust density becomes

$$\rho_d(r) = \frac{\dot{M}\delta}{4\pi v_{\rm exp}} \frac{1}{r^2} \left[1 + f \times e^{-\left(\frac{r-r_a}{\Delta r_a}\right)^2}\right]. \tag{3.7}$$

It is straightforward to relate the constant f to the mass ΔM_a in the annulus:

$$\Delta M_a = \frac{\dot{M} f}{v_{\rm exp}} \int_{r_{in}}^{r_{out}} e^{-\left(\frac{r-r_a}{\Delta r_a}\right)^2} dr \tag{3.8}$$

To mimic an outward moving density enhancement, we computed three models with $\Delta r_a = 0.1\, r_{out}$ and $r_a = 0.2\, r_{out}$, $r_a = 0.5\, r_{out}$ and $r_a = 0.8\, r_{out}$. Note that the corresponding density enhancement barely affects the optical depth of the envelope, though it may affect the emission in a given spectral region. Indeed the fraction of column density due to the enhancement in the annulus is $\simeq 3 \times 10^{-2} f$, $\simeq 7 \times 10^{-4} f$ and $\simeq 3 \times 10^{-4} f$, respectively, for the three adopted values of r_a/r_{out}. On the other hand the mass–loss rates relevant for this paper are $\gtrsim 10^{-5} M_\odot$/yr while typical values of the outflow velocity are ≤ 20 km/s. Eq. 3.8 yields then $f \leq 5$ which means that the optical depth is always dominated by the standard r^{-2} term.

3.3 The isochrones

To investigate the infrared properties of SSPs we coupled the dusty envelope model with the large library of stellar evolutionary tracks existing in Padova. These tracks are computed for different values of the initial metallicity, keeping constant and equal to the solar partition the relative proportion of the metals. The initial mass of the evolutionary tracks is in the range 0.6 to 120 $M_\odot$ corresponding to ages from few Myr to several Gyr. Since the main interest of this paper is to focus on the photometric properties of AGB stars, isochrones have been computed only for intermediate age and old stellar populations, thus between say 10^8 yr to $16 \cdot 10^9$yr. The initial chemical composition of the evolutionary sequences adopted here (Bressan at al. 1993 and Fagotto et al. 1994a, b), is [Z=0.004, Y=0.24], [Z=0.008, Y=0.25], [Z=0.02, Y=0.28], and [Z=0.05, Y=0.352], respectively.

The evolution of low mass stars is computed at constant mass and mass loss is applied during the procedure of isochrones construction. The mass-loss rate along the RGB is parameterized by the usual Reimers formulation with η=0.45.

Since the Padova models do not extend into the thermally pulsating AGB phase (TP-AGB), an analytic description is adopted to complete the isochrones up to the phase of the formation of the planetary nebula. We adopt the analytic procedure of Bertelli et al. (1994) which rests on some well defined relations provided by full numerical calculations, namely the core-mass luminosity relation and the reference AGB locus in the Hertzsprung-Russell (HR) diagram as a function of the mass and metallicity of the star (see e.g. VW).

3.3.1 Mass-loss rate along the AGB

The mass-loss rate along the AGB is a key parameter for the evolution of these stars because it affects the lifetime and the average luminosity of the phase. Both these

quantities bear on the contribution of the whole phase to the integrated light because higher mass-loss rates imply shorter lifetimes of the phase and dimmer brightest stars, thus a lower contribution to the total light of the population. The mass-loss rate also affects the core mass of the subsequent post-AGB stars, hence the ultraviolet properties of the stellar population.

A great effort has been devoted to clarify the role of the mass-loss on the evolution of AGB stars, however the actual mechanism which drives it is still presently not well understood. Moreover mass-loss rate determinations, derived mainly from IR and millimetric measurements, are characterized by a significant uncertainty, related to the unknown distance of the source, the assumed dust to gas ratio and the expansion velocity.

All bright AGB stars are observed to be variables with amplitudes that may reach about a couple of magnitudes; Mira and OH/IR stars show the characteristic IR emission features of a dusty envelope. Therefore observations suggest that pulsations and dust may play an important role in the mass-loss process. In fact, hydrodynamic calculations (e.g. Bowen & Willson 1991) show that the shock waves generated by large amplitude pulsations of AGB stars levitate matter out to a radius where dust grains can condensate; from this point, radiation pressure on grains and subsequent energy redistribution by collisions, accelerate the matter beyond the escape velocity.

Moreover, it has been shown, from both theory and empirical relations, (Bowen & Willson 1991, VW, Blöcker 1995a, Groenewegen & De Jong 1994, Marigo et al. 1996, 1997) that the mass-loss rate rises almost exponentially with time (i.e. luminosity or period) during the AGB phase until it turns into a superwind that completely evaporates the envelope of the star, leaving a bare core which then evolves toward very high temperatures. For instance, a simple fit to the relation $\dot{M}$–period, along with the analytical relations between period, mass, luminosity and effective temperature of an AGB star (see e.g. VW), show that $\dot{M}$ increases exponentially with the luminosity and, above a critical threshold, turns into a superwind limited only by the reservoir of the momentum in the radiation field.

Here we adopt the formalism of VW. Following their empirical relation, the mass loss rate $\dot{M}$ grows exponentially with the pulsation period P until a constant upper limit is reached at about 500 days, which corresponds to the superwind phase. The relation between $\dot{M}$ and P has been derived from observational determinations of mass-loss rates for Mira variables and pulsating OH/IR stars both in the Galaxy and in the LMC. The two regimes are equivalent for a period of about 500 days for solar composition.

The adopted relations are (here and in the following, $\dot{M}$ is in $M_{\odot}\mathrm{yr}^{-1}$, the stellar luminosity L in $L_{\odot}$, P in days, c, the speed of light, and v_{exp} in km s^{-1}):

$$\log \dot{M} = -11.4 + 0.0123P \qquad P \lesssim 500 \text{ days} \tag{3.9}$$

$$\dot{M} = 6.07023\ 10^{-3}\beta \frac{L}{c v_{\mathrm{exp}}} \qquad P \gtrsim 500 \text{ days} \tag{3.10}$$

The second expression, $\dot{M}$ for the superwind phase, is found by VW by equating the final mass momentum flux $\dot{M} v_{\mathrm{exp}}$ to the momentum flux of the entire stellar luminosity, according to the radiation-driven-wind theory (Castor et al. 1975), with $\beta = 1$. While the Galactic OH/IR stars suggest a value of the order unity (Wood et al. 1992), there is

no reason why the same value should hold the same for other environments such as the LMC because, as clarified by Netzer & Elitzur (1993), the momentum transfer cannot constrain the value of β. Furthermore Wood et al. (1992) found that the expansion velocity is clearly lower in more metal poor stars and thus adopting a constant value for β one would predict that $\dot{M}$ increases at decreasing metallicity, contrary to what is observed.

We thus included a metallicity dependence of $\dot{M}$ in the superwind phase by imposing that β scales linearly with the metallicity Z and calibrated this dependence by fitting the infrared spectrum of the OH/IR star TRM 60 in the LMC (Groenewegen et al. 1995). With our envelope model we estimate $\tau_1 = 8$. With a distance modulus for LMC (m-M)$_0$=18.5, the luminosity of the star is 5.4 10^4 L$_\odot$. Since the observed expansion velocity of TRM 60 is 12 km s^{-1} (Wood et al. 1992) we get a dust mass-loss rate of 1.1 10^{-7}M$_\odot$/yr. To convert it in gas mass-loss rate we derive from Eq. 3.3 a dust to gas ratio of 10^{-3} so that, assuming this object is in the superwind phase, we get $\beta = 1.13$. If we adopt a metallicity of Z=0.008 for this star (an average value for the LMC) we have:

$$\dot{M} = 6.07023\ 10^{-3} \frac{L}{c v_{\rm exp}} \times 1.13 \frac{Z}{0.008} \tag{3.11}$$

For the Galactic OH/IR stars this relation implies that $\beta \sim 2$, which is a reasonable value (Wood et al. 1992).

As for the expansion velocity, VW provide the following relation between $v_{\rm exp}$ and the period of the star:

$$v_{\rm exp} = -13.5 + 0.056P \tag{3.12}$$

with the additional constraints that $v_{\rm exp}$ is greater than 3 km s^{-1} and less than the average value of 15 km s^{-1} (both typical values for Mira and OH/IR stars). However, as shown by Wood et al. (1992), there seems to be a trend between the expansion velocity and the period even for P $\geq$ 500 days (corresponding to $v_{\rm exp}$=15 km s^{-1} in the above equation) and, perhaps more important, there seems to be a trend with the metallicity of the star, because the observations suggest that $v_{\rm exp}(LMC)$=0.5-0.6 $\times$ $v_{\rm exp}(Galaxy)$. We thus let the maximum velocity depend on the period and the metallicity of the star according to the relation

$$v_{\rm exp} \leq 6.5 \frac{Z}{0.008} + 0.00226\, P \quad . \tag{3.13}$$

The slope of this relation has been derived from a linear fit to the data for the Galactic OH/IR stars within 1^o of the Galactic plane (Fig. 6 of Wood et al. 1992), while the metallicity dependence of the zero point rests on the assumption that the few data for the LMC OH/IR stars in the same figure obey the same relationship, however scaled to a lower metallicity Z=0.008 instead of Z=0.02.

Finally the pulsation period P is derived from the period-mass-radius relation (see Eq. 4 in VW) which is obtained by assuming that variable AGB stars are pulsating in the fundamental mode:

$$\log P = -2.07 + 1.94\ \log R - 0.9\ \log M \tag{3.14}$$

where the stellar radius R and mass M are expressed in solar units.

A final comment concerns the validity of the core mass–luminosity relation, which has been adopted to compute the analytic TP-AGB phase. It is well known that hot bottom burning in stars of initial mass larger than about 4 $M_{\odot}$ causes a brightening of about 20% with respect to the usual core mass–luminosity relation. However the above effect disappears when the star reaches the superwind phase (see e.g. VW) which is the most relevant for the present purpose. We also neglected the modulation of the luminosity introduced by thermal pulses (e.g. Marigo et al. 1996, 1997) on the notion that also this effect constitutes a higher degree of approximation which is beyond the current scope as we need to keep only a minimum number of free parameters at work.

3.3.2 The PAGB stars

As a consequence of the superwind the star eventually reaches a maximum luminosity after which it loses most of its envelope and rapidly evolves toward the Post-AGB (PAGB) phase. Thereafter the star reaches a maximum temperature at almost constant luminosity and then it cools and dims along the White Dwarf cooling sequence. The observed initial-final mass relation of PAGB stars (Weidemann 1987) constitutes a further test for the AGB phase and supports the kind of mass-loss rate adopted here (VW, Bertelli et al. 1994)

PAGB stars have been suggested as one of the main contributors to the integrated ultraviolet light of nearby elliptical galaxies. In the bulge of M31 their estimated contribution to UV light amounts to $\simeq$ 20%. However in M32 their number per unit UV light, as seen from the same HST FOC 1550 optical combination, is an order of magnitude lower. This indicates that age and metallicity effects may significantly affect the contributions of the PAGB stars that are ultimately related to the AGB evolution.

Characteristic evolutionary paths of PAGB stars of different mass and composition have been computed by Paczyński (1971), Schönberner (1981), Iben (1984), Blöcker & Schönberner (1991), Fagotto et al. (1994) and Blöcker (1995b). For the present isochrones we assembled the data from Schönberner (1981), Blöcker & Schönberner (1991), Fagotto et al. (1994), and Blöcker (1995b).

3.4 Isochrones in the infrared

Transformations from the theoretical to the observational plane were performed by making use of the stellar spectral library of Bressan et al. (1994), Silva (1995) and Tantalo et al. (1996). The core of the spectral library is the atlas by R. Kurucz (1993). At temperatures higher than $T_{\rm eff} = 50,000$ K pure black-body spectra are adopted, whereas for stars cooler than $T_{\rm eff} = 3500$ K the catalog of stellar fluxes by Fluks et al. (1994) is implemented. The latter library is based on stars of solar metallicity ($Z \sim 0.02$) whereas the library of SSPs presented here spans the range of metallicity $0.004 \leq Z \leq 0.05$. To account for a dependence on the metal content even for M giants, we adopted the same library at different metallicities but assigned the spectral class, identified by the (V-K) color, adopting the (V-K)-$T_{\rm eff}$ relation of Bessell et al. (1991) which depends on the metallicity.

To account for the effect of the dust envelope for each star along the TP-AGB we proceed in the following way. For a given radius R, luminosity L, mass M and

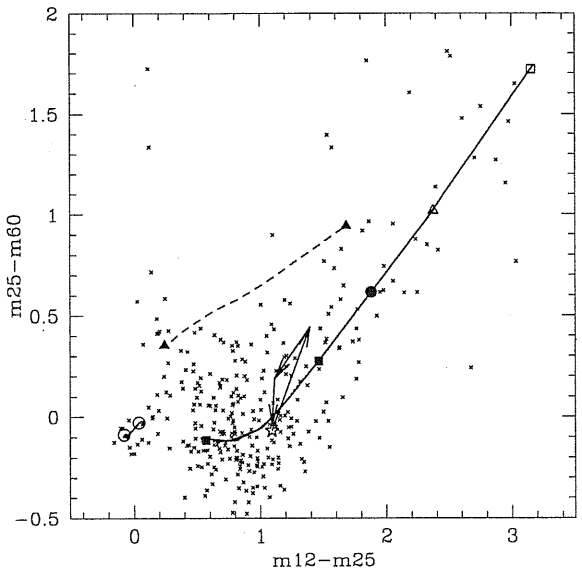

Figure 3.3: Two color diagram of the sample of IRAS sources defined by Van der Veen & Habing (1988). Following Ivezic & Elitzur (1995) the sources with cirr3/F(60)>2 have been excluded in order to minimize contamination by cirrus emission. Superimposed are 1.5 Gyr isochrones of different metallicity (which differs only for the extension toward the upper-right corner) and a model of an AGB star with T_{eff}=2500K, LogL/$L_{\odot}$=4, τ_1=1 and $v_{\rm exp}$=15 km/s (empty star), surrounded by an expanding shell (see Sec. 3.2) of 0.02$M_{\odot}$ at 0.2, 0.5 and 0.8 r_{out} (arrows). See text for more details.

metallicity Z, the semi–empirical set of equations collected in Sec. 3.3.1 provides the outflow velocity v_{exp} and the mass–loss rate $\dot{M}$. These quantities in Eq. 3.6 yield the value of τ_1. With this input the radiative transfer code computes the dust–modified stellar spectrum.

We compare our results with the infrared colors of Mira and OH/IR stars and discuss the reliability of our circumstellar envelope models. Fig. 3.3 shows several isochrones of 1.5 Gyr and different metal content in the two color IRAS diagram, superimposed to the sample of IRAS sources defined by Van der Veen & Habing (1988). The original sample includes about 1400 sources for which [60] − [25] < 0 and [25] − [12] < 0.6, ([λ_2]-[λ_1]=log($F_{\lambda_2}/F_{\lambda_1}$)), these limits define the regions occupied by galactic late type stars in the IRAS two color diagram. However, in order to minimize contamination by cirrus emission, we excluded all the sources with cirr3/F(60)>2 (Ivezic & Elitzur, 1995). The sample plotted in Fig. 3.3 reduces to about 300 sources. A thorough discussion of this diagram together with the regions occupied by galactic Mira and OH/IR stars can be found in Habing (1996). Fig. 3.3 reports data and models in form of magnitudes. Theoretical IRAS monochromatic fluxes were obtained by convolving the stellar SED with the proper transmission curve as detailed in Bedijn (1987). IRAS magnitudes were thus derived according to

$$M_i = -2.5 \times Log(S_i) + 2.5 \times Log(S_{0_i}) \tag{3.15}$$

where S_i is the flux in Jansky and the constants S_{0_i} are derived from the IRAS PSC-explanatory supplement (1988) and are 28.3 Jy, 6.73 Jy, 1.19 Jy and 0.43 for the 12, 25, 60 and 100 μm passband respectively. This procedure is adopted to facilitate the construction of mixed optical-IR two color diagrams as described below.

In Fig. 3.3 the isochrones before reaching the AGB phase are confined in a small region delimited by two open circles, with (m12-m25) and (m25-m60) $\simeq$0. These figures correspond to the Rayleigh-Jeans spectral regime and indicate that this approximation is fairly accurate till the most advanced phases of the isochrone, where dust comes into play. As the star reaches the TP–AGB phase the effect of mass-loss suddenly increases and the circumstellar envelope starts to modify the spectral emission. The first envelope model corresponds to τ_1=0.01 and it is indicated by a filled square at (m12-m25) $\simeq$0.6 and (m25-m60) $\simeq -0.1$ for the case of the silicate mixture and by a filled triangle at (m12-m25) $\simeq$0.2 and (m25-m60) $\simeq$0.35 for the carbonaceous mixture, respectively. Fig. 3.3 depicts isochrones of different metallicity but they are barely distinguishable in this diagram (but for the ending point). This is because our envelope models are characterized by a single parameter, the optical depth, so that different conditions (metallicity, mass-loss rate and expansion velocity) resulting in the same value of τ_1 provide the same dust envelope and in turn give rise to the same overall spectrum. In contrast, a noticeable feature of this diagram is the dispersion of the data. Ivezic & Elitzur (1995) thoroughly discussed this problem and they were able to show that the bulk of the data are delimited by the τ_1 curves corresponding to grains of either pure silicates or graphite. The thick dashed line in Fig. 3.3 refers to an isochrone we computed accounting for carbonaceous grains only, characteristic of C rich stars, and it is meant to illustrate the effects of the variation of the chemical composition of the dust. Thus we confirm the results of Ivezic & Elitzur (1995). Fig. 3.3 also depicts the path an AGB star would follow during a shell ejection of 0.02 $M_\odot$ (Sec. 3.2), but additional effects possibly at work are difficult to predict on the basis of simple stellar parameters.

It is remarkable that isochrones of different metallicity and age reach different maximum values of τ_1. The larger the metallicity the higher the value of τ_1 and the further the isochrone extends in the IRAS two color diagram. The largest value of τ_1 reached by models of different metallicity are indicated in Fig. 3.3 by a filled square (τ_1=4.4), a filled circle (τ_1=11.1), an open triangle (τ_1=22.3) and an open square (τ_1=57.5) for the metallicity Z=0.004, Z=0.008, Z=0.02, Z=0.05 respectively. The filled triangle at (m12-m25) $\simeq$1.7 and (m25-m60) $\simeq$0.9 refers to the case of Z=0.02 and a mixture of carbonaceous dust grains (τ_1=99).

In summary, while we analyzed both the case of a different mixture and a shell enhancement, we consider the ability of our simple models to reproduce the bulk of the data in the IRAS two color diagram as a meaningful test of reliability, also in view of the errors on the quoted fluxes ($\simeq$ 5%) reported in the IRAS PSC-explanatory supplement (1988).

To check our models in the near–IR, we have compared our isochrones with a sample of M giants and Miras in the Southern Polar Cap, for which Whitelock et al. (1994, 1995) obtained J, H, K and L magnitudes. Fig. 3.4 shows the two color (J-H)–(H-K) diagram of M giants (filled squares) and Miras (filled triangles) of the sample superimposed to some selected isochrones at different age and metallicity. Both the bulk of M giants at (J-H) $\simeq$1 and (H-K)$\simeq$0.3 and of Miras are well reproduced by the models. The fit to the

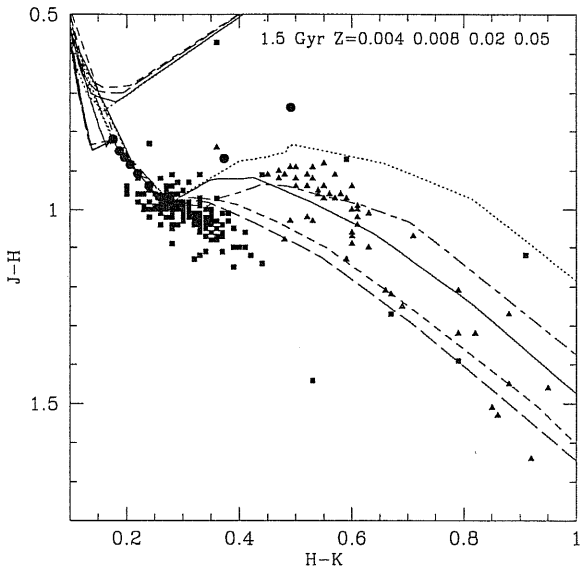

Figure 3.4: (J-H)-(H-K) two color diagram of a sample of galactic M (squares) and Mira (triangles) stars from Whitelock et al. (1994, 1995). Superimposed are some selected isochrones of 1.5 Gyr with metallicity Z=0.004 (long-dashed line), Z=0.008 (short-dashed line), Z=0.02 (continuous line) and Z=0.05 (dotted line) for the mixture A, and Z=0.02 (long-short dashed line) for the mixture B. Large filled dots indicate the location of the adopted M giant atmospheric models.

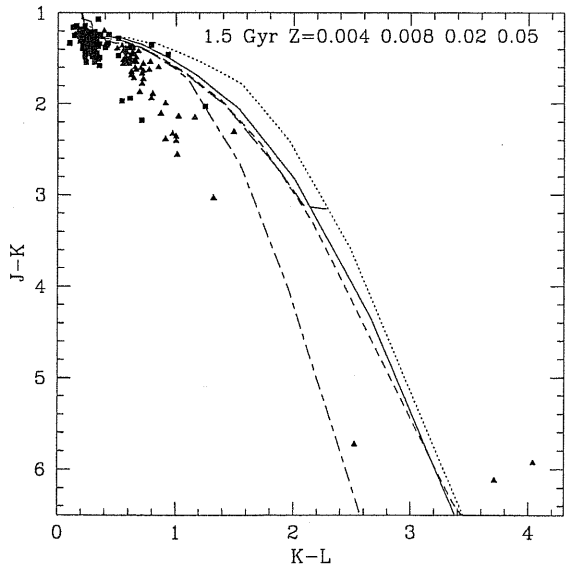

Figure 3.5: Same as in Fig. 3.4 but for the (J-K) and (K-L) colors

latter sample however depends on the adopted temperature scale, in particular to the temperature assigned to the more advanced M spectral types of the Fluks atlas. Only by reaching the most advanced spectral types during the superwind phase we are able to match the Miras, as can be seen from the location of our adopted photospheric M giant spectra (large filled circles in the figure). Assigning a metallicity on the basis of the isochrone fitting of near–IR colors is thus a quite delicate process, whose reliability must be clearly improved by more accurate atmospheric models. Note that in our case the bulk of Mira stars are well fitted by models of solar metallicity, while it is impossible to assign a metallicity to the M giants. Finally notice that the highly reddened data are relatively well fitted by our dusty models. On the contrary isochrones based on pure photospheric models would never be able to fit the data, as can be seen from the location of late type giants of our spectral library.

Fig. 3.5 is analogous to Fig. 3.4 but for the colors (J-K)–(K-L). Here the fit to the Mira sample is poor, suggesting that the problem for the latter may be related to the adopted atmospheric models (see also Bessell et al. 1991 and Whitelock et al. 1994). However, as in the previous case, the fit improves significantly at high optical depths.

3.5 SSP integrated spectra and colors

The spectrum of each single star is weighted by the appropriate number of stars in the elemental mass interval of the isochrone and summed up to obtain the integrated spectrum of the SSP. The isochrones and corresponding SSP spectra displayed in this chapter are computed for a Salpeter IMF (see Sec. 2.3). The integration is performed from 0.15 $M_\odot$ up to the largest initial mass which still contributes to the integrated spectrum of the isochrone.

3.5.1 Integrated spectra

The spectra (F_ν vs λ in μm) of SSP of 0.2, 1.5 and 5 Gyr are shown in Fig. 3.6. In each panel three cases are depicted. In the standard SSP (dot-dashed line) the effects of dusty envelopes around AGB stars are neglected. In the other two cases they have been included. The continuous line refers to the mixture of silicate grains (mixture A), well suited for an AGB dominated by M giants, while the dashed line is for the mixture of carbonaceous grains (mixture B), more appropriate for a population rich in C-stars. In the latter case the mid–IR spectra are featureless as it is expected from the optical properties of the carbonaceous grains; note however that our mixture for stellar envelopes does not include PAH molecules, whose possible formation in the photosphere of C-stars is discussed by Helling et al. 1996).

Differences with respect to the standard SSP appear beyond a few μm where the contribution of the brightest AGB stars to the integrated light is large. After a decrease of the flux from 1 to 3 μm because the brightest stars are heavily obscured by their envelopes, at larger wavelengths the contribution of dust dominates, reaching an order of magnitude at 10 μm over the pure photospheric models. While there are clear differences between the two selected dust mixtures, they constitute a modulation over the main effect brought about by the inclusion of the dusty envelopes. At increasing age the

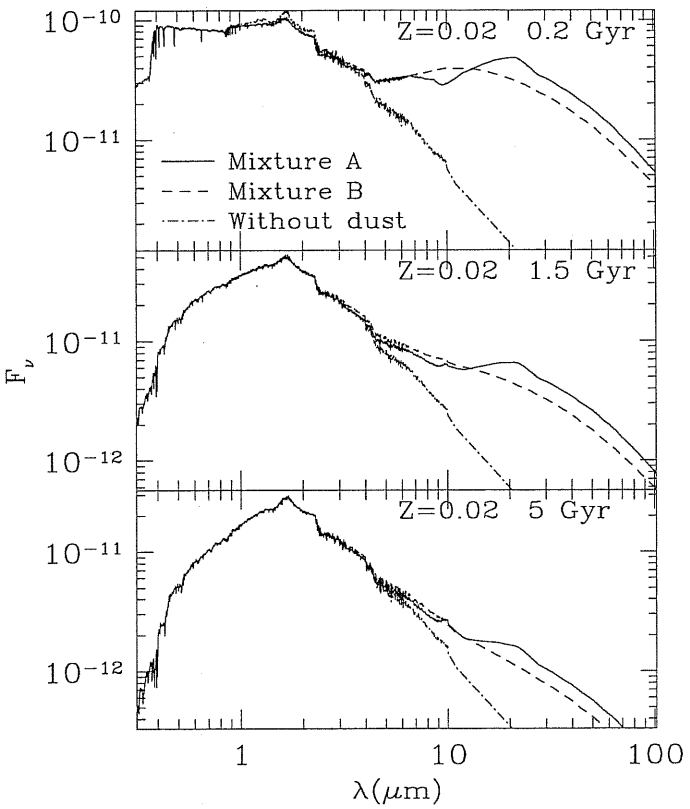

Figure 3.6: Integrated spectrum F_ν vs. λ in μm of SSPs of 0.2, 1.5 and 5 Gyr and solar composition. Three cases are depicted. In the first case dust is not taken in to account (dot-dashed line), in the second dust is a mixture of silicates grains (continuous line), and in the third dust is a mixture of carbonaceous grains (dashed line).

contribution of AGB stars to the integrated light decreases and, correspondingly, the inclusion of circumstellar envelopes becomes less and less important.

Metallicity effects are depicted in Fig. 3.7 where we plot SSPs of 3 Gyr for Z=0.008, 0.02 and 0.05. Dust emission shifts toward larger wavelengths for increasing metal content, indicating cooler dusty envelopes. The metallicity linearly affects the envelope optical depth through Eqs. 3.6 and 3.11 and the maximum value of τ attainable at a given Z scales as $L^{-0.2}$. Therefore, at a given Z, older isochrones reach a larger value of the maximum τ, but this effect is compensated by the lower contribution to the integrated light.

3.5.2 Integrated colors: a possible solution for the age-metallicity degeneracy

Accurate analysis of the integrated properties of SSPs at optical wavelengths have been done in a number of recent studies (Bertelli et al. 1994, Bressan et al. 1994, Tantalo et al.

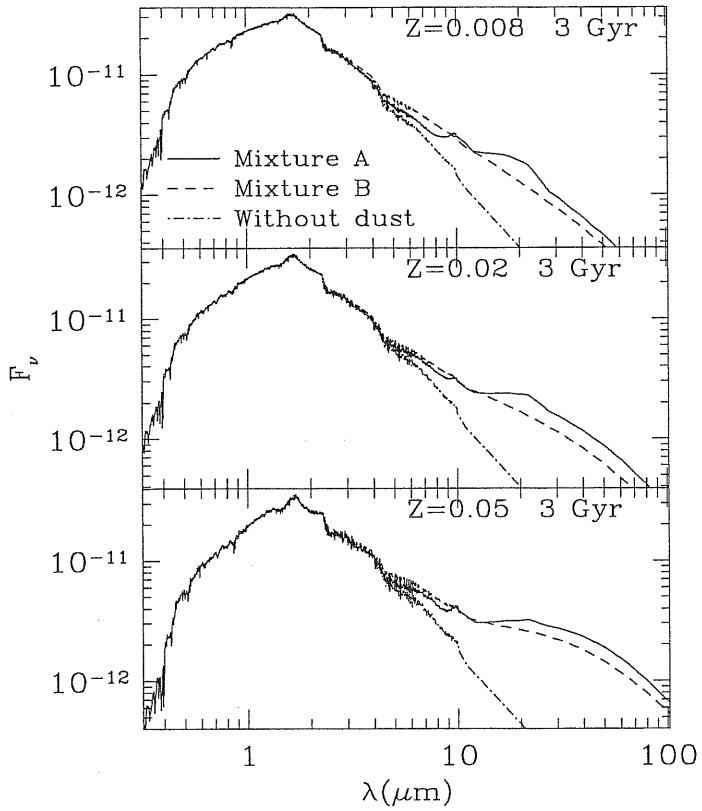

Figure 3.7: The same as in Fig. 3.6 but for a fixed age of 3 Gyr and metallicity Z=0.008, Z=0.02 and Z=0.05, respectively.

1996, Charlot et al. 1996). Fig. 3.8 depicts optical and near-IR two color plots of SSPs at different age and metallicity and reveals one of the major problems encountered when working with integrated properties: age and metallicity vectors are almost superimposed in these diagrams and it is virtually impossible to disentangle the two effects. This means that if a set of observed colors or narrow band indices are fitted with models of a given age and metallicity, it is always possible that either a younger more metal rich population or an older more metal poor one provides an equally acceptable fit. This degeneracy is the main source of uncertainty in deriving absolute ages of early–type galaxies (Bressan et al. 1994, Charlot et al. 1996).

However, we find a possible solution of the degeneracy through the orthogonal behaviour of otical, near–IR and mid–IR colors for SSP where dusty envelopes are taken into account. This could be particularly powerful for elliptical galaxies at $z > 0$, where intermediate age stars should be present.

To illustrate the point, Figs. 3.9 and 3.10 show combined optical, near-IR and mid-IR two color diagrams of several SSPs computed for the silicate mixture. The 6.7μm and 15μm magnitudes are obtained with zero point fluxes of 94.7 Jy and 17 Jy respectively

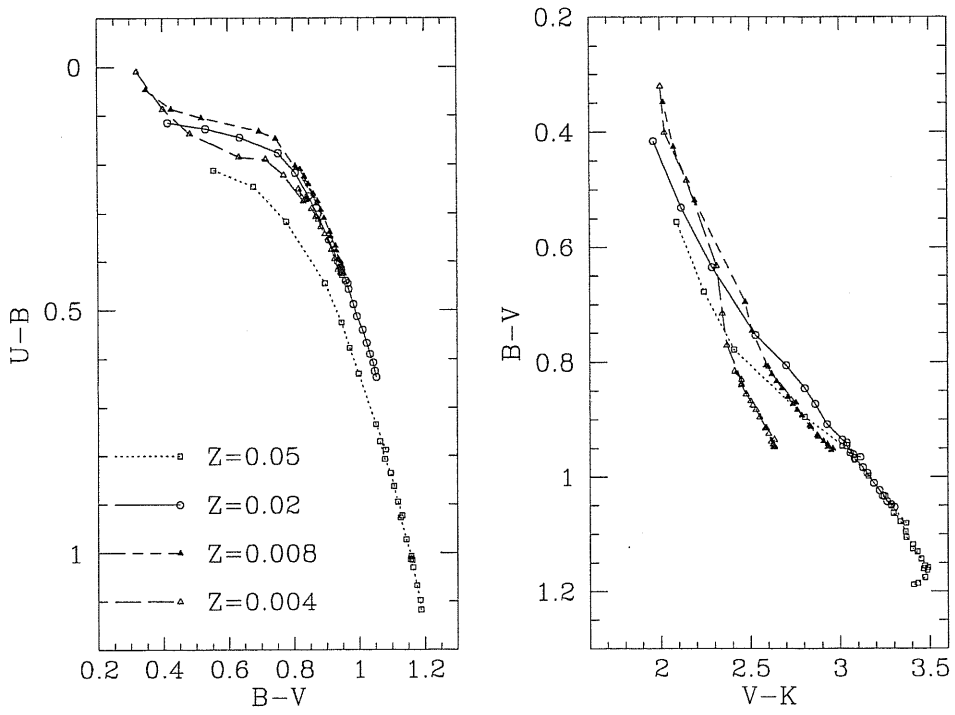

Figure 3.8: Optical and near–IR two color diagrams of SSPs at varying age and metal content illustrating the problem of the age-metallicity degeneracy. Age runs from 0.5 Gyr (top left) to 15 Gyr (bottom right) in steps of 0.5 Gyr up to 7 Gyr and thereafter in steps of 1 Gyr.

and have been selected for comparison with ISO data. Fig. 3.9 depicts the run of (V-K) against (K-6.7) for different metallicities (Z=0.004, 0.008, 0.02 and 0.05) and some selected ages. Above 1.5 Gyr the different sequences are well separated. At intermediate ages the effect of the metallicity is clearly at odd with that of the age because AGB stars drive the mid-IR fluxes of the populations: younger isochrones are bluer in the (V-K) color but redder in the (K-6.7) because of dust, while more metal rich isochrones are redder in both colors. The plots of (V-K) against (K-15μm) or (K-25μm) provide similar results.

The (V-6.7) vs (6.7-15) plot (upper panel of Fig. 3.10) is also a suitable diagnostic diagram. Note that there is a variation of more than half a magnitude in the (V-6.7) color going from Z=0.004 to Z=0.02 at intermediate ages. In contrast, optical colors change by less than 0.1 mag in the same age range. Plotting an optical magnitude (e.g. V) seems required in order to obtain useful diagnostic diagrams. Indeed for intermediate age SSPs, optical, near and mid-IR absolute magnitudes have the same trend with the age (increasing by $\sim$ 1 magnitude from 2 to 6 Gyr, irrespective of the metallicity). The behaviour with metallicity is instead different: optical magnitudes become fainter for higher Z, while near and mid-IR bands brighten. This is particularly important at at 6.7μm, 15μm and 25μm. In the lower panel of Fig. 3.10, for (K-6.7) vs (6.7-15), the two colors show the same behavior with respect to the metallicity.

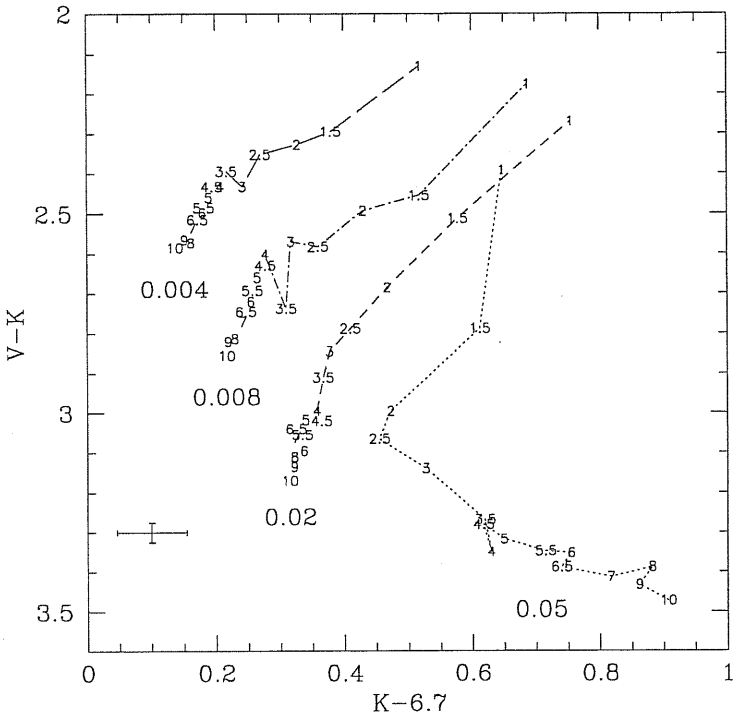

Figure 3.9: A mixed optical (V), near (K) and mid (6.7μm) infrared two color diagram of SSPs. The metallicity Z is indicated in the figure. Numbers along the curves indicate the age in Gyr. The error bar corresponds to a 5% and 10% uncertainty in the flux measurement in the near and mid IR respectively. Due to dust effects in the envelope of AGB stars, age and metallicity differences may be fairly well recognized in intermediate age populations.

Both the (V-K) vs (K-6.7) and the (V-6.7) vs (6.7-15) two color plots seem well suited for the purpose of disentangling age and metallicity effects but some cautionary notes are necessary:

(1) we have *assumed* a linear dependence of the mass loss on the metallicity (Eq. 3.11). This affects in particular τ_1 for the most metal rich populations and it is responsible of the odd behavior of the corresponding models in the two color plots. Such a relation should be tested against forthcoming ISO observation of AGB stars.

(2) SSPs with different dust mixture display different IR spectra (Figs. 3.6 and 3.7); in particular the SSPs with the silicates mixture show features around 10-20 μm. Therefore the relative percentage of O-rich and C-rich stars may affect the mid-IR shape of the integrated spectrum. The evolution of an O star to a C star (III dredge–up) and possibly back again to an O star (hot bottom burning) is still a matter of debate, as well as its dependence on the metallicity of the environment. Moreover we neglected transient phenomena such as shell ejection or luminosity dip, that may also affect the infrared colors of the star (e.g. Fig. 3.3).

(3) Environmental effects must be considered together with these models to interpret

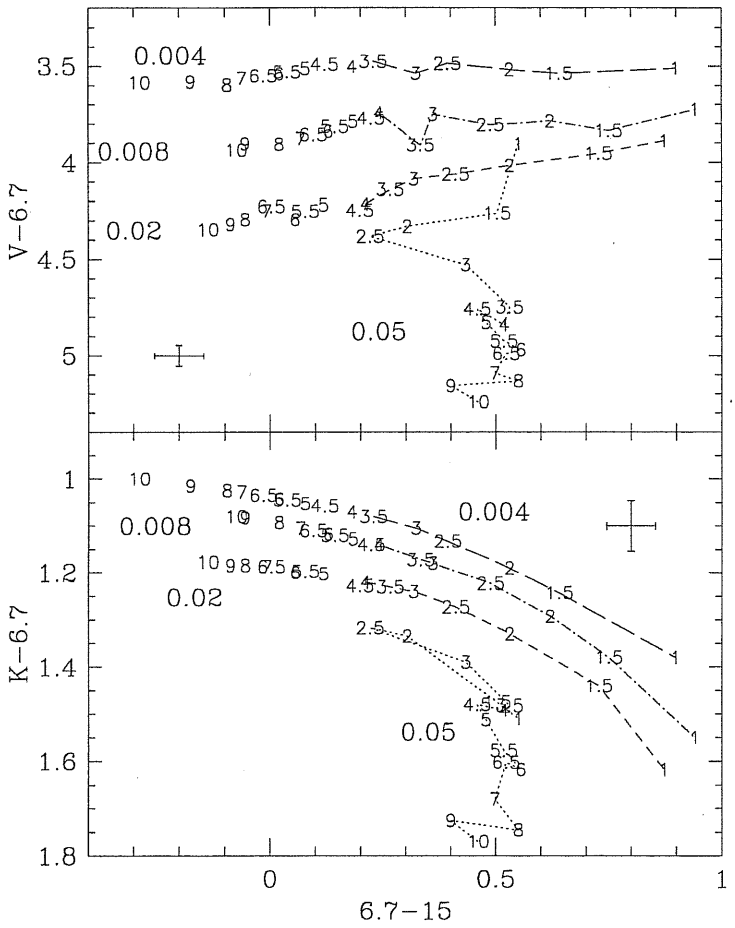

Figure 3.10: The same as in Fig. 3.9 but for the (V-6.7μm) and (6.7μm-15μm) colors, and (K-6.7μm) and (6.7μm-15μm) colors.

the spectra of galaxies: the IR emission due to star formation masks the one from AGB (e.g. see the fits in Chap. 4). We expect these stars to dominate a few Gyrs after the SF activity has ceased in early–type galaxies. If this is due to the onset of galactic winds, the AGB dust emission should dominate over the diffuse dust emission. In this context the new SSP could provide a powerful tool to investigate the age of high-z ellipticals.

3.6 Conclusions

Existing models of SSP either do not account for the effect of dust in the envelope of AGB stars or simply give a rough estimate. Therefore they are not fully suitable to investigate the integrated properties of stellar systems in the infrared.

We modelled the infrared emission of late type stars surrounded by an outflowing dusty envelope driven by radiation pressure on dust grains. To this aim we solved the

radiative transfer equation for a spherically symmetric stationary flow of matter, in order to derive the dust-modified stellar spectrum. Several envelope models were constructed as a function of the optical depth of the envelope τ_1, a suitable scaling parameter for the models (see also Ivezic & Elitzur 1995). We expressed τ_1 as a function of the mass-loss rate, expansion velocity, and luminosity. By adopting semi-empirical relations we then express mass-loss rate and expansion velocity as a function of the basic stellar parameters, mass, luminosity, radius and metal content.

This allowed us to assign a suitable dust envelope to the each star along the AGB of the isochrones of different ages and metallicity. Since in our model the mass-loss along the AGB determines both the lifetime and the spectral properties of the stars, the integrated spectra are obtained in a consistent way. The direct effect of the metallicity is included by a simple parameterization of the superwind mass-loss rate, which provides the scaling parameter τ_1. However the metal content also affects the effective temperature of the AGB phase and consequently the mass-loss rate determined by the empirical relation with the pulsational period.

We compared the isochrones with the IRAS two color diagram of the sample of sources defined by Van der Veen & Habing (1988). The dispersion of data with respect to the sequence of models corresponding to different values of τ_1 is briefly discussed. Possible explanations are a different grain mixture or the occurrence of a density enhancement caused by an outward expanding shell. While both these effects can account for the dispersion, we consider the ability of our stationary models to fit the bulk of the data in the IRAS two color diagram as a good test of reliability. As a further test we compared the isochrones with a sample of galactic M and Mira stars from Whitelock et al. (1994, 1995). In the near infrared colors [(J-H) vs (H-K)] the models fit nicely both kind of stars. Models without dusty envelopes cannot fit the location of the Mira stars, as indicated by the location in this diagram of our adopted model atmospheres. Apparently the sample of Mira stars is best fitted by models with solar metallicity, however this conclusion depends more on the adopted temperature scale of the more advanced M spectral types than on the atmospheric model itself.

Effects of AGB stars show up in the integrated spectra of stellar populations at wavelength above few μm, where they are about one order of magnitude brighter than in those not including the dusty envelopes.This effect decreases at increasing the age of the SSP. We show that by selecting suitable passbands, the integrated colors of these new SSPs can potentially be used to disentangle age from metallicity effects because of the strong dependence of the dusty envelope model on the metal content.

Intermediate redshift elliptical and post-starburst galaxies, wherein intermediate age stars are present, could be the targets where to exploit this method. Indeed in galaxies with ongoing star formation the mid–IR dust emission from AGB appears overwhelmed by dust associated with star–forming regions, mostly heated by radiation from young stars (see the fits in Chap. 4).

Chapter 4

Comparison with observed SED of galaxies

Summary. We[1] present the comparison and calibration of our model GRASIL described in Chap. 2 with data of normal and starburst galaxies in the local universe. We study the dependence of the SED on the input parameters and show the capability of our model to yield information (SFR, mass in dust and stars, IMF, SNR) for galaxies with different star formation activities and amount of extinctions from the availability of data over the whole spectral range. The preliminary results of the inclusion in GRASIL of nebular emission lines are shown for the case of M82. We then apply our model to retrieve information on HR10, an extremely red object at z=1.44. Applications to high-z galaxies are further considered in the following chapters.

4.1 Introduction

In this chapter we first discuss a few examples showing the capability of our model to provide quantitative estimates of the properties of galaxies with different star formation activity and extinction (starburst and normal galaxies) in the local universe, by reproducing their SED. We consider galaxies for which available photometric observations allow a precise evaluation of the broadband SED for UV to far–IR (and possibly radio) wavelengths. We discuss starburst galaxies in Sec. 4.2 and normal spirals in Sec. 4.3. Local giant ellipticals are addressed in Sec. 4.4. Then, since our model is able to describe in detail the evolution of galaxies in a wide range of wavelengths, in Sec. 4.5 we apply it to study HR10, an extremely red object at z=1.44. In the following chapters we consider further analysis of local and high-z galaxies where, when required, we exploit the calibration of the parameters established in this chapter.

[1]This Chapter is partly from the paper Silva et al. (1998).

Fitting parameters for local galaxies

For the local galaxies considered in Secs. 4.2, 4.3 and 4.4, the values of the parameters for the models fitting the observed SED are reported in Tables 4.1 and 4.2 for the chemical model and for the photometric model (respectively step 1 and 2 as described in Sec. 2.1). Table 4.3 summarizes a few relevant quantities derived from those parameters. Since the purpose of this comparison is to test our procedure to take into account the radiative effects of the ISM (Chap. 2), the parameters τ_{inf} and ν in Table 4.1 (defined in Sec. 2.2), ruling the SF history of the galaxy, were set following the general results of papers dealing with the chemical evolution of different types of galaxies (see Matteucci 1996), under the major constraint to get a suitable amount of residual gas. The following parameters have been fixed to reasonable values:

galactic age $t_G = 13$ Gyr;
dust–to–gas mass ratio $\delta = 9 \times 10^{-3}$;
exponent of Schimdt SFR $k = 1$;
maximum temperature of dust in MCs $T_s = 400$ K;
mass of single MC $m_{mc} = 10^6 M_\odot$.

As for the latter value, the SED of the MCs component is set mainly by its optical depth $\propto m_{mc}/r_{mc}^2$ (Table 4.3; see Sec. 2.5.2), which is in fact the true "fitting parameter" for this component (together with t_o, Eq. 2.22), rather than r_{mc} reported in Table 4.2. In other words the values found for r_{mc} depend on having set $m_{mc} = 10^6 M_\odot$, as typical for Giant Molecular Clouds in the Galaxy, and r_{mc} could be set to a different value producing identical fits, provided m_{mc} is adjusted to keep m_{mc}/r_{mc}^2 constant.

Moreover the mass limits of the Salpeter IMF are the standard $M_{max} = 100 M_\odot$ and $M_{low} = 0.1$, but for starburst galaxies where the estimates of dynamical mass require $M_{low} \gtrsim 0.2$, as discussed below.

We also remind (see Sec. 2.5.1) that, in order to keep the number of free parameters to the minimum required by present quality data, we set the scale lengths of stars and gas distributions in spirals to the same values, i.e. $R_d^* = R_d^c$ and $z_d^* = z_d^c$ (see Eq. 2.18).

4.2 Local starburst galaxies

M82

In the prototype starburst galaxy M82 the burst was probably triggered by the interaction with M81, some 10^8 yr ago (Solinger, Morrison, & Markert 1977). Thanks to the proximity of this system ($D = 3.25$ Mpc) a wealth of data do exist, providing a well sampled full coverage of the SED at different angular resolutions, as well as other observational constraints. The fit (Fig. 4.1) is obtained by evolving for 13 Gyr a galaxy model with a final baryonic mass of $1.8 \times 10^{10} M_\odot$, a factor 6 less than the estimated total dynamical mass (Doane & Mathews 1993). We adopted $M_{low} = 0.2 M_\odot$ as lower limit of the Salpeter IMF. A lower value would require a baryonic mass closer to the dynamical mass. The assumed parameters provide a SFR raising from 0 to about 3 $M_\odot$/yr in the first 3 Gyr, then smoothly declining to 1.35 $M_\odot$/yr at $t = 13$ Gyr. To this gentle star formation history, which leaves a gas fraction of 0.064, we have super-

object	D [Mpc]	M_G [$10^{10}M_\odot$]	ν [Gyr^{-1}]	τ_{inf} [Gyr]	M_{burst} [$10^{10}M_\odot$]	t_{burst} [Gyr]	t_e [Gyr]
(1)	(2)	(3)	(4)	(5)	(6)	(7)	(8)
M82	3.25	1.8	1.2	9	0.02	12.95	0.05
NGC 6090	175	41	0.6	9	0.16	12.95	0.05
ARP 220	115	23	0.3	9	2.5	12.95	0.05
M51	9.6	15.5	0.6	4	...	...	...
M100	20	20	0.75	4	...	...	...
NGC 6946	6.7	12.5	0.6	5	...	...	...
gE	...	100	2.0	0.1	...	...	...

Table 4.1: Parameters for the star formation history (Sec. 2.2): (2) adopted distance; (3) final baryonic galaxy mass; (4) SF efficiency; (5) infall timescale; (6) gas mass converted into stars during the burst; (7) galaxy age at beginning of the burst (when included); (8) e–folding time for SFR in the burst. All models have an age of 13 Gyr. In the case of gE the SF has been stopped at 1.15 Gyr.

object	f_{mc}	r_{mc} [pc]	t_o [Myr]	r_c^* [kpc]	r_c^c [kpc]	R_d [kpc]	z_d [kpc]
(1)	(2)	(3)	(4)	(5)	(6)	(7)	(8)
M82	0.08	16	57	0.15	0.2	...	...
NGC 6090	0.005	17	18	0.5	1.0	...	...
ARP 220	0.5	10.6	50	0.5	0.5	...	...
M51	0.7	14	8	...	...	4.7	0.4
M100	0.8	15	3	...	...	5.0	0.4
NGC 6946	0.6	14	2.5	...	...	8.0	1.0
gE	...	...	...	0.4	6.0	...	...

Table 4.2: Parameters for the photometric model estimated from SED fitting: (2) fraction of residual gas in MCs; (3) radius of MC; (4) parameter regulating the escape of young stars from MCs (Eq. 2.22); (5)–(8) parameters for the spatial distribution of stars, MCs, and cirrus (Eqs. 2.18 and 2.20). For disks the inclination angles have been taken from the literature (see text) and are $i = 20^o$ (M51), $i = 30^o$ (M100), and $i = 34^o$ (NGC 6946).

object	$< SFR >$ $M_\odot$/yr	M_{dust} $10^7 M_\odot$	τ_1^{mc}	$\bar{\tau}_1$	$\bar{\tau}_B$	L_{mc} 10^{44}erg/s	L_c 10^{44}erg/s	L_{Lyc} 10^{44}erg/s
(1)	(2)	(3)	(4)	(5)	(6)	(7)	(8)	(9)
M82	5.5	0.8	25	0.62	1.30	1.1	0.25	.09
NGC 6090	68	45	24	0.84	1.37	13	13	1.3
ARP 220	580	30	58	1.67	2.80	100	5.7	8.7
M51	6	10.4	33	0.06	0.28	1.01	0.90	0.11
M100	7	9.6	29	0.03	0.15	0.84	0.85	0.12
NGC 6946	6	10.4	33	0.03	0.12	0.62	0.53	0.10
gE	...	0.15	...	0.00	0.01	...	0.02	0.03

Table 4.3: A few quantities derived from the models: (2) SFR averaged over the last 5×10^7 yr, which is the time from burst onset for starburst models; (3) total mass in dust in the galaxy; (4) 1 μm optical thickness of the MCs from the centre; (5) 1 μm 'average' optical thickness of the model, defined such as (observed flux) = (dust–free flux $\times$ exp$(-\bar{\tau})$) (6) same as (5) but at 0.44 μm; (7) luminosities of the MCs, (8) of the diffuse dust and (10) in the Lyman continuum *before dust absorption.*

posed an exponential burst processing 18% of the residual gas in the last 5×10^7 yr, with an e–folding time also of 5×10^7 yr (Fig. 4.2). Note that our results are almost independent on the precise evolution of the SFR in the burst: even a constant burst yields very similar estimates of the relevant quantities. Also the duration of the burst could be doubled or halved with small adjustments of the other parameters without damaging the quality of the SED fit. Thus we end with a total gas mass of $8.6 \times 10^8\, M_\odot$, 8% of which is ascribed to the molecular component, organized in clouds with $m_{mc} = 10^6\, M_\odot$ and $r_{mc} = 16$ pc. These clouds reprocess almost completely the starlight due to the burst. The system is assumed to follow a King profile (Eq. 2.20) with $r_c^\star = 150$ pc for stars and $r_c^c = 200$ for diffuse gas.

The masses we ascribe to the various components favorably compare with radio estimates of total gas masses $\sim 10^9\, M_\odot$ (Solinger et al. 1977), with CO determinations of gas in molecular form $\sim 10^8\, M_\odot$ (Lo et al. 1987; Wild et al. 1992), and with an upper limit $\lesssim 3 \times 10^8\, M_\odot$ to the mass of stars formed in the burst, suggested by dynamical considerations (McLeod et al. 1993).

Also, in our proposed model the predicted supernovae rate (Sec. 2.2) is between 0.05 and 0.1 yr^{-1}, depending on the adopted lower limit of stellar mass yielding to supernovae explosion 8 or 5 $M_\odot$ respectively. Observational estimates suggest a SNR in the range 0.07–0.3 yr^{-1} (McLeod et al. 1993; Doane & Mathews 1993). Increasing the lower limit of the IMF in the burst to, for instance, $M_{low} = 1.0\, M_\odot$ would increase the SNR by a factor ~ 2. In conclusion the model required to nicely reproduce the observed SED turns out to be in agreement with independent estimates of masses and of SNR.

As an example of the work in progress to include nebular emission in GRASIL

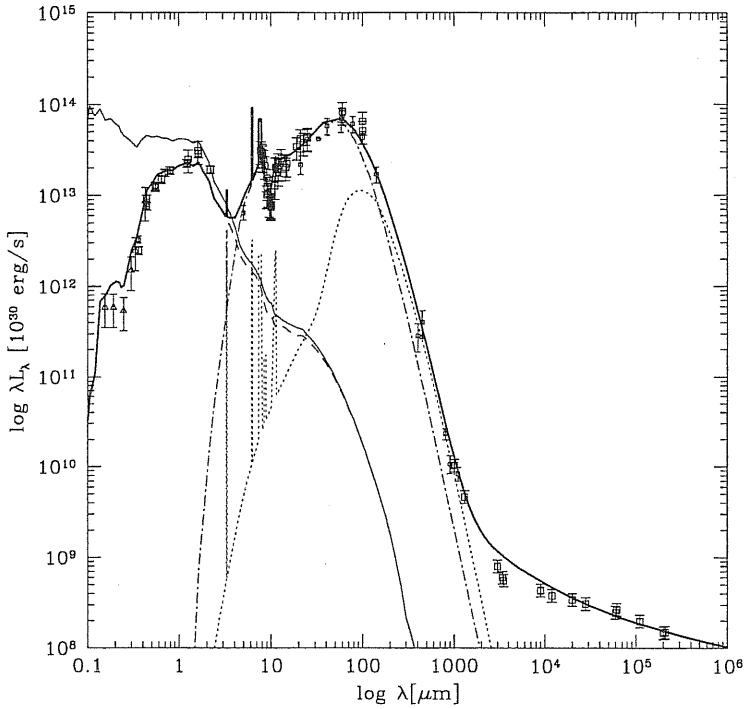

Figure 4.1: Fit to the SED of M82. Data are from Code & Welch (1982), Soifer et al. (1987), Klein et al. (1988),Cohen & Volk (1989), Van Driel et al. (1993), Ichicawa et al. (1994,1995). The different lines represent: *thin continuous*= pure stellar spectrum; *dotted*= emission from diffuse dust; *dot-dashed*= emission from dust in Mcs; *dashed*= starlight extinced by dust; *thick continuous* line is the resulting total SED of the model.

(Panuzzo et al. 1999; see Sec. 2.7), we show the first results for M82 in Figs. 4.3 and 4.4. In the first figure, the predicted line spectrum is superposed to the broadband one of Fig. 4.1. As already mentioned in Sec. 2.7, we find that, in order to reproduce UV–optical–NIR emission lines in starburst galaxies, $\sim 10\%$ of the youngest stars must be extinguished by MCs with an optical depth lower by a factor ~ 20 than the one of MCs hosting most of the recent star formation. This is clearly shown in Fig. 4.4. In the lower panel, the model for M82 assumes only one component of thick MCs, the same as in Fig. 4.1 and indeed no nebular UV-optical-NIR lines can escape the starburting regions, while the UV radiation field from older stars in the diffuse ISM is too faint to ionize. Instead, in the upper panel both the thick and thin MCs are included. The latter component is the site where optical lines are originated. This is particularly important in the estimates of SFR from optical lines, since the latter reveal only a tiny fraction, the bulk of the SFR being reavealed by IR lines.

In these plots, the MIR PAH emission features are computed with the profiles described in Sec. 2.4.2. These observed profiles result fairly suited to reproduce the bands for normal starforming galaxies, both starbursts and spirals, but not for ultra luminous ones, as ARP 220. Indeed the ratios of PAH features in ULIR galaxies differ from those

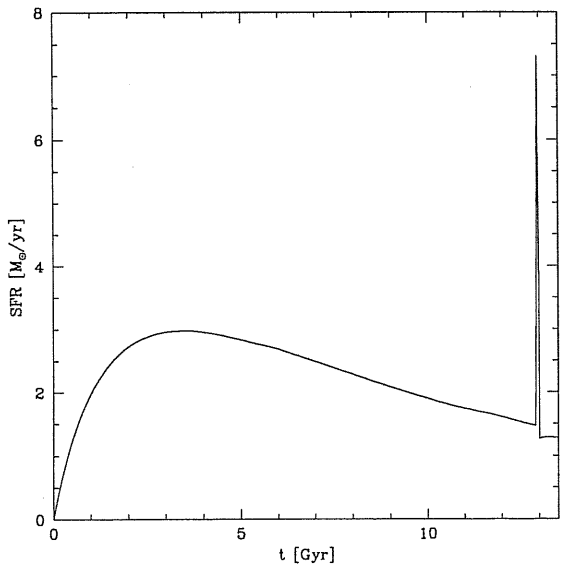

Figure 4.2: Star formation rate of the model fittiong M82.

in lower luminosity starbursts, which instead exibit very homogeneus PAH properties (Lutz et al. 1998).

NGC 6090

This strongly interacting galaxy at 175 Mpc (H_o = 50 km/s/Mpc) has been observed by ISO from 2.5 to 200 μm (Acosta-Pulido et al. 1996). The SED resulting from the combination of these data with previously published optical photometry is nicely reproduced by our model (Fig. 4.5). The differences in the parameters with respect to M82, apart from an up-scale in involved baryonic mass ($4.1 \times 10^{11} M_{\odot}$), are aimed at enhancing the diffuse dust emission at $\lambda \gtrsim 100\,\mu$m, which, as noticed by Acosta-Pulido et al., is not reproduced by published starburst models. Thus the pre-burst SFR has been adjusted to leave a larger gas fraction (0.127), 3.2% of which is processed by the burst. The molecular star-forming clouds accounts only for 0.5 % of the gas left by the burst.

Arp 220

Arp 220 is an archetypal ultraluminous infrared galaxy (ULIRG), most likely the result of a recent merging between two gas-rich galaxies, for which ISOPHOT data have been now published (Klaas et al. 1997), and whose K–band light profile resembles that of a typical elliptical galaxy. In this object there is evidence of both starburst as well as Seyfert activity, but ISO spectroscopy led to the conclusion that the IR luminosity is primarily ($\gtrsim$ 90%) powered by starburst (Sturm et al. 1996). The fitting model requires a strong burst, converting into stars $2.5 \times 10^{10} M_{\odot}$, i.e. as much as 11% of the total baryonic mass, and a high fraction 50% of residual gas in star–forming clouds. The

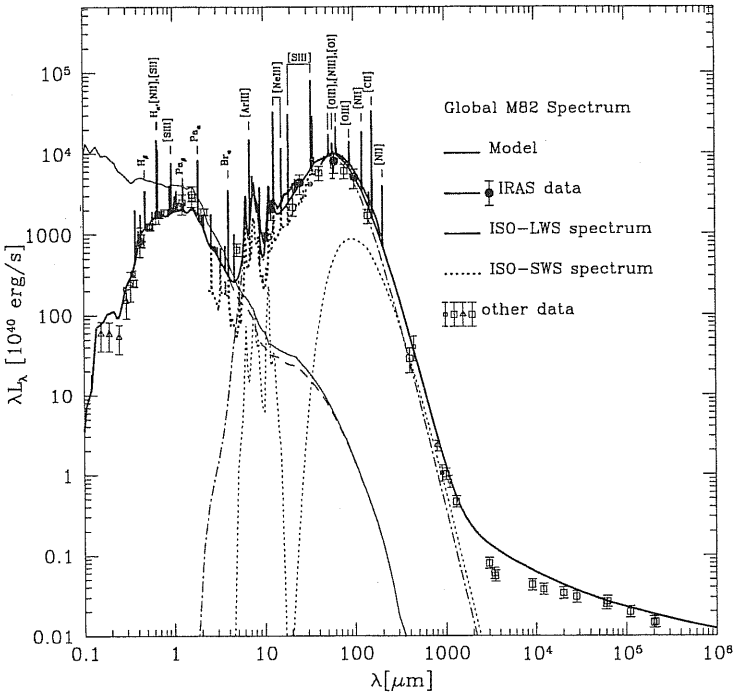

Figure 4.3: The predicted nebular emission line spectrum for M82 is superposed to the broadband one. In this plot, as in the next one, the PAH emission bands have been computed with the profiles described in Sec. 2.4.2.

gas fraction before the burst is 0.25. As a result, the IR and sub–millimetric emission is everywhere dominated by dust associated with star forming regions. The mass in molecular gas is $\sim 1.6 \times 10^{10}\, M_\odot$, in agreement with CO estimates (Solomon et al. 1997; Scoville, Yun, & Bryant 1997). From a determination of the CO rotation curve Scoville et al. (1997) infer a dynamical mass of $\sim 3 - 6 \times 10^{10} M_\odot$ within $r \simeq 1.5$ kpc (depending on the adopted potential), in agreement with the mass requested by our model within the same radius $\simeq 4.1 \times 10^{10}\, M_\odot$.

We find that the sub–millimetric data of Arp 220 are underpredicted by a factor $\sim 2-3$ by any model which successfully reproduces the remaining SED, unless the long wavelength decline of grain absorption efficiency is reduced, say from $\propto \lambda^{-2}$ to $\propto \lambda^{-1.6}$ above $\simeq 100\mu$m (see Agladze et al. 1996 for laboratory measurements supporting this possibility for silicate grains). In Fig. 4.6 we report fits obtained adopting either the modified as well as the standard DL cross–sections.

4.2.1 Discussion for starbursts and ULIRGs

The SFR in a starbursting region can be estimated on the basis of the FIR luminosity, under the assumption that dust reradiates the overall bolometric luminosity and after calibration with stellar synthesis models. Kennicutt (1998) proposes $\mathrm{SFR}[M_\odot\,\mathrm{yr}^{-1}] = L_{FIR}/(2.2\times10^{43}\,\mathrm{ergs\,s}^{-1})$, with calibration derived from models of Leitherer & Heckman (1995). This relationship properly applies to star forming regions, while the extension

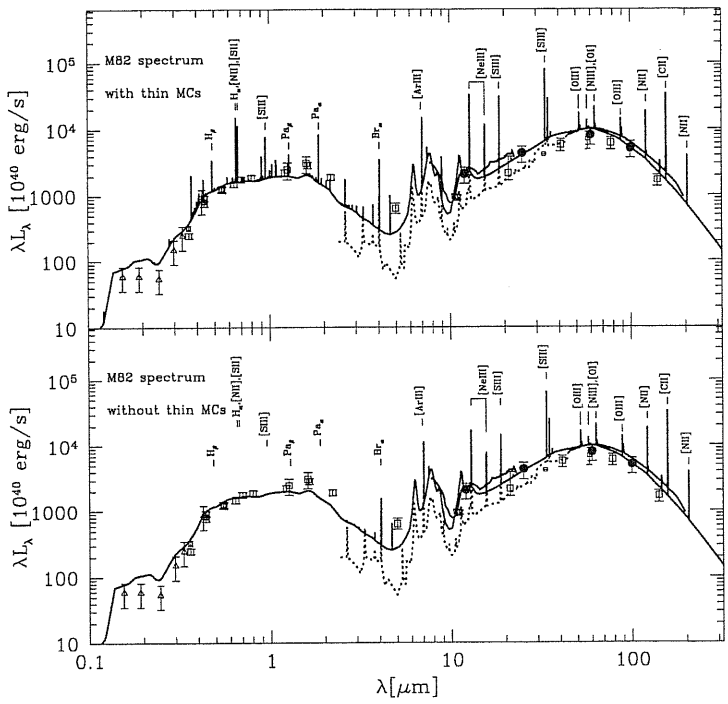

Figure 4.4: The model for M82 in the upper panel includes both the thick and thin MCs. The latter are the sites where UV-optical-NIR nebular lines are originated. In the lower panel the model assumes only one component of thick MCs: no nebular optical lines can escape the starburting regions. Data as in Fig. 4.3.

to a galaxy as a whole is dangerous, since a non negligible portion of the FIR luminosity may arise from cirrus emission powered also by relatively old stars. However our model accurately determines the warm component associated to the MCs where star formation is occurring (L_{mc} in Table 4.3). For M82 our fit predicts an overall FIR luminosity associated to the MCs component of 1.1×10^{44} ergs/s, which following Kennicutt translates in SFR=5.0 $M_\odot$ yr^{-1}. Similarly, the SFRs inferred from the luminosity of the warm component is 57 $M_\odot$ yr^{-1} and 460 $M_\odot$ yr^{-1} for NGC 6090 and Arp 220 respectively. These figures are in very good agreement with those derived by fitting the SEDs and reported in Table 4.3. Thus while Kennicutt's calibration is confirmed, we stress that this refers only to the warm component, which contributes $\simeq$ 50% of L_{FIR} in NGC 6090. This source of uncertainty adds to the obvious effect of the adopted IMF in the conversion from observed IR luminosity to SFRs.

Whilst the very recent (say in the last 10 Myr) SFR is relatively well constrained by the observed warm IR emission, the burst duration, and therefore the total mass converted into stars, can be varied within a factor $\sim$ 2, still yielding the correct L_{FIR} and spectra after readjustments of other parameters. However the supernovae rates deduced from observations put further constraints on the average SFR and duration of the burst. In the well studied case of M82 the model predicts a SN rate in the interval

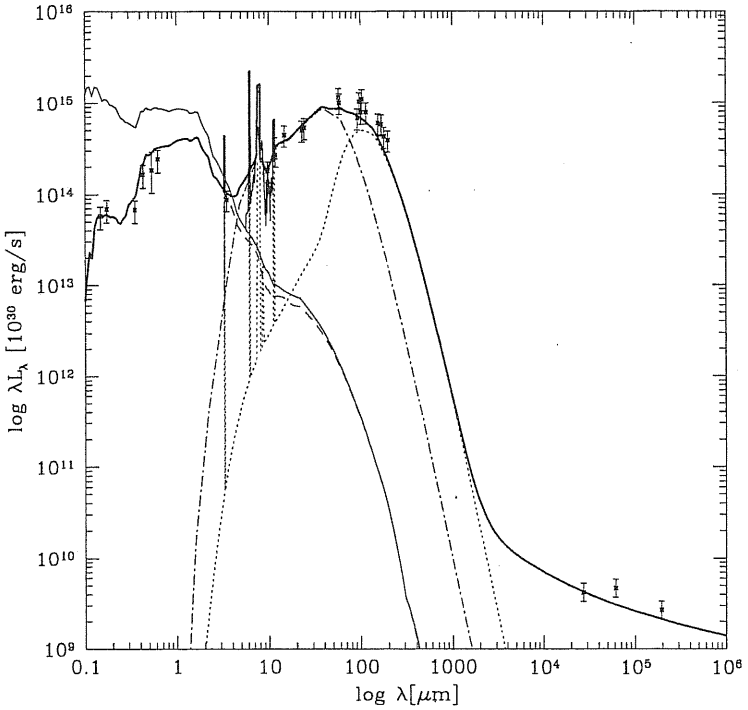

Figure 4.5: Fit to the SED of NGC 6090. Data are from Mazzarella & Boroson (1993), Acosta–Pulido et al. (1996), Gordon et al. (1997). Meaning of lines as in Fig. 4.1.

deduced by observations.

The SFR can also be inferred from the ionizing luminosity L_{Lyc}, which can be derived from recombination lines. With the adopted IMF we find $L_{Lyc}[10^{44}\,\mathrm{ergs\,s^{-1}}] \simeq 0.017\,\mathrm{SFR}(M_\odot\,yr^{-1})$, which holds with very small deviations for the six studied star–forming galaxies (see Table 4.3). The uncertainties connected to extinction corrections of observed line fluxes are minimized employing transitions occurring in the IR regime, such as Brγ line ($\lambda = 2.17\mu$m). Calzetti (1997) and Kennicutt (1998), using Leitherer & Heckmann (1995) results, find $\mathrm{SFR}[M_\odot \mathrm{yr}^{-1}] = L(Br\gamma)/1.6 \times 10^{39}\mathrm{ergs\,s^{-1}}$ adopting a Salpeter IMF within 0.1–100 $M_\odot$ or $\mathrm{SFR}[M_\odot \mathrm{yr}^{-1}] = L(Br\gamma)/3.7 \times 10^{38}\mathrm{ergs\,s^{-1}}$ when the mass range is 0.1–30 $M_\odot$.

The $(Br\gamma)$ line luminosity $L(Br\gamma) = 9.2 \times 10^{40}\,\mathrm{ergs\,s^{-1}}$ of NGC 6090 (Calzetti, Kinney, & Storchi–Bergmann 1996) corresponds to a SFR=56 $M_\odot$ yr^{-1} with the assumption of the 0.1–100 $M_\odot$ mass range, only 18% less than that used in our model, while the smaller range in the IMF would predict a SFR higher by a factor 4. Kennicutt (1998) has shown that there is a clear trend for SFRs derived from L_{FIR} to be larger than those estimated from the $L(Br\gamma)$, suggesting that extinction is non negligible even at near–IR wavelengths.

Genzel et al. (1998) reported the ratio of the far–IR to Lyman continuum luminosity L_{FIR}/L_{Lyc} of starbursts (including M82) and ULIRGs, derived from near and mid–IR recombination lines. For 12 starburst galaxies the median value is $L_{FIR}/L_{Lyc} \simeq 16$.

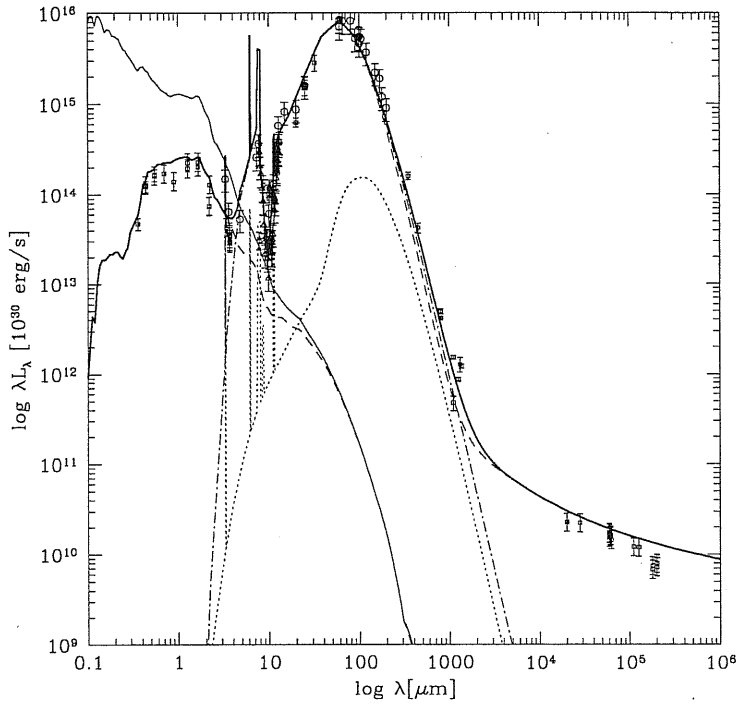

Figure 4.6: Arp 220: in this case the wavelength dependence of grain cross–section has been modified above 100μm from $\propto \lambda^{-2}$ to $\propto \lambda^{-1.6}$. The dashed line above 100 μm represents the model prediction with standard λ^{-2} decline. Data are from Carico et al. (1988), Sanders et al. (1988), Smith et al. (1989), Carico et al. (1990), Wynn–Williams & Becklin (1993), Rigopoulou et al. (1996), Klaas et al. (1997). Meaning of lines as in Fig. 4.1.

The model ratio depends on the adopted IMF. Our fit to M82 overall SED yields $L_{FIR}/L_{Lyc} \simeq 12$, where L_{Lyc} is the unextincted luminosity of the (young) stellar populations below 912 Å in very good agreement with the value found by Genzel et al. (1998). For NGC 6090 the fit predicts $L_{FIR}/L_{Lyc} \simeq 10$, using L_{mc} to evaluate the model L_{FIR} powered by the burst, well within the range of the values inferred by the same authors. As for Arp 220, which properly belongs to the ULIRG class, higher values $15 \lesssim L_{FIR}/L_{Lyc} \lesssim 112$ are inferred from IR recombination lines, whereas our model predicts $L_{FIR}/L_{Lyc} \simeq 11$. The discrepancy is likely due to the uncertain large correction for IR extinction in this object. Actually Genzel et al. (1998) use a screen obscuration with $A_V = 45$, while we find $A_V \simeq 150$ in MCs of this object. Interestingly enough, the 15 ULIRGs (including Arp 220) studied by Genzel et al. (1998), exhibit a median $L_{FIR}/L_{Lyc} \simeq 40$, larger by a factor of ~ 2.5 than that inferred for starburst galaxies. This result can be explained by larger obscurations or by a softer intrinsic Lyman continuum, pointing to an IMF less rich in massive stars or to an older starburst. In the models we used bursts began 0.05 Gyr ago, but still rather active due to the large e–folding time $t_e = 0.05$ Gyr.

It is worth noticing that in the broadband fits presented in this chapter, and in this discussion, we do not account for the ionizing radiation converted into recombination lines, which are much less absorbed by dust than the Lyman continuum. The UV radiation has been converted directly to IR photons through dust absorption. However the energy budget is not significantly affected, since the observed luminosity in recombination lines is only a few percent of the bolometric luminosity of starburst galaxies (e.g. Genzel et al. 1998).

The observed UV emission at $\lambda \gtrsim 1000$ Å is crucial in determining the fraction of the SSPs escaped from the parent molecular clouds. In our model the UV flux emerging from a single galaxy depends on the age t_o after which a SSP starts to get out from the molecular cloud. The UV photons are affected also by absorption in the diffuse ISM. In the case of M82 and Arp 220 the measured UV flux is a tiny fraction of the bolometric luminosity (see Figg. 4.1 and 4.6). This implies that the stars of the burst are still inside their parent clouds. Indeed in these two objects t_o is about equal to the time since burst ignition, 0.05 Gyr. By converse for NGC 6090 the data show that the UV is not a negligible fraction of the total, implying for our model $t_G - t_{burst} > t_o = 0.018$ Gyr. As a result stars with lifetime ≥ 18 Myr (corresponding to $M \lesssim 10 M_\odot$) are no more embedded within the clouds and contribute significantly to the ISRF. Actually the luminosity we ascribe to the diffuse cold component equals the warm one in NGC 6090, whereas it is 25% and 9% for M82 and Arp 220 respectively.

Calzetti, Kinney, & Storchi–Bergmann (1994) computed the "intrinsic depth" of the 2175 Å dust absorption feature η (see their Eq. 23) in a number of starburst galaxies, finding that $-0.15 < \eta < 0$. For the three starbursts we find η ranging from -0.15 to -0.08. Since the dust properties we adopt follows very well those of our galaxy, at least in these objects the relative weakness of the 2175 Å feature can be ascribed to the adopted geometry, without invoking possible variations of extinction curve.

In conclusion for starbursts, the spectral coverage from UV to submillimeter wavelengths allows a robust evaluation of the luminosity of stars involved in the bursts and of the general interstellar radiation field. The latter is contributed by the long-lived stellar populations and by the stars produced in the burst but old enough to get out from the original MCs. Our model well describes the complexity of a starburst galaxy, and is flexible enough to reproduce the differences among them. It uses a reasonable number of parameters, which have a well defined physical meaning and compare favorably to values derived from observations other than broad band spectra.

4.3 Local normal spirals

In this section we examine objects that do not show clear signs of enhanced star formation or nuclear activities in the SED nor in the morphology, namely 3 late–type spirals. We fit spirals later than Sb, which are clearly disk–dominated, and we adopt for them an exponential geometry (see Sec. 2.5.1).

M51

In Fig. 4.7 we present a fit to the SED of the nearly face–on ($i = 20^o$, Tully 1974) Sbc galaxy M51 (NGC 5194), taken at a distance $D = 9.6$ Mpc (Sandage & Tammann

1975). Since the discrepancy between ISO and IRAS data at 60 and 100 μm could be due to an excess of the ISO point spread function (Hippelein et al. 1996), we fit the IRAS data. The model has a baryonic mass of $1.55 \times 10^{11}\, M_\odot$, whose evolution leaves at 13 Gyr a gas fraction of 0.067, 70% of which in molecular form. The mass of ISM in the molecular and diffuse components, as well as their relative fraction is in agreement, within a factor ≤ 2, with estimates by Scoville & Young (1983), Young et al. (1989), and Devereux & Young (1990). Gas and stars are exponentially distributed with the same scale–lengths, 4.7 and 0.4 kpc for the radial and vertical scales respectively. The former value is in good agreement with those estimated by Beckman et al. (1996) from observed brightness distributions in different optical bands. Due to the low energy output observed at $\lambda \lesssim 0.2\mu$m, stars born during the last 5×10^6 yr are hidden inside molecular clouds.

The striking correspondence between the 15 μm emission mapped by ISOCAM and the H_α emission indicates that the MIR is powered by recent star–formation (Sauvage et al. 1996). As for the FIR, somewhat contradictory claims have been reported: Devereux & Young (1992), comparing the radial distributions of FIR, H_α, H I, and H_2 emission, concluded that the same holds true in the range 40–1000 μm, while Hippelein et al. (1996) found no obvious correlation between FIR ISOPHOT maps and H_α fluxes. This apparently complex situation is not surprising, since according to the model the MIR emission is provided by the MCs component, while above $\sim 60\,\mu$m the diffuse dust gives a comparable contribution, which however is in part powered by young stars.

M100

The Sbc galaxy M100 (NGC 4321) is the largest spiral in the Virgo Cluster. We adopt a distance $D = 20$ Mpc and an inclination angle $i = 30^o$. The model in Fig. 4.8 has a baryonic mass of $2 \times 10^{11}\, M_\odot$, with a residual gas fraction of 0.048, 80% in molecular form. Indeed, according to the gas masses estimated by Young et al. (1989) and Devereux & Young (1990), larger than ours by a factor $\simeq 2$, the ISM seems to be dominated by the molecular component. The location of M100 in the central regions of the Virgo Cluster could affect some of its properties, as the H I distribution that shows a sharp edge in correspondence to the optical radius (Knapen et al. 1993). This could be the reason for the warm FIR SED observed in M100, as compared to M51 and NGC 6946, despite their morphological similarity. The steep decline of the spectrum in the sub–mm region has been interpreted by Stark et al. (1989) as indicating that the emitting grains are warm and small. In our model this is not required since the fit is obtained with standard diffuse dust. Stars and dust share the same radial and vertical scale–lengths, 5 and 0.4 kpc respectively, in agreement with the values derived by Beckman et al. (1996) for the stellar component and with the H I distribution.

NGC 6946

The fit to this Scd galaxy at distance $D = 6.72$ Mpc (Rice et al. 1988) and inclination angle $i = 34^o$ (Considere & Athanassoula 1988), is shown in Fig. 4.9. The total gas mass in the model, $1.04 \times 10^{10}\, M_\odot$ i.e. 8.3% of the baryonic mass, agrees with the molecular plus neutral hydrogen mass given by Young et al. (1989) or Devereux & Young (1990)

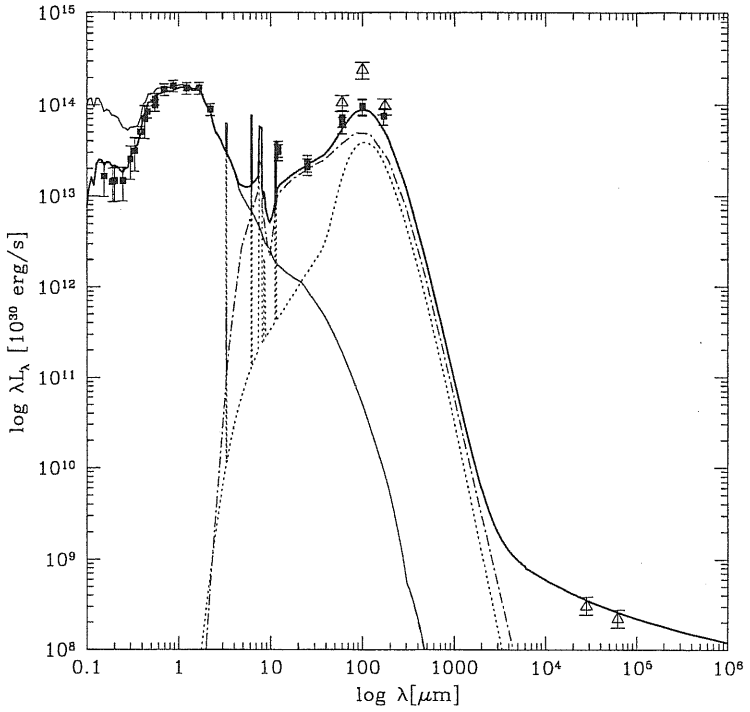

Figure 4.7: Fit to the SED of the Sbc galaxy M51. Data are from Buat et al. (1989), Evans (1995), de Vaucouleurs et al. (1991) (RC3), Code & Welch (1982), Young et al. (1989), Rice et al. (1988), Devereux & Young (1990,1992), Smith (1982), Hippelein et al. (1996) (ISO, triangles). Meaning of lines as in Fig. 4.1.

(reported at 6.72 Mpc), while the fraction we ascribe to the molecular component is a factor $\simeq 2$ higher.

The contribution of young and old stellar populations to dust heating in this object has been considered by several authors. Devereux & Young (1993), comparing the radial distributions of FIR, H_α, H I, and H_2, conclude that the 40 to 1000 μm luminosity is dominated by dust associated with molecular gas heated by young stars. However ISO data reported by Tuffs et al. (1996) reveal an extended FIR emission out to a radius of 8′, with a scale–length similar to the R–band one, while little H_α emission has been detected beyond $r \sim 6'$. This suggests that part of the observed cold FIR SED of NGC 6946 could be due to dust associated with a diffuse H I gas, which indeed extends out to $r \sim 15'$ (Boulanger & Viallefond 1992), and heated mainly by old stellar populations. Malhotra et al. (1996) find that the radial scale–lengths at 7 and 15 μm are similar to those in H_α and H_2 but much shorter than those in R–band and H I, consistent with a warm dust emission primarily heated by young massive stars. In the proposed fit the MIR emission arises from MCs dust heated by newly born stars. The SED above $\sim 60\,\mu$m is almost equally contributed by MCs and diffuse dust, but, since $t_o = 2.5$ Myr, even the latter is predominantly heated by young stars.

Tacconi & Young (1986) estimate a scale–length of 9.6 kpc for the cold ISM compo-

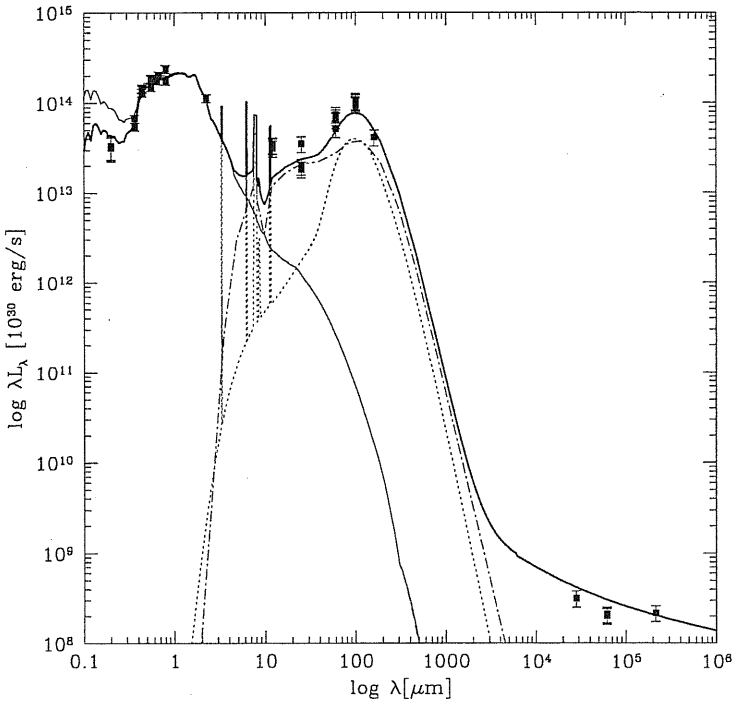

Figure 4.8: Fit to the SED of the Sbc galaxy M100. Data are from Buat et al. (1989), Donas et al. (1987), De Jong et al. (1994), Stark et al. (1989), RC3, Devereux &Young (1990), Young et al. (1989), Helou et al. (1988), Knapp et al. (1987). Meaning of lines as in Fig. 4.1.

nent, whilst for the star distribution their values range from 4 to 8 kpc, depending on the band and on the galactic component (disc or arms) considered. The model scale–lengths are set to 8 for both stars and the diffuse gas. The vertical scale–lengths are 1 kpc to keep the diffuse dust emission sufficiently cold.

4.3.1 Discussion for spirals

The SEDs of the three spiral galaxies we considered, M51, M100, and NGC 6946, have been well reproduced by our model. An interesting result is the significantly lower t_o in spirals with respect to starbursting objects. This derives from their smaller observed ratios L_{FIR}/L_{UV}. In the three spirals analyzed here, the newly born SSPs quite soon get out from the parent clouds and significantly contribute to the heating of the diffuse dust. The expected contribution is larger for NGC 6946 and M100 than for M51. As a consequence, a significant portion of the far–IR luminosity emitted by the diffuse dust (almost all for NGC 6946 and M100) should be inserted in the budget to infer the SFR in spiral galaxies, in agreement with the findings of Devereux et al. (1994) and Buat & Xu (1996). Taking into account this, the SFRs derived from the FIR luminosities, through the conversion suggested by Kennicutt (1998), are in very good agreement with those used by the model.

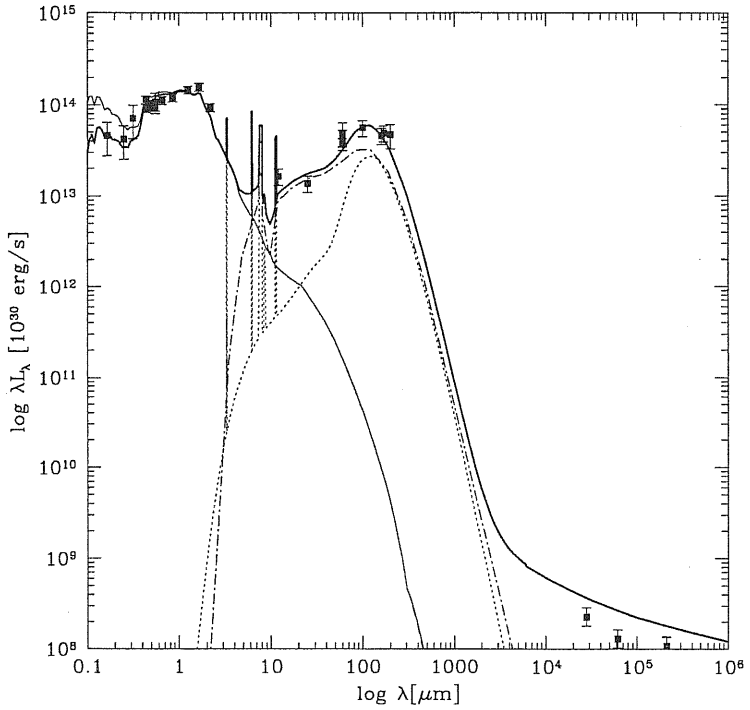

Figure 4.9: Fit to SED of the Scd galaxy NGC 6946. Data are from Rifatto et al. (1995), RC3, Engargiola (1991), Devereux & Young (1993), Rice et al. (1988), Tuffs et al. (1996). Meaning of lines as in Fig. 4.1.

The SFRs in our models, through the conversion of Kennicutt (1998) $L(H_\alpha)[\text{ergs s}^{-1}] = 1.26 \times 10^{41} \times SFR[M_\odot\,\text{yr}^{-1}]$, yield H_α luminosities of 7.6, 8.8, and 7.6 10^{41} ergs s^{-1} for M51, M100, and NGC 6946 respectively, to be compared with observed values (Kennicutt, Tamblyn, & Congdon 1994, reported to our adopted distances) of 4.9, 5.0, and 2.2 $\times$ 10^{41} ergs s^{-1}. These lower values would imply an internal H_α extinction of $A_{H\alpha} = 0.5$, 0.6, and 1.3 magnitudes in the three spirals, consistent with the average value 1.1 adopted by Kennicutt (1998), based on a comparison of free–free radio and H_α fluxes.

It is also worth noticing that masses in stars, dust, and gas derived by the model, as well as geometric parameters such as the disc scale length are in good agreement with independent estimates. Our model includes the main physical aspects of star formation, stellar evolution, and dust absorption in spiral galaxies and allows a full exploitation of the broad band data in order to explain their present status and their past history.

4.4 Local giant ellipticals

Ellipticals constitute a class of objects with fairly homogeneous spectral properties. It is then interesting to test our model against an average SED of giant E galaxies, constructed combining the Arimoto's template (1996) from 0.12 to 2.2 μm with the

median IRAS over B band fluxes of bright ellipticals estimated by Mazzei et al. (1994) and the average (K-L) color by Impey et al. (1986) (Fig. 4.10).

The fit has been obtained with a 'classical' star formation history model for ellipticals, an open model with infall and galactic wind (see Sec. 2.2): the high efficiency $\nu = 2$ Gyr^{-1} causes a huge SFR in the first 1.2 Gyr, after which the SFR is supposed to stop for the onset of galactic wind. The ensuing evolution is purely passive. The object is observed at 13 Gyr, when a comparatively small fraction of galactic mass in a diffuse dusty component is sufficient to produce the observed IRAS emission. The residual gas provided by the chemical model arises from evolved stars of the passively evolving galaxy, since the galactic wind is supposed to sweep away any gas present at time t_{wind}. As already mentioned in Sec. 2.2, we had to decrease the gas in the ISM due to stellar feedback by a factor $\sim 2 \times 10^{-3}$ in order to reproduce the observed IR emission. The resulting mass in the diffuse dust is $1.5 \times 10^7\, M_\odot$.

It is also worth noticing that r_c needs to be much greater for the ISM than for stars (6 and 0.4 kpc respectively): for smaller values of r_c^c the cirrus emission would be too warm because dust would be more concentrated in the central regions where the radiation field is higher. Other authors already suggested that diffuse dust in elliptical galaxies needs to be less concentrated than stars, on the basis of either optical color gradients (e.g. Wise & Silva 1996) or IRAS colors (e.g. Tsai & Mathews 1996). As discussed in Sec. 2.5.3, an alternative proposed way to describe this lower concentration is to adopt the same r_c for both stars and diffuse dust, decreasing the exponent $\gamma = 1.5$ in the King law of stars. However for this SED, adjusting γ^c and r_c with the constrain $r_c^c = r_c^*$, we found only marginally acceptable fits in the IRAS regime, significantly worse than that presented in Fig. 4.10.

4.4.1 Discussion for ellipticals

The model with a relatively small number of parameters is able to produce a very good fit to the template SED of giant elliptical galaxies (see Fig. 4.10). Most excitement about spheroidal galaxies is related to their evolution. Indeed it has been suggested that, during the initial phases of star formation, they might look very similar to local violent starbursts (such as Arp 220, Sec. 4.2), since the chemical enrichment and, as a consequence, the dust formation are very quick processes when SFRs are very high (Mazzei et al. 1994; Franceschini et al. 1994). This initial phase, if confined to high enough redshifts $z \leq 2 - 2.5$, is the most natural way to produce the total energy and the shape of the FIR Background (Franceschini et al. 1991; Franceschini et al. 1994; Burigana et al. 1997), which has been tentatively detected by Puget et al. (1996) and recently confirmed by Hauser et al. (1998) and Fixsen et al. (1998). The IR and submm bright galaxies detected in the ISO deep surveys and by SCUBA, interpreted as high-z dusty starbursts, may be objects of this kind (e.g. Rowan-Robinson 1997, Elbaz et al. 1999). Moreover, the so-called extremly red objects are often interpreted as high-z starbursting spheroids (see below).

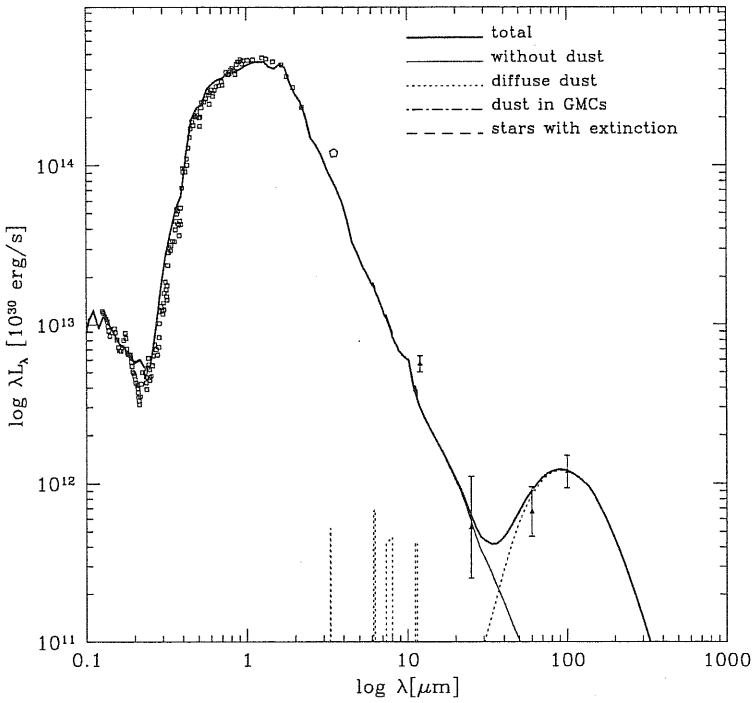

Figure 4.10: A fit to a template SED of a giant elliptical galaxy.

4.5 A case study for high-z galaxies: HR10

Since our model is able to describe in detail the evolution of galaxies in a wide range of wavelengths, it is well suited to investigate on the properties of high-z galaxies from the analysis of their SED.

As an example, we consider in this section the case of HR10, an Extremely Red Object. Galaxies with R-K> 6 are classified as EROs: they are optically very faint (R> 24.5) but relatively bright in the K band (K $\lesssim$ 19, Graham & Dey 1996). Their extremely red colors are interpreted as due to either very old stellar populations or a dust-enshrouded starburst (e.g. see in Fig. 5.3 an example of the degeneracy between age and extinction). Near-IR surveys have revealed a substantial population of these galaxies but only for HR10 a redshift has been estimated (z=1.44, Hu & Ridgeway 1994). This galaxy has been observed also in the submm by Cimatti et al. (1998) and Dey et al. (1999) revealing dust emission. Therefore the red colors of HR10 are probably the consequence of strong extinction.

We find a good fit to the SED of this galaxy (Fig. 4.11) with a model observed at t_G = 1.5 Gyr, with SFR$\sim$ 240 $M_\odot yr^{-1}$, baryonic mass $\sim 10^{12}$ $M_\odot$ and mass of dust $\sim 6 \times 10^9$ $M_\odot$ (H_0 = 50 km/s/Mpc). In order to reproduce the huge optical-NIR extinction, we model the galaxy as a unique staburst region, i.e. all the gas is in the MC component with optical depth $\tau^{mc}_{1\mu m} = 2$. Since, as already mentioned, $\tau_{mc} \propto \delta\, m_{mc}/r^2_{mc}$ is the true fitting MC parameter, if $\delta = 9 \times 10^{-3}$ the required value can be obtained for instance with $m_{mc} = 10^8$ $M_\odot$ and r_{mc} = 600 pc. The escape time from MCs, t_0, is set to

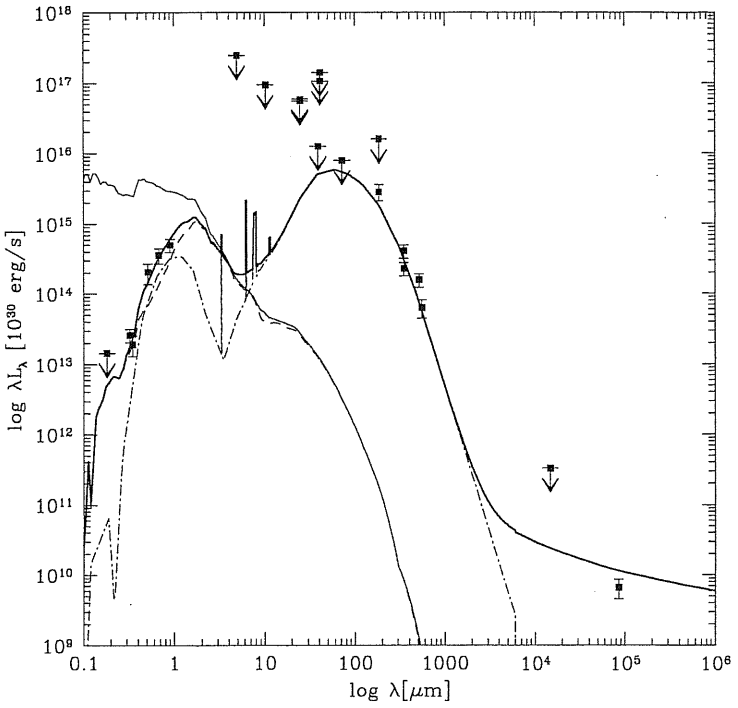

Figure 4.11: Fit to the rest-frame SED of HR10, an Extremely Red Object at z=1.44. Data are from Graham&Dey (1996), Cimatti et al. (1998), Dey et al. (1999). The fitting model, for $H_0 = 50$ km/s/Mpc, has $t_G = 1.5$ Gyr, SFR=240 $M_\odot$/yr, $\tau^{mc}_{1\mu m} = 2$, $M_{dust} = 6 \times 10^{11}$ $M_\odot$ and $L_{IR} = 2.6 \times 10^{12}$ $L_\odot$. In the submm, we choose to fit the new SCUBA data of Dey et al. ($\lambda_{obs} = 450$, 850 and 1350μm), who report a 850μm flux density $\sim$ half the one by Cimatti et al.

1.2 Gyr, this means that only stars older than this value have escaped the starbursting region. All this extinguished starburst is then observable in the IR-submm. However the energy level in the IR is set by the $60 - 100\mu$m region, where only upper limits are at present available. Therefore the baryonic mass of the model, and to a lesser extent the strengh of the burst, could be rescaled downwards according to the true values of the IR energy.

4.6 Conclusion

We showed that our model GRASIL is extremely efficient in deriving a wealth of information from broadband spectra of starburst and spiral galaxies. Indeed, when SEDs from the UV to the sub–mm range are available, we are able to quantify the effects of dust reprocessing on observations, gaining information on very substantial quantities such as SFR, the IMF and the past history of the galaxies.

When reproducing starburst galaxies, our model is characterized by the variations of 6 parameters related to the total mass and star formation history and of 5 geometrical

parameters (Tables 4.1 and 4.2). For normal disc galaxies, the parameters become 3 and 5 respectively. In order to fit the elliptical galaxy template, 7 parameters have been adjusted, including the epoch at which the SF activity is stopped and the amount of residual gas determining the IR emission.

The masses reasonably constrained by matching the SED are the baryonic mass (though dependent on the IMF, particularly its lower limit) mostly from the energy emitted in the NIR by the old stellar component, and the mass of dust, from its MIR–FIR emission. Therefore the mass of gas present in the galaxy is constrained from the fit, provided δ is known. Our assumption $\delta = 9 \times 10^{-3}$ is likely the best guess for our Galaxy, however in different systems and in the Galaxy itself, variations of a factor of a few are commonly quoted, e.g. Rand, Kulkarni, & Rice (1992) for M51 or Tuffs et al. (1996) for NGC 6946. As a consequence, our estimated gas masses suffer by a similar uncertainty. The SFR history of the old stellar component is constrained by the spectrum and, for starburst galaxies, also by the requirement that a certain amount of gas is available for the latest burst. The three analyzed starbursts exhibit rather different star formation histories, with the average SFR of the old component inversely proportional to the strength of the SFR in the burst. Estimates of masses in stars and gas, as well as of SF and SN rates from observations other than broad band spectra, discussed in the previous sections and below, nicely agree with those provided by our SED fitting.

Therefore the model is well suited to study local starburst and normal galaxies as well as to trace back the history of the different classes of galaxies in order to investigate on their cosmological evolution (by comparing predictions with observations of number counts and redshift distributions in different bands), as described in the following chapters.

Chapter 5

Early-type galaxies in the HDF: the star formation history

Summary. We[1] have investigated the properties of a complete K-band selected and morphologically classified sample of 35 E/S0 galaxies brighter than $K = 20.15$ mag in the HDF, as representative of the field galaxy population. Fifteen objects have spectroscopic redshifts, while for the remaining 20 a photometric redshift is estimated from a seven–color broadband spectrum (4 HST + 3 NIR bands). The broadband spectra allow us to date the dominant stellar populations. The majority of bright early–type galaxies in this field are found at redshifts $z \lesssim 1.3$ to display colors indicative of a fairly wide range of ages (1.5 to 3 Gyrs). We find that the major episodes of SF building up typical $M^\star$ galaxies have taken place during a wide redshift interval, $1 < z < 4$ for q_0=0.5, $1 < z < 3$ for q_0=0.15. There seems to be a tendency for lower mass ($M < 5\ 10^{10}\ M_\odot$) systems to have their bulk of SF protracted to lower redshifts. Our estimated galactic masses are found in the range from a few $\sim 10^9\ M_\odot$ to a few $10^{11}\ M_\odot$ already at $z \simeq 1$. So the bright end of the E/S0 population is mostly in place by that cosmic epoch, with space densities, masses and luminosities consistent with those of the local field E/S0 population. What distinguishes our sample is a remarkable absence of objects at $z > 1.3$, which should be detectable during the star formation phase expected at these redshifts. Investigating on this issue with our code GRASIL (Chap. 2), we argue this could be due to dust enshrouded starbursts occurring during the first few Gyrs of the galaxy lifetime. Our main conclusions are moderately dependent on the assumed value of q_0. An open universe is favored in our analysis by the match of the K–band local luminosity functions with the observed numbers of faint distant galaxies. Two sources of uncertainty in our analysis (the possible presence of a background cluster or group at $z \sim 1$ in the HDF possibly contaminating the z distribution, and the lack of a complete spectroscopic identification) are shown unlikely to affect our main results. This same kind of analysis for a

[1]This Chapter is based on the paper *Franceschini A., Silva L., Fasano G., Granato G.L., Bressan A., Arnouts S. & Danese L., 1998, ApJ, 506, 600* (Franceschini et al. 1998).

K-selected sample of late-type galaxies in the HDF is presented in App. B.

5.1 Introduction

Early–type galaxies have been studied in great detail in rich clusters up to redshift 1 and above (see Stanford et al. 1998), with the basic result that passive evolution in luminosity and no evolution in mass is ruling them to at least $z \simeq 1$. Old ages and an early coeval epoch of formation are then implied by these observations. It is still unclear, however, how much the rich–cluster environment is representative of the general population. Indeed, contradictory results have been reported about the evolutionary properties of early–type field galaxies.

The analysis by Im et al. (1996) of a sample of elliptical galaxies in the HST Medium Deep Survey seems to indicate that these galaxies share similar properties with the cluster objects, a result based however on a sample of 376 galaxies with only 24 spectroscopic redshifts and photometric redshifts based on (V–I) colors. Similarly, Lilly et al. (1996) find that the luminosity function of red galaxies in the Canada–France Redshift Survey (CFRS) does not exhibit significant changes in the redshift interval $0.2 \leq z \leq 1$. These observations imply an early epoch of formation for the elliptical galaxies.

These conclusions have been questioned by Kauffmann et al. (1996) (see also Baugh et al. 1996), who claim evidence for a decrease in the mass density already at $z \leq 1$ for early–type galaxies in the CFRS, these too selected from (V–I) colors.

An exceedingly deep and clean view of the field galaxy populations to high redshifts is provided by a long integration of HST in the so–called *Hubble Deep Field* (HDF, Williams et al. 1996). Although it has provided relevant constraints on galaxy formation and evolution and about the epoch of production of metals (e.g. Madau et al. 1996; Connolly et al. 1997; Sawicki et al. 1997), the interpretation of these data alone is made difficult by the relatively short selection wavelengths (essentially those of the U, B, V, I bands), which imply strong evolutionary and K–corrections as a function of redshift (Giavalisco et al. 1996). These may be particularly severe for the early–type galaxies, because of their quickly evolving optical spectra and extreme K–corrections (e.g. Maoz 1997).

Another unsolved problem specifically affecting short wavelength observations concerns the possible effects of dust present in the line of sight to the object: even small amounts may seriously affect spectra corresponding to rest frame far–UV wavelengths. Various analyses attempting to solve this issue have compared the observed UV spectra with templates of young dusty galaxies (e.g. Meurer et al. 1997). It is evident, however, that even small variations in the dust properties and in the assumed spectral templates imply widely discrepant predictions for the extinction corrections (published estimates range from less than 1 to more than 3 magnitudes of extinction in high–z galaxies). Any inferences about the star formation history are correspondingly uncertain.

We try an alternative approach to the past history of galaxies based on a thorough photometric and morphological analysis of a complete K–band selected sample of elliptical and S0 galaxies in the HDF. The selection in the K infrared band helps to overcome most of the above problems of optical selection, in particular it minimizes the

effects of K- and evolutionary corrections and of extinction by any residual intervening dust. Another crucial advantage of using NIR data is that the integrated fluxes at these wavelengths are contributed by all (low mass) stars dominating the baryonic content of a galaxy.

Various deep integrations have been performed in the HDF at NIR (Cowie et al. 1996; Dickinson et al. 1997) and MIR wavelengths (Rowan-Robinson et al. 1997; see also Aussel et al. 1998), which, combined with the extreme quality of the morphological information and the very good spectroscopic coverage, make this area unique, in particular for the investigation of early–type galaxies outside rich clusters.

We concentrate here on a (morphologically selected) sample of 35 early–type galaxies. Our interest for this subpopulation rests on its homogeneous morphological properties, indicative of a purely stellar emission (hence requiring a relatively simple modelling), and on the expected old ages (by comparison with their rich–cluster analogues). Altogether, this class of objects is expected to provide information about the high–redshift side of the star formation history, which has perhaps been only partly sampled by direct optical selection via the dropout technique. In our approach, the inferred evolutionary history of stellar populations is essentially unaffected by the mentioned problems related to dust extinction.

Sec. 5.2 provides details about the selection of the sample, the adopted procedures in the photometric and morphological analyses, and statistical tests of completeness carefully dealing with observational limits on the total flux and surface brightness. In Sec. 5.3 we analyze physical properties of galaxies as inferred from the morphology and from fits to the broadband UV–optical–IR spectra. Sec. 5.4 addresses the statistical properties of the sample (counts, redshift distributions, identification statistics), and compare them with those of local samples of early–type galaxies. We discuss, in particular, evidence that the redshift distribution breaks above $z \gtrsim 1.3$. Various interpretations of these results are discussed in Sec. 5.5, where the effects of repeated merging events, probably in the presence of a dust–polluted medium, are considered. This information is used in Sec. 5.6 to constrain the history of star formation of stellar populations, and to compare it with other published estimates. The results of this chapter are summarized in Sec. 5.7.

We adopt $H_0 = 50\ Km/s/Mpc$ throughout this Chapter. The analysis is made for two values of the cosmological deceleration parameter, $q_0 = 0.5$ and 0.15, assuming zero cosmological constant Λ. Note that the effects of increased time scales and volumes of an open universe might be also obtained in a closure world model with a non zero Λ.

5.2 Sample selection and photometry

Dickinson et al. (1997) obtained deep NIR images of the HDF with the IRIM camera mounted at the KPNO 4m Telescope. The camera employs a 256x256 NICMOS-3 array with $0''.16$/pixel, but the released images are geometrically transformed and rebinned (with appropriate pixel weighting) into a 1024x1024 format. IRIM has observed the same area in the J, H and K filters, for a total of 12, 11.5 and 23 hours, respectively. Formal 5σ limiting magnitudes for the HDF/IRIM images, computed from the measured sky noise within a $2''$ diameter circular aperture, are 23.45 mag at J, 22.29 mag at H,

and 21.92 mag at K, whereas the image quality is $\sim 1''.0$ FWHM.

Our galaxy sample has been extracted from the HDF/IRIM K–band image through a preliminar selection based on the automatic photometry provided by SExtractor (Bertin and Arnouts 1996). It is flux limited in the K–band and it includes only galaxies whose morphology strongly suggests an early–type classification. The measure of magnitude is based on fixed $2.5''$ aperture photometry (which best accounts for the seeing of the K image) and applying a stellar correction for the outer part.

5.2.1 Monte Carlo tests of completeness

In order to set the appropriate value of the magnitude limit K_L for inclusion in our sample, we have produced a synthetic frame containing a 10×10 grid of toy galaxies with $r^{1/4}$ luminosity profiles, having total K magnitudes and effective radii r_e spanning the ranges $19.00 \div 21.25$ mag (step 0.25 mag) and $0''.08 - 0''.80$ (step $0''.08$), respectively. These limits were chosen to provide a full characterization of the performances of SExtractor (i.e. identification capability and magnitude estimate of galaxies) in the critical range of K magnitudes and for values of the true effective radius typical of the HDF ellipticals (Fasano & Filippi 1998, hereafter FF98; see also Fasano et al. 1998, hereafter FA98).

We are particularly interested in evaluating the probability of detection, as well as possible biases in the magnitude estimation, as a function of the magnitude itself and of r_e (i.e. of the 'true' average surface brightness $< \mu_e^K >$, and, ultimately, of the redshift). We have convolved this synthetic frame using a PSF derived by multigaussian fitting of the few stars included in the K–band image. Then, a bootstrapping procedure has been carried out in order to produce 10 different images mimicking the 'true' image noise. These images have been processed with SExtractor to get, for each toy galaxy, ten different SExtractor estimates of the total K magnitude, and then the average magnitude $< K_{SEx} >$, the standard deviation $\sigma_{K_{SEx}}$ (or the difference $\Delta K =< K_{SEx} > - K_{true}$).

From these simulations of galaxies having $r^{1/4}$ luminosity profiles we conclude the following. (1) For the whole range of tested magnitudes and radii, the fraction of detections is equal to unity up to $< K_{SEx} > \simeq 21.4$ mag and $< \mu_e^K > \simeq 22.0$ mag. (2) The magnitudes estimated by SExtractor are systematically fainter than the true magnitudes, the bias mainly depending on the galaxy surface brightness.

The left–hand side of Fig. 5.1 shows that, if we consider only galaxies with $< K_{SEx} > \lesssim 20.7$ mag (K_{lim} hereafter), the standard deviation of the SExtractor magnitude estimates is less than 0.05 mag (σ_{max} hereafter). The right–hand side of Fig. 5.1 reports ΔK as a function of $< \mu_e^K(SEx) >$ for the subsample of toy galaxies with $< K_{SEx} > \lesssim K_{lim}$. It shows that ΔK systematically increases at increasing $< \mu_e^K(SEx) >$, approaching the maximum value $\Delta K_{max} \sim 0.5$ mag for $< \mu_e^K(SEx) > \simeq 22.0$ mag. The solid line in Fig. 5.1 (right) is a polynomial fit to the data:

$$\log(\Delta K) = -0.830 + 0.147 < \mu_*^K > +0.019 < \mu_*^K >^2 \qquad (5.1)$$

where $< \mu_*^K >=< \mu_e^K(SEx) > -19$. The plots in Fig. 5.1 provide a straightforward indication of the strategy to be used in order to obtain a complete flux limited sample of early–type galaxies from the IRIM K–band image using SExtractor. The procedure

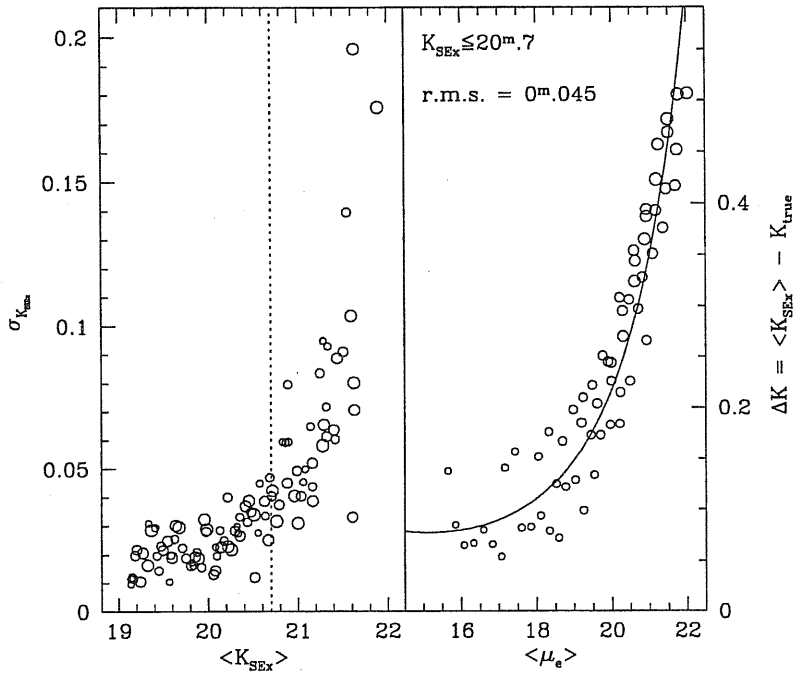

Figure 5.1: *Left*: standard deviation of the SExtractor magnitude estimates as a function of the average magnitude for galaxies in the simulated images: the standard deviation is very small for $< K_{SEx} > \leq 20.7$ mag. *Right*: difference between true flux and the SExtractor flux as a function of the average surface brightness for the subsample of simulated galaxies with $< K_{SEx} > \lesssim 20.7$ mag: it shows that only very low surface brightness objects ($< \mu_e^K(SEx) \geq 22$) could be missed by the IRIM K–band image.

consists in the following steps: (1) produce a catalog of objects with $K_{SEx} \lesssim K_{lim} = 20.7$ mag; (2) check the morphology of each object on the WFPC2 frames, removing stars and late–type (or irregular) galaxies from the sample; (3) exploit the high resolution and depth of the V_{606} and/or I_{814} images to derive the effective radii of the galaxies and use these values of r_e to compute $< \mu_e^K >$, assuming a roughly constant color profile; (4) apply to the K_{SEx} magnitudes the statistical corrections given in the previous equation; (5) include in the final sample only galaxies with corrected magnitude less than or equal to $K_L = K_{lim} - \Delta K_{max} - \sigma_{max} = 20.15$ mag.

5.2.2 The morphological filter

The most delicate steps in the previous scheme are those concerning the morphological analysis and the evaluation of the effective radii (points 2 and 3 of the previous list). We follow the procedure discussed in FF98 and FA98 summarized below, but we refer to these papers for details. The SExtractor automatic photometry of the IRIM K–band image produced a preliminar sample of 109 objects with $K_{SEx} \leq 20.7$ mag (first point of the previous selection scheme). All these objects were examined with the IMEXAM–IRAF tool to produce a first (conservative) screening against stars or late–type and irregular galaxies, resulting in a temporary list of 47 early–type candidates.

Our quantitative morphological classification filter assumes a dominant $r^{-1/4}$ profile for the bulk of the light distribution in the galaxy.

For 29 galaxies in this list the surface photometry in the ST–V_{606} band is available in FF98 and the total AB magnitudes in the four WFPC2–HDF bands are given in FA98, together with the equivalent effective radii derived after deconvolution of the luminosity profiles. Four more galaxies included in both our and FF98 samples, were not analyzed by FA98. For these galaxies we computed optical AB magnitudes and effective radii according to the prescriptions given in FA98. The remaining 14 galaxies in the temporary list are not in the FF98 sample, since in the V_{606} band they did not satisfy the selection criteria adopted in order to secure a reliable morphological analysis. We performed the detailed surface photometry of these galaxies in the I_{814} band (where they show a better S/N ratio), producing luminosity and geometric profiles of each galaxy. From this analysis, 3 objects were recognized to be 'disk–dominated' galaxies (likely Sa), whereas two more objects showed peculiar or unclassifiable profiles. These galaxies were excluded from the temporary list. The remaining 9 galaxies with surface photometry in the I_{814} band were analyzed following the same procedure described in FA98 to derive the total AB magnitudes in the optical bands, as well as the 'true' (deconvolved) equivalent effective radii. Fig. 5.2 shows the luminosity profiles of these galaxies derived from the surface photometry in the I_{814} band.

5.2.3 The final sample

Altogether, of the 47 candidate E/S0 galaxies with $K_{SEx} \leq 20.7$, 33 were already classified as E/S0 by FA98 and FF98, while 9 are confirmed as E/S0 through the previous analisys, for a total of 42 objects in the incomplete sample at $K_{SEx} \leq 20.7$. To ensure a highly reliable completeness limit, following steps (4) and (5) of the selection scheme discussed in Sec. 5.2.1, we used Eq. 5.1 to correct the K_{SEx} magnitudes of the 42 galaxies in the temporary sample. In this way we obtain our final sample of 35 galaxies with corrected magnitude $K \leq 20.15$ mag over the HDF (3 WF + 1 Planetary Camera) area of 5.7 square arcmin. Some basic data on the sample are listed in Table 5.1.

The H and J magnitudes listed in the Table have been obtained running SExtractor on the corresponding IRIM images and accounting for the expected biases with the same procedure adopted for the K magnitudes (simulations of toy galaxies, convolution with proper PSF, noise bootstrapping and correlation between bias and average surface brightness). The corresponding equations are:

$$\log(\Delta H) = -0.903 + 0.288 < \mu_*^H > -0.0158 < \mu_*^H >^2 \tag{5.2}$$

$$\log(\Delta J) = -1.014 + 0.162 < \mu_*^J > +0.0140 < \mu_*^J >^2 \tag{5.3}$$

where $< \mu_*^H >=< \mu_e^H(SEx) > -20$ and $< \mu_*^J >=< \mu_e^J(SEx) > -19$.

At the time we performed this analysis, for 15 galaxies in Table 5.1 spectroscopic redshifts were available in the literature or in the WEB (see notes to Table 5.1), while for the remaining 20 objects a reliable estimate of z was obtained from fits of the optical–IR broadband spectra (see Sec. 5.3.1).

The last three columns in Table 5.1 give some information on the surface photometry. In particular, the symbol P814 indicates galaxies whose surface photometry has been

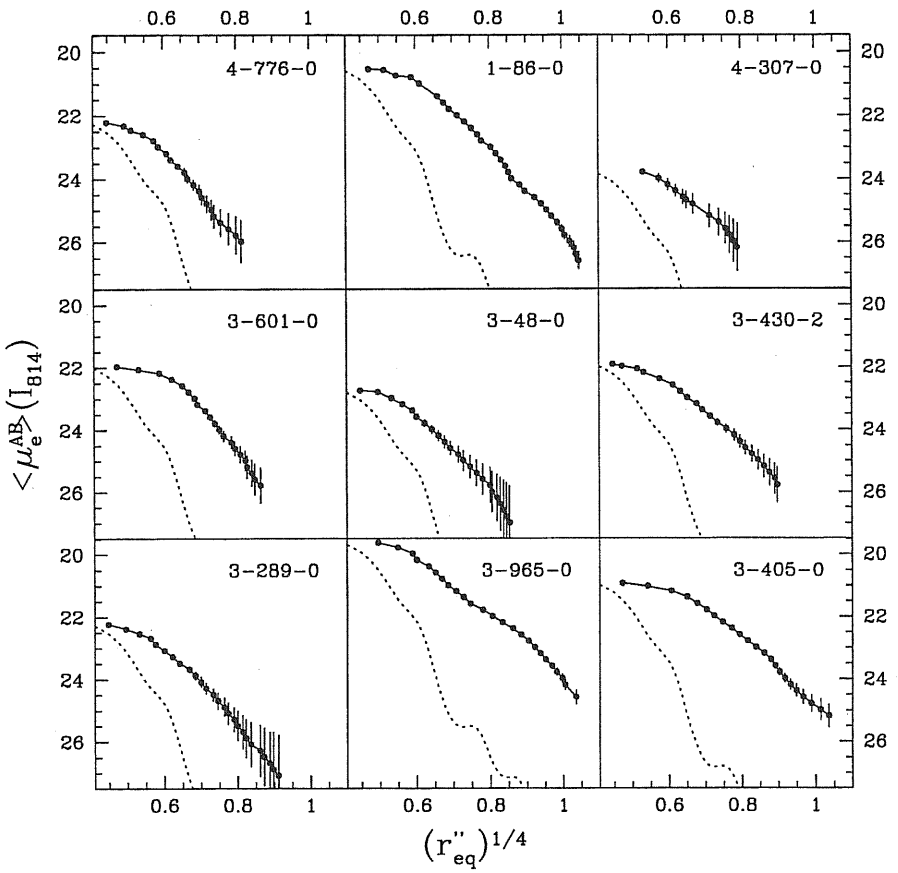

Figure 5.2: Luminosity profiles in the I_{814} for nine galaxies in the sample. The dotted line is a fit to the PSF.

obtained in the I_{814} band, while the symbols (T1), (T2) and (T3) indicate galaxies which, according to FF98, belong to the '*Normal*', '*Flat*' and '*Merger*' class, respectively. These attributes refer to the classification by FF98 (see also Fasano et al. 1996), based on the luminosity profiles, of early–type galaxies in the HDF: (1) the normal class, for which the de Vaucouleurs law is closely followed down to the innermost isophote not significantly affected by the PSF; (2) the flat class, characterized by an inward flattening of the luminosity profiles (with respect to the de Vaucouleurs' law) which cannot be ascribed to the effect of the PSF; (3) the merger class, in which isophotal contours show the existence of complex inner structures (two or more nuclei) embedded inside a common envelope, which roughly obeys the $r^{1/4}$ law.

The completeness of the sample has been evaluated from numerical simulations as described in Sec. 5.2.1. We have not used the classical V/V_{max} test to this purpose, since it is equally sensitive to departures from spatial homogeneity as it is to completeness. The question of the distribution of objects in the spacetime will be addressed in Sec. 5.4.

5.3 Broadband spectra and surface brightness distributions

The surface photometry of the images of our sample galaxies has shown that for the large majority of them there are no morphological signatures of the presence of dust, e.g. obscured lanes across the galaxy, asymmetric brightness distributions or profiles deviating from the $r^{-1/4}$ over the bulk of the galaxy (see however Witt, Thronson, & Capuano 1992, for a cautionary remark about the latter point). Only three galaxies belong to the morphological class T3, where ongoing star formation, possibly enshrouded by dust, is likely to have a role. Four more objects belong to the class T2, for which any dust, whenever present, should most probably be confined to the inner core of the galaxy, hence should not affect the global emission. Five out of 7 of the morphologically peculiar objects have blue (class *a*, as discussed in Sec. 5.3.1) spectra.

An obvious way to test for the presence of dust would be to look for its reradiation at infrared wavelengths. The Infrared Space Observatory (ISO) has observed the HDF in two broadband filters centered at 6.7 and 15 μm. While the former, for redshifted objects, is dominated by photospheric emission of old stars, the latter is contributed by very hot dust, if SF is ongoing, transiently heated molecules and very small dust grains present in the ISM, and by circumstellar dusty shells around evolved stars. Mann et al. (1997) and Goldschmidt et al. (1997) report catalogues of sources down to rather conservative flux limits ($\sim$ 0.2 mJy at 15μm). At 15 μm only one ISO source is in common with our list (ID 2-251-0), a galaxy with a point source evidencing in the U and B, probably an AGN. Though a conclusion has to wait for a refined analysis of the ISO observations, aimed at deeper flux limits (Aussel et al. 1998, Désert et al. 1988), the available information seems to confirm that there is little room for dust emission by our E/S0 galaxies.

In Fig. 5.3 we show the expected IR emission for one of the sample galaxies due to AGB dusty envelopes alone (Chap. 3), that should be the only source of IR emission if these E/S0s are observed short after the end of their star formation activity, possibly ended because of the onset of galactic winds or gas consumption. The spectrum is predicted to be far too low to be dected by ISO at 15μm. In the lower panel, the same observed spectrum is compared to our models for M82 and ARP 220 (see Chap. 4). The limits of ISO at 15μm ($\sim$ 0.2 mJy) and of SCUBA at 850μm (2 mJy, Hughes et al. 1998) in the HDF are indicated. While only a huge starburst as in ARP 220 is predicted to be detectable in the submm, the MIR emission from warm dust powered by star formation should be well above the ISO limit.

The present analysis will take advantage of the simplified behavior for the bulk of our objects, i.e. the lack of evidence for dust, by allowing modelling of galaxy spectra as the integrated emission of purely stellar populations. The inclusion of the additional effect of dust extinction, whenever present, would have substantially weakened our conclusions, since degenerate sets of solutions could have been possible, implying uncertain estimates of the photometric redshift and of the galaxy age (see e.g. Fig. 5.3 lower panel). Indeed the degenaracy introduced by dust extinction is the major problem affecting the analysis of the optica-NIR SED of a sample of late-type galaxies in the HDF, described in App. B.

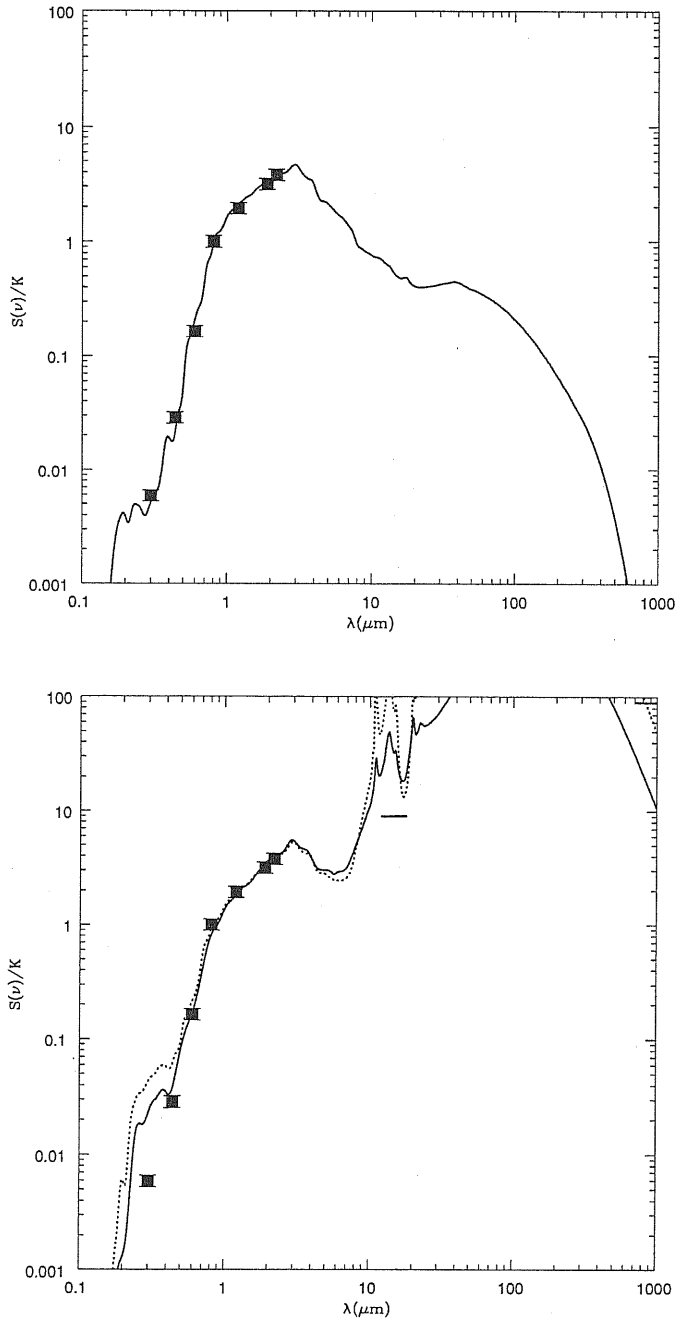

Figure 5.3: *Above*: The expected IR broadband spectrum from AGB circumstellar dusty envelopes is shown for one of the sample galaxy, ID 4-744-0, z=0.764. The constant of normalization is $K = 2.228 \times 10^{-5}$ Jy. The predicted flux at 15μm is below the ISO sensitivity of $\sim$ 0.2 mJy. *Below*: The spectra of our models for M82 (continuous) and Arp 220 (dotted), described in Chap. 4, are redshifted and rescaled in order to be compared with the same spectrum as above. The limits of ISO at 15μm and of SCUBA at 850μm in the HDF are indicated. The MIR dust emission due to star formation should be detected by ISO while only a huge starburst as in ARP 200 is predicted to be observable in the submm. Note also the well known problem of the degeneracy between age and extinction in optical-NIR spectra.

5.3.1 Fitting the galaxy broadband spectra: evaluation of the photometric redshifts and of the galactic ages

The UV–optical–NIR SED for all galaxies in the sample have been fitted with synthetic spectra computed with our chemical and spectrophotometric model GRASIL described in Chap. 2.

We consider models with a Salpeter IMF with a lower limit $M_l = 0.15\ M_\odot$, a Schmidt–type law for the SFR $\Psi(t) = \nu\, M_g(t)^k$ and infall time scale τ_{inf} (see Sec. 2.2). A number of evolutionary patterns for the time dependent SFR $\Psi(t)$ have been tried to reproduce the galaxy SED, to estimate the photometric redshifts for galaxies lacking the spectroscopic identification, and to fit the global statistical properties of the sample. However, we will mostly refer in the following to two paradigmatic evolution cases.

The first model (hereafter Model 1) reproduces a classical scheme for the formation of ellipticals (e.g. Larson 1974), i.e. a huge starburst on short timescales, expected to occur at high redshifts. In our approach the SF has a maximum at a galactic age of 0.3 Gyr and continues at substantial rates up to 0.8 Gyr, after which it is assumed to stop because of the onset of galactic wind. The evolution at later epochs is due to passive aging of already formed stellar populations. This evolution pattern is achieved with the following choice of the parameters: $\tau_{inf} = 0.1$ Gyr, $k = 1$, $\nu = 2\ Gyr^{-1}$. The precise time dependence of the SFR is reproduced in Fig. 5.4 (dotted line).

Our second model (hereafter Model 2) gives up the concept that the stellar populations in field early–type galaxies are almost coeval, and assumes instead that the SF lasts for a significant fraction of the Hubble time. This is obtained with the following parameters: $\tau_{inf} = 1$ Gyr, $k = 1$, $\nu = 1.3\ Gyr^{-1}$. The corresponding SF law has a broad peak at 1.4 Gyr and goes on at a substantial rate for about a couple Gyr more (continuous line in Fig. 5.4). This SF law is clearly an oversimplified picture of a process which has been likely more complex. In particular a protracted SF is likely to have occurred through a set of successive starbursts (e.g. due to mergers or strong dynamical interactions). Since we are dealing with the integrated emission of all stellar generations, there is virtually no difference, as for the broadband spectral appearance in the afterburst phase, between a set of starbursts occurring over 3 Gyr and a continuous SF during this period.

The redshift for the onset of starformation z_F in the galaxy is a free SED fitting parameter. To provide the simplified schemes of Model 1 and 2 with more flexibility, we have allowed a residual SF Ψ_0 at a basal level to be added to the flux emitted by the passively evolving populations. This allows to fit the spectra of the four bluest objects, and to improve the fits at the shortest (U, B) wavelengths for additional galaxies. Since typical values for Ψ_0 are much less than 1 $M_\odot/yr$ and this residual SF does not contribute significantly to the mass and energetics, this parameter is used only in the spectral fits of Fig. 5.5 and never more in the subsequent analyses. Ψ_0 is then a second free parameter. The baryonic mass M and the photometric redshift (for cases where it is needed) are further parameters in the spectral fitting procedure.

The photometric redshifts

Fig. 5.5 is a collection of the observed spectra for the 35 sample galaxies. The figure displays essentially two kinds of spectral behaviors: class *(a)* spectra, which are rather

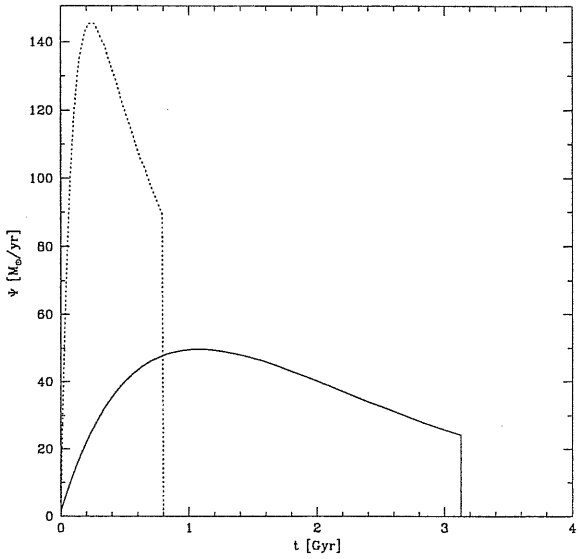

Figure 5.4: The star formation rate as a function of the galactic time for our two reference models (*dotted line*: Model 1; *continuous line*: Model 2). The falloff at t=0.8 and 3.15 Gyr corresponds to the onset of the galactic wind. The normalization is for a galactic baryonic mass of $M = 10^{11}\ M_{\odot}$.

blue at all wavelengths, dominated by young stellar populations (10 objects out of 35) and class *(b)* spectra, with overall redder properties, displaying a typical two power–law behavior, with a break at $\lambda \simeq 0.4\ \mu$m in the rest frame spectrum in correspondence of the Balmer decrement (25 sources). No objects, even those at the lowest redshifts, are found to display very red colors, as would be expected for a very old stellar population dominating the spectrum. This result is consistent with a statistical study by Zepf (1997) revealing a lack of very red objects in the field.

A crucial step in our analysis is the evaluation of redshifts from broadband spectral fitting for sources lacking a spectroscopic identification. The uncertainties related with this estimate have been discussed by many authors (see in particular Connolly et al. 1997; Hogg et al. 1998), with the general outcome that the inclusion of NIR data in the analysis (added to the 4 HST bands) makes the redshift estimate quite more reliable.

With respect to these analyses we benefit here of various advantages. The first one is due to the lack of evidence for dust in our objects, which breaks down at least one possible degeneracy in the parameter space (that is estimating a lower photometric z from a dust–reddened template). The second one is that most of the observed spectra are rather homogeneous as typical of early–type galaxies, with an easily discernible Balmer feature. A third potential advantage, as verified a posteriori, is given by our relatively bright K–band selection, which tends to select objects only up to moderate redshifts ($z < 1.5$, see Secs. 5.4 and 5.5) and to exclude very high–z galaxies, whose redshift estimate would be quite more uncertain because of the strong evolutionary corrections in the template spectra.

More specifically, for class *(b)* sources lacking spectroscopic redshifts (i.e. 15 galaxies in total) the estimate of the redshift from spectral fitting is quite robust, thanks to a well–defined spectral break corresponding to the Balmer decrement, typically occurring

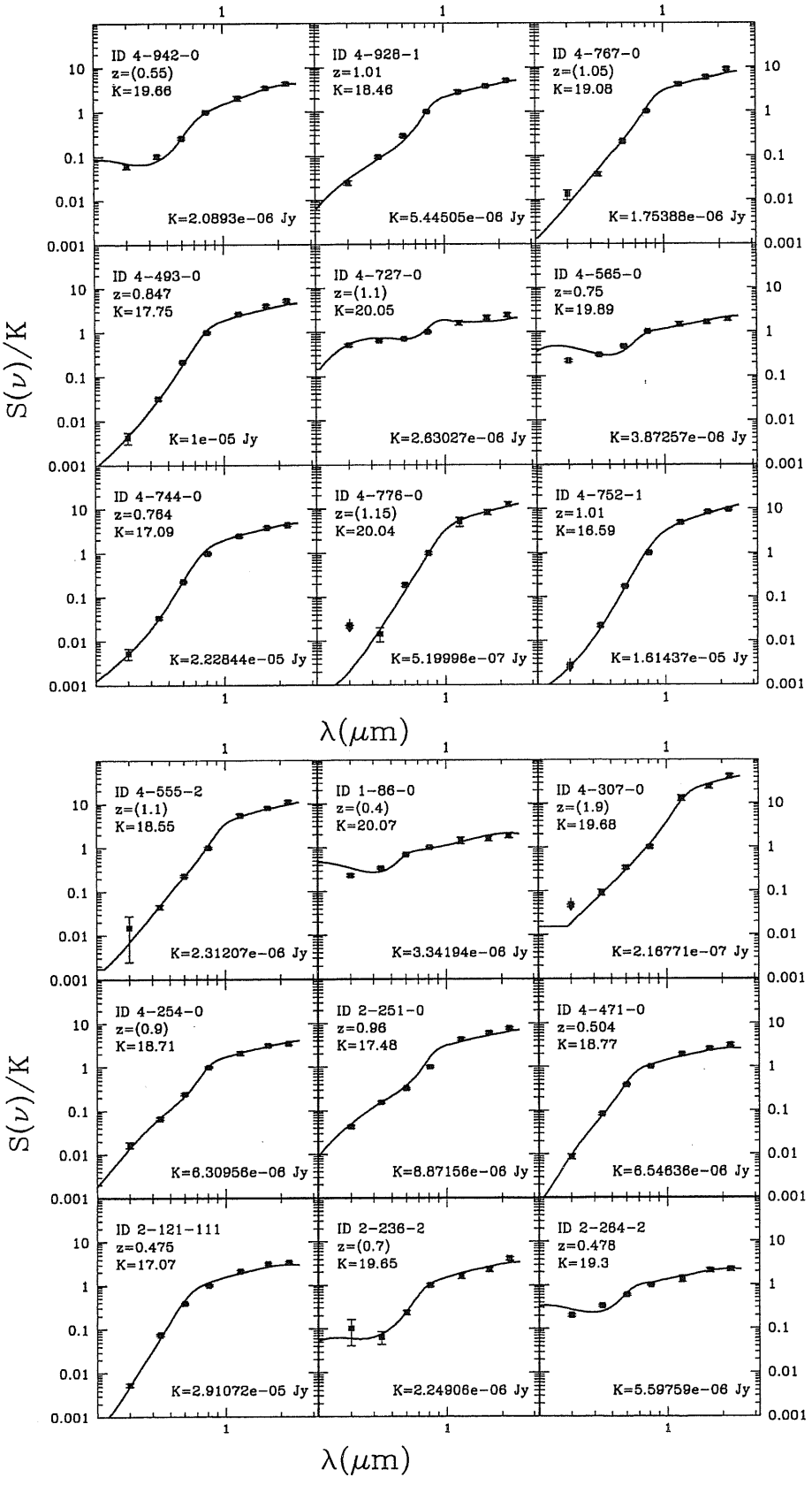

Figure 5.5: Observed broadband spectra for all sample galaxies, fitted with Model 2 for $q_0 = 0.15$. For some objects we add to Model 2 a residual SF (Ψ_0 in Table 5.2). Photometric redshift is in parenthesis.

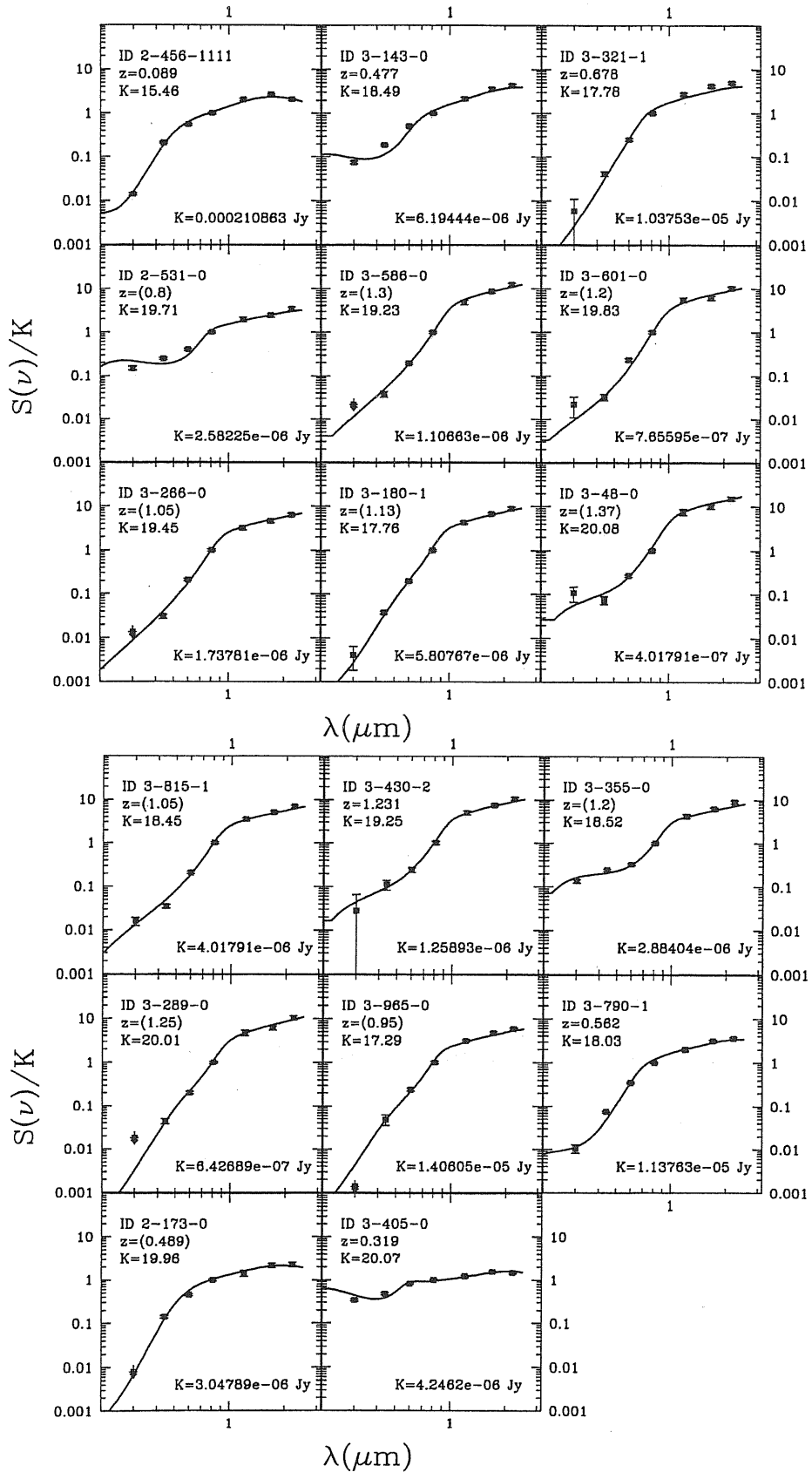

Figure 5.5: *Continued*

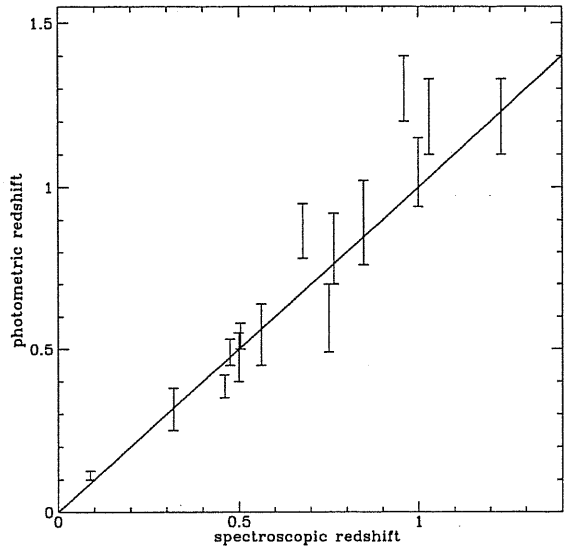

Figure 5.6: Comparison of photometric redshifts, based on 7-band spectral data, with spectroscopic redshifts. Errorbars are $\sim$ 95% intervals based on χ^2 fitting of Model 2. The discrepant object at $z = 0.96$ (ID 2-251-0) contains a nuclear nonthermal source, and it is the only galaxy in our sample with this feature.

at $\lambda \sim 0.6$ to 1 μm. The combined use of the 3 NIR and the 4 HST bands, with very small photometric errors, allows an accurate determination of the 4000 Å break from a model–assisted spectral interpolation. For class *(a)* spectra without spectroscopic redshifts (5 more galaxies), there is still clear evidence for a 4000 Å break, which is however less precisely characterized in some instances. In these cases the photometric redshift may turn out to be significantly more uncertain.

Fig. 5.6 summarizes a comparison of our redshift estimate based on broadband spectral fitting with the actual measurement from midresolution spectroscopy, for the 15 galaxies in our sample with this information. The errorbars associated with the photometric estimate are conservative $\sim$95% confidence intervals based on χ^2 fitting using Model 2 as spectral template. In only one case (object 2-251-0) the photometric measure is significantly discrepant with respect to the spectroscopic one, but this happens for the galaxy containing a nuclear pointlike source, which affects the match of HST and NIR photometry. Fig. 5.6 shows that our process exploiting 7 band spectral data is overall quite reliable and that no systematic effects are present. On the other hand, it is clear that the 15 galaxies with optical spectroscopy are not randomly sampled from our source list, as shown in particular by Fig. 5.8: they tend to be lower redshift, bluer objects, with SF protracted to recent cosmic epochs. Such spectral behaviour has encouraged a spectroscopic follow–up, while the redder higher–z ones will require a substantial dedicated future effort. Altogether, we estimate that the errors associated with redshifts evaluated from class *(b)* spectra should not typically exceed 10% in z, while a conservative estimate may be closer to 20% for class *(a)* spectra (see also Connolly et al. 1997 and Hogg et al. 1998 for similar conclusions). None of our results will be significantly affected by these uncertainties.

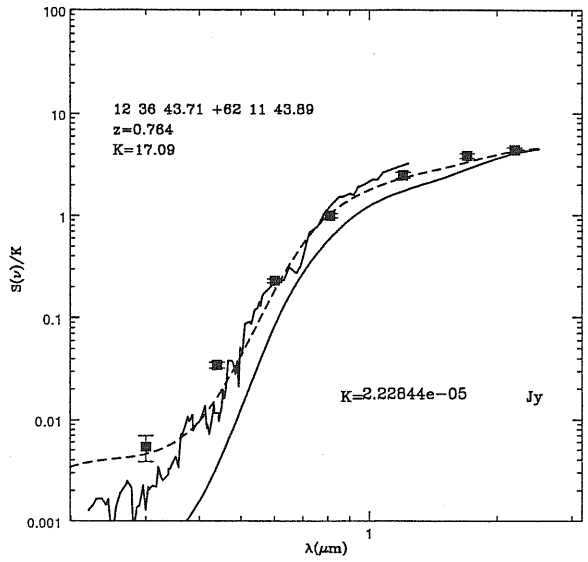

Figure 5.7: Spectrum of a typical class (b) galaxy in the sample compared with two synthetic spectra based on Model 1 with $q_0 = 0.15$. *Continuous line*: case with $z_F = 5$; *dashed line*: $z_F = 3$. This is compared with the optical spectrum of the local early-type M32 (see text for more details).

Evaluation of the galactic ages

For all sample galaxies, except for object 4-727-0, we found acceptable fits with Model 2. These solutions were found by optimizing the free SED fitting parameters previously discussed (z_F, ψ_0, M and possibly photometric z). The spectral solutions illustrated in Fig. 5.5 (whose parameters are reported in Table 5.2) refer to the case $q_0 = 0.15$. Consistent solutions were also found for Model 2 in a closure world model (see again Table 5.2 for the corresponding best–fitting parameters).

The failure of Model 1 to reproduce the data is illustrated in Fig. 5.7, which compares the broadband spectrum of a typical galaxy in the sample with two predictions of the model at varying z_F. The continuous curve is the spectrum predicted by Model 1 with $z_F = 5$ and $q_0 = 0.15$. With this choice of the parameters, this corresponds to a stellar population beginning formation at z=5 and ending it at z=3.6 (hence observed 5.5 Gyr after the end of the SF in the source frame): the prediction is clearly far too red both in the optical and even in the NIR. The dashed curve corresponds to the same model with $z_F = 3$, and the additional contribution of ongoing SF by 0.2 $M_\odot/yr$ to better reproduce the U–band flux. If the overall fit is better, there is still a significant excess flux in the observed B band with respect to the model spectrum. We have found this excess, as well as sometimes one in the V band, to be a general characteristic of the observed spectra: even for the reddest galaxies in the sample it seemed difficult to reproduce the spectra with stellar populations formed during a relatively brief time interval (as in Model 1), even including the additional contribution of ongoing star formation.

We interpret the better performance of Model 2 as indicating a rather protracted star formation activity within each galaxy (typically 3 Gyr in the model), rather than a single short–lived starburst (even one occurring at low redshift). A qualitatively similar

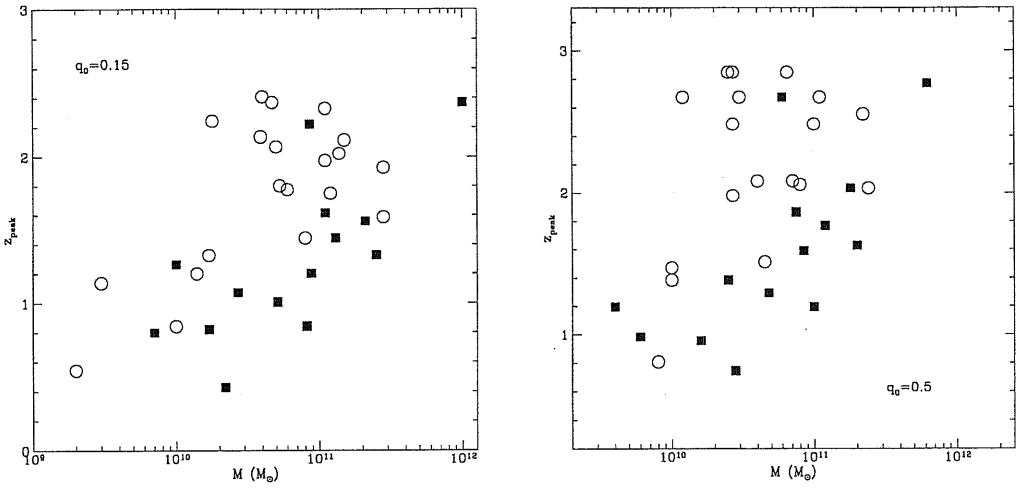

Figure 5.8: Baryonic mass versus redshift of peak star formation, according to spectral best fits based on Model 2. *Left*: the solutions assume $q_0 = 0.15$. *Right*: solutions based on $q_0 = 0.5$ (see Table 5.2 for the best-fit parameters). Filled squares refer to objects with spectroscopic redshift, open circles to those with photometric redshift.

result is achieved by FA98 analyzing a sample of HDF early–type galaxies selected in the V_{606} band.

Our best fit models allow us to estimate the epoch when the bulk of stellar formation has taken place in the typical sample galaxy. Fig. 5.8 is a plot of the redshift corresponding to the peak of the star formation versus the mass in baryons, according to our best fits. The two panels refer to the two solutions with $q_0 = 0.15$ and $q_0 = 0.5$. There are clearly two zones of avoidance in the figure: low-mass objects ($M < 2\ 10^{10}\ M_\odot$) have peak SF confined to $z \lesssim 1$, while the high-mass ones appear to form stars mostly at $z \gtrsim 1$. This is partly an artifact of the magnitude limits (in the former case) and of the small sampled volume combined with the low space density of very massive galaxies (in the latter). While only a careful examination of all selection effects will allow to obtain unbiased estimates of the cosmic SF history from this dataset (see Sec. 5.6), *it is clear from Fig. 5.8 that the redshift interval of z=1 to 2 (1 to 3 for $q_0 = 0.5$) corresponds to a very active phase of SF for the sample galaxies.*

To translate this into a constraint on the age for the typical early–type galaxy in the field, we report in Fig. 5.9 the rest-frame (V–K) and (B–J) colors as a function of redshift, compared with the predictions of SSP with solar metal abundances. The rest frame (B–J) colors are computed by interpolating the galaxy observed spectra using the best–fit models of Table 5.2, while the values of (V–K) require substantial extrapolation at the longer wavelengths, hence are to be taken with some care. The figure shows that the typical ages range from 1.5 to 3 Gyr, rather independently from the redshift (if any, there is quite a marginal tendency for the higher z galaxies to display bluer colors). For comparison, the average (V–K) color of local galaxies is $\simeq$ 3.2-3.3, quite significantly redder. This difference is probably enhanced by a bias induced by the flux limit in the

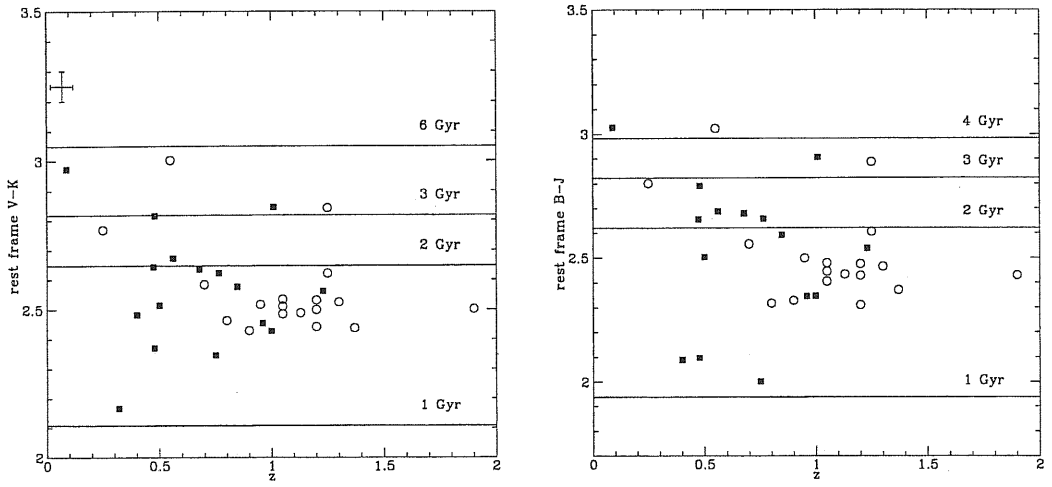

Figure 5.9: Rest-frame (V–K) and (B–J) colors, compared with predicted values for SSP with solar metallicity. The ages for the latter are indicated, as well as the mean (V–K) color of local galaxies. Meaning of the symbols as in Fig. 5.8.

K-selected sample, emphasizing relatively bluer objects observed close to their main event of star formation. This is further inspected in the following sections.

Another check of this is reported in Fig. 5.7, where the broadband spectrum of the typical galaxy is compared with that of the local early-type M32 (F. Bertola, private communication). The present interpretation of M32's blue light is that it may be dominated by the HR turnoff stars of a $\sim$ 4 Gyr old stellar population of about solar metallicity (O'Connell 1986), whose bright RGB and AGB stars have been recently resolved (Freedman 1992, Grillmair et al. 1996). Older ages might fit only for a metal-deficient dominant population (Renzini & Buzzoni 1986). Our typical galaxy is bluer than M32 and, assuming a solar metallicity, it turns out to be younger than 4 Gyr.

These considerations are affected by the problem the age-metallicity degeneracy of optical-NIR broadband spectra of stellar populations (see Sec. 3.5.2). As already discussed, the very regular morphologies and the lack of evidence for the presence of dust in the large majority of our sample galaxies suggest that they have already mostly completed their bulk of the SF, therefore should have metallicities comparable to those of the local counterparts (solar on average, see Carollo & Danziger 1994). If true, then a conclusion seems unavoidable, that their typical age is close to 1.5 to 2 Gyr on average, at the observed redshifts.

Fig. 5.10 illustrates the effects of changes in the metallic content of the stellar populations on the rest frame colors. The two horizontal lines in both panels bracket the typical colors for the sample galaxies. Large age differences are found as a function of the metallicity for a given color and for old stellar populations. On the other hand, *since our observed colors are rather blue, the uncertainty due to the unknown metallicity is moderate in absolute terms.* For example, the typical observed color (B–J)$\simeq$ 2.5 (Fig. 5.10) would correspond to an age of 1 Gyr for 2 times solar, to 2 Gyr for a 0.4 solar and 3 Gyr for a 0.2 solar metallicity. The conclusion is that, *unless we accept that the observed*

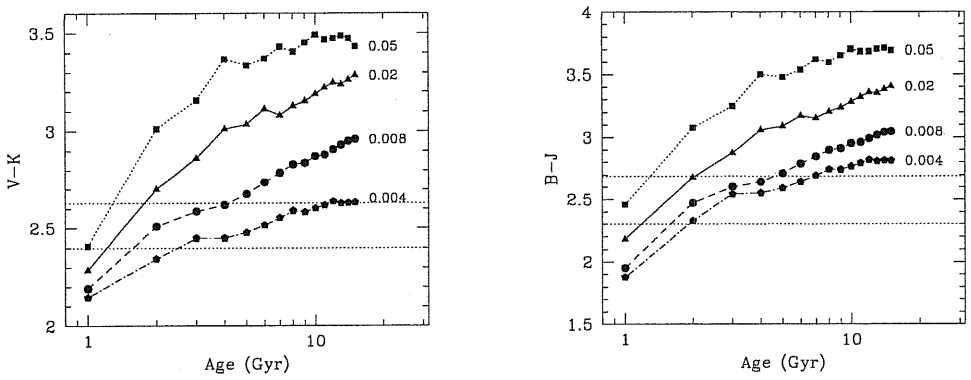

Figure 5.10: Predicted (V-K) and (B-J) color evolution of SSP as a function of galactic age for different metallicities (indicated in the figure). The dotted horizontal lines mark the boundaries of the observed distribution.

galaxies are very significantly metal-deficient (which would be difficult to reconcile with observations of local objects), our age determinations should not be seriously in error.

5.3.2 Constraints from the size versus surface brightness distributions

Further significant constraints onto the nature and evolutionary status of our sample galaxies may be gained from a detailed analysis of their morphological properties.

The study of the galaxy spectral shapes has indicated that intermediate (rather than old) ages, with large spreads, are typical. If so, then one would expect quite appreciable luminosity evolution due to the – mostly passive – aging of the stellar populations from the redshift of the observation to the present time. A way to check it, as discussed in FA98, would be to compare the sizes and the average surface brightness (within the effective radius) of distant galaxies with those of the local ones. Table 5.1 (columns [4] and [13]) reports these data for all galaxies in our sample.

Fig. 5.11 compares the same data with the mean locus (thick continuos line) of the relation between the effective radius r_e and the corresponding average surface brightness in the V band $< \mu_e >_V$ (the Kormendy relation). In this figure the effective radii are expressed in Kpc, and the surface brightness has been corrected (K- and evolutionary corrections) according to Model 1.

There is a clear offset in Fig. 5.11, by ~ 1.5 mag, with respect to the locus representing local galaxies (see FA98 and Jorgensen et al. 1995 for more details on the latter): the surface brightness of distant galaxies is more luminous on average than implied by Model 1 (for which the bulk of SF was completed by $z = 3.5$). Fig. 5.12 shows that much better consistency is achieved with Model 2, both in the V and in the K bands. The local Kormendy relation plotted for the K band is taken from Pahre et al. (1995). In this case the evolution in luminosity between the redshift of the observation and the

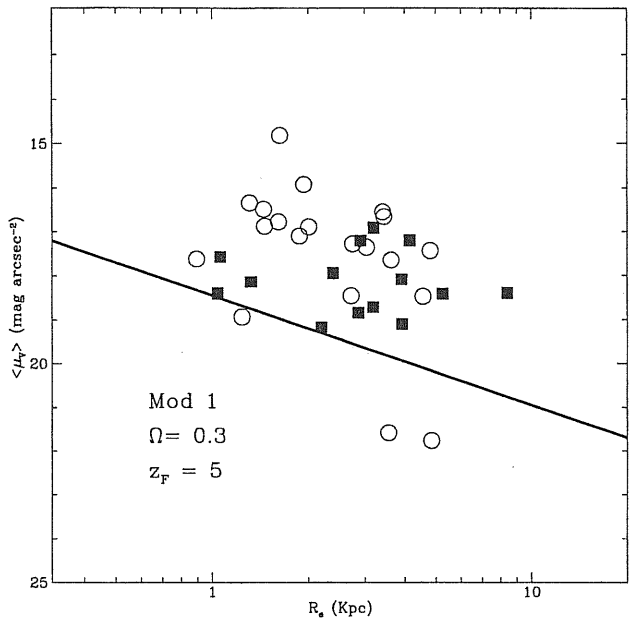

Figure 5.11: The Kormendy relation in the V band, i.e. the average surface brightness versus effective radius. The continuous line represents the local relation. The data are obtained applying to the observed surface brightness K- and evolutionary corrections according to Model 1 ($q_0 = 0.15$, $z_F = 5$). Meaning of the symbols as in Fig. 5.8.

present time is stronger (stars are younger on average), with local and distant galaxies consistently tracing the same population, as expected.

5.4 Statistical properties of the complete sample

Though small, our K–selected sample has been tested with great care for completeness and reliability in source selection, and it is then suitable for a detailed statistical analysis. In consideration of the high–quality morphological and photometric data available, this study may provide an accurate characterization of the distribution of elliptical/S0 galaxies in the spacetime.

We consider here two statistical observables, the counts as a function of morphological type and of limiting K magnitude, and the redshift distribution D(z).

Fig. 5.13 is a collection of galaxy counts in the K and H+K bands, split into two morphological components: the early–type galaxies (open squares), selected according to the criteria described in Sec. 5.2, (see Table 5.1), and late–type systems – including spirals, irregulars, and starbursts (open triangles). The K band counts on the left–hand side are derived from our sample down to $K = 20.15$. The counts in the H+K band on the right–hand side are derived from a sample by Cowie et al. (1996), including complete morphological information for H+K brighter than 21.5. The number counts for early- and late–type galaxies display rather different slopes at the faint end, with the early–types converging very fast at $K > 19$ and the late–types showing steadily increasing counts. Similar results about the morphological number counts are reported

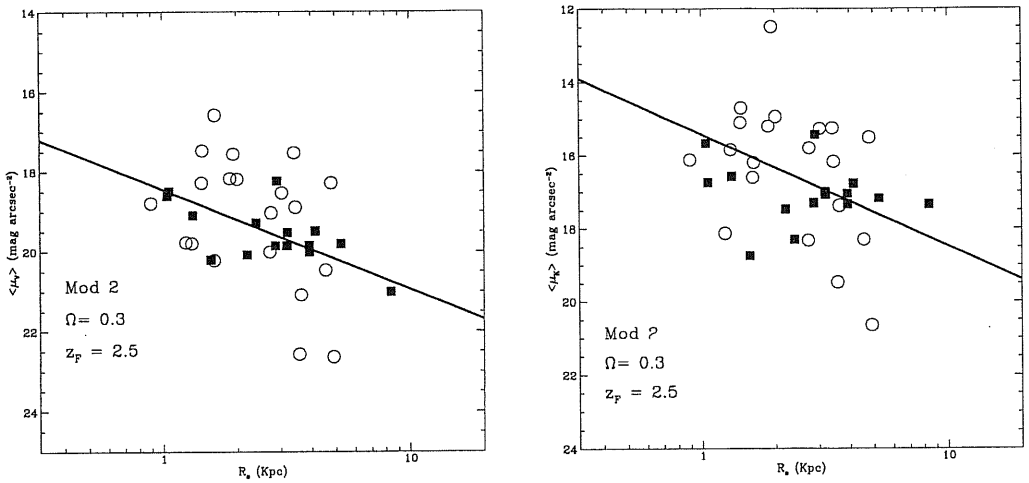

Figure 5.12: *Left*: Same as the Fig. 5.11, but correcting the observed surface brightness according to Model 2 ($q_0 = 0.15$, $z_F = 2.5$). *Right*: Kormendy relation in the K band, data corrected as above. The mean locus of local galaxies comes from Pahre et al. (1995).

by Driver et al. (1988), who find in particular a deficit of E/S0 at $I_{814} > 22$ compared with passively evolving models.

The distribution of the – either spectroscopic or photometrically estimated – redshifts for the 35 sample galaxies is reproduced as a thick line in Fig. 5.14. The observational distribution shows monotonic increasing values from z=0 to $z \simeq 1.3$, with a marked peak at $z \sim 1.1$. A remarkable feature in the distribution is a sudden disappearance of objects at $z \gtrsim 1.3$. This absence may look surprising at first sight, taking into account that the dominant stellar populations for objects observed at $z \sim 1$ are 1 to 3 Gyr old, whose luminosity has then to increase, if any, at $z > 1$. Let us first discuss the significance of this apparent redshift cutoff, in the light of all selection effects operating in the sample.

The first obvious concern is our ability to identify in the K–band image extended emissions corresponding to high redshift elliptical/S0 when going from the typical observed redshift $z \sim 1$ to larger cosmic distances. Fig. 5.15 illustrates the effect of increasing redshift on the average surface brightness and the effective radius, for two evolutionary paths (both adopting $q_0 = 0.15$). The top line corresponds to a typical galaxy in our sample having $< \mu_e^K >= 18$, $r_e = 2$ Kpc (cf. the distribution of values scaled to zero redshift in Fig. 5.12), and observed at z ranging from 0 to 2.5. The scaling with z of the surface brightness has been calculated taking into account all cosmological, K and evolutionary effects. The upper curve in the figure is computed according to Model 2 with a low formation redshift $z_F = 3$. It turns out that the brightening of the stellar populations, while approaching the SF phase at $z > 1.5$, counter–balances any cosmological and K–correction dimming. In this case there is no significant dependence of the surface brightness on redshift. A limiting situation is provided by the bottom curve in Fig. 5.15, representing the lowest surface brightness galaxy in the sample and luminosity evolution after Model 1 with a high formation redshift $z_F = 5$. In this

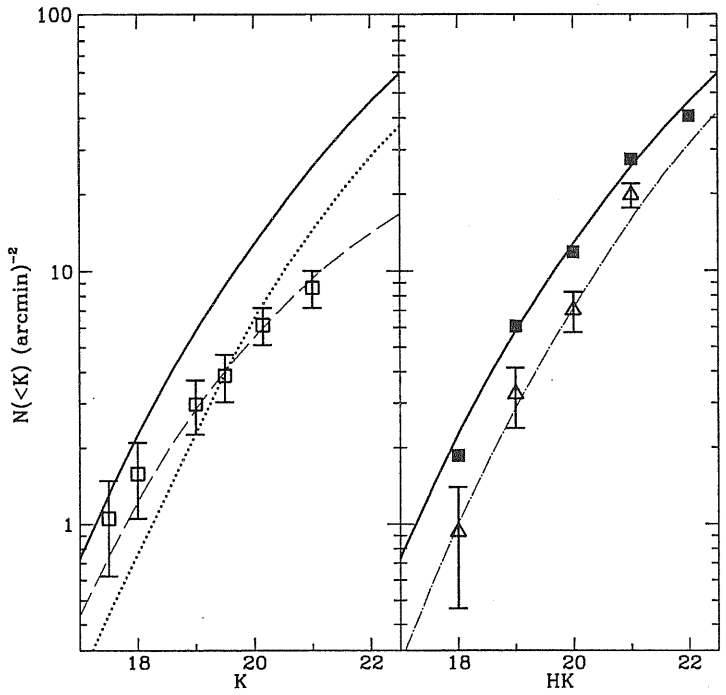

Figure 5.13: Counts as a function of the morphological type in the K and H+K bands. Open squares (*left*) are the counts for E/S0 of our sample. The datum at K=21 is based on the HDF Active Catalogue by Cowie et al. (1996). These data are compared with the predicted counts by Model 1 with $q_0 = 0.15$, $z_F = 4$ (dotted line), and with counts by Model 2 with dust extinction during the SF phase (dashed line). A comparison is made with the total predicted counts from Model 2 (thick continuous line). *Right*: We report counts in the H+K band for galaxies classified as spirals and irregulars in the catalogue by Cowie et al. (open triangles), compared with the total counts (filled squares). The dot-dashed line is based on a moderately evolving model for late–type galaxies as discussed in the text.

case the brightness dimming effects dominate and there is an appreciable excursion in $< \mu_e^K >$ as a function of z. In spite of this, in this case as well as in all other more favorable ones, the faint object would still be detectable up to z=2.5 above the completeness limit, estimated by simulations in Sec. 5.2 to be $< \mu_e^K >= 22$. Altogether, the K–band image is sensitive enough to allow easy detection of even moderately or non evolving galaxies up to at least $z \sim 2.5$. Then the turnover in D(z) apparently occurring at much lower z cannot be due to limitations in detecting faint extended structures.

We investigate in the following how the other fundamental selection condition, that in the total flux ($K < 20.15$), operates for different cosmological and evolutionary models.

To perform this exercise, a reliable local luminosity function (LLF) of galaxies in the K band is required. Our adopted LLF is taken from Gardner et al. (1997), which significantly updates previous determinations. The separate contributions of early-type (E/S0) and late–type (Sp/Ir) galaxies have been calculated using the optical LLFs split into various morphological types by Franceschini et al. (1988) and translated to the K

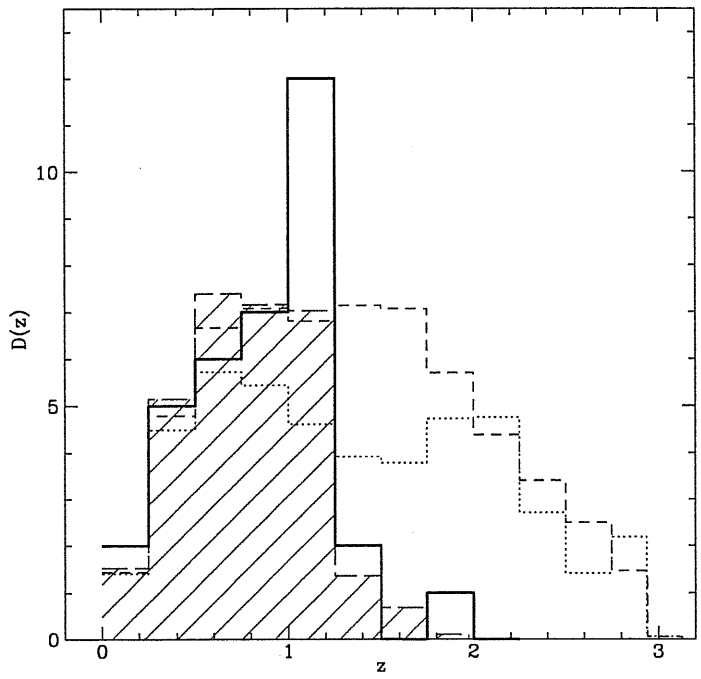

Figure 5.14: Redshift distributions. The continuous-line histogram is our observed distribution, for $K < 20.15$, over an area of 5.7 square arcmin. The dotted line is the prediction of Model 1 ($q_0 = 0.15$, $z_F = 4$). For Model 2 without dust extinction (short-dashed line) the misfit is even more severe. Dashed line shaded region: predicted distribution according to Model 2 with a dusty SF phase.

band with type-dependent (B-K) colours.

The K–band luminosity function of galaxies has been combined with various evolutionary models to predict sample statistics, under the simplifying assumption of a galaxy mass function constant with cosmic time. We find that the shape of the LLF estimated by Gardner et al. (1997) can be more naturally reconciled with the total faint K-band counts of Fig. 5.13 in an open universe with $\Lambda = 0$, while a closure one would require some ad hoc evolutionary prescriptions. This is because the latter has not enough volume at $z \sim 1$ to fill in the counts, given the space density of galaxies implied by the K LLF. Then Model 1 for E/S0 galaxies, supplemented with a moderate evolution for Sp/Ir galaxies as in Mazzei et al. (1992), could in principle provide a fair fit to the total counts for $q_0 = 0.15$.

A further constraint is set by the observed z distribution D(z) of early-type galaxies in the K HDF (Fig. 5.14). From $z = 0$ to $z = 1.2$, D(z) is consistent with a (mostly passive) evolution in an open universe (with q_0=0.1-0.2) with zero cosmological constant. Again, a closure world model with $\Lambda = 0$ would require a much larger comoving luminosity density of massive E/S0s at z=1 than locally.

Hence, there is no evidence, up to this epoch, of an evolution of the baryon mass

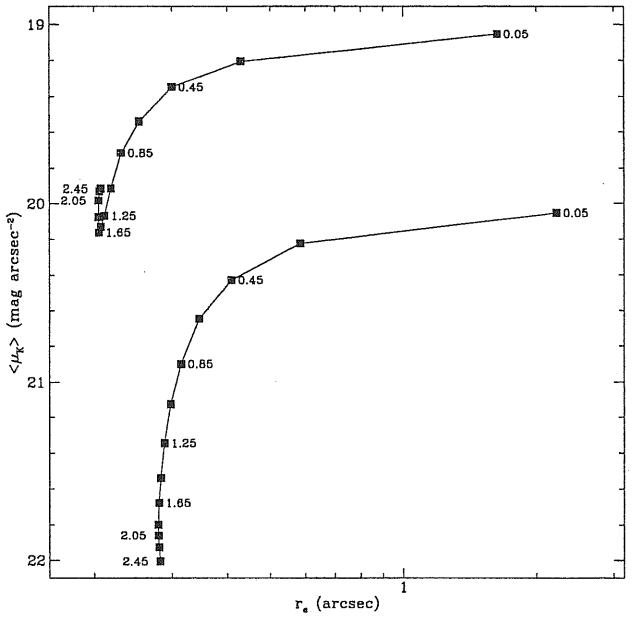

Figure 5.15: Scaling of the surface brightness and effective radius as a function of redshift. Two paths are shown: the top one corresponds to a typical galaxy in our sample allowed to evolve following Model 2. The bottom line corresponds to the lowest surface brightness object in the sample evolving according to Model 1 ($q_0 = 0.15$, $z_F = 5$). The stronger decrease with redshift of the average surface brightness in this second case is due to a strong K-correction and almost no luminosity evolution implied by this model. The latter represents a very conservative evolution patter, yet the galaxy would remain detectable up to $z \simeq 2.5$ above the limiting brightness indicated by the simulations (see Sec. 5.2.1). It is then unlikely that the surface brightness limitation could affect the selection of E/S0 galaxies above z=1.3.

function. This is difficult to reconcile with a decrease of the mass and luminosity due to progressive disappearance of big galaxies in favor of smaller mass units, as implied by some specifications of the hierarchical clustering scheme (e.g. Baugh et al. 1996). The case for a strong negative evolution of the early-type population (by a factor 2-3 less in number density at z=1; e.g. Kauffmann et al. 1996) does not seem supported by our analysis of the HDF.

Above z=1.2, however, both Models 1 and 2 (whichever formation redshift z_F is assumed) have difficulties to reproduce the redshift distribution reported in Fig. 5.14 and the identification statistics in Fig. 5.13. In particular it is not able to explain the large number of sources at $z = 1$ followed by the rapid convergence above: the prediction would be of a much more gentle distribution, with less a pronounced peak and a large tail of galaxies (including typically half of sample objects) observable above $z = 1.2$. Lower values of q_0 would allow better fits of the observed D(z) up to $z = 1.3$, but would also worsen the mis-fit at higher z. A similar effect is observed in the counts as a function of the morphological class (Fig. 5.13). Here again sources identified as

E/S0s show steep counts to K=19 and a sudden convergence thereafter, while Model 1 would predict a much less rapid change in slope. These problems remain forcing in various ways the model parameters.

5.5 Dust extinction and merging effects during a protracted SF phase

We briefly discuss here possible explanations of the results obtained in Secs. 5.3 and 5.4. We look for solutions explaining the global statistical properties of the sample as well as the variety of the single galactic spectra.

5.5.1 Merging

In the previous section we have found that at redshifts larger than 1.3 early–type galaxies suddenly disappear from the K-selected sample, while we would expect to observe them to much higher z, given the predicted luminosity enhancement when approaching the most intense phase of star formation. A comparison of Figs. 5.8 and 5.14 suggests that there may be a relation between the redshift interval where such a disappearance occurs and the one bracketing the major episodes of star formation, as evaluated from the analysis of the stellar populations in distant galaxies. It is clear from Fig. 5.8 that the interval $1 < z < 3$ is where the peak of star formation occurs for the bulk of our sample galaxies, and this roughly coincides with the redshift interval where virtually no objects are found in our sample.

As discussed in Sec. 5.3, there is not only a substantial spread in the formation epochs z_F of the sample galaxies (see Table 5.2), but also in single galaxy spectra there is evidence for the presence of stellar populations with widely different ages. A model with SF distributed over a 3 Gyr time interval was able to fit such spectra.

So, *during this relatively long-lasting period of formation of stars, our sample galaxies escape detection by our selection procedure.* Two filters may operate in producing this: either the morphological filter, or the K-band limiting flux, or possibly both simultaneously.

An obvious morphological transformation accompanying the formation of a sizable fraction of stars is predicted by the merging picture for the formation of early–type galaxies: two gas–rich systems undergo a deep dynamical interaction, eventually bringing to a single merge product. During this process there is a full reshuffling of both the gas component, with dynamically triggered SF, and also of the old stellar population, reflecting the rapidly changing gravitational field. Numerical simulations show that an $r^{-1/4}$-law stellar distribution may originate in this way (Barnes & Hernquist 1996). Given the spread of ages in our observed objects, it is likely that a few to several of these merging events have taken place per single massive galaxy during the first few Gyr of the galaxy's lifetime. Merging, mostly occurring at $z > 1$, is then a very appealing interpretation for our results.

Another effect of merging would be to lower the flux detectability during the SF phase, due to the mass function rapidly evolving at $z > 1$. We did not attempt to quantify the possible effects of merging on the visibility of the early evolution phases

of E/S0 galaxies. We defer for an exercise of this kind to dedicated treatments (e.g. Baugh, Cole, & Frenk 1996).

Another plausible reason of flux leakage during SF is related to the extinction by dust in the medium where stars are forming. This dust is very likely present, left over by preexisting generations of massive stars. We spend the rest of this section in a more quantitative evaluation of the possible effects of dust. An argument strongly suggestive of its occurrence will be given in Sec. 5.6.

5.5.2 Dust effects during a prolonged SF phase in field ellipticals

Dust is observed in significant, or even large, amounts in a wide variety of objects at any redshift. The most distant astrophysical sites explored so far, the quasars at redshift 4 to 5, have shown to contain, at that early epoch, dust amounts comparable with those of the most massive galaxies today (Omont et al. 1997; Andreani, Franceschini, & Granato, 1997). But also distant radio galaxies, Lyman dropouts, and damped Lyα galaxies (Pettini et al. 1997) have invariably shown the presence of dust. In several galaxies, among the infrared selected, IRAS has found that the dust reprocesses a dominant fraction of the stellar UV radiation into the infrared (the ultraluminous and hyperluminous IR galaxies, see e.g. Sanders and Mirabel, 1996; Rowan-Robinson 1998).

Indeed, a single short-lived starburst may produce enough metals via massive stellar outflows during the AGB and supernova phase. Recent ISO observations (Lagage et al. 1996) have proven that dust grains are synthesized almost simultaneously with the metals, as soon as they are made available to the medium.

A common interpretation of ultraluminous IR galaxies is that, during a merger or a close interaction, even moderate amounts of dust are spread around to make an extended dusty core in the starburst. In these conditions it is very likely that any major merger happens in a dust enshrouded medium, several examples of which have been found at both low redshifts (e.g. Arp 220, NGC 6090, M82) and high redshifts (e.g. IRAS F10214; HR10; see also Ivison et al. 1998).

We provide here a simplified description of the effects of dust during the star formation phase and test it on the statistical properties of our sample as discussed in the previous section.

The simplification we adopt is to assume, instead of a discrete set of successive merging-driven starbursts as would be a realistic physical situation, a more continuous process of star formation with a temporal evolution following that of Model 2 in Fig. 5.4 and occurring in a dust-enriched medium (we do not consider the effects of dust in Model 1, as it would only remove the $z > 3$ sources and because it is in any case inconsistent, see Sec. 5.3.1). Dust associated with the residual ISM extinguishes the light emitted by high redshift objects. The idea is that the SF efficiency in field galaxies with deep dark-matter potentials is not so high to produce a galactic wind on short timescales after the onset of SF. Hence an ISM is present in the galaxy for an appreciable fraction of the Hubble time, during which the ISM is progressively enriched of metals and dust. While the gas fraction diminishes as stars are continuously formed, its metallicity increases and keeps the dust optical depth roughly constant with time.

We have then complemented the Model 2 of Sec. 5.3.1 to account for the effect of extinction and reradiation by dust during the SF phase, with our model GRASIL

described in Chap. 2. We used the following values for the parameters defined in Chap. 2: $f_{mc} = 0.3$ (fraction of gas in the MC component), $m_{mc} = 5\,10^5 M_\odot$, $r_{mc} = 16$pc (mass and radius of MCs), $t_0 = 0.1$Gyr (see Eq. 2.22), $r_c = 200$pc (core radius of King profile). The model baryonic mass is $M = 10^{11} M_\odot$, typical for our sample galaxies. After SF ceases for the onset of galactic wind, a very low–level SF may keep on, due to either partial efficiency of the wind, or to stellar recycling. The average stellar metallicity of the remnant is roughly solar. This scheme naturally accounts for the evidence previously discussed in Sec. 5.3 of a substantial spread in the ages of distant field E/S0, showing a combination of massive amounts of old stellar populations and younger stars.

The same scheme, when convolved with a K-band LLF, successfully accounts for the statistical distributions in Figs. reffig12 and 5.14, in addition to other galaxy counts in the K band. Now the cutoffs of both D(z) at $z > 1.3$ and of the counts for E/S0s at $K > 19$ are reproduced as the effect of dust extinction during the SF phase.

We stress again that, though not physically unplausible, our treatment of the SF as a continuous process during a substantial fraction of the Hubble time at high z is likely an oversimplification of a more complex process characterized by a discrete set of SF episodes. However, there is virtually no difference between the two cases as far as the "observable" later, passively evolving, phase is considered.

5.6 The star formation history of early-type field galaxies

This section is devoted to a quantitative evaluation of the star formation history of early-type galaxies in the field. Though it is not certainly the first time this is attempted, our approach is substantially different and complementary, and brings some significant advantages with respect to previous efforts (see e.g. Lilly et al. 1995; Madau et al. 1996; Connolly et al. 1997; Madau, Pozzetti, & Dickinson 1998).

Most of the previous analyses have concentrated on very large (e.g. thousands of objects for analyses dealing with the HDF itself or the CFRS) samples of galaxies without morphological differentiation and with sometimes very limited fractions (typically $< 10\%$ if we exclude CFRS) of spectroscopic identifications, directly observed throughout the whole redshift range sampled by the very sensitive optical images. In addition to the admittedly uncertain redshift estimation via the Lyman dropout technique, a recognized difficulty inherent in these "direct" evaluations of the cosmological star formation rate is due to the essentially unknown effect of dust. Given the poor knowledge of dust properties, an extinction correction is subject to tremendous uncertainties even for high-z galaxies with good optical spectra, which are in any case a minority.

Our present approach attempts to bypass all these problems by confining the analysis to a relatively small sample (35 objects) with extremely accurate information per object. Such an information concerns high-quality photometric data over a large wavelength interval ($0.3 < \lambda < 2.2$ μm), a good fraction (43%) of spectroscopically confirmed redshifts, a very accurate morphological information allowing to select a sample with likely homogeneous properties of star formation. The sample galaxies have been processed through a grid of synthetic galaxy spectra, with the essential aim to date the stellar populations present in the galaxy at the time of observation. The selection waveband, the K band, has been chosen not only to minimize the selection effects, due to

the evolutionary and K-corrections, but also to allow testing a wide range of stellar ages and masses, not possible if only optical data were considered. The basic uncertain factor when dating stellar populations, i.e. the metallicity of stars, was discussed in Sec. 5.3.1: our conclusion was that, given the relatively blue colors of galaxies at the time of observation, our results on the ages cannot be drastically in error unless we consider highly non solar (either supersolar or subsolar) metallicities. In particular our results should be correct if our objects, having mostly completed their star formation, are characterized by the same solar metallicities that are typically observed in local galaxies. The results of this best-fitting process are summarized in Table 5.2.

Our task here is to account for all reasonable selection effects operating in the sample, to correct for incompleteness (that is for the part of the LF unobserved because of the flux limit) and to build up a "population" history from those of the single galaxies. This derivation of the SF history, though subject to the mentioned modellistic uncertainties, should be minimally or not affected at all by the dust extinction problem, as it deals with stellar populations during a relatively late dust-free phase.

Our approach is otherwise the same as attempted by Lilly et al. (1996) and Madau et al. (1996), among others. We consider the contribution of all galaxies in our sampled volume to the star formation rate per unit comoving volume. The time-dependent star formation rate per any single galaxy is given by that of the best-fitting model (i.e. Model 2 in the vast majority of galaxies, Model 1 for a couple of them), and by the formation redshift z_F, everything scaled according to the best-fit baryonic mass M. The contribution of each galaxy to the global comoving SF rate has been estimated by dividing the time-dependent SF by the maximum comoving volume V_{max} within which the object would still be visible above the sample flux limit. We defer to Lilly et al. (1995, 1996) for a detailed treatment of how V_{max} is computed. A further correction factor to apply to the comoving SF rate takes into account the portion of the luminosity function lost by the flux-limited sample within any redshift interval (at any z only galaxies brighter than K=20.1 can be detected). The correction is simply computed as the ratio of the total luminosity density to the luminosity-weighted integral of the LF above the luminosity corresponding to the flux limit at that z. This correction for completeness is not very large (of the order of a few tens percent), because our adopted K-band LLF is relatively flat at the faint end (see Connolly et al. 1997, for further details on this point).

The global rate of SF $\Psi(z)$, which is the mass in stars formed per year and unit comoving volume (expressed in $M_\odot\, yr^{-1}\, Mpc^{-3}$), is then the summed contribution by all galaxies in our sample. Fig. 5.16 reports different estimates of $\Psi(z)$ based on the two assumptions of $q_0 = 0.15$ and $q_0 = 0.5$. The latter, in particular, is compared with estimates by Lilly et al. (1996), Madau et al. (1996) and Connolly et al. (1997), while a similar match is not possible for our best guess solution with $q_0 = 0.15$. The calculation of V_{max} and of the completeness correction depend on the assumed rate of luminosity evolution. The shaded regions in Fig. 5.16 mark two boundaries estimated with two different evolutionary corrections for luminosity evolution, to provide an idea of the uncertainties. The lower limit is computed from Model 1 (moderate evolution at $z < 3.5$, no z cutoff). As such, it provides a strict lower boundary to $\Psi(z)$. For the upper curve, V_{max} is computed after Model 2, i.e. assuming stronger luminosity evolution and a cutoff in the available volume at $z \simeq 1.5$. This upper curve corresponds

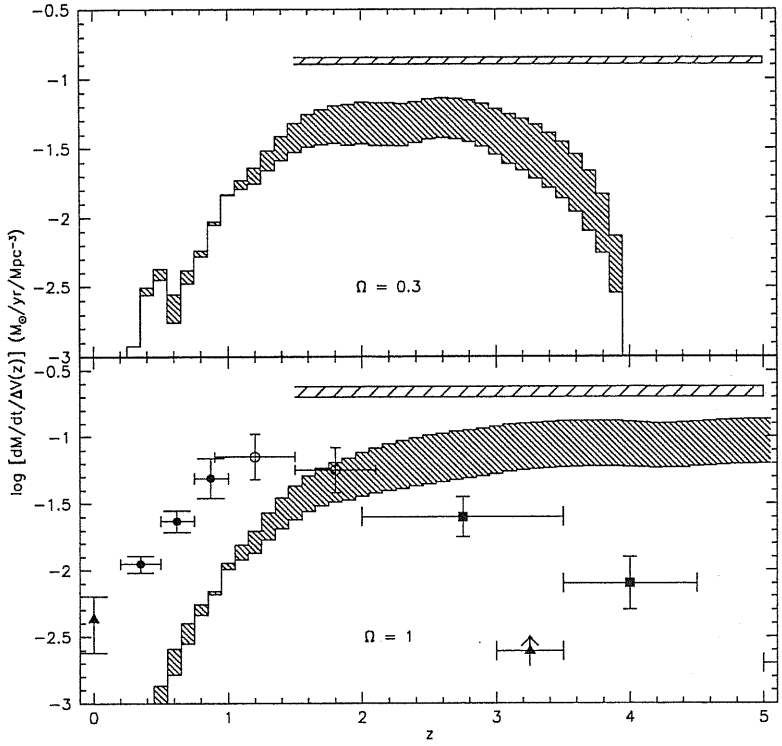

Figure 5.16: The star formation history per unit comoving volume and unit time $\Psi(z)$ of early-type galaxies, as inferred from our analysis of the K HDF sample. *Top*: The thick shaded region is bounded by two solutions (for $q_0 = 0.15$) corresponding to two different estimates of the maximum volume V_{max} available to each source. The lower curve is a limit based on a very conservative estimate of V_{max} assuming no redshift cutoff for E/S0 galaxies. The upper curve corresponds to our best guess for $\Psi(z)$ computed assuming a cutoff in V_{max} at $z \sim 1.5$ (as implied by our statistical analysis). The shaded horizontal region marks the universal rate of star formation (for our adopted Salpeter IMF) estimated by Mushotzky & Loewenstein (1997), assuming that all field E/S0 galaxies behave as the cluster objects in terms of the efficiency of metal production. *Bottom*: Same as top for our best-fit solutions with $q_0 = 0.15$. Here a comparison is possible with independent evaluations of $\Psi(z)$ by Lilly et al. (1996), Madau et al. (1996) and Connolly et al. (1997)

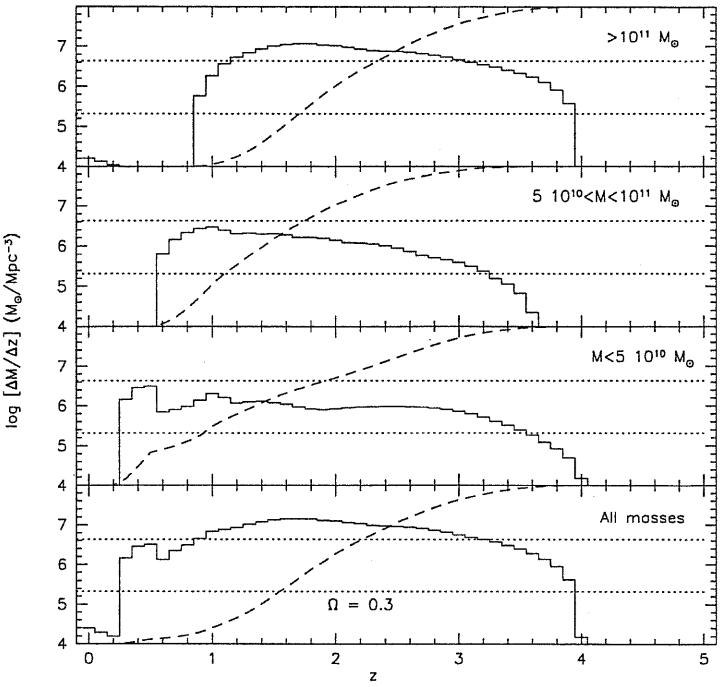

Figure 5.17: Distributions of the density of stellar mass per unit comoving volume generated in the redshift bin as a function of redshift. The units are $M_{\odot}\,Mpc^{-3}$ born in the redshift bin. The distributions are split into the contributions of various galactic mass ranges. The dashed lines in the various panels report the cumulative distributions of the mass density generated as a function of redshift, on a linear vertical scale ranging from 0% to 100%. The dotted horizontal lines mark the 33 and 66% percentiles. A value $q_0 = 0.15$ is adopted.

to our best-guess $\Psi(z)$. Unfortunately, a precise evaluation of the uncertainties is not possible at this stage.

Figs. 5.17 and 5.18 transform the information on the global SF rate $\Psi(z)$ of Fig. 5.16 into one on the actual mass density in stars synthesized within any redshift interval (in solar masses per unit comoving volume and per redshift interval). This is simply the time integral of the function $\Psi(z)$, and better quantifies when the various stellar populations are actually formed. Figs. 5.17 and 5.18 correspond to the usual two choices for q_0, with V_{max} computed from Model 2. In each figure this information is also differentiated into various galactic mass intervals. As it is apparent, there is a tendency for low mass galaxies to have a star formation activity protracted to lower redshifts. Indeed, several moderate to low-mass galaxies show young ages at low redshifts (see Fig. 5.8). However, although we have been as careful as possible in correcting for all various selection and incompleteness effects, we cannot be conclusive about this, in particular because of the limited size of our sample. Deeper and richer samples are needed to settle the issue.

The dashed lines in the various panels of Figs. 5.17 and 5.18 provide the integral

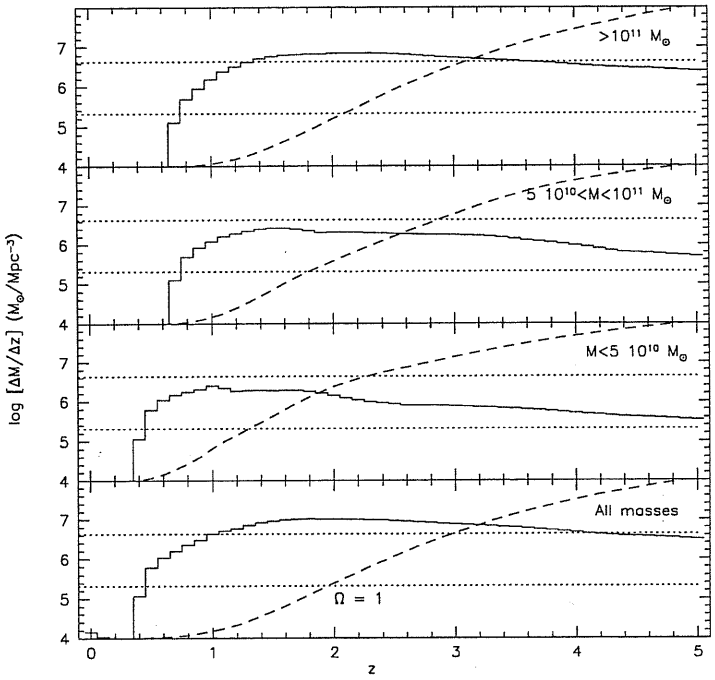

Figure 5.18: Same as in Fig. 5.17 but for $q_0 = 0.5$.

distributions (reported on a linear vertical scale ranging from 0 to 100% in each panel) of the stellar mass synthesized as a function of z. For example, for $q_0 = 0.15$, the dashed line in the top panel of Fig. 5.17 shows that in massive galaxies the SF is already over at $z = 1$, while the third panel indicates that, for $M < 5\ 10^{10}\ M_{\odot}$, 40% of the stars are generated at $z < 1$.

It is evident from Figs. 5.16 to 5.18 that the two cases considered, of an Einstein-de Sitter or an open universe, entail somehow different solutions for the evolutionary star formation rate. In the closure world model with $\Lambda = 0$ there is a limited amount of time between the redshift of the observation (typically $z \sim 1$) and the big bang: this implies relatively higher values of z_F and a function $\Psi(z)$ keeping flat to the highest z. An open universe, instead, with more cosmic time available, entails typically lower values of z_F and a $\Psi(z)$ peaked at slightly lower redshifts.

This reflects on the mass fractions of stars generated at the various redshifts. For $q_0 = 0.15$, 80% of the mass in stars is formed between z=1 and z=3, while the remaining 20% is made at higher or lower z. For $q_0 = 0.5$, the same 80% of stars are formed between z=1.2 and z=4.2. The median redshifts in the stellar formation process turn out to be close to z=1.8 and z=2.5 in the two cases respectively.

The SF rate $\Psi(z)$ for our early-type field galaxy population is compared in Fig. 5.16 with the average rate (shaded horizontal regions) expected for early-type galaxies in rich clusters, assumed that these synthesize between z=5 and 1.5 all metals observed in the intra-cluster medium (Mushotzky & Loewenstein 1997). The comparison is mediated

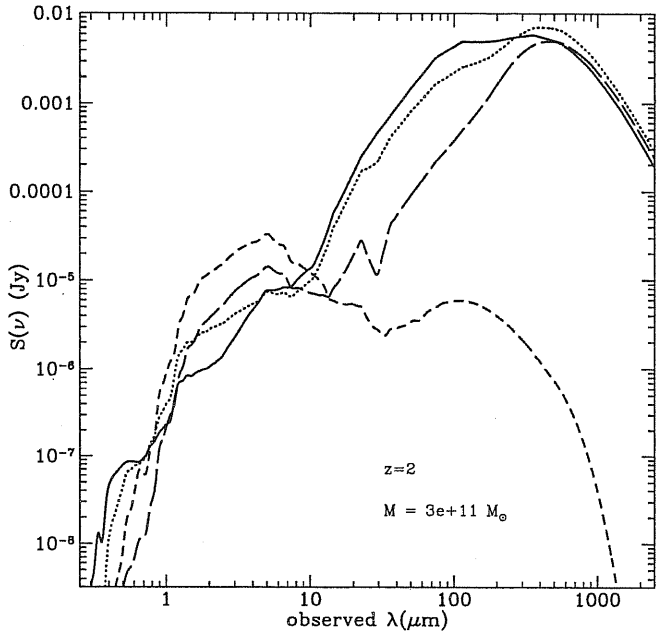

Figure 5.19: Predicted spectra of a $M = 3\ 10^{11}\ M_{\odot}$ galaxy at $z = 2$ observed at 0.5 (continuous), 1 (dotted), 3 (long dash), and 4 (short dash) Gyr, according to Model 2. The former three are spectra during the dusty starburst phase.

by a crucial assumption we made on the stellar IMF to have a Salpeter's form. An IMF more weighted in favor of massive stars would decrease the SF requirement for cluster ellipticals. There is in any case an indication that field ellipticals behave as less efficient metal producers than the rich cluster counterparts. It is quite conceivable that the large number of dynamical interactions underwent by galaxies in the denser cluster environment might have triggered a more intense SF during the early Gyrs of the cluster lifetime, with a globally more efficient metal yield. This evidence also matches a likely difference in the ages of cluster versus field ellipticals: while the properties of cluster galaxies imply that the SF was completed already before z=2 (Stanford et al. 1998), typically 50% of stars in the field are produced at more recent epochs.

Finally, it is interesting to compare in Fig. 5.16 (bottom) the indications on the SF history $\Psi(z)$, as inferred from direct inspection of high-redshift galaxies (see data points in the figure), with our predictions based on modelling of the stellar populations. The latter refer to only a sub-class of galaxies, those classified as early-types. Yet, this prediction already exceeds the global amount inferred by high-z dropouts. There is a suggestion, in particular, that for $z > 1.5$ the direct estimate based on optical-UV measurements misses some light, if a subpopulation alone already exceeds the global estimated amount. This may be taken as an evidence that dust indeed played a role in at least partly obscuring the young stars during the active phase of star formation. If moderately true for the average gas-rich spiral, this might have been particularly relevant during the starburst events bringing to the formation of early-type galaxies.

5.7 Conclusions and perspectives

Early-type galaxies are commonly believed to contain among the oldest stellar systems in the universe. Analyses of galaxies in rich clusters, which found weakly evolving spectra and non-evolving dynamical conditions up to z=1 and slightly above, have confirmed this intuition.

In spite of a morphological similarity which may be taken as indicative of a common origin, no conclusive results were achieved so far about the early-type galaxies in the field. Our contribution here has been devoted to exploit a NIR sample of 35 distant early-types in the HDF with $K < 20.15$, with optimal morphological information and spectrophotometric coverage, to study properties of distant early-type galaxies outside rich clusters. Near-IR observations provide a view of galaxy evolution minimally biased by the effects of the evolutionary K-correction, dust extinction and changes in the M/L ratio due to the aging of stellar populations. The basic conclusions of our analysis may be summarized as follows.

(1) The broadband SEDs of the sample galaxies, together with the assumption of a Salpeter IMF within $M_l = 0.15$ and $M_u = 100\ M_\odot$, allow us to date their dominant stellar populations. The majority of bright early-type galaxies in this field are found at redshifts $z \lesssim 1.3$ to display colors indicative of a fairly wide range of ages (typically 1.5 to 3 Gyrs). This evidence adds to that of a substantially broad distribution of the formation redshifts z_F from galaxy to galaxy in the sample. So, there is no coeval event of star formation for early-types in this field, probably at variance with what happens for cluster galaxies. There is a tendency for lower mass systems to be typically younger than the massive ones, but a firm conclusion has to wait for deeper and richer samples. A spread in the ages and a somewhat protracted SF activity in field, as opposed to cluster ellipticals may be consistent with their observed narrow-band spectral indices (H_β, $Mg2$, etc.; see Bressan et al. 1996). A protracted SF activity in field ellipticals may also bear some relationship with their observed preferentially "disky" morphology (Shioya & Taniguchi 1993). Unfortunately, our sample is too faint to allow testing of this. Of the 15 galaxies (out of 35) bright enough to have the c_4 morphological parameter measured, 11 show rather clearly a "disky" morphology, and the other 4 a "boxy" shape.

(2) The basic uncertainty when dating stellar populations – the metallicity of stars – has been the subject of a careful discussion. Given the relatively blue colors of the detected galaxies at the typical redshift of 1, the age uncertainty cannot be very large, as it would when considering old populations in local galaxies. Our result should then be fairly robust.

(3) Because of the different cosmological timescales, the redshift-dependent star formation history inferred from these data depends to some extent on the assumed value for the cosmological deceleration parameter. We find that the major episodes of star formation building up 80% of the mass in stars for typical $M^\star$ galaxies have taken place during the wide redshift interval between $z = 1$ and $z = 4$ for q_0=0.5, which becomes $z = 1$ to $z = 3$ for q_0=0.15. Lower mass ($M < 5\ 10^{10}\ M_\odot$) systems tend to have their bulk of SF protracted to lower redshifts (down to almost the present time).

(4) The previous items deal with the ages of the dominant stellar populations in distant field galaxies. The evolution history for the dynamical assembly of these stars

into a galactic body might have been entirely different. However, our estimated galactic masses, for a Salpeter IMF, are found in the range from a few $\sim 10^9\ M_\odot$ to a few $10^{11}\ M_\odot$ already at $z \simeq 1$. So the massive end of the E/S0 population appears to be mostly in place by that cosmic epoch, with space densities, masses and luminosities consistent with those of the local field population. It is to be investigated how this result compares with published findings (see e.g. Kauffmann & Charlot 1998) of a strong decrease of the comoving mass density of early-type galaxies already by $z \simeq 1$. We suggest that a question to keep under scrutiny in these analyses concerns the color classification, as we find, after a detailed morphological and photometric analysis, that these objects usually display blue young populations mixed with old red stars.

(5) The present sample is characterized by a remarkable absence of objects at $z > 1.3$, which should be detectable during the luminous star formation phase expected to happen at these redshifts. This conclusion seems robust: if optical spectroscopy has difficulties to enter this redshift domain, our analysis, using broadband galaxy SEDs when spectroscopic redshifts are not available, has no obvious biases. The uncertainty in the photometric estimate of z for this kind of spectra is small. We discuss solutions for this sudden disappearance in terms of: (1) merging events, triggering the SF, which imply strongly perturbed morphologies and which may prevent selecting them by our morphological classification filter, and (2) a dust-polluted ISM obscuring the (either continuous or episodic) events of star formation, after which gas consumption (or a galactic wind) cleans up the galaxy. We conclude that the likely solution is a combination thereof, i.e. a set of dust-enshrouded merging-driven starbursts occurred during the first few Gyrs of the galaxy's lifetime.

(6) A comparison between the observed SF rates with the level needed to synthesize the metals in the ICM indicates that field ellipticals could have been slightly less efficient metal producers than the cluster galaxies. This difference adds to the one in the ages and age spread.

(7) The comparison in Fig. 5.16 of our estimated SF rate $\Psi(z)$ at $z > 1.5$ with those inferred from the optical colors of high-z galaxies (via the Lyman dropout or other photometric techniques) provides a *direct indication that a fraction of light emitted during the starburst episodes (in particular those concerning the formation of early-type galaxies) has been lost, probably obscured by dust.* The recently detected IR/submm extragalactic background may be a trace of this phenomenon. Our results on the cosmological SF rate reported in Fig. 5.16 (bottom; note that our best-guess coincides with the upper limit of the shaded region) are very close to the level predicted by Burigana et al. (1997) to reproduce the spectral intensity of the cosmic infrared background.

It is obviously essential to have a direct test of such a dust-extinguished SF, that require powerful dedicated instrumentation. This is illustrated in Fig. 5.19, showing possible spectra corresponding to various ages of a massive ($M = 3\ 10^{11}\ M_\odot$) galaxy at $z = 2$, according to Model 2, during the starburst and poststarburst phases. Various planned missions (in launch-time order, SIRTF, ESA's FIRST, NASA's NGST and some ground-based observatories in exceptionally dry sites, like the South Pole) could discover intense activity of star formation at $z = 1.5$ to 3 or 4. Also tests on these issues are ongoing with SCUBA on the JCMT and with ISO. In any case, observations at long wavelengths are needed to completely characterize the early evolutionary phases of (spheroidal) galaxies.

(8) While our main conclusions are moderately dependent on the assumed value of q_0, an open universe or one with nonzero Λ are favored in our analysis by the match of the K-band local luminosity functions with the observed numbers of faint distant galaxies.

(9) There are two main sources of uncertainty in our analysis. The redshift distribution in Fig. 5.13 (and in particular the pronounced peak at $z = 1.1$) may be somehow affected by the possible presence of a background cluster or group at $z \sim 1$. A few to several of the galaxies with photometric redshifts in the interval $1 < z < 1.2$ have a non-random distribution in the HDF, being clustered in one region (at RA$\simeq$87.98, DEC$\simeq$62.218). Until we will not have a complete spectroscopic identification of most of the galaxies with precisely measured redshifts, it will be impossible to check this. However the effect should be limited to a small fraction of the sample galaxies and should not drastically influence our statistics. The second basic uncertainty is due to the photometric estimate of the redshift for half of the sample. In this case too, however, this is not likely to affect our main conclusions. In any case, these uncertainties will be reduced soon by the new observations in the southern HDF and deep spectroscopic surveys from ground with large telescopes.

FOCAS ID	R.A.(2000)	Decl.(2000)	r_e''	U_{AB}	B_{AB}	V_{AB}	I_{AB}	J_{ST}	H_{ST}	K_{ST}	z	μ_e^K	Type	Morphology Class	I_{814}
(1)	(2)	(3)	(4)	(5)	(6)	(7)	(8)	(9)	(10)	(11)	(12)	(13)	(14)	(15)	(16)
4-942-0	36 39.43	12 11.76	0.44	26.13	25.58	24.55	23.10	21.35	20.41	19.66	(0.55)	19.88	E	(T1)	
4-928-1	36 40.01	12 7.37	0.32	26.08	24.60	23.41	22.06	19.99	19.29	18.46	1.010[a]	17.95	S0	(T1)	
4-767-0	36 41.49	12 14.98	0.13	<27.99	26.83	24.96	23.29	20.79	20.05	19.08	(1.05)	16.68	S0	(T2)	
4-493-0	36 43.16	12 42.20	0.41	27.34	25.14	23.06	21.40	19.39	18.55	17.75	0.847[a]	17.79	S0	(T1)	
4-727-0	36 43.41	11 51.57	0.16	23.59	23.31	23.23	22.85	21.37	20.70	20.05	(1.10)	18.13	E	(T2)	
4-565-0	36 43.63	12 18.25	0.26	24.07	23.74	23.26	22.43	21.05	20.57	19.89	0.750[a]	18.96		(T3)	
4-744-0	36 43.80	11 42.88	0.57	26.20	24.18	22.13	20.53	18.58	17.74	17.09	0.764[a]	17.85	E	(T1)	
4-776-0	36 43.88	11 34.20	0.14	28.70	29.18	26.42	24.61	21.87	20.99	20.04	(1.25)	17.78	E	(T1)	P814
4-752-1	36 44.38	11 33.20	0.84	27.26	25.01	22.77	20.88	18.19	17.24	16.59	1.010[a]	18.21	E	(T1)	
4-555-2	36 45.33	11 54.52	0.27	27.55	26.36	24.59	22.99	20.20	19.41	18.55	(1.20)	17.73	E/S0	(T1)	
1-86-0	36 45.40	13 25.92	0.18	24.17	23.75	23.00	22.59	21.22	20.77	20.07	(0.40)	18.37	E/S0	(T1)	P814
4-307-0	36 45.65	12 41.89	0.18	28.83	28.14	26.73	25.56	21.80	20.79	19.68	(1.90)	17.98	E/S0?	(T?)	P814
4-254-0	36 46.13	12 46.50	0.47	26.34	24.83	23.44	21.90	20.14	19.32	18.71	(0.90)	19.08	E	(T1)	
2-251-0	36 46.34	14 4.62	0.42	24.95	23.55	22.76	21.53	18.98	18.25	17.48	0.960[a]	17.61	E/S0	(T1)	
4-471-0	36 46.51	11 51.32	0.17	27.01	24.57	22.91	21.86	20.21	19.51	18.77	0.504[a]	16.93	E	(T1)	
2-121-111	36 48.08	13 9.02	0.52	25.91	23.06	21.28	20.24	18.46	17.66	17.07	0.475[a]	17.66	S0	(T1)	
2-173-0	36 48.47	13 16.62	0.64	27.93	24.81	23.54	22.69	21.34	20.52	19.96	(0.25)	20.98	E	(T2)	
2-236-2	36 48.96	13 21.88	0.10	25.49	26.00	24.61	23.02	21.53	20.80	19.65	(0.70)	16.73	E	(T1)	
2-264-2	36 49.38	13 11.22	0.14	23.77	23.22	22.60	22.03	20.71	19.87	19.30	0.478[a]	17.06	E	(T1)	
2-456-1111	36 49.44	13 46.88	0.46	22.72	19.77	18.73	18.09	16.35	15.71	15.46	0.089[a]	15.77	S0	(T1)	
3-143-0	36 49.64	12 57.43	0.29	24.74	23.73	22.65	21.92	20.12	19.20	18.49	0.477[a]	17.79		(T3)	
3-321-1	36 50.27	12 45.75	0.36	26.95	24.82	22.85	21.36	19.30	18.47	17.78	0.678[a]	17.58	S0	(T1)	
2-531-0	36 51.97	13 32.18	0.29	24.94	24.38	23.86	22.87	21.19	20.59	19.71	(0.80)	19.02		(T3)	
3-586-0	36 52.10	12 26.31	0.29	<27.96	27.35	25.57	23.79	21.14	20.13	19.23	(1.30)	18.54	E	(T1)	
3-601-0	36 55.04	12 34.21	0.14	28.34	27.91	25.76	24.19	21.38	20.90	19.83	(1.20)	17.59	S0	(T1)	P814
3-266-0	36 55.16	13 3.60	0.16	<27.96	27.08	24.99	23.30	21.08	20.31	19.45	(1.05)	17.45	E	(T1)	
3-180-1	36 55.46	13 11.19	0.47	27.94	25.53	23.74	21.99	19.44	18.59	17.76	(1.13)	18.11	E/S0	(T1)	
3-48-0	36 56.14	13 25.15	0.19	27.31	27.70	26.32	24.89	21.73	21.04	20.08	(1.37)	18.46	E	(T1)	P814
3-815-1	36 56.65	12 20.12	0.36	26.88	26.04	24.09	22.39	20.07	19.28	18.45	(1.05)	18.22	E/S0	(T1)	
3-430-2	36 56.73	12 52.49	0.28	27.55	26.04	25.20	23.65	20.93	20.13	19.25	1.231[b]	18.44	E	(T1)	P814
3-355-0	36 56.92	13 1.56	0.33	24.92	24.29	23.96	22.75	20.22	19.43	18.52	(1.20)	18.14	E	(T1)	
3-289-0	36 57.22	13 07.60	0.18	28.74	27.77	26.11	24.38	21.75	21.10	20.01	(1.25)	18.28	E	(T1)	P814
3-965-0	36 57.48	12 10.55	0.35	28.19	24.31	22.58	21.03	18.84	18.02	17.29	(0.95)	17.00	E/S0	(T1)	P814
3-405-0	36 58.07	13 00.36	0.26	23.51	23.13	22.56	22.33	21.15	20.52	20.07	0.319[a]	18.92	S0	(T2)	P814
3-790-1	37 0.56	12 34.60	0.35	26.21	24.08	22.40	21.26	19.55	18.69	18.03	0.562[a]	17.73	E	(T1)	

Table 5.1: Basic data on the sample. FOCAS=Faint Object Classification and Analysis System. Units of right ascension are minutes and seconds, units of declination are arcminutes and arcseconds. Photometric redshifts in parenthesis. Spectroscopic redshifts are from (*a*) Cohen et al. (1996) and (*b*) Cowie et al. (1996). Morphology: (T1)=normal; (T2)=flat; (T3)=merger; P814= surface photometry in the I_{814} band.

	$\Omega = 0.3$				$\Omega = 1$			
FOCAS ID	z	z_{form}	M $(M_\odot/10^9)$	Ψ_0(SFR) $(M_\odot\, yr^{-1})$	z	z_{form}	M $(M_\odot/10^9)$	Ψ_0(SFR) $(M_\odot\, yr^{-1})$
4-942-0	0.55	3.70	18	0.20	0.55	8.00	12	0.15
4-928-1	1.010	2.40	110	0.20	1.010	3.60	75	0.10
4-767-0	1.05	2.70	60	0.03	1.05	4.40	40	0.02
4-493-0	0.847	2.10	130	0.02	0.847	3.30	120	0.01
4-727-0	1.10	(1.16)	15	0.00	1.10	(1.20)	12	0.00
4-565-0	0.750	1.80	10	3.30	0.750	1.90	4	2.80
4-744-0	0.764	1.90	250	0.05	0.764	2.90	200	0.15
4-776-0	1.25	4.00	47	0.00	1.20	10	27	0.00
4-752-1	1.010	4.00	999	0.00	1.010	9.00	620	0.00
4-555-2	1.20	3.40	150	0.07	1.20	8.00	110	0.04
1-86-0	0.40	1.60	3	0.08	0.40	1.90	1.5	0.80
4-307-0	1.90	3.10	225	0.20	1.90	(4.40)	105	0.08
4-254-0	0.90	2.10	80	0.05	0.85	2.60	45	0.03
2-251-0	0.960	2.30	210	0.40	0.960	4.20	180	0.60
4-471-0	0.504	1.13	17	0.00	0.504	1.45	16	0.02
2-121-111	0.475	1.16	82	0.00	0.475	1.90	100	0.10
2-173-0	0.25	0.75	2	0.00	0.25	0.90	1.9	0.00
2-236-2	0.70	1.70	14	0.25	0.70	2.30	10	0.20
2-264-2	0.478	1.10	7	1.40	0.478	1.50	6	1.00
2-456-1111	0.089	0.60	22	0.04	0.089	1.10	28	0.05
3-143-0	0.477	1.50	27	0.60	0.477	2.30	25	0.60
3-321-1	0.678	1.70	88	0.00	0.678	2.80	85	0.10
2-531-0	0.80	1.90	17	1.20	0.70	2.50	10	1.00
3-586-0	1.30	3.90	110	0.04	1.30	10	65	0.00
3-601-0	1.20	3.30	50	0.02	1.10	6.50	27	0.02
3-266-0	1.05	2.75	53	0.02	0.90	4.00	27	0.04
3-180-1	1.13	3.00	280	0.00	1.10	7.00	220	0.02
3-48-0	1.37	4.10	40	0.13	1.25	10	25	0.10
3-815-1	1.05	2.65	120	0.08	1.00	4.30	80	0.10
3-430-2	1.231	3.65	86	0.40	1.231	8.00	60	0.25
3-355-0	1.20	3.20	138	2.00	1.20	6.50	100	1.30
3-289-0	1.25	3.45	39	0.00	1.25	8.00	30	0.00
3-965-0	0.95	2.35	280	0.00	0.99	4.20	240	0.00
3-405-0	0.319	0.55	0.3	0.80	0.319	1.90	0.05	0.83
3-790-1	0.562	1.40	51	0.20	0.562	2.10	48	0.20

Table 5.2: Parameters of spectral solutions for the sample galaxies. Spectroscopic redshifts are reported with 3 decimal digits. z_{form} in parenthesis indicates that the best fit of the broadband spectrum has been obtained using Model 1.

Chapter 6

The local universe in the semi-analytical framework

Summary. We[1] analyze the spectro-photometric properties of local galaxies of different morphological type, from the UV to the sub-mm range. To this aim we adopt the framework of the semi-analytic modelling technique (Cole et al. 1999) and build a manifold of galaxies starting from different density environments in the CDM scenario with the GALFORM code. These models provide the star formation history, the metal enrichment law, the amount of hot and cold gas and the geometrical parameters of the bulge and disk components. With these inputs, we then model the spectral energy distribution of galaxies with the GRASIL code (Silva et al. 1998, Chap. 2) suitably modified in order to be interfaced with GALFORM. In this way our spectro photometric model is now multicomponent as far as both the stellar mix as a function of time and the geometry are concerned. A synthetic galaxy catalogue is generated, made of a 'normal' and a 'burst' sample of galaxies, and compared with observations: SEDs, extinctions, luminosity functions. We find an overall good agreement. Some preliminaty results for high-z galaxy catalogues, compared with number counts and cosmic background in different bands, are also presented. The mismatch found in the submm number counts, lower by a factor of 10 with respect to observations, suggests star formation is distributed in too many low luminosity objects.

6.1 Introduction

In recent years, our understanding of galaxy formation and evolution has advanced very rapidly, as a result of both observations and theory. On the observational side, new telescopes have allowed the direct study of galaxy populations at different wavelengths

[1]This Chapter is from the paper *Granato G.L., Lacey C.G., Silva L., Bressan A., Baugh C., Cole S. & Frenk C., 1999, in preparation* (Granato et al. 1999).

out to high redshifts ($z \lesssim 5$). By combining observations in the UV, optical, IR and sub-mm, we can now start to reconstruct the history of star formation in galaxies over the epochs when the bulk of the stars have formed (e.g. Madau et al. 1996, Steidel et al. 1999, Hughes et al. 1998). On the theoretical side, models based on the paradigm of structure formation through hierarchical clustering (which has successfully confronted a wide range of observations on large scale structure and microwave background anisotropies) have now been developed to the point where they can make definite predictions for the observable properties of galaxies (luminosities, colours, sizes, morphologies etc) at all redshifts, starting from an assumed initial spectrum of density fluctuations. The key technique for making these predictions has been that of *semi-analytical modelling* (White & Frenk 1991, Lacey & Silk 1991, Kauffmann et al. 1993, Cole et al. 1994). In this technique, one applies simplified analytical descriptions of the main physical processes of gas cooling and collapse, star formation, feedback effects from supernovae, galaxy merging etc, with the backbone being a Monte Carlo description of the process of formation and merging of dark matter halos through hierarchical clustering. The predicted star formation histories are then combined with detailed stellar population models to calculate galaxy luminosities at different wavelengths. Direct numerical simulations have been enormously successful in studying the evolution of structure in the dark matter on a huge range of scales, but currently do not have sufficient spatial resolution to simultaneously follow all the processes involved in galaxy formation, leaving semi-analytical modelling as the only presently available method.

The semi-analytical models have been successful in predicting and/or explaining a large range of galaxy properties, both at low and high redshift, for instance, luminosity functions and colours in different optical and near-IR bands (Lacey et al. 1993, Kauffmann et al. 1993, Cole et al. 1994), the mixture of galaxy morphologies and the evolution of elliptical galaxies (Kauffmann et al. 1993, Baugh et al. 1996, Kauffmann 1996), the properties of Lyman-break galaxies at high redshift (Baugh et al. 1998), the sizes and circular velocities of galaxies (Cole et al. 1999), and galaxy clustering evolution and the nature of the clustering bias (Kauffmann et al. 1997, Baugh et al. 1999). However, with very few exceptions, these semi-analytical models have ignored both absorption and emission by interstellar dust, and calculated only the direct stellar emission in the UV, optical and near-IR. This has been partly because the importance of dust was generally under-appreciated, especially for high redshift galaxies, but also because of the lack of physically realistic models for predicting dust effects on a level of sophistication comparable to that of stellar population synthesis models.

This situation has now begun to change. On the one hand, there have been several observational discoveries demonstrating the importance of dust effects for building a complete picture of galaxy formation. (1) The discovery of a cosmic far-IR/sub-mm background by the COBE satellite, with energy density comparable to that in the UV and optical background (Puget et al. 1996, Fixsen et al. 1998, Hauser et al. 1998, Schlegel et al. 1998), indicating that a large fraction of all the energy radiated by stars over the history of the universe has been reprocessed by dust. (2) The discovery that the population of star forming galaxies at $z \sim 2-4$ that have been detected through their strong Lyman-break features are heavily extincted in the rest-frame UV, so that the star formation rates in these objects are $\sim 3-10$ times higher than would be inferred by ignoring dust (Pettini et al. 1998, Steidel et al. 1999). (3) The discovery of a population

of sub-mm sources at high redshift ($z \gtrsim 1$) using SCUBA, whose luminosities, if they are powered by star formation in dust-enshrouded galaxies, imply very large star formation rates ($\sim 10^2$ $M_\odot yr^{-1}$), and a total star formation density comparable to what is inferred from the UV luminosities of the Lyman-break galaxies (Smail et al. 1997, Hughes et al. 1998, Lilly et al. 1999). For (1) and (3), there is the caveat that the contribution from dust-enshrouded AGNs to the sub-mm counts and background is currently uncertain, but probably the AGNs do not dominate (Granato et al. 1997). These discoveries demonstrate that in order to understand the history of star formation in the universe from observational data, one must have a unified picture that covers all wavelengths from the far-UV to the sub-mm, but especially the UV and the far-IR, since young stellar populations emit most of their radiation in the rest-frame UV, and the part of this that is absorbed by dust is re-radiated mostly in the rest-frame far-IR, so that luminosities in these two wavelength ranges are the best tracers of the star formation rate at different redshifts.

On the theoretical side, it is now possible for the first time to construct true *ab initio* models in which both galaxy formation itself and stellar emission and dust absorption and emission are calculated from first principles, based on physical models, and avoiding observational parameterizations for various key ingredients (e.g. shape of the luminosity function, dependence of dust temperature on galaxy properties). These new galaxy formation models, which provide a unified treatment of emission from stars and dust, and predict the evolution of galaxy luminosities from the far-UV to the mm, are the subject of this chapter.

The effects of dust on galaxy luminosities at different wavelengths have been included in some previous galaxy evolution models, at various levels of sophistication, but mostly in the context of *backwards evolution* models, where one tries to evolve back from observed galaxy properties at the present day, in contrast to the *semi-analytical* models, where one evolves forward from cosmological initial conditions. In backwards evolution models, one starts from the observed luminosity functions of different types of galaxy at the present day, assumes a different star formation history for each type, and calculates the luminosity evolution for each type, to predict what the galaxy population would have looked like in the past. Guiderdoni & Rocca-Volmerange (1987) were the first to include *dust absorption* in a model of this type, based on a 1D slab model for the star and dust distribution, and calculating the dust content self-consistently from a chemical evolution model. The same treatment of dust was later used in the semi-analytical galaxy formation models of Lacey et al. (1993). In both cases, the models were used to calculate galaxy luminosities and number counts in the UV and optical. Mazzei et al. (1992) were the first to try to model the evolution of stellar emission and dust emission together in a consistent framework based on stellar population synthesis models and a physical calculation of dust absorption. This model was then used by Franceschini et al. (1994) to calculate galaxy evolution and number counts in bands from the optical through to the far-IR, based on the backwards evolution approach. However, these models still made a number of simplifying assumptions (e.g. slab geometry for disks), and set a number of present-day properties of galaxies from observations (e.g. the optical depth of galactic disks, and the intensity of the radiation field heating the dust), rather than predicting them.

Recently, dust absorption has been included in several different semi-analytical mod-

els (Kauffmann et al. 1999, Somerville & Primack 1999, Cole et al. 1999). The first two of these calculate dust effects only for present-day galaxies, using a 1D slab model, and taking the dust optical depth from observational measurements. On the other hand, Cole et al. (1999) predict the dust optical depth and how it evolves, based on chemical evolution and a prediction of disk sizes, and use the 3D disk+bulge radiative transfer models of Ferrara et al. (1999) to calculation the dust attenuation. The only previous semi-analytical model to calculate dust emission as well as absorption is that of Guiderdoni et al. (1998). However, that model also has several limitations: the galaxy formation model does not include merging of either dark halos or visible galaxies, and the fraction of star formation occuring in bursts is simply an arbitrary function; dust absorption is again modelled assuming a 1D slab geometry; and the dust temperature distribution is not predicted. Instead, the dust emission spectrum is modelled as the sum of several components, whose temperatures and relative strengths are chosen so as to reproduce the observed correlations of IR colours with IR luminosity found by IRAS.

The present work represents a major advance over this earlier work in terms of scope, physical self-consistency and predictiveness. We combine the semi-analytical galaxy formation model of Cole et al (1999) with the stellar population + dust model of Silva et al. (1998) (Chap. 2). The galaxy formation model includes formation of dark halos through merging, cooling and collapse of gas in halos to form disks, star formation in disks regulated by energy input from supernovae, merging of disk galaxies to form elliptical galaxies and bulges, bursts of star formation triggered by these mergers, predictions of the radii of disks and spheroids, and chemical enrichment of the stars and gas. The stellar population + dust model includes a realistic 3D geometry, with a disk and bulge, dust both in clouds and in the diffuse ISM, star formation in the clouds, radiative transfer of starlight through the dust distribution, a realistic dust grain model including PAHs, and a direct prediction of the dust temperature distribution at each point in the galaxy based on a calculation of dust heating and cooling. The output is the luminosity and spectrum of the stellar population, attenuated by dust, and the luminosity and spectrum of the dust emission from grains at a range of temperatures. From this, we can calculate the distribution of galaxy properties at any redshift, including the complete spectrum of each galaxy in the model from the far-UV to the sub-mm.

In the following sections we describe how we combine the galaxy formation and dust models, and compare the predicted galaxy properties with a wide range of observational data on present-day galaxies. Preliminary results of the model for high-z galaxies are also presented.

6.2 Semi-Analytical Galaxy Formation Models: GALFORM

6.2.1 Overview of semi-analytical models

We calculate the formation histories and global properties of galaxies using the semi-analytical galaxy formation model (GALFORM) of Cole et al. (1999). This model is a development of that described in Cole et al. (1994) and Baugh et al. (1998). The principle of the model is to calculate the formation and evolution of dark matter halos starting from an assumed cosmology and initial spectrum of density fluctuations, and then to calculate the evolution of the baryons (gas and stars) within these evolving halos

Ω_0	0.3
Λ_0	0.7
h	0.7
Ω_b	0.02
Γ	0.19
σ_8	0.93
ϵ_{*disk}	6.7×10^{-3}
α_*	-1.5
α_{hot}	2.0
V_{hot} (km/s)	150.0
f_{ellip}	0.3
IMF	Kennicutt (1983)
Υ	1.4
p	0.02
R	0.29
ϵ_{*burst} †	0.5
χ †	0.1

Table 6.1: The parameters of the galaxy formation model. They are the same as those of the standard ΛCDM model of Cole et al. (1999). Apart from ϵ_{*burst} and χ, the timescale and radius of bursts not considered in Cole et al., they were obtained by comparing the model to observations of nearby galaxies, without any consideration of the far-IR properties. Values for ϵ_{*burst} and χ are obtained by detailed comparison of the results of the combined GALFORM+GRASIL models with observed properties of bursting galaxies as described in Sec. 6.3.2.

using a set of simple, physically-motivated rules to model gas cooling, star formation, supernova feedback and galaxy mergers. We describe here only the main features of the model, see Cole et al. (1999) for more details. The specific values used in the present model of the parameters described below are given in Table 6.1.

(a) Cosmology: The cosmology is specified by the present-day density parameter Ω_0, cosmological constant Λ_0, and baryon fraction Ω_b (all in units of the critical density) and the Hubble parameter h (in units of $100 kms^{-1}Mpc^{-1}$). We assume a cold dark matter (CDM) model, with the initial spectrum of density fluctuations having shape parameter Γ and amplitude σ_8 (the r.m.s. density fluctuation in a sphere of radius $8h^{-1}Mpc$).

(b) Halo evolution: Dark matter halos form through a process of hierarchical clustering, building up through merging from smaller objects. At any cosmic epoch, we calculate the number density of halos as a function of mass from the Press-Schechter (1974) formula. We then calculate halo merger histories, describing how a halo has formed, for a set of halos of different masses, using a Monte-Carlo algorithm based on the extended Press-Schechter formalism. We generate many different realizations of the merger history for each halo mass. We then follow the process of galaxy formation separately for each of these realizations.

(c) Cooling and collapse of gas in halos: Diffuse gas is assumed to be shock-heated to the virial temperature of the halo when it collapses, and to then cool radiatively out to a radius determined by the density profile of the gas and the halo lifetime. The gas which cools collapses to form a rotationally supported disk, for which the half-mass radius r_{disk} is calculated assuming angular momentum conservation during the collapse. The gas supply by cooling is assumed to be continuous over the lifetime of the halo.

(d) Star formation in disks: Stars form from the cold gas in the disk, at a rate

$$\psi = M_{cold}/\tau_{*disk}, \tag{6.1}$$

where the star formation timescale is assumed to be

$$\tau_{*disk} = \epsilon_{*disk}^{-1}\tau_{disk}\left(V_{disk}/200kms^{-1}\right)^{\alpha_*} \tag{6.2}$$

where V_{disk} is the circular velocity at the half-mass radius of the disk, and $\tau_{disk} = r_{disk}/V_{disk}$ is the dynamical time. ϵ_{*disk} is the fraction of gas converted into stars in one dynamical time, for a galaxy with circular velocity $V_{disk} = 200kms^{-1}$.

(e) Supernova feedback in disks: The energy input from supernovae is assumed to reheat gas in the disk and eject it into the halo at a rate

$$\dot{M}_{eject} = \beta_{disk}\psi, \tag{6.3}$$

where for β_{disk} we assume

$$\beta_{disk} = (V_{disk}/V_{hot})^{-\alpha_{hot}} \tag{6.4}$$

Gas which has been ejected is assumed to be unavailable for cooling until the halo has doubled in mass through merging.

(f) Galaxy mergers and morphology: The galaxy morphology (i.e. whether it is a spiral or elliptical) is determined by merging. Following the merger of two halos, the largest pre-existing galaxy is assumed to become the central galaxy in the new halo, while the other galaxies become satellite galaxies. The central galaxy can continue to grow a disk by cooling of gas from the halo. The satellite galaxies merge with the central galaxy on a timescale equal to that for dynamical friction to make the orbits decay. The merger is classed as a *major merger* if the mass ratio of the satellite to central galaxy exceeds a value f_{ellip}, and as a *minor merger* otherwise. In a *major merger*, any pre-existing stellar disks are destroyed, producing a stellar spheroid (elliptical galaxy or bulge), and any remaining cold gas is consumed in a burst of star formation. The star formation timescale in the burst is related to the dynamical time of the bulge as described below. The spheroid can grow a new disk by cooling of halo gas. In a *minor merger*, the stars from the satellite galaxy add to the bulge of the central galaxy, while the cold gas adds to the disk, but no burst is triggered. In either case, the half-mass radius r_{bulge} of the spheroid produced in a merger is calculated using an energy conservation argument. Galaxies are classified into different morphological types based on their bulge-to-disk ratios.

(g) Star formation and feedback during bursts: As already mentioned, star formation bursts are assumed to be triggered by major mergers of galaxies. In Cole et al. (1999), these bursts were modelled in a very simple way, with the conversion of gas into stars being assumed to be instantaneous, since the galaxy properties examined there were not sensitive to the detailed time dependence. Here we model the bursts in more detail. We assume that star formation during bursts follows a law analogous to that for star formation in disks:

$$\psi = M_{cold}/\tau_{*burst}, \tag{6.5}$$

with star formation timescale

$$\tau_{*burst} = \epsilon_{*burst}^{-1}\tau_{bulge} \tag{6.6}$$

where $\tau_{bulge} = r_{bulge}/V_{bulge}$ is the dynamical time of the spheroid formed in the merger, V_{bulge} being the circular velocity at r_{bulge}. As in Cole et al. (1999), feedback is modelled as in disks except with V_{bulge} replacing V_{disk} in Eq. 6.4, assuming the same values for V_{hot} and α_{hot}, giving a feedback factor β_{burst}. Since we assume that no new gas is supplied by cooling during the burst, the star formation rate and cold gas mass decay during the burst as $\exp(-t/\tau_e)$, where

$$\tau_e = \tau_{*burst}/(1 - R + \beta_{burst}), \tag{6.7}$$

and R is the recycled fraction, discussed below. The burst is assumed to occur in an exponential disk of half-mass radius r_{burst}, where

$$r_{burst} = \chi r_{bulge} \tag{6.8}$$

(h) Chemical evolution: We assume that stars form everywhere and at all times with the same IMF. We assume that a fraction $1/\Upsilon$ of the mass formed into stars goes into visible stars ($0.1 < m < 125M_\odot$), while the remainder goes into brown dwarfs ($m < 0.1M_\odot$). The visible stars have an IMF similar to that in the solar neighbourhood. Specifically, in Cole et al. (1999) and here, we use the form proposed by Kennicutt (1983):

$$\begin{aligned} dN/d\ln m &\propto m^{-0.4} \quad (m < 1M_\odot) \\ &\propto m^{-1.5} \quad (m > 1M_\odot) \end{aligned} \tag{6.9}$$

We use the instantaneous recycling approximation to calculate the evolution of the abundance of heavy elements of the cold gas (Z_{cold}) and stars (Z_*) in each galaxy, together with that of the hot gas in the halo (Z_{hot}), including the effects of inflows and outflows between the galaxy and halo. The chemical evolution depends on the recycled fraction R and the yield of heavy elements p.

(i) Stellar population synthesis and Dust Extinction: In Cole et al. (1999), we calculated the luminosity evolution of each galaxy at different wavelengths using the stellar population synthesis models of Bruzual & Charlot (1999). The effects of dust *absorption* were calculated in a simple way using the dust models of Ferrara et al.

(1999), which assume a smooth (unclumped) distribution for both the dust (in a disk) and stars (in a disk and a bulge). In the present work, we use instead the combined stellar population and dust model GRASIL (Silva et al. 1998, Chap. 2) to calculate the galaxy luminosities and spectra including both *absorption* and *emission* by dust. The stellar population part of GRASIL is similar to the Bruzual & Charlot model, as both are based on similar stellar evolution tracks and stellar spectra. The dust part of GRASIL is however considerably more sophisticated than the Ferrara et al. models, in that GRASIL allows for clumping of both dust and stars, and calculates the grain heating and emission as well as the absorption.

The parameters we have chosen for the GALFORM model are the same as those of the standard ΛCDM model of Cole et al. (1999), apart from ϵ_{*burst} and χ describing the timescale and radius of bursts, which were not considered in Cole et al. The parameters from Cole et al. are given in Table 6.1, and were obtained by comparing the model to observations of nearby galaxies, without any consideration of the far-IR properties. Values for ϵ_{*burst} and χ are obtained later in this chapter by detailed comparison of the results of the combined GALFORM+GRASIL models with observed properties of bursting galaxies.

6.2.2 Generation of model galaxy catalogues

In summary, the GALFORM code is run for a set of dark matter halos covering a large range in mass, and generates a catalogue of model galaxies, including information about the following properties for each galaxy at the chosen epoch: stellar masses M_{disk}, M_{bulge}, and half mass radii r_{disk} and r_{bulge}, of the disk and bulge, mass M_{cold} and metallicity Z_{cold} of gas in the disk, and the star formation histories $\Psi(t, Z)$ of the disk and bulge separately, including both star formation in disks and during bursts, and specifying the metallicity distribution of the stars of each age. In addition, each galaxy has a weight or number density n, such that that galaxy should appear $N = nV$ times in an average volume of the universe V.

The GALFORM code outputs all the galaxies for each different halo that is calculated, down to a minimum mass controlled by the mass resolution of the merger tree. In practice, this means that the model catalogue contains many more low mass galaxies than high mass galaxies. Running the GRASIL code on every galaxy in the original catalogue is neither feasible (because of computer time) nor necessary. We therefore select a subset of galaxies from the catalogue chosen to sample galaxies more evenly in mass, and redistribute the weights to give the same total number density in each mass range. The GRASIL code is then run on each galaxy in this reduced catalogue to give the SED L_λ including both stellar emission and dust absorption and emission, and statistical properties (e.g. luminosity functions) are then calculated making use of these weights. In fact, we calculate 2 samples of galaxies, a "normal" sample and a "burst" sample, as follows:

(a) Normal galaxies: By "normal" galaxies, we here simply mean galaxies not selected to have had a recent burst. From the parent GALFORM catalogue, we select a sample with equal numbers of galaxies in equal bins in $\log M_*$, M_* being the total stellar mass of the galaxy. Within each mass bin, galaxies are randomly selected (allowing for multiple selection of the same galaxy) with probability proportional to their weight n. The

selected galaxies are then assigned new weights n_i, such that each galaxy within the same bin has the same weight (multiply selected galaxies being counted as separate objects), and that the sum of the weights (i.e. number densities) within a bin is the same as in the parent catalogue. In practice, we have used bins with $\Delta \log M_* = 0.3$ and about 40 galaxies per bin.

(b) Burst galaxies: By "burst" galaxies we mean galaxies which have had a burst in the recent past, at whatever redshift we are looking. Bursts have short durations compared to the age of the universe, so the fraction of galaxies undergoing a burst at any one time is very small, but they can be very luminous, and so may dominate the galaxy luminosity function at the highest luminosities. In practice, our "normal galaxy" catalogue contains too few galaxies in total to provide a representative sample of galaxies seen during their burst phase. Rather than use a greatly enlarged "normal galaxy" sample, it is more efficient to calculate a separate sample of "burst" galaxies, as follows: for a redshift z, we choose a subsample of galaxies which have had bursts during the time interval $t(z) > t > t(z) - T$, where $t(z)$ is the age of the universe at redshift z, with equal numbers of galaxies in equal bins in $\log M_{burst}$, M_{burst} being the mass of stars formed in the most recent burst. The galaxies are assigned new weights n_i analogously to the case of normal galaxies, but now conserving the total number density in bins of M_{burst} for the galaxies which have had bursts more recently than T. For each burst galaxy, we then run GRASIL to calculate the total galaxy luminosity at a set of times after the start of the burst, chosen to sample all phases of the burst evolution, including the highest luminosity phase of short duration. If $T << t(z)$, then the rate of bursts during the time interval T can be taken as constant. Then, for the ith galaxy in the jth phase in the burst evolution that lasts a time Δt_j, the number density of galaxies that should be found in this phase is

$$n_{ij} = n_i \left(\frac{\Delta t_j}{T} \right) \tag{6.10}$$

These weights can then be used to calculate statistical properties such as luminosity functions. When combining the "normal" and "burst" galaxy samples, the normal galaxies with bursts more recent than T are explicitly excluded, to avoid statistical double-counting. In practice, we chose $T = t(z)/20$ at all z, with bins $\Delta \log M_{burst} = 0.3$, around 10 galaxies per bin, and around 10 output times per galaxy, for $0 < t - t_{burst} \lesssim 100\tau_e$. For many calculations of statistical distributions, we then interpolate between these output times to have more burst phases.

6.3 The Stellar Population and Dust Model: GRASIL

Luminosities of model galaxies are calculated at all wavelengths from the far-UV to the mm range using the GRASIL code (Silva et al. 1998, Chap. 2), which follows both the evolution of stellar populations and extinction and emission by dust. GRASIL calculates the following: (i) emission from stellar populations; (ii) radiative transfer of starlight through the dust distribution; (iii) heating, thermal equilibrium and fluctuations of dust grains; and (iv) emission by dust grains.

6.3.1 Synthesis of starlight spectrum

Our stellar population model is described in Sec. 2.3. Here we use SSP computed with the Kennicutt (1983) IMF, since this is the stellar mass distribution adopted in the chemical evolution of GALFORM (point (h) in Sec. 6.2.1).

The stellar spectral synthesis for the integrated light from a galaxy is formally performed as in Eq. 2.8, but now we must take into account that for each component, bulge and disk, the SFR is an explicit function of the metallicity, not only of time, since stars of the same age but different Z may merge into the same galaxy.

Specifically, the semi-analytical galaxy formation model calculates $\Psi(t, Z)$ for each galaxy by summing over all the progenitor galaxies which have merged to produce that galaxy. The summation is done separately for the disk and bulge component in each model galaxy. Each of these progenitor galaxies had its own star formation and chemical history, so that the composite birthrate function $\Psi(t, Z)$ obtained by summing over the individual progenitor histories in general has a broad distribution of metallicity at each each age, i.e. there is no unique age-metallicity relation $Z(t)$. This is illustrated in Fig. 6.1, which shows the birthrate function extracted for one of our model galaxies. Therefore the age and metallicity distribution of a composite stellar population is specified by the birthrate function $\Psi(t, Z)$, where $\Psi(t, Z)\, dt\, dZ$ gives the mass of stars that were formed in the time interval $(t, t + dt)$ with metallicities in the range $(Z, Z + dZ)$. The SED for the composite stellar population at time t is then obtained using

$$F_\lambda(t_G) = \int_0^{t_G} dt \int_0^1 SSP_\lambda(t_G - t, Z)\Psi(t, Z)dZ \tag{6.11}$$

In practice, this integration is carried out by using discrete bins in t and Z.

To explicitly compare the latter equation with Eq. 2.8, now SSP_λ at age $t_G - t$ in Eq. 2.8 is substituted with a weighted mean of the SSP spectra over all the metallicities, with weights provided by $\Psi(t, Z)$:

$$SSP_\lambda(t_G - t) = \frac{\int_0^1 SSP_\lambda(t_G - t, Z)\, \Psi(t, Z)\, dZ}{\int_0^1 \Psi(t, Z)\, dZ} \tag{6.12}$$

and $\Psi(t)$ with the total SFR at time t:

$$\Psi(t) = \int_0^1 \Psi(t, Z)\, dZ \tag{6.13}$$

6.3.2 Radiative transfer model

Our model GRASIL is described in detail in Chap. 2. In particular, the radiative transfer through dusty media is in Sec. 2.5. In summary, GRASIL calculates the extinction of starlight by dust, the heating of dust grains, and the emission from these grains self-consistently, for an assumed geometrical distribution of the stars and dust, and a specific grain model (see in Fig. 2.6 the sketch of the geometry of our model). We report here the main features most relevant for this work and list the adjustable parameters. The values of these parameters for our standard case are listed in Table 6.2 (a list of all the GRASIL parameters is in Table 2.2).

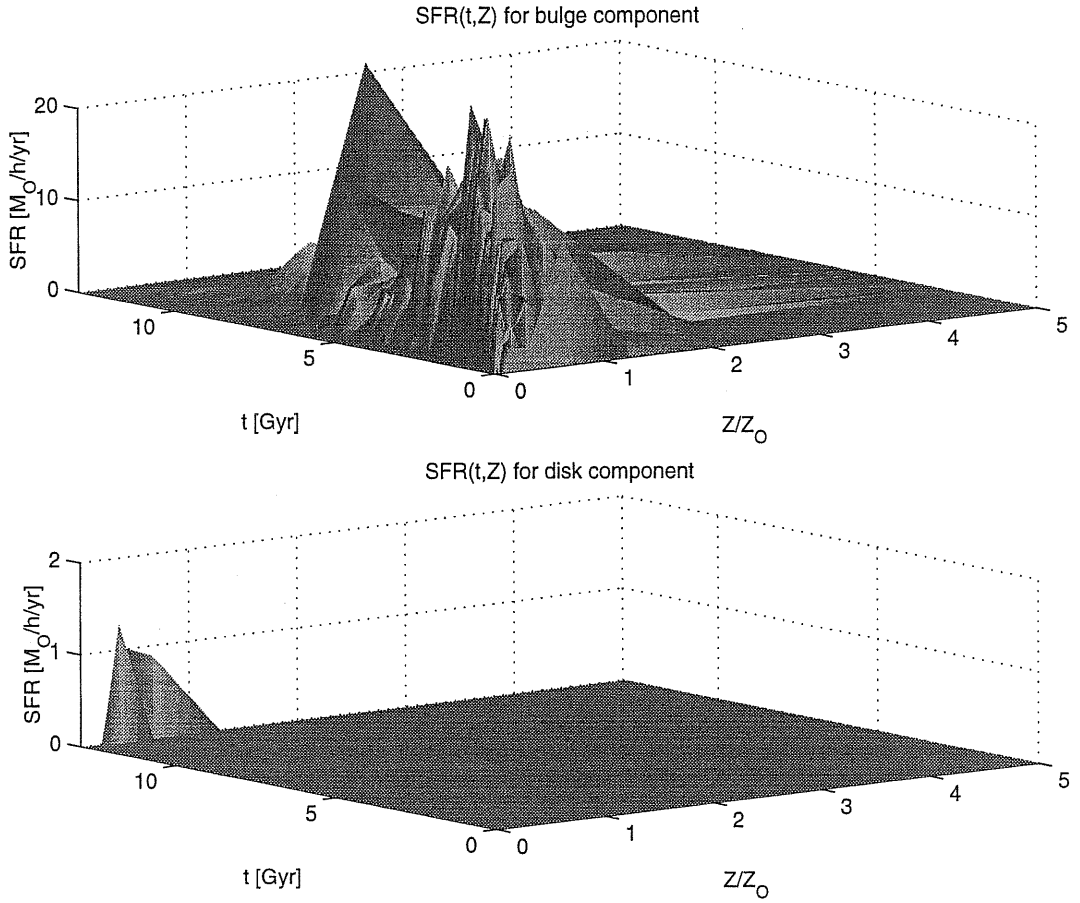

Figure 6.1: An example of the SFH calculated by the semi–analytical models: the evolution of the different sub–units merging into a galaxy is represented as a metallicity binned SFR, separately for the components merging into the bulge and disk of the final galaxy.

(a) Geometry of stars: The stars are in two components: (i) a spherical bulge with an analytic King model profile with core radius r_c^* (Eq. 2.20). The bulge core radius is related to the bule half-mass radius by $r_c^* = r_{bulge}/14.63$; (ii) a disk with a radially and vertically exponential profile, scalelength R_d^* and scaleheight z_d^* (Eq. 2.18). The disk scalelength R_d^* is related to the disk half-mass radius by $R_d^* = r_{disk}/1.68$. In galaxies undergoing bursts, stars are also assumed to be in an exponential disk, but with half-mass radius $r_{burst} = \chi r_{bulge}$ rather than r_{disk}.

As mentioned in Sec. 2.5.1, this two-component geometry is an improvement over Silva et al. (1998), who considered only pure disk and pure bulge systems.

As already noted in Sec. 6.2.1, the disk and bulge masses, M_{disk} and M_{bulge}, and half-mass radii, r_{disk} and r_{bulge}, for any galaxy are predicted by the galaxy formation model. The star formation histories are also calculated separately for the disk and bulge by GALFORM. However, the disk axial ratio z_d^*/R_d^*, for disks of both burst regions and normal galaxies, is a free parameter of the GRASIL model.

$z_d^*/R_d^*(disk)$	0.1
$z_d^*/R_d^*(burst)$	0.5
$z_d(dust)/z_d^*$	1
$R_d(dust)/R_d^*$	1
f_{mc}	0.25
m_{mc}	$10^6 M_\odot$
r_{mc}	16 pc
$t_0(disk)$	5 Myr
$t_0(burst)$	10 Myr

Table 6.2: Standard parameter values for GRASIL. Note that for each galaxy at the chosen epoch GALFORM provides the following: star formation histories $\Psi(t, Z)$ of the disk and bulge separately, including both star formation in disks and during bursts, and specifying the metallicity distribution of the stars of each age; stellar masses M_{bulge}, M_{disk}; half mass radii r_{bulge} and r_{disk}, from which $r_c^* = r_{bulge}/14.63$, $R_d^*(burst) = \chi r_{bulge}/1.68$, $R_d^*(disk) = r_{disk}/1.68$; mass M_{cold} and metallicity Z_{cold} of gas in the disk. The parameters of this table are those not provided by GALFORM.

(b) Geometry of gas and dust: In galaxies not undergoing bursts, the gas and dust are in an exponential disk, with the same radial scalelength as the disk stars, $R_d(dust)/R_d^* = 1$, but in general with a different scaleheight, so that $z_d(dust)/z_d^*$ is a free parameter. The gas and dust are in two components within the disk, molecular clouds and the diffuse ISM. The total gas mass M_{cold} and its metallicity Z_{cold} are calculated by the galaxy formation model, but the fraction of the gas in clouds, f_{mc}, and the cloud mass m_{mc} and radius r_{mc} are free parameters of GRASIL.

In the exponential disk of galaxies undergoing bursts $R_d(dust)/R_d^*$, $z_d(dust)/z_d^*$, f_{mc}, m_{mc} and r_{mc} are assumed to be the same as for non-bursting galaxies. The mass of gas involved in the burst is obtained from the galaxy formation model. For simplicity, the metallicity of the gas in the burst and of the stars formed during the burst are taken to be constant, and equal to the mean metallicity of the stars formed during the burst as calculated by the GALFORM model.

(c) Young stars and Molecular Clouds: Stars are assumed to form inside the molecular clouds, and then to escape on a timescale t_0 (see Sec. 2.5.2 and Eq. 2.22). We allow t_0 to take different values in normal disks and in bursts. In the case of non-bursting galaxies, star formation is going on in clouds throughout the disk, and young stars are assumed to become distributed throughout the disk after they escape. In the case of bursting galaxies, stars are assumed to be forming only in clouds in the burst region, and to become distributed throughout the burst region after they escape. Once the burst has ceased, these stars are assumed to become part of the bulge.

(d) Dust abundance: The dust grain model is described in Sec. 2.4. As for the dust abundance, the dust/gas ratio δ is assumed to be proportional to the gas metallicity, with a value $\delta = 1/110$ for $Z = Z_\odot = 0.02$ (Sec. 2.4.4). Thus, the total dust mass in the galaxy scales as $M_{dust} \propto M_{gas} Z_{gas}$.

The radiative transfer through the dust, dust heating and reemission are calculated as described in Sec. 2.5. In summary, with these improvements our model is now *multicomponent* as far as both the stellar mix as a function of time and the geometry are concerned.

Practical and computational aspects

(1) The starburst model: The star burst galaxy model is characterized by the parameters of the underlying galaxy and of the burst itself, i.e. the total mass of gas converted into star M_{burst}, the time at which the burst started t_{burst}, the star formation timescale τ_{*burst} and burst scale-radius r_{burst}.

In our spectrophotometric code the starburst region is a disk with axial ratio 0.5 and half mass radius 10% of that of the parent galaxy. All of the previous stellar activity of the normal disk is assumed to become part of the bulge. This means that the major mergers that trigger bursts are also assumed to destroy any pre-existing disk and rearrange the stars into a spheroid. This model is very crude and a three component solution (bulge, disk and nuclear activity) should be more suitable. But at present it is adequate since it provides the possibility of testing the spectrophotometric results quite easily.

For practical reasons, the star formation in a burst is assumed to be truncated at a time $5\tau_e$ after the burst began, where τ_e is the exponential decay time in the burst defined in Sec. 6.2.1, i.e. after 99% of the gas in the burst has either been converted into stars or blown out of the galaxy by supernova feedback. At this time, the remaining gas and dust in the burst region are assumed to be dispersed. Star formation then starts again in a normal galactic disk surrounding the bulge, if one has formed by cooling of halo gas since the major merger that triggered the burst.

(2) Computational aspects: To properly compute dust extinction and emission in this disk+bulge geometry in a reasonable CPU time, we optimized the angular and radial grids that define the galaxy volume elements. Since the gas is always in a disk component, we adopted a θ grid suited for disks, i.e. finer near the equatorial plane, as a function of the disk flattening, i.e. of the ratio z_d/R_{gal} of the disk scaleheight to the galaxy radius (the latter defined in Sec. 2.5.1). The best radial grid was obtained by merging one suited for bulges, dominating the inner part, with one for disks. Both were obtained by imposing $\rho(r_i)/\rho(r_{i+1})$ =const, with $\rho(r)$ given by a King and an exponential profile respectively. This yields a radial array dependent on *scale–radius*$/r_{gal}$, with *scale–radius* equal to core or disk scale–radius r_c and R_d (see also App. A.3).

Moreover, to cope with the huge number of model runs, the computing time was speeded up by avoiding a bottleneck of the code, namely the line integrals of gas density between the galaxy volume elements. These were computed just once and stored for sets of compatible models (see App. A.5).

Choice of parameters in GRASIL

We chose values for the free parameters in the GRASIL model based on a variety of observational data for galaxies in the local universe. For some of the parameters, these

choices were made by trying to match model predictions to the observational data, as is discussed in more detail in the relevant sections of this chapter. Table 6.2 lists the values we adopted for our standard model. We now summarize the reasons for these choices:

- ϵ_{*burst}: this is chosen mainly so as to reproduce the bright end of the IR luminosity function, which is dominated by bursts triggered by galaxy mergers (Sec. 6.7.4). A secondary constraint is to try to reproduce the relation between L_{IR}/L_{UV} and total luminosity or UV slope β observed for starburst nuclei (Sec. 6.5.1). The value controls both the luminosity and lifetime (and thus number density) of starbursts.

- $\chi = r_{burst}/r_{bulge}$: the choice of this is mainly based on the observational fact that starburst regions are generally much smaller than the galaxy as a whole. The value controls the amount of extinction of starlight from bursts by the diffuse ISM.

- z_d^*/R_d^*: for normal disks, we choose a value to match the typical observed values for local $L \sim L_\star$ spiral galaxies and also to try to match the observed difference in extinction between edge-on and face-on spiral galaxies (Sec. 6.4.2). Apart from the inclination test, most predicted properties are insensitive to z_d^*/R_d^*, as the net dust extinction only depends on z_d^*/R_d^* for galaxies seen nearly edge-on, $\cos i \lesssim z_d^*/R_d^*$. The choice of z_d^*/R_d^* for starbursts is based on observational indications that they are only moderately flattened.

- $z_d(dust)/z_d^*$: this parameter has a significant effect on how much of the starlight is absorbed in the diffuse medium. From observations of our own galaxy, it is known that the scaleheight of stars increases with the age of the stellar population, being comparable to that of the gas for the youngest stars, so that there is no unique value for the ratio $z_d(dust)/z_d^*$. In practice, we are particularly interested in having a realistic estimate of the extinction in the UV, both because it is strongest there and because this is an important source for dust heating. Therefore we choose $z_d(dust)/z_d^* = 1$ to match what is seen for the young stars.

- f_{mc}: this can be estimated observationally from the ratio of molecular to atomic hydrogen in galaxies, since in normal spiral galaxies, most of the hydrogen in molecular clouds is in H_2, while most of the intercloud medium is atomic HI. We have chosen f_{mc} to match the typical H_2/HI ratio for $L_\star$ spirals found by Sage (1993). Much larger values significantly reduce the extinction in the diffuse ISM.

- m_{mc},r_{mc}: the predicted SEDs depend on the ratio m_{mc}/r_{mc}^2, i.e. the optical depth of clouds (see Secs. 2.5.2 and 4.1). Thus m_{mc} has been chosen to match typical giant molecular clouds in our and nearby galaxies, while r_{mc} is basically chosen based on the results of Sec. 4.3 of the fit of GRASIL model to observed SEDs of 3 nearby spirals.

- t_0: this is a very important parameter in the model, since it is this that mainly controls how much of the radiation from young stellar populations is absorbed by dust. For normal spirals, our choice is essentially an average of the values found in

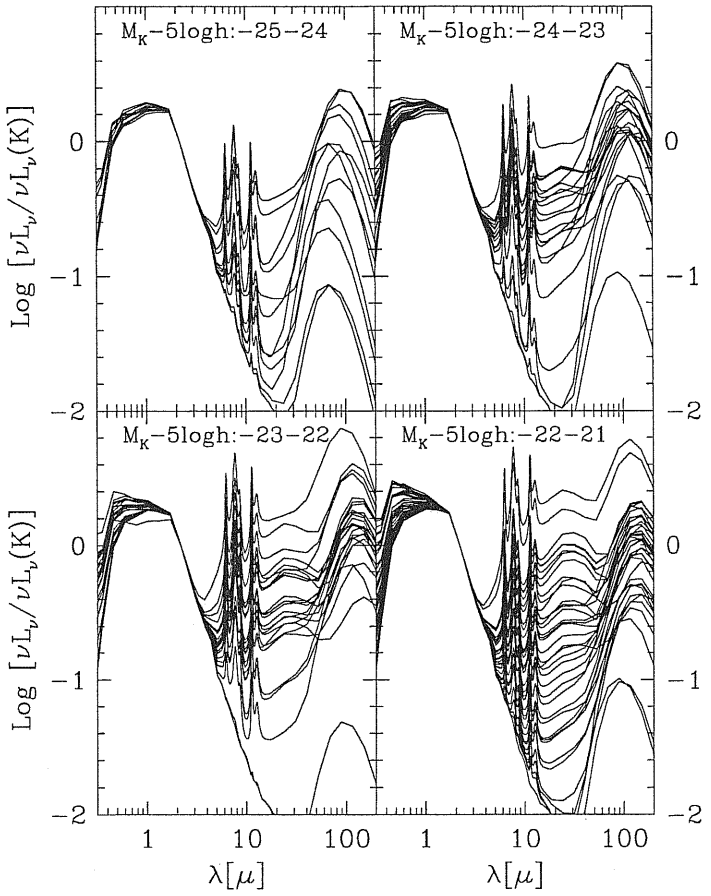

Figure 6.2: A plot of synthetic SEDs for face-on spiral galaxy models. Fluxes are normalized to the K-band and models are binned in K-band absolute magnitude, as indicated in the corresponding panels.

Sec. 4.3 from detailed fits to 3 nearby spirals. For starbursts, the value we choose is based mainly on the comparison with properties of UV-bright starbursts in Sec. 6.5.1. Our standard value is significantly smaller than those found from fitting the 3 nearby starbursts in Sec. 4.2. However, the geometry we assume here for starbursts is different and in any case, the 3 starburst galaxies considered in Sec. 4.2 may not be representative of the whole population.

6.4 Comparison with observations of spiral galaxies

In this section, we compare the model predictions for disk galaxies with observed properties of nearby spirals.

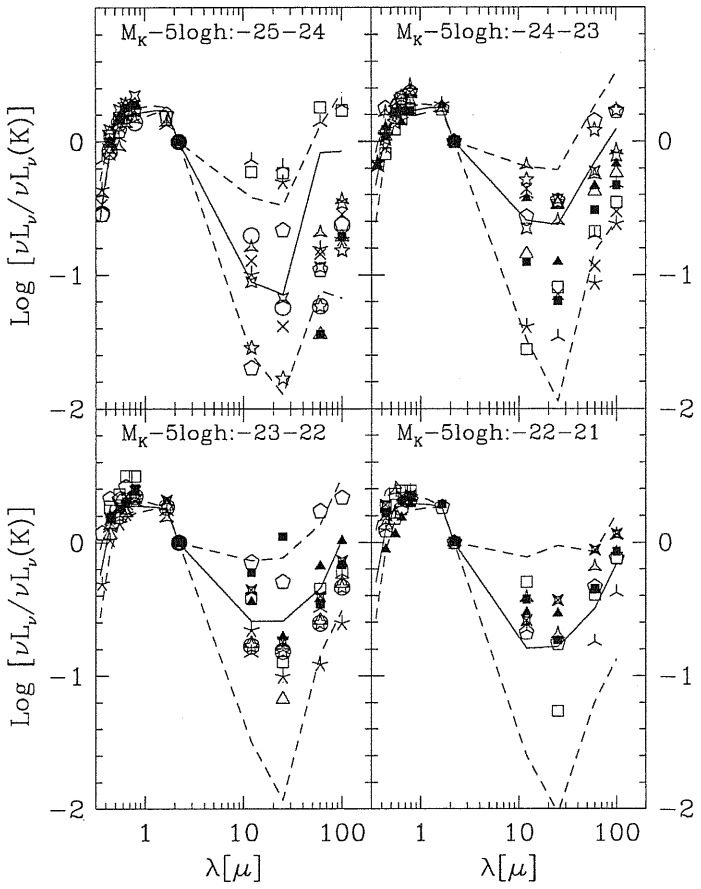

Figure 6.3: The models of Fig. 6.2 are compared with the observed SEDs of a sample of face-on galaxies within the same K luminosity bins. The sample is from de Jong & van der Kruit (1994). The SEDs are obtained by combining broad band colors from de Jong & van der Kruit (1994) with IRAS observations (Saunders 1997). Fluxes are normalized to the K-band. For the models, the median and the lower 10% and upper 90% percentiles are shown.

RC3 T	Morph. type	B/T
-5	E0	1.00
-3	S0-	0.59
-2	S0	0.58
-1	S0+	0.56
0	S0/a	0.51
1	Sa	0.35
2	Sab	0.33
3	Sb	0.22
4	Sbc	0.18
5	Sc	0.10
6	Scd	0.04
7	Sd	0.02

Table 6.3: Conversion from RC3 type T, morphological type and bulge over total B band ratio B/T.

6.4.1 SEDs of face-on spirals

In order to test the predicted optical through far-IR SEDs of our model galaxies, we compare to the broadband SEDs of a complete sample of nearby spiral galaxies. The sample is that of de Jong & van der Kruit (1994), and consists of a diameter-limited sample of 86 nearly face-on, disk-dominated galaxies. de Jong & van der Kruit (1994) measured luminosities of these galaxies in the BVRIHK bands, and we have supplemented these with U-band fluxes from the literature and IRAS $12, 25, 60, 100\mu$m fluxes from Saunders (1997). All of this data is collected together in Table 6.4.

In order to perform a meaningful comparison with the data, we first extracted from the models those with bulge to total light ratio B/T typical of spiral galaxies. According to Table 6.3 the value that separates early type galaxies from spirals is B/T = 0.5 in B band. Models with B/T $\leq$0.5 were subsequently binned in different K-band luminosity ranges (where dust effects are minimized) and compared to the observed galaxies in the same luminosity range. Luminosities of the galaxies were derived from the distances in Table 6.4.

In Fig. 6.2 the synthetic broadband SEDs of face-on spiral galaxy models are shown. These are compared with observations Fig. 6.3. The range in infrared fluxes covered by the observed SEDs is fairly large when compared to that in the optical bands. In any given absolute magnitude interval, there is a wide distribution of gas content causing the above dispersion. The same is true for the models: the dust content and temperatures in models of the same magnitude range can be very different, determining a dispersion in the infrared fluxes comparable to the observed one. Therefore the dust model is able to reproduce fairly well the observed shape of the optical to FIR SEDs.

6.4.2 The global extinction in spiral galaxies

The distribution and effects of dust within spiral galaxies is still a matter of debate. There have been many attempts to measure or constrain the total dust extinction in

disks, using a variety of techniques, for instance from the inclination dependence of magnitudes or colours (e.g. de Vaucouleurs et al. 1991, Giovanelli et al. 1995), from fitting detailed models of the star and dust distributions (e.g. Kylafis & Bahcall 1987), and from the ratio of FIR to UV luminosities (e.g. Xu & Buat 1995, Buat & Xu 1996, Wang & Heckman 1996). In general, different techniques have given somewhat different answers.

de Jong (1996c) analysed the colour profiles in the de Jong & van der Kruit (1994) sample of face-on spiral galaxies using combined stellar population and dust models (including dust scattering). The galaxies of this sample show a typical colour variation $\Delta(B-K) \lesssim 1$ mag over five scalelengths, from the center to the outskirts. He finds that, while the $B-K$ colour variation could be reproduced by an exponential dust distribution with a high central face-on optical depth, $\tau_V^0 \gtrsim 10$, this model does not simultaneously reproduce the observed colour variations in other bands (V,R,I and H). Instead, he finds that the observed colour gradients are best explained as a combination of stellar age gradients and moderate dust extinction ($\tau_V^0 \lesssim 4$). Models with a high central dust optical depth are not able to reproduce the observed trends, even when combined with age gradients.

Xilouris et al. (1999) have estimated dust extinctions by fitting detailed models of the star and dust distributions to the observed surface brightness distributions of edge-on spiral galaxies, in the B, V, I, J and K bands. Their dust models include scattering. For six edge-on Sb-Sc spirals with luminosities in the range $-17.5 > M_B - 5\log h > -19.0$, they find the mean central optical depth is < 1 in all optical bands (e.g. $\langle \tau_V^0 \rangle = 0.54$, with a dispersion $\sigma = 0.23$), suggesting that typical spiral galaxies are transparent when viewed face-on.

Fig. 6.4 shows the distribution of the face-on B-band central optical depths for Sb-Sc galaxies from our model in the K luminosity range -18 $\geq$ M_K-5log(h) $\geq$ -21. We separated the model galaxies according to the morphological type as reported in Table 6.3. Almost all the Sd galaxies have face on $\tau_B \leq 1$, with a mean $< \tau_B > \simeq 0.55$ and a $\sigma \simeq 0.5$. The distribution flattens significantly when we consider galaxies of Sc type with $< \tau_B > \simeq 0.9$ and $\sigma \simeq 0.7$. Finally Sb galaxies show a similar mean value but a narrower dispersion, $< \tau_B > \simeq 0.9$ and $\sigma \simeq 0.4$. These values compare well with the observed ones, indicating that the predicted central column density of dust is in fair agreement with what is observed.

As a further test of the models, we consider the dependence of the net extinction A_λ^{i-0} (i.e. extinction relative to the face-on view) on the inclination angle i at which a galaxy is viewed. This has been considered in many papers using different methods, most recently by Tully et al. (1998). They measure the dependence of $B-K$, $R-K$ and $I-K$ colours on galaxy inclination at a given K-band luminosity, the K-band being chosen to minimize extinction effects. They have a complete sample of spirals covering a large range in luminosity, $-18.5 \gtrsim M_K - 5\log h \gtrsim -24.5$. They find a strong luminosity dependence: the net B-band extinction between edge-on and face-on galaxies is about 2 mag for the brightest galaxies in their sample, and almost negligible for the faintest ones.

Tully et al. (1998) adopt the standard empirical description for the net extinction

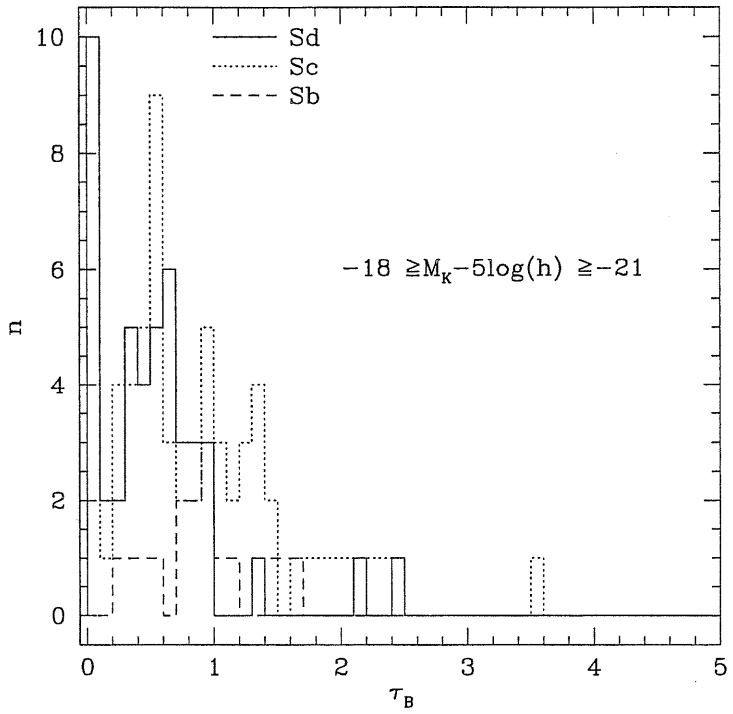

Figure 6.4: Distribution of the B central face-on optical depth in our model galaxies in the K luminosity range -18 $\geq$ M_K-5log(h) $\geq$ -21. Models are separated according to the morphological type as given in Table 6.3).

as a function of inclination i:

$$A_\lambda^{i-0} \equiv m_\lambda(i) - m_\lambda(0) = \gamma_\lambda \log(a/b) \tag{6.14}$$

where γ_λ is a function of the passband. The axial ratio a/b is assumed to be related to the inclination angle i by

$$\cos\ i = \sqrt{\frac{(b/a)^2 - q^2}{1 - q^2}} \tag{6.15}$$

where $i = 0$ for a face-on system, and q is the axial ratio of a galaxy viewed edge-on.

To compare our models with the observations, we plot in Fig. 6.5 the difference between the total B magnitude at inclination i and the corresponding face-on magnitude, as a function of $\log(a/b)$ for a sample of model galaxies. We use Eq. 6.15 to convert from the model inclination angle to the axial ratio, assuming $q = 0.1$, equal to the ratio z_d/R_d we have adopted in our galaxy models. We considered only models corresponding to the morphological types Sb-Sc, and four ranges in K-band luminosity corresponding to those chosen by Tully et al. (1998) and indicated by the different symbols in the figure. The model galaxies approximately follow the linear dependence on $\log(a/b)$ assumed in the observational parameterization, Eq. 6.14, but with slopes γ_B that are somewhat smaller at a given luminosity than Tully et al. (1998) infer from the observations. For instance, for the luminosity range $-23.0 < M_K - 5\log h < -22.0$, our models follow

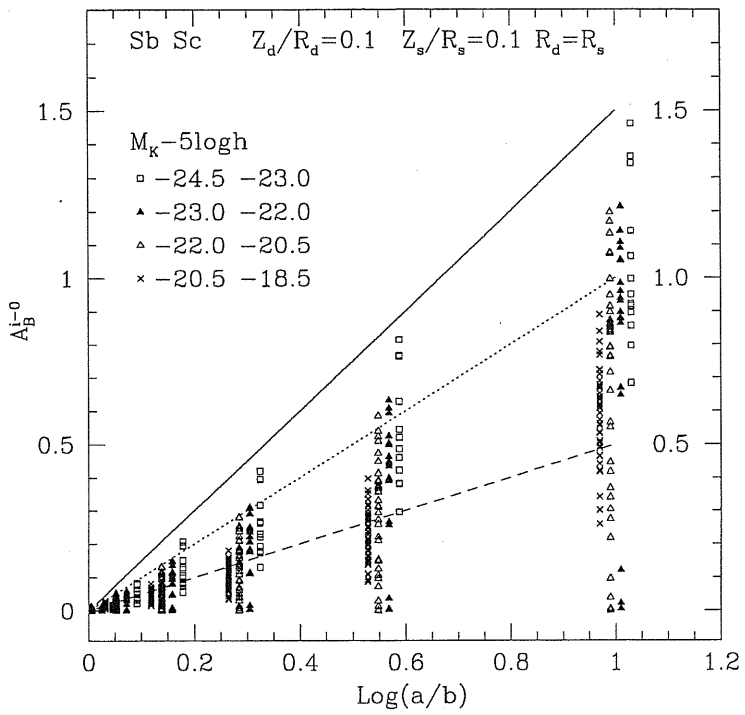

Figure 6.5: Relative edge-on to face-on extinction predicted by our galaxy models. The quantity $A_B^{i-0} = M_B(i) - M_B(0)$ is plotted against the axial ratio a/b, for the Sb-Sc models. The galaxies are plotted with different symbols in four K-band luminosity ranges, as detailed in the figure. At each inclination, the mean value is plotted for each luminosity range with a large symbol. The same galaxies are plotted seen at different inclinations. The 3 lines correspond to three different slopes $\gamma_B = 0.5$, 1 and 1.5. A small horizontal offset is applied to the different data in order to avoid confusion.

an average slope $\langle\gamma_B\rangle \approx 0.8$, while Tully et al. find $\gamma_B = 1.1 \pm 0.5$, after allowing for extinction.

The agreement is accetable; part of the discrepancy is certainly due to our simplified treatment of scattering by the dust. As outlined in Sec. 2.5.3, we use an approximation which is valid only for isotropic scattering. Test comparisons of our model with that of Ferrara et al. (1999) (Sec. 2.5.3), where the treatment of scattering is more accurate, show that this effect can account for about 0.2 mag of the differential extinction in the B band, for the brightest objects.

6.5 Starburst galaxies

Starburst galaxies are broadly defined as galaxies in which the current star formation rate is much greater than its time-averaged value, and the star formation timescale correspondingly much shorter than the age of the universe. Observationally, this definition covers a very wide range of objects, with a wide range of properties, from bursting

dwarf irregular galaxies to the ultra luminous IR galaxies found by IRAS (Sanders & Mirabel 1996). In our galaxy formation model, bursts are assumed to occur following major mergers of galaxies, producing elliptical galaxies from disk galaxies. For the ULIR galaxies, the link between the starburst activity and galaxy mergers is clearly established (e.g. Sanders & Mirabel 1996), while for low-luminosity starbursts, additional triggering mechanisms probably operate, which are not included in our model. In practice, a large variety of observational criteria have been applied to select samples of starburst galaxies, ranging from optical morphologies and spectra (Balzano 1983) to IR colours and luminosities (e.g. Armus et al. 1990, Lehnert & Heckman 1995). In the following sections we will compare the properties of starbursts predicted by our model with those of various observational samples.

Given the small size where, and the intensity with which, star formation activity takes place in these galaxies, it is conceivable that the environment is quite different from that of the normal spiral galaxies. Several parameters may affect the shape of the spectrum of a starburst galaxy, but the most critical are the escape time (t_0, see Table 2.2) with which newly born stars get rid of their parental cloud, and the ratio between the characteristic time of the star formation rate and the dynamical time ($\epsilon^{-1}_{*burst} = \tau_{*burst}/\tau_{bulge}$). From the fit of the SED of the 3 nearby starburst galaxies in Sec. 4.2 we found t_0 of the order of 20 to 50 Myr. This critical time is significantly larger than that adopted for the starburst sample. However the model used there is quite different from what we have adopted here, both from the point of view of the geometrical description and the population content. Furthermore those three objects may not be representative of the manifold of the observed starburst galaxies.

6.5.1 Properties of UV-bright starbursts

A large amount of work has been done on samples of *UV-bright* starbursts selected from the catalogue of UV spectra of star-forming galaxies of Kinney et al. (1993). The criteria for a starburst galaxy to appear in this catalogue are (a) that it has been previously classified as a starburst based on optical data, usually meaning that it has a compact optical morphology and strong optical emission lines (but not be an AGN) (e.g. Balzano 1983); and (b) that it has been observed by IUE and had a high enough surface brightness within the IUE aperture to produce a reasonable quality UV spectrum. The catalogue is not in any sense statistically complete.

In this section we test whether our models are able to reproduce several relationships observed among these UV-bright starburst galaxies, namely the relations between the slope of the ultraviolet continuum (β), the relative IR to UV emission and the bolometric luminosity. Meurer et al. (1995,1997) explain the relation between L_{IR}/L_{UV} and β with a foreground screen dust geometry of varying E(B-V) but notice that the spread of the data around this relation, $\sim$ 0.4 dex, suggests a possible more complex dust distribution. The relation between the bolometric output and L_{IR}/L_{UV} is less tight and it is interpreted as indicating that the brightest starbursts are the most obscured by dust.

Both relations could result from a mixture of metallicity effects – the brightest galaxies are more obscured because their gas is more metal rich –, and age effects

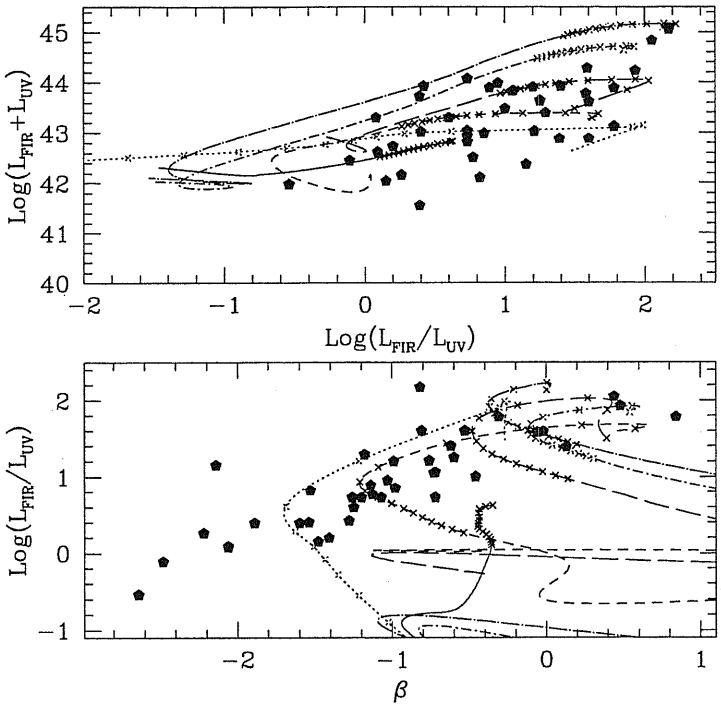

Figure 6.6: *Upper panel*: the bolometric luminosity of the models, $\mathrm{Log}(L_{IR}+L_{UV})$, versus the IR to UV luminosity ratio, $\mathrm{Log}(L_{IR}/L_{UV})$. *Lower panel*: the relation between L_{IR}/L_{UV} and the slope of the UV continuum β. Five different models are depicted in both panels. Crosses mark burst age in steps of 5 Myr. Filled symbols represent local starbursts (Heckman et al. 1998).

– the most powerful starbursts are older so that their UV spectrum is intrinsically redder. However the positive correlation between the UV slope and the strength of the absorption features of massive stars (Heckman et al. 1998), indicates not only that the powerful starbursts contain very young stellar populations, but that these are possibly more metal rich than those found among less bright (and UV bluer) galaxies.

The observational sample that we compare with is derived from Heckman et al. (1998). They selected 45 starburst and star-forming galaxies with high IUE spectral S/N ratio, from the original atlas of Kinney et al. (1993). These cover a range of UV luminosity $L_{UV} \equiv \lambda L_\lambda(1900\text{Å}) \sim 10^{6.5}-10^{9.5}L_\odot$, with a typical value $L_{UV} \sim 3\times10^8 L_\odot$. The IR luminosity L_{IR} used in Heckman et al. is in fact the "FIR" luminosity defined by Helou et al. (1988):

$$L_{FIR} = 0.65\nu L_\nu(60) + 0.42\nu L_\nu(100) \tag{6.16}$$

where $L_\nu(60)$ and $L_\nu(100)$ are the 60 and 100 μm luminosities measured by IRAS. L_{FIR} provides an estimate of the $40-120\mu$m luminosity. Only the nuclear part of the galaxy is involved in the star burst phenomenon. As a rough estimate, the activity is confined inside a region whose size typically fits into the IUE aperture (20"×10"), while the optical diameter of the underlying galaxy is typically of the order of few arcminutes.

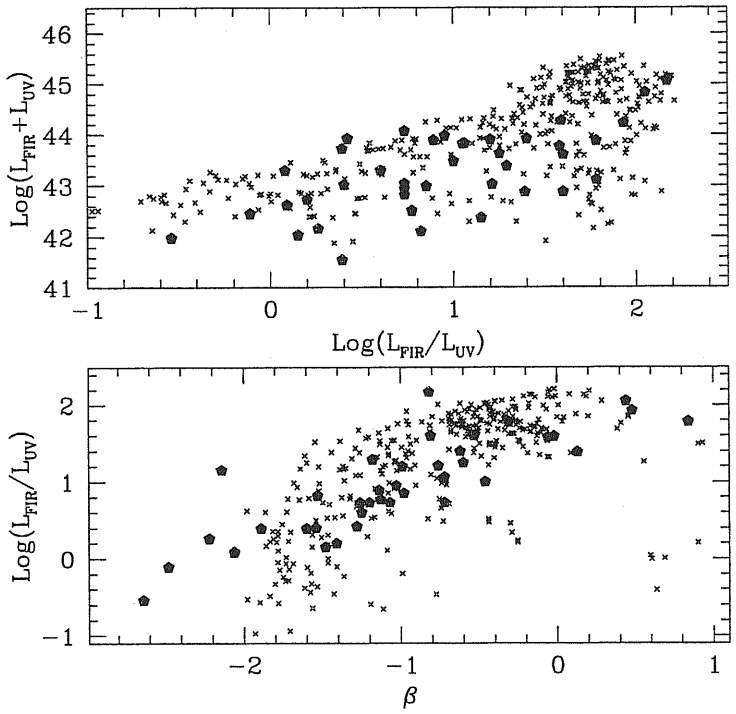

Figure 6.7: Same as in Fig. 6.6 but for a sample of randomly selected models (crosses) as described in the text. Filled symbols represent local starbursts (Heckman et al. 1998)

In order to perform a meaningful comparison of our staburst models with observations, we have to define a criterion able to isolate true starburst models, that share the observed properties of starbursts. A strong UV luminosity is not suited: in our models, where the SFR of the burst declines exponentially, the UV luminosity starts low, grows to a maximum as the dust exhausts, and then declines again as the burst extinguishes. Generally the UV luminosity peaks when the model is already quite old. Moreover, after a few e-folding times the SFR of the burst becomes comparable to that of the underlying galaxy. For this reason also some normal spirals follow the same relations of starburst models. Therefore, also the observed relationships between the bolometric luminosity and the spectral index β with the IR to UV luminosity ratio, cannot be used to discriminate between normal spirals and starburst models. This is illustrated in Fig. 6.6, where the behavior of some selected models is compared with observations.

The upper panel shows that at larger bolometric luminosities a higher fraction of energy is dust reprocessed. However this is true only for the first few Myrs; after a few 10^7 yrs, the models move toward lower values of the bolometric luminosity and L_{IR}/L_{UV} but roughly remain in the region of the observaed starburts, except for the very advanced phases. All our models begin their evolution with a IR to UV luminosity ratio greater than 1. The lower panel shows the relation between L_{IR}/L_{UV} and the slope of the UV continuum β. Again, the models are compatible with the observed relation only for the first phases of the evolution. After a few Myr they move away

almost orthogonally to the observed sequence. The brightest galaxies have null or even positive slopes β, but without a strong correlation. Less bright galaxies have initially a positive slope and then evolve toward negative values, roughly following the observed relation. The strong correlation observed between β and the oxygen content of the gas (Heckman et al. 1998) would suggest that the effect of reddening are mainly due to a different metal enrichment. Our models indicate that a significant spread around the mean relation could be due to evolutionary effects, in both the dust content and the age of the burst. This is even more apparent in the less bright objects.

Given the spread of the starburst models in the observational planes, we carried out a simulation of the observed sample by randomly selecting the age of the burst between 0 and a maximum value $t_{max} = 50$ Myr. A larger value would have increased the spread toward a higher value of β and a lower value of the IR to UV ratio. These randomly selected models are compared with the observed sample in Fig. 6.7.

A criterion that could be used to define starburst galaxies is to check for the presence of absorption features of hot stars. Indeed, following Kinney et al. (1993), starbursts are characterized by blue UV spectra and the presence of these features. Their UV slopes span the range $-1.85 < \beta < 0.26$, with an average of -1.25. Blue compact and blue compact dwarf galaxies, also present in the Heckman et al. sample, have generally a lower metallicity and a bluer UV slope, $-2.57 < \beta < 0.06$ with an average of -1.75. At present our code is not yet suited to predict detailed stellar absorption lines and nebular emission lines (for which work is in progress, see Sec. 2.7), so that we cannot investigate the whole observed parameter space of starburst galaxies. It will be very interesting to check whether in our models, after a few 10^7 yr, comparable to the dynamical time, the signatures of a nuclear burst of star formation have already disappeared. Possibly this will not be the case because the star formation rate decreased of only a factor e. In that case our assumption of a continuous decrease of star formation rate may be wrong and a better assumption could be a discontinous one.

6.6 The infrared fluxes, extinction, and star formation rates

6.6.1 The infrared colours

We have compared the infrared colors of our models with those of the IRAS bright galaxy sample (IRAS BGS, Soifer et al. 1989, Soifer & Neugebauer 1991), which is a complete sample flux-limited at 60μm.

Following Soifer & Neugebauer (1991), the total IR luminosity is defined as

$$L_{IR} = 0.97\,\nu L_\nu(12) + 0.77\,\nu L_\nu(25) + 0.93\,\nu L_\nu(60) + 0.60\,\nu L_\nu(100) \qquad (6.17)$$

where $L_\nu(12)$, $L_\nu(25)$, $L_\nu(60)$ and $L_\nu(100)$ are the luminosities measured through the 12,25,60 and 100μm IRAS bandpasses. L_{IR} provides an estimate of the total $8-1000\mu$m luminosity. For the models, the luminosities are calculated by convolving the SEDs with the response functions for the different IRAS bands, and applying the same definitions as for observed IRAS fluxes.

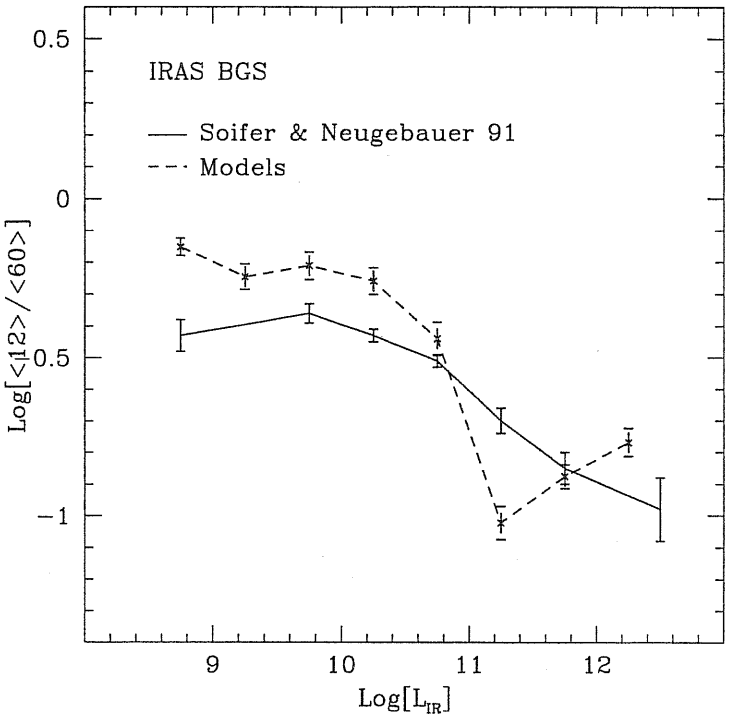

Figure 6.8: The mean 12–60 color (<Log $\nu L_\nu(12\mu\text{m})/\nu L_\nu(60\mu\text{m})$>) versus the total infrared luminosity, compared with the observational data from Soifer & Neugebauer (1991).

The behaviour of the mean 12–60 color versus the total IR luminosity of our models is compared with the observations in Fig. 6.8. For our models, where we combined both normal and starburst galaxies, the latter dominate above $10^{11}L_\odot$. The average value and the error on the mean have been obtained by properly weighting each galaxy in our mock catalogue in order to reproduce a flux limited sample. In the case of starbursts the models were also weighted by the fractional time they spend in a given total luminosity bin as described in Sec. 6.2.2.

In Fig. 6.9 the FIR colours $F_\nu/F_\nu(60\mu\text{m})$ of our starburst models are compared with those of 14 luminous infrared galaxies with IRAS and SCUBA fluxes (Lisenfeld et al. 1999). Five galaxies with only SCUBA upper limits were not included here. Only starburst models with $L_{IR} \geq 10^{11}L_\odot$ were selected, in order to follow the criteria of Lisenfeld et al. The error bar in the figure is the standard deviation of the model fluxes. The FIR shape of the emission of starburst models is in fair agreement with the observations, probing the reliability of our models down to the sub-mm range.

6.6.2 The extinction

An intriguing problem encountered in the study of properties of star forming galaxies is related to the nature of the observed extinction. Differences existing among the known

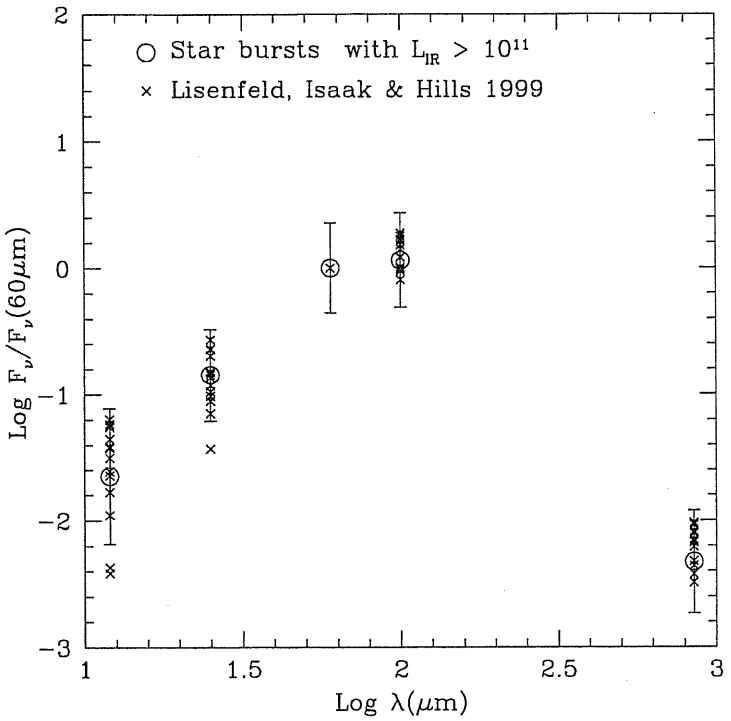

Figure 6.9: The average fluxes of our starburst models with $L_{IR} \geq 10^{11} L_\odot$ (empty circles) compared to the observational data (crosses) of 14 galaxies from Lisenfeld et al. (1999). All data are normalized to the 60μm flux.

extinction curves of the Galaxy, the Large Magellanic Cloud and the Small Magellanic Cloud below $\lambda \leq 2600$Åare often interpreted as being due to the different metallicity of these systems. Calzetti et al. (1994) analyzed the extinction properties in a sample of 39 starburst galaxies. From the analysis of their UV and optical spectra they conclude that the average attenuation law in these galaxies is characterized by a slope which is shallower than that of the Milky Way and by the absence of the 2175 Å feature. This is quite surprising because the typical metallicity of these systems is likely similar to that of the Milky Way, and suggests that the causes of the differences in the observed attenuation laws are complex and not simply related to the different metallicity.

Understanding the reason of this difference, whether it is due to a different nature of the dust grains responsible of the attenuation or to a complex geometry of emitting and absorbing regions, bears immediately on our ability of interpreting the high redshift observations of star forming galaxies.

Our adopted dust properties were chosen to reproduce both the observed extinction from the UV to the IR and the emission properties of the galactic diffuse interstellar medium (see Sec. 2.4). The resulting extinction law, characterized by a distinct 2175 Å feature, is shown as a solid line in Fig. 6.10. This is compared to the mean *attenuation law* obtained considering in the mock catalog (a) all the synthetic normal galaxies with E(B-V)>0.05, (b) all normal galaxies with E(B-V)>0.1, and (c) starburst models. Also

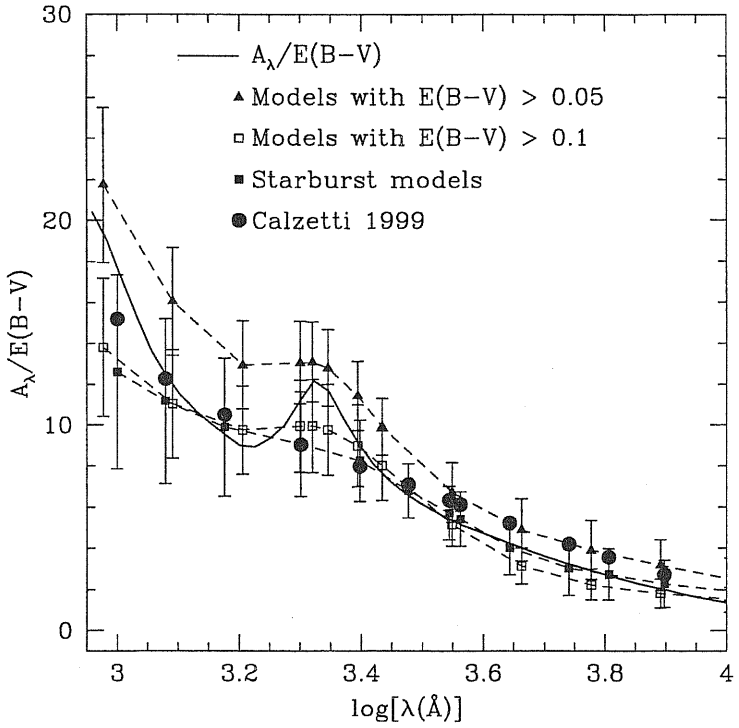

Figure 6.10: The extinction law resulting from the dust grain model adopted in this paper (solid line), and the resulting average attenuation after considering a) all models with E(B-V)> 0.05 (triangles); b) all models with E(B-V)> 0.10 (opens squares); c) starburst models (filled squares). Filled circles refer to the attenuation law derived by Calzetti (1999a).

the attenuation law derived by Calzetti (1999a) from the analysis of starburst galaxies is reported.

The attenuation is defined as the difference between the total magnitudes of the model computed with and without dust, as a function of wavelength. This quantity, normalized to the color excess $A_B - A_V$, depends only on the optical properties of grains in the very unrealistic (for a galaxy as a whole) *screen* geometry, in which a slab of dust is assumed to lie between the source and the observer. In our models we have instead a complex and wavelength dependent geometry, where the UV emitting regions are heavily embedded inside molecular clouds, while the older stars, mainly emitting in the optical and near infrared, are well mixed with the diffuse interstellar medium. This produce in general an attenuation law shallower than the extinction law and with a weaker 2175 Å bump. In particular, the similarity between the observed (Calzetti's) and the model curve for starbursts is striking.

Any difference between the attenuation law in our models and the galactic extinction law is a result of the geometry, since, as already remarked, our grain model nicely fits the latter. In particular the weakness of the 2175 Å feature can be understood as follows. In Fig. 6.11 we report examples of the attenuation laws for four normal galaxies in the

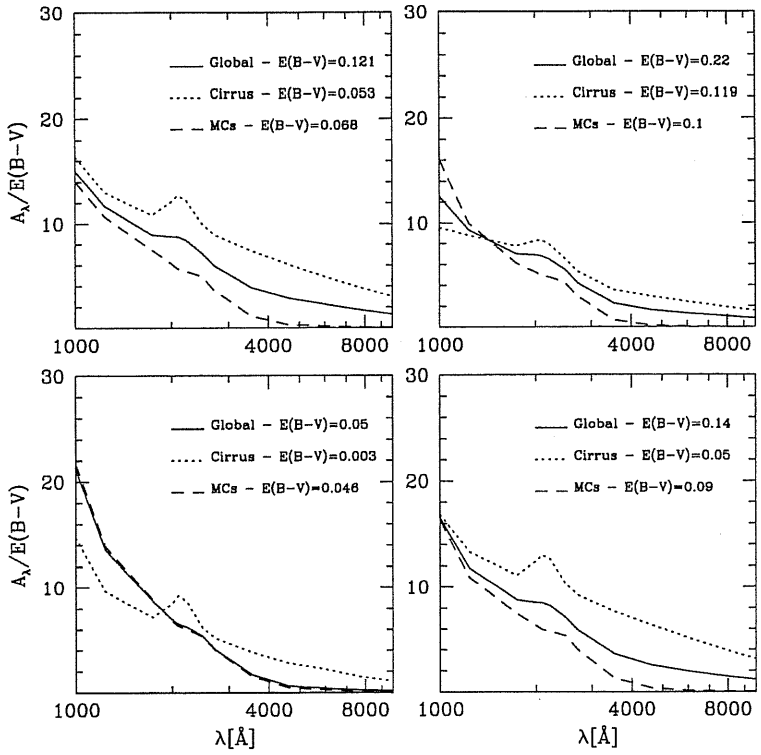

Figure 6.11: The attenuation laws for four normal galaxies in the mock catalog.

mock catalog. In each case the global attenuation law $(A_\lambda/E)_g$ is shown together with that in the MCs component $(A_\lambda/E)_{MCs}$ and in the cirrus $(A_\lambda/E)_c$. These three curves are related by:

$$(A_\lambda/E)_g = \frac{(A_\lambda/E)_{MCs}E_{MCs} + (A_\lambda/E)_c E_c}{E_g} \tag{6.18}$$

As can be seen, in the models the global attenuation law is strongly contributed, or even dominated, by the MCs in the spectral region around the feature. The latter has little to do with the optical properties of grains, in the sense that our MCs have usually a so large UV optical depth that the light from stars inside them is completely unseen. The wavelength dependence of the MCs attenuation law arises instead from the fact that the shorter the wavelength, the greater is the fraction of starlight which is produced by young generations, and on the other hand younger generations have a larger fraction inside the MCs (see Eq. 2.22). The additional attenuation arising in the cirrus component can imprint sometimes a weak 2175 Å feature, but this is not the case for starbursting objects, where the primary stellar light is dominated by very young populations.

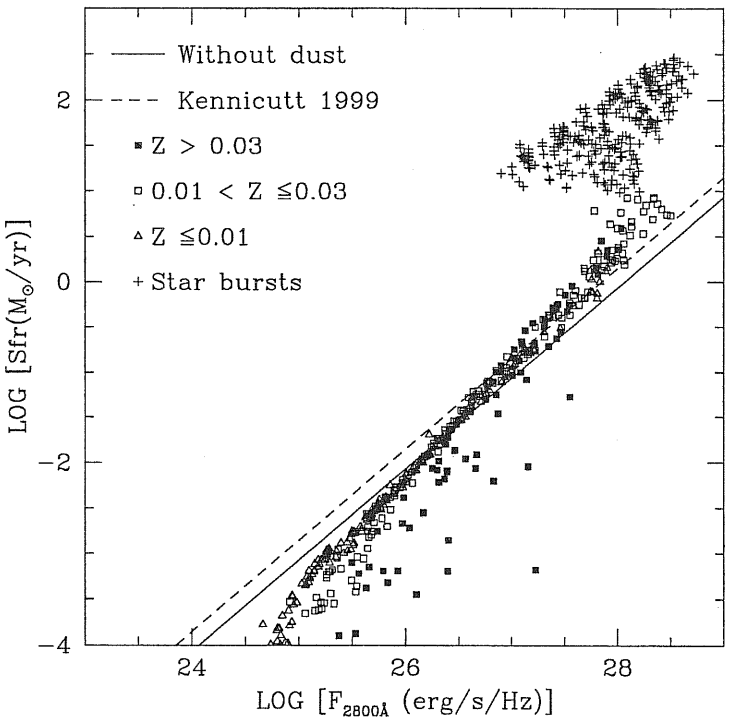

Figure 6.12: SFR versus UV flux at 2800 Å. Only models corresponding to spirals (B/T $\leq$ 0.5) and luminous starburst galaxies ($L_{IR} \geq 10^{11} L_{\odot}$) are plotted. Different symbols are used for the spiral galaxies depending on the metallicity of the gas. The solid line is the relation we obtain from the brightest models neglecting dust effects; the dashed line is the relation by Madau et al. (1998) rescaled by Kennicutt (1998), for a Salpeter IMF.

6.6.3 Star formation rate calibrations

The star formation rates in our mock catalogue span a wide range of values, from almost negligible ($\geq 10^{-4} M_{\odot}$/yr) to the those corresponding to luminous starburst galaxies ($\simeq 10^{2} M_{\odot}$/yr). In this section we consider the theoretical relations between the SFR and UV and IR luminosities.

Fig. 6.12 shows the relation between the UV luminosity at 2800Å and the SFR for our models. The location of starburst models is offset by more than one order of magnitude with respect to the average relation holding for normal spiral models. Furthermore their dispersion at a given luminosity is also quite large, though it decreases at increasing UV luminosity. If our models represent well the case of starburst galaxies, then we may conclude the SFR deduced from their UV flux is on the average underestimated by one order of magnitude and uncertain by another order of magnitude.

The SFR/L_{ν} ratio in our models without dust (solid line) is about 40% lower than the one by Kennicutt (1998) (dashed line). A part the different IMF, the offset is probably due to the fact that the relation by Kennicutt (1998) holds for ages larger than 10 Myr. The presence of significantly younger stellar populations in our models

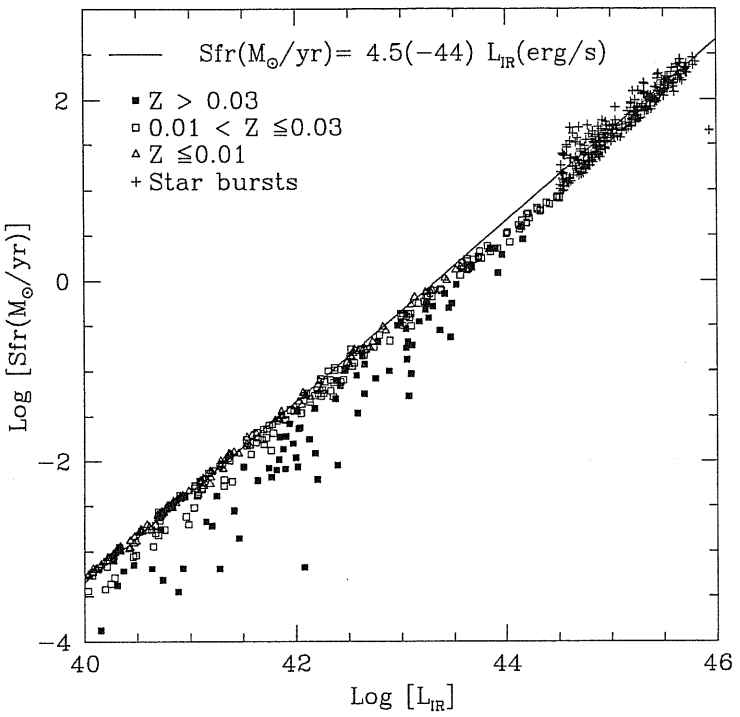

Figure 6.13: The relation between the IR luminosity and the SFR. The models are as in Fig. 6.12. The solid line is the relation by Kennicutt (1998).

lowers the SFR/L_ν ratio (Kennicutt 1998).

The effects of dust are visible above $L_{2800} \gtrsim 10^{27}$ erg/sec/Hz and are stronger at increasing luminosity, modifying the slope of the relation. Instead, below that value, dust effects become negligible. We suspect that the bending of the relation toward the faint luminosity end, is due to the contribution in the UV from old populations (e.g. Post-AGB) in the diffuse medium.

Fig. 6.13 shows the relation between the SFR and the estimated IR luminosity between 8μm and 1000μm (Eq. 6.17). The models are as in Fig. 6.12 and the solid line is the relation derived by Kennicutt (1998) for the starbursts, assuming that the bolometric output in a continuous burst of age between 10–100 Myr is completely reprocessed by dust. This relation well represents the bright ($L_{IR} \geq 10^{11} L_\odot$) starburt models, though a not negligible scatter still exists. In the case of normal galaxies the relation can be considered as an upper limit. The increase of the gas metallicity determines the dispersion of the models because of the adopted proportionality between metallicity and dust abundance.

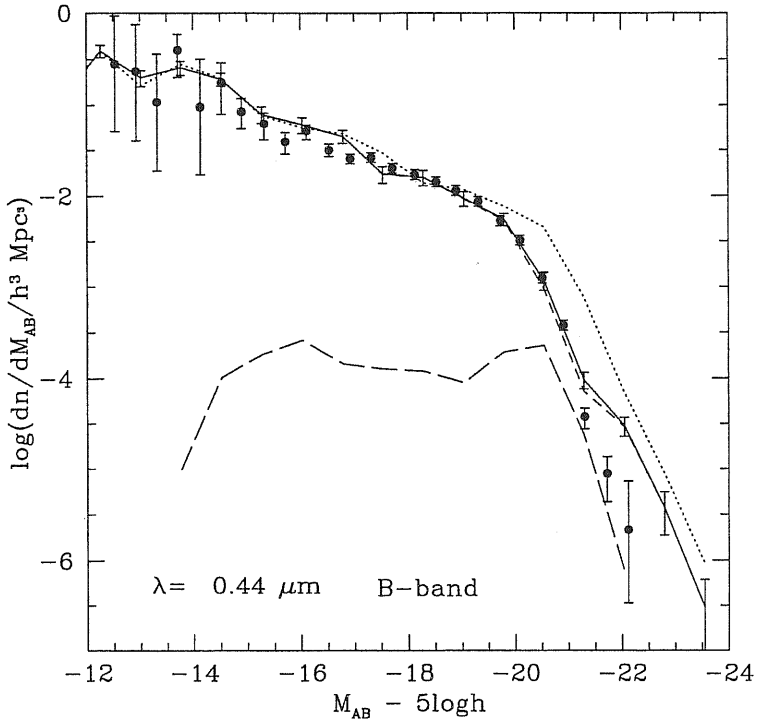

Figure 6.14: The luminosity function in the B-band (0.44μm), compared to observational data from Zucca et al. (1997). The solid line shows the total luminosity function including the effects of dust, while the short-dashed and long-dashed lines show the contributions to this from galaxies without and with recent bursts. The dotted line shows the luminosity function without dust. All magnitudes have been converted to the AB system, assuming $B_{AB} = B - 0.12$.

6.7 Galaxy Luminosity Function

6.7.1 Method

The luminosity function of galaxies is of fundamental importance. We calculate the galaxy luminosity function at different wavelengths by combining the model SEDs with the weights (described in Sec. 6.2.2) for the individual galaxies. For the normal galaxy sample we have, for the number density of galaxies per $\ln L$ at some wavelength λ

$$\frac{dn}{d\ln L_\lambda} = \frac{1}{\Delta \ln L} \sum_{|\ln L_i - \ln L| < \frac{1}{2}\Delta(\ln L)} n_i \tag{6.19}$$

where n_i is the number density for the ith galaxy, L_i is its luminosity at wavelength λ, the centre of the bin is at L and its width is $\Delta(\ln L)$. For the burst galaxy sample, we have to sum over the burst phase j also, giving

$$\frac{dn}{d\ln L_\lambda} = \frac{1}{\Delta \ln L} \sum_{|\ln L_{ij} - \ln L| < \frac{1}{2}\Delta(\ln L)} n_{ij} \tag{6.20}$$

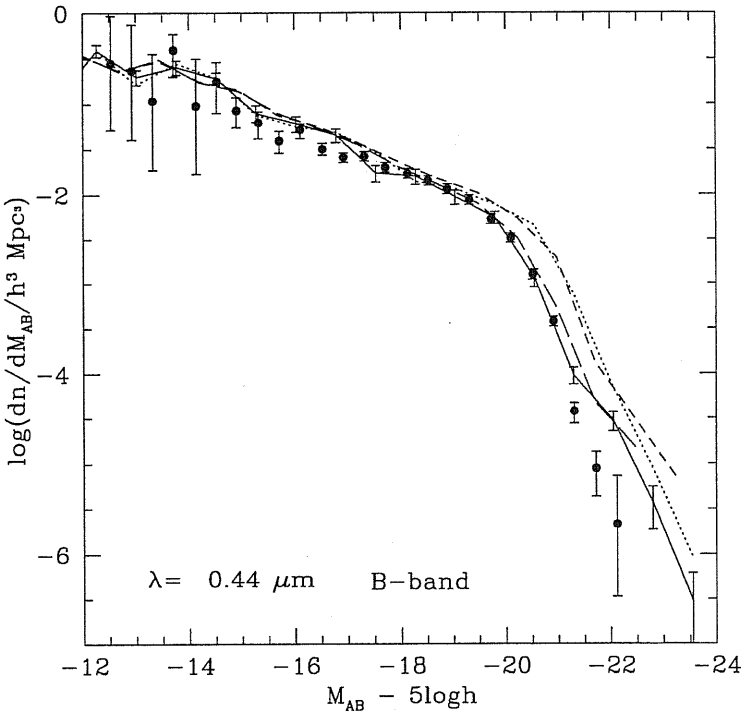

Figure 6.15: The luminosity function in the B-band, comparing the results from GRASIL to those computed by GALFORM using the Bruzual & Charlot (1999) stellar population models and the Ferrara et al. (1999) dust models. The solid and dotted lines show the GRASIL luminosity function with and without dust, while the long-dashed and short-dashed lines show the GALFORM luminosity function with and without dust.

where n_{ij} is the number density for galaxy i at evolutionary phase j, and L_{ij} its the luminosity at that phase.

6.7.2 Optical and Near Infra-Red

We begin by considering the nearby galaxy luminosity function at optical and near-IR wavelengths, where the emission is mostly from older stars and the effects of dust obscuration are generally modest. Fig. 6.14 shows the luminosity function in the B-band ($\lambda = 0.44\mu$m), compared to the observed luminosity function measured from the ESP redshift survey by Zucca et al. (1997). It can be seen that the predicted luminosity function agrees well with the observed one, except at the highest luminosities. Extinction by dust makes galaxies around 0.7 mag fainter on average, for bright ($L \gtrsim L_\star$) galaxies. We see that galaxies which have had recent bursts (defined as being in the last 1/20 of the age of the universe, i.e. 0.7 Gyr, do not dominate the luminosity function at any luminosity, when the effects of dust are included.

The B-band luminosity function is used as one of the primary observational constraints for setting the parameters in the GALFORM model, in particular, the parameters α_{hot} and V_{hot} controlling feedback and Υ which sets the fraction of brown dwarfs in

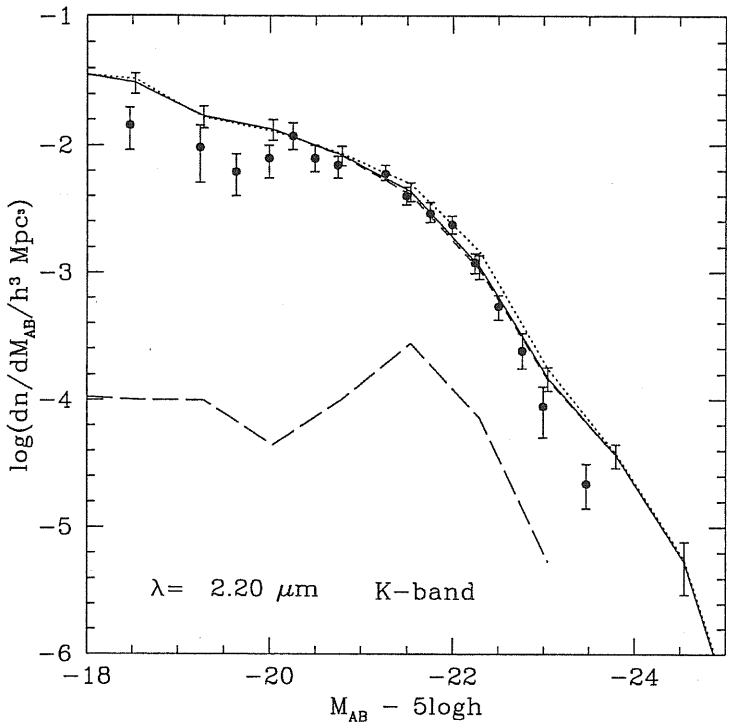

Figure 6.16: The luminosity function in the K-band (2.2μm), compared to observational data from Gradner et al. (1997). The line types are the same as in Fig. 6.14. All magnitudes have been converted to the AB system, assuming $K_{AB} = K + 1.87$.

the IMF. The good agreement with the observed B-band luminosity function is therefore not a surprise, but it was not guaranteed, since the stellar population and dust models used in Cole et al. are not identical to those used here. Cole et al. used the stellar population models of Bruzual & Charlot (1999), and calculated the effects of dust using the models of Ferrara et al. (1999). The stellar population model in GRASIL is based on similar stellar evolution tracks and stellar spectra to those used in the Bruzual & Charlot models, but the treatment of dust extinction is significantly different. The Ferrara et al. models assume that stars and dust are smoothly distributed, while in GRASIL a fraction of the dust is in clouds, and young stars are confined to these clouds. Fig. 6.15 directly compares the B-band luminosity functions, both with and without dust, calculated by GALFORM using Bruzual & Charlot and Ferrara et al. with those computed using the GRASIL stellar population/dust model. As can be seen, the agreement is very good, demonstrating the consistency of the procedure of using the galaxy formation parameters derived in Cole et al. The effects of dust computed using the two models are quite similar in the B-band, in spite of the differences in the star and dust geometry, because most of the B-band light is produced by stars which are old enough to have escaped from the clouds in which they formed, so in GRASIL the attenuation is due mostly to the diffuse component of the dust, which is modelled in a similar way to that in the Ferrara et al. models.

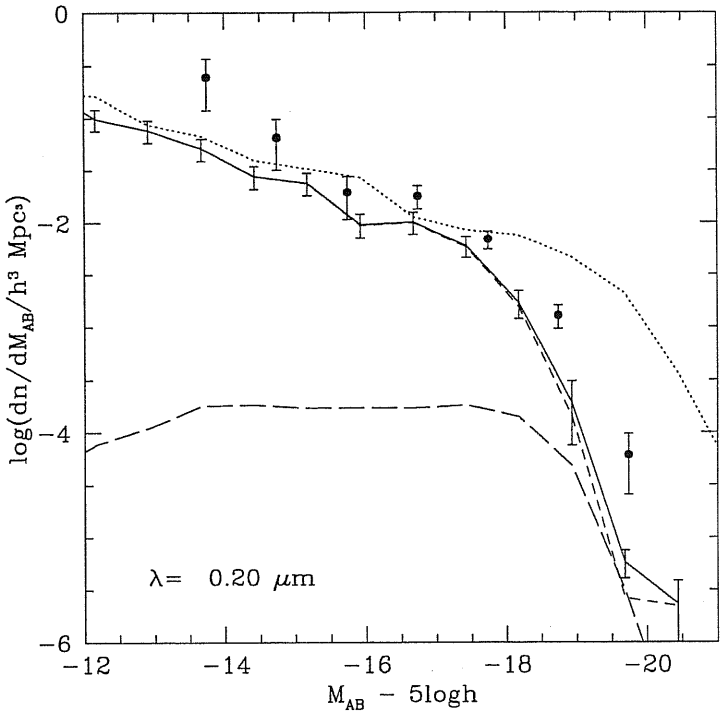

Figure 6.17: The far-UV 0.2μm luminosity function. The solid line shows the model prediction for the LF at $z = 0$ including dust, while the short-dashed and long-dashed lines show the contributions to this from galaxies without and with recent bursts. The dotted line shows the model luminosity function obtained if absorption by dust is neglected. The symbols with error bars show the observed 0.2μm luminosity function measured from a UV-selected redshift survey by Treyer et al. (1998). Magnitudes converted to AB system, assuming $m_{AB} = m_{2000} + 2.26$.

In Fig. 6.16, we compare the model and observed luminosity functions in the K-band ($\lambda = 2.2\mu$m). In this case, the effects of dust are very small, so the comparison is essentially independent of assumptions about dust. Again, the model agrees well over most of the luminosity range, as was also found by Cole et al. (1999). The contribution of galaxies with recent bursts is very small at all luminosities.

6.7.3 Far Ultra-Violet

In Fig. 6.17 we compare the predicted luminosity function in the far-UV ($\lambda = 0.2\mu$m) with that measured by Treyer et al. (1998) from a UV-selected redshift survey. This comparison has not previously been made for any semi-analytical galaxy formation models. The effect of dust are much larger than in the optical, as one would expect. In this case, the effects of the more realistic geometry for the stars and dust assumed by GRASIL compared to the Ferrara et al. models (clumpy rather than smooth distributions for the stars and dust) have a significant effect, since the stars that produce most of the UV light spend a large fraction of their lifetimes still in the molecular clouds in

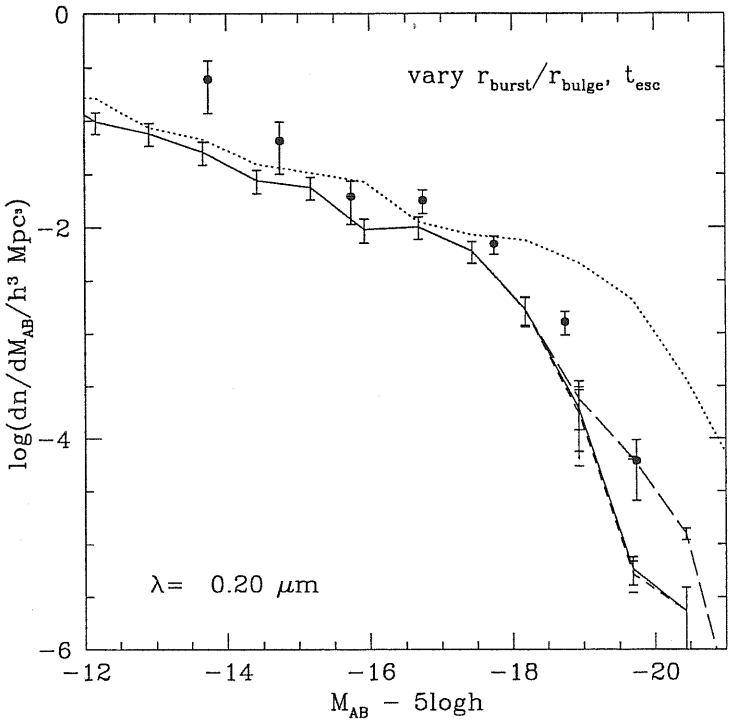

Figure 6.18: The effect of varying t_0 and r_{burst} on the far-UV 0.2μm luminosity function. The solid line is for our standard model (t_0 = 10 Myr in bursts, r_{burst}/r_{bulge} = 0.1), including dust. The short-dashed line shows the effect of increasing t_0 to 30Myr. The long-dashed line shows the effect of increasing r_{burst}/r_{bulge} to 0.5. The dotted line shows the LF without dust, which is the same in each of these cases. The observational data are as in Fig. 6.17

which they form, so that the mean extinction is larger than in the case of a smoothly distributed dust component with the same total dust mass. We also see that bursting and non-bursting galaxies contribute roughly equally at the highest luminosities. This result is however sensitive to the details of how bursts are modelled, since this determines what small fraction of the UV light escapes from currently or recently bursting galaxies. The agreement of the model with the observations is not quite as good as in the optical - overall, the predicted luminosity is somewhat lower than observed, once the effects of dust are included. However, part of this difference is because the observed luminosity function is based on a survey covering a significant range of redshift, with a mean $\langle z \rangle \approx 0.2$. The model luminosity function increases with redshift, so if the redshift range of the survey is taken into account, the model prediction would move closer to the observational data.

Fig. 6.18 shows the effect of increasing r_{burst}/r_{bulge} from 0.1 to 0.5. The effect of this is to reduce the optical depth in the diffuse component during bursts, allowing more of the UV light from bursts to escape, and increasing the LF at the highest luminosities. Fig. 6.18 also shows that increasing the escape time from clouds t_0 in bursts from 10

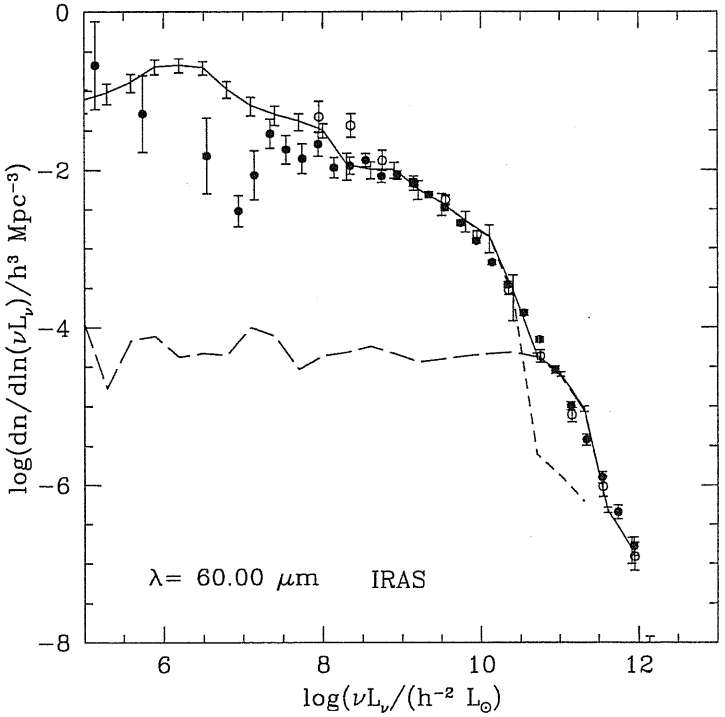

Figure 6.19: The 60μm luminosity function. The solid line shows the model luminosity function, while the short-dashed and long-dashed lines show the contributions to this from galaxies without and with recent bursts. The symbols with error bars show the observed 60μm luminosity function measured from galaxies observed by IRAS by Saunders et al. (1990) (solid symbols) and Soifer & Neugebauer (1991) (open symbols).

Myr to 30 Myr has negligible effect on the UV LF.

6.7.4 Mid and Far Infra-Red

In the mid- and far-infrared, the luminosity of galaxies is dominated by re-emission from dust. Using the GRASIL code, we can now directly predict the far-IR luminosities of galaxies from our galaxy formation model, and compare with observations. The luminosity functions of galaxies at 12, 25, 60 and 100μm have been measured using data from the IRAS satellite. IRAS was most sensitive at 60μm, so the IR luminosity function is best determined at this wavelength. Fig. 6.19 compares the predicted 60μm LF with observations from Saunders et al. (1990) and Soifer & Neugebauer (1991). The predicted luminosity function agrees extremely well with that observed, except at very low luminosities, where the measured LF is fairly uncertain. At luminosities above $\nu L_\nu \gtrsim 3 \times 10^{10} h^{-2} L_\odot$, the model LF is dominated by galaxies undergoing bursts triggered by mergers. This is in agreement with observations of ultra-luminous IRAS galaxies, which are all identified as recent mergers based on their optical morphology (Lawrence et al. 1989, Sanders & Mirabel 1996).

In Fig. 6.20 we show the effect on the predicted 60μm LF of varying the parameter

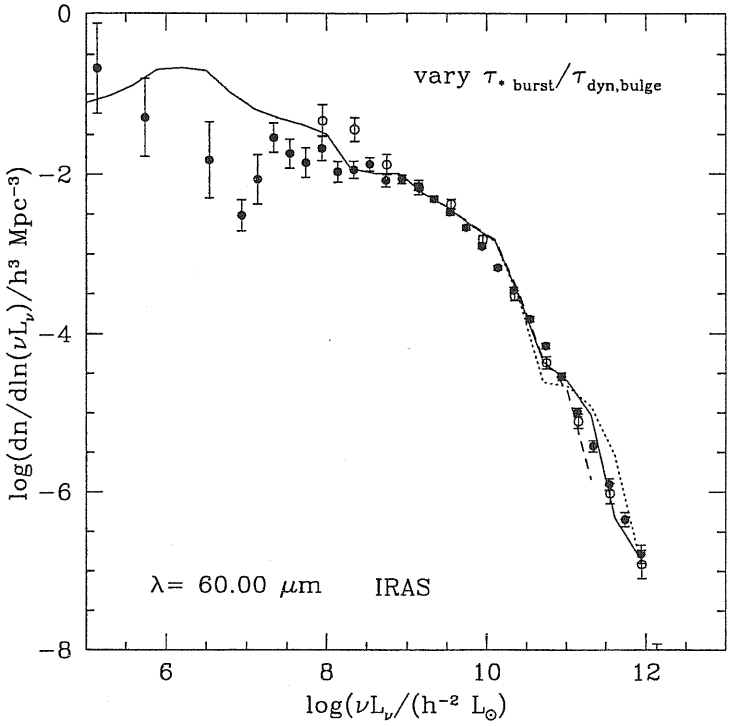

Figure 6.20: The 60μm luminosity function, showing the effect of varying the burst timescale: $\tau_{*burst}/\tau_{dyn,bulge} = 1$ (dotted), 2 (solid), 4 (dashed). The observational data are as in Fig. 6.19.

ϵ_{*burst}, which relates the star formation timescale in bursts to the dynamical time of the bulge (Eq. 6.6). Unlike the other parameters in the GALFORM model, Cole et al. (1999) did not try to choose a best-fit value, because the observational data in the optical and near-IR that they compared with were not sensitive to its value (in fact, the Cole et al. results were calculated assuming $\tau_{*burst} = 0$). However, the far-IR LF is sensitive to the burst timescale for the most luminous bursts, so we can use this as a constraint on ϵ_{*burst}. Fig. 6.20 shows predictions for $\epsilon_{*burst} = 1, 0.5, 0.25$, corresponding to $\tau_{*burst}/\tau_{bulge} = 1, 2, 4$ respectively. Increasing ϵ_{*burst} means bursts are more luminous, but last for a shorter time, and so have a lower number density. This trend is seen at the high-luminosity end of the 60μm LF, which is dominated by bursting galaxies. A value $\epsilon_{*burst} = 2$ seems to fit somewhat better than higher or lower values, so we adopt this as our standard value.

We have also calculated the luminosity functions at 12, 25 and 100 μm, and compared them with the observational data from Soifer & Neugebauer (1991). The results are shown in Fig. 6.21. It can be seen that the predicted luminosity function agrees well with the measured one in each case.

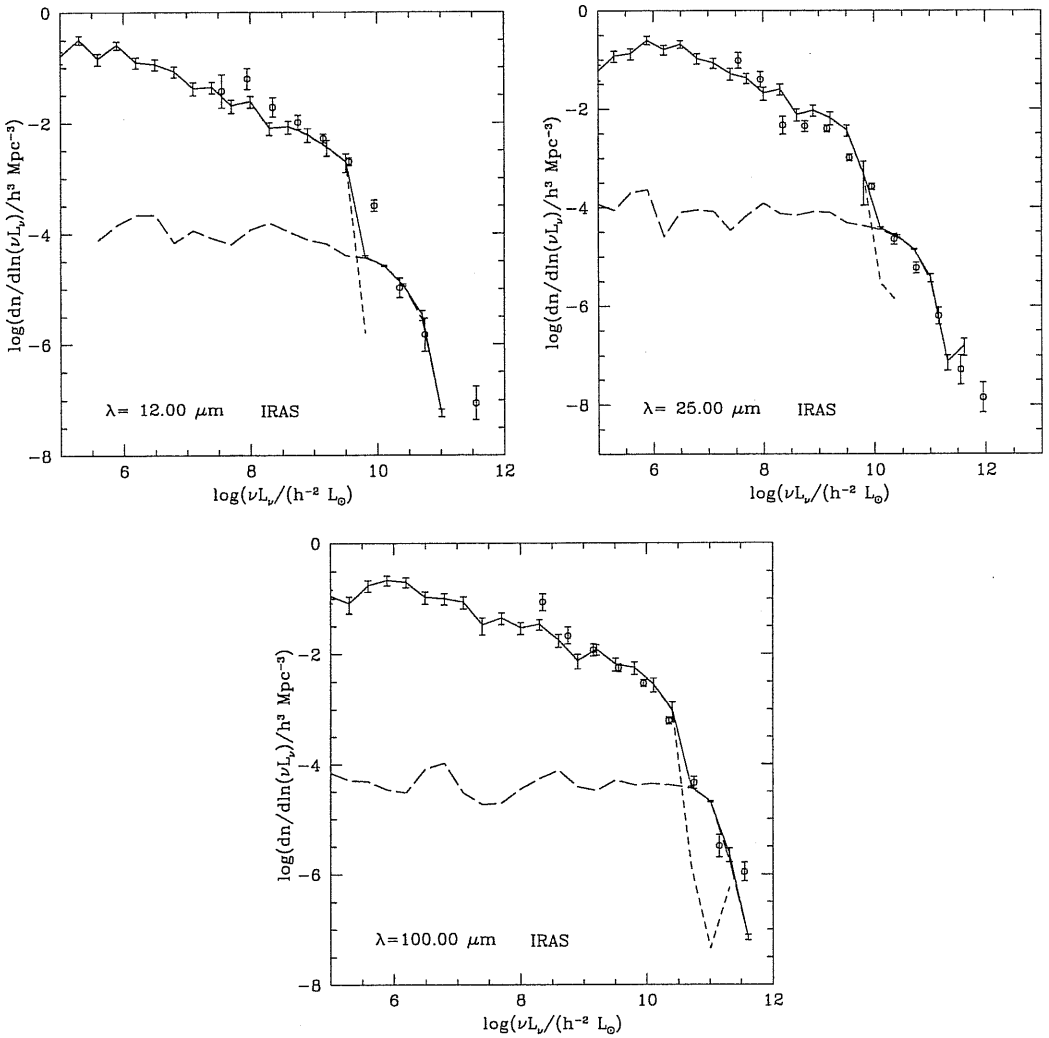

Figure 6.21: The 12, 25 and 100 μm luminosity functions, compared to observational data from Soifer & Neugebauer (1991).

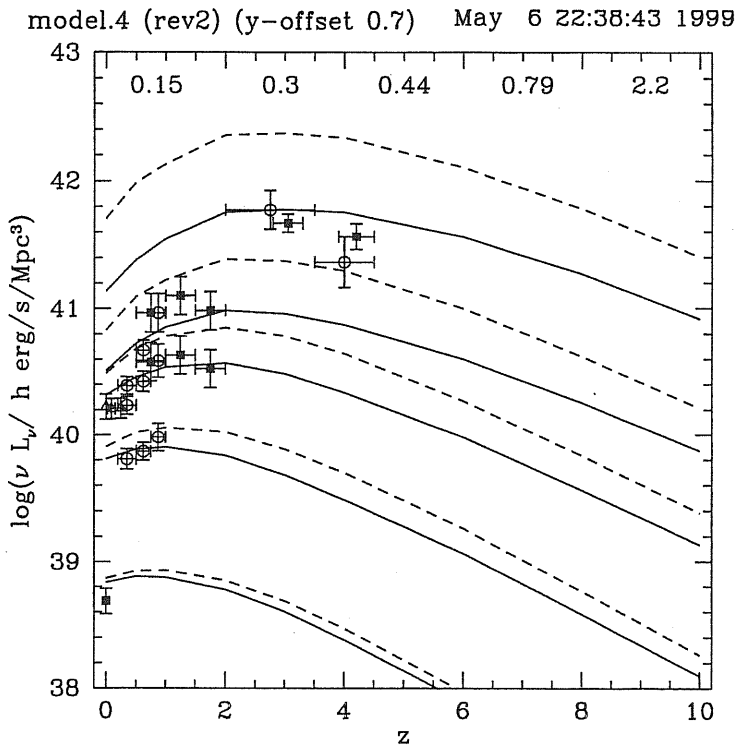

Figure 6.22: Luminosity density evolution at different wavelengths compared with a compilation of observational data by Madau et al. (1998). Dashed lines are without dust, solid include dust. An artificial offset has been applied to each wavelength for clarity, and from top to bottom the curves refer to 0.15, 0.3, 0.44, 0.8 and 2.2 μm.

6.8 Preliminary results for the high–z universe

In this section we will compare the results of the combined GALFORM+GRASIL model to observables concerning the high redshift universe. These are in general more integrated pieces of information, such as number counts and integrated background. Nevertheless, as we shall see, they put interesting contraints on the model.

Fig. 6.22 shows the evolution of the luminosity density at different wavelengths. Dashed lines are without dust, solid include dust. Curves for different wavelengths have been shifted relative to each other for clarity. The comparison is made with a selection of observational data, mostly from the compilation by Madau et al. (1998). We find a reasonable agreement if dust effects are included, otherwise the mismatch would be in general rather large. The only exception is the K–band, whose curve is almost unaffected by extinction.

Fig. 6.23 compares the predicted integrated background to available data. Observations are well reproduced at all wavelengths. In Fig. 6.24 the contribution to the integrated background as a function of redshift is shown at some selected IR–FIR wavelengths, together with the redshifts below which 50% and 90% of the background comes. It is worth noticing that the typical source redshift contributing to the background is

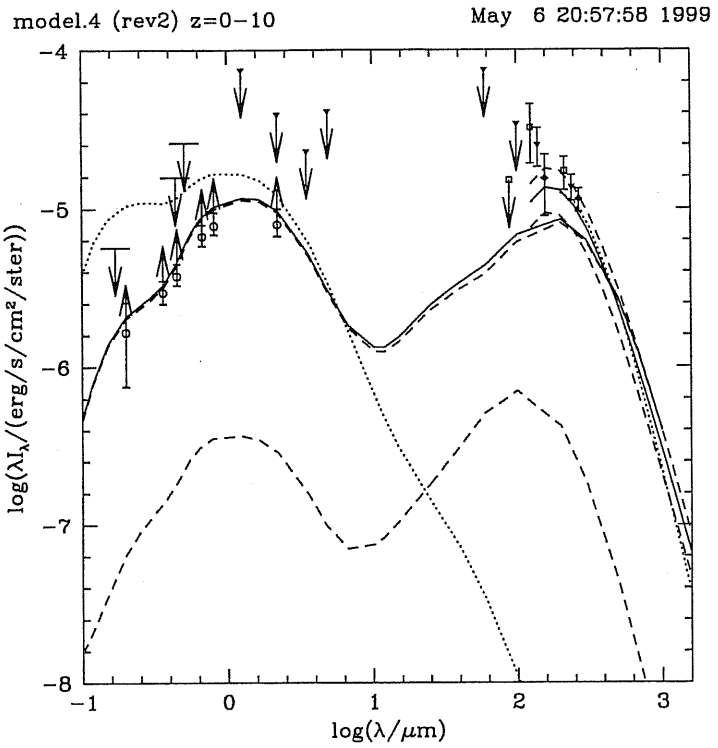

Figure 6.23: The predicted integrated background is compared to available data. Solid line is total including dust, dotted is total without dust, the two dashed lines are contributions of normal (higher) and burst (lower) galaxies.

similar to what has been measured so far, i.e. most of background coming from range $z = 1 - 3$.

Fig. 6.25 reports the number counts we predict at different wavelengths compared with the current available dataset. The 2.2 and 850 μm counts probe higher redshifts ($z \gtrsim 1$) than the 60μm IRAS and the 175μm ISO counts. The 850μm counts are too low, up to a factor $\sim 10 \div 30$ at the bright end, even though we match the corresponding integrated background, meaning that the sources are too faint.

This mismatch is the most serious and stimulating problem we have found from the combination of the semi–analytical scheme, as implemented in GALFORM, with the treatment of dust reprocessing of GRASIL. We guess most of the problem resides in the former, since most of the energy produced by stars at high redshift is already emitted in the IR–FIR regime. The possible contribution from AGNs is probably not dominating (Granato et al. 1997, Almaini et al. 1999). The only adjustment viable in the treatment of dust is a less steep decline of the optical efficency at long wavelengths, which has been suggested at least for a few objects (e.g. Arp 220, see Sec. 4.2). This would enhance the emitted luminosity above $\sim$ 200 μm without significant effects in other regions of the SED. But this seems at the moment a rather arbitrary assumption, at least for the whole population, and in any case would only alleviate the problem by a factor $\sim$ 3, leaving another factor $\geq$ 3 to be explained. Moreover, without some other adjustements, the

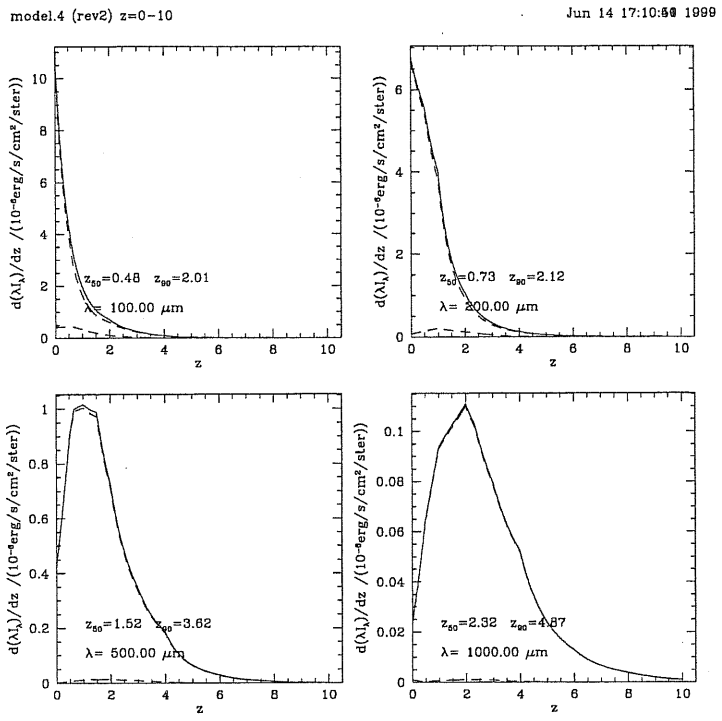

Figure 6.24: The contribution to IR-FIR integrated background as a function of redshift. Also, the redshifts below which 50% and 90% of the background comes are reported in each panel. Dashed lines as in Fig. 6.23.

background would then be overproduced. On the other hand, Figs. 6.23 and 6.24 show that we have more or less the correct amount of star formation at the correct redshift range. Thus the problem arises because most of the 850μm emission is contributed by many objects having a too low luminosity. It seems therefore unavoidable to change in some way the prescriptions for star formation in order to move most of the SF taking place within the redshift range $z = 1 \div 3$ into fewer but more luminous objects. Work is in progress to pick out possible physical mechanisms to obtain this.

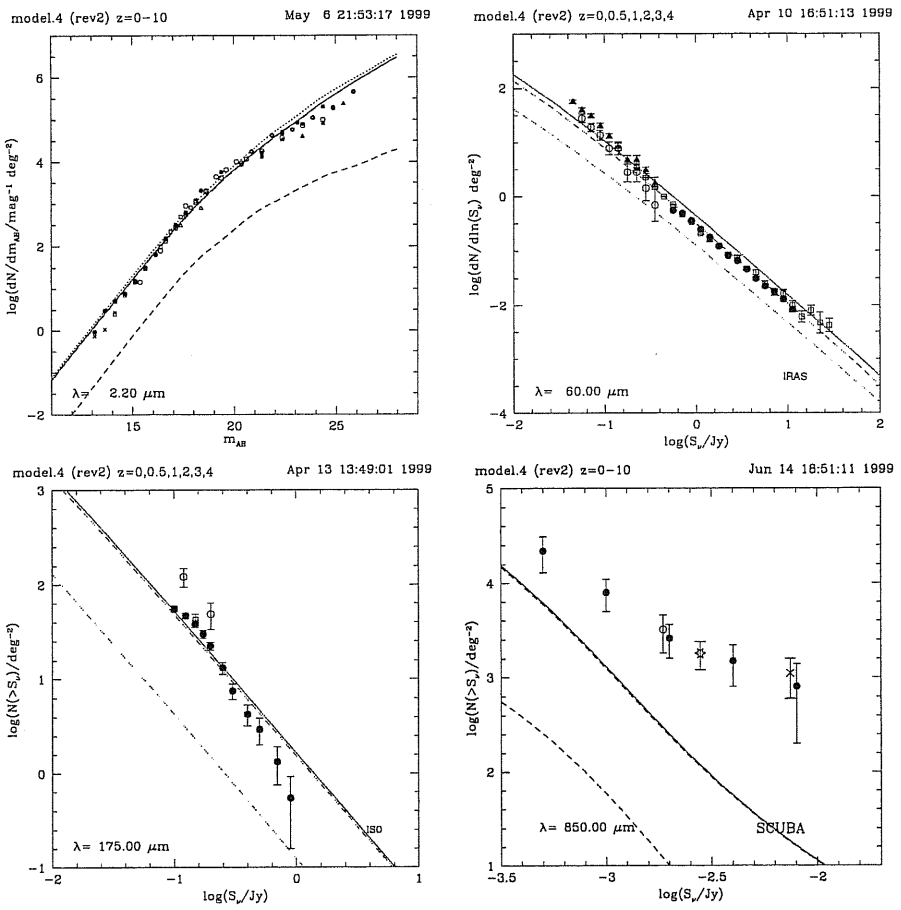

Figure 6.25: Number counts at 2.2, 60, 175 and 850 μm. The dotted line in the 2.2μm number counts plot is for counts without including dust. The two dashed lines in all the plots show the contribution from normal, always dominating, and burst galaxies.

Table 6.4: The de Jong & van der Kruit spiral galaxy sample

de Jong & van der Kruit (1994) performed accurate surface photometry in the B,V,R,I, H and K passbands of a complete diameter-limited sample of 86 disk-dominated galaxies, with axial ratio larger than 0.625. This paper provides total apparent magnitudes in these bands. R. de Jong provided us with other relevant data, namely Galactic foreground extinction(from RC3), distance (from the recession velocity, corrected for Virgo flow and assuming H_0=100 Km/s/Mpc) and morphological type (from RC3) in electronic form as described in de Jong (1996b). We supplemented the de Jong & van der Kruit sample with IRAS observations of the same galaxies provided by Saunders (1997, private communication). IRAS fluxes were recalculated from the original scans, assuming that the objects have the same extension at 12, 25 and 100 as at 60μm. Finally we added to the sample the U magnitude obtained from the NED archive. Table 6.4 collects the above data. Column 1 is the UGC number, columns 2 to 12 are the optical (U,B,V,R,I), near infrared (H,K) and IRAS fluxes, all expressed as $\log f_\nu$ (erg/cm^2/s/Hz). Column 13 indicates the RC3 T-type, column 14 the Galactic foreground extinction in the B band, and column 15 the distance. The reported fluxes are already corrected for Galactic extinction by assuming the B extinction quoted in the table and the Cardelli et al. (1989) reddening law.

Ned	U[a]	B[b]	V[b]	R[b]	I[b]	H[b]	K[b]	12μm[c]	25μm[c]	60μm[c]	100μm[c]	T[d]	A_B^e	D[f]
89	-	-1.36	-1.13	-1.01	-0.92	-0.65	-0.71	-0.20	0.11	0.98	1.18	1	0.16	47.12
93	-	-2.01	-1.82	-1.62	-1.53	-	-1.58	-1.26	-1.42	-0.49	-0.15	8	0.17	51.16
490	-	-1.74	-1.46	-1.32	-1.16	-	-0.95	-1.77	-0.99	-0.19	0.25	5	0.06	47.01
508	-1.81	-1.35	-1.05	-0.90	-0.77	-	-0.56	-0.72	-0.89	0.03	0.55	2	0.23	48.19
1305	-1.58	-1.37	-1.07	-0.91	-0.70	-	-0.62	-0.24	-0.71	-0.12	0.51	4	0.24	27.89
1455	-	-1.55	-1.30	-1.19	-1.04	-	-0.94	-1.26	-1.06	-0.45	0.25	4	0.40	52.23
1551	-	-1.71	-1.52	-1.43	-1.34	-	-1.28	-0.84	-1.49	-0.24	0.26	8	0.36	28.01
1577	-	-1.82	-1.51	-1.34	-1.26	-	-1.13	-1.05	-0.51	0.08	0.42	4	0.17	54.13
1719	-	-1.91	-1.64	-1.48	-1.37	-	-1.20	-	-	-1.21	-0.26	3	0.24	82.50
1792	-	-1.88	-1.60	-1.53	-1.44	-	-1.22	-1.39	-1.36	-0.30	0.11	5	0.33	51.04
2064	-	-1.89	-1.60	-1.49	-1.31	-	-1.23	-1.34	-0.65	-0.17	0.19	4	0.40	43.44
2081	-	-2.15	-2.01	-1.95	-1.71	-	-1.79	-	-1.08	-0.65	-0.29	6	0.04	26.23
2124	-	-1.73	-1.40	-1.14	-0.95	-	-0.90	-1.24	-	-0.53	-0.02	0.50	0.08	26.23
2125	-	-1.91	-1.63	-1.50	-1.43	-	-	-1.19	-0.86	-0.20	0.26	5	0.39	53.18
2368	-2.09	-1.76	-1.55	-1.42	-1.29	-0.93	-1.07	-0.50	-0.29	0.63	0.92	3	0.41	36.20
2595	-2	-	-1.52	-1.39	-1.22	-0.89	-	-0.65	-1.05	0.02	0.55	4	0.44	58.88
3080	-	-1.87	-1.68	-1.54	-1.41	-1.16	-1.35	-0.97	-1.04	-0.32	0.17	5	0.30	35.25
4126	-2	-1.61	-1.43	-1.28	-1.11	-0.89	-1.02	-0.68	-1.43	-0.29	0.32	3	0.14	49.74
4256	-1.83	-1.61	-1.48	-	-	-0.91	-0.91	-0.31	-0.04	0.67	1.02	5	0.16	54.36
4308	-	-1.58	-1.41	-1.30	-1.13	-0.98	-1.10	-0.54	-0.64	0.08	0.49	5	0.14	37.15
4368	-	-1.77	-1.60	-1.48	-1.29	-	-1.25	-0.74	-0.15	-0.28	0.24	6	0.08	40.24
4375	-	-1.62	-	-1.29	-	-0.83	-0.98	-1	-1.10	-0.13	0.37	5	0.16	22.55
4422	-1.87	-1.46	-1.34	-1.10	-0.98	-0.68	-0.70	-0.76	-	0.05	0.52	4.50	0.12	44.63
5103	-1.81	-1.45	-	-1.25	-	-0.71	-0.86	-0.55	-0.71	0.24	0.63	3	0.07	39.05
5303	-	-1.23	-1.04	-0.90	-0.78	-0.53	-0.64	-0.73	-0.39	0.30	0.78	5	0.08	16.50
5510	-	-1.29	-	-1.06	-0.96	-	-0.87	-0.72	-0.25	0.51	0.85	4	0.07	15.79
5554	-	-1.48	-	-1.12	-0.98	-0.66	-0.81	-0.67	-0.50	0.23	0.56	1	0.10	14.96
5633	-2.36	-2.01	-1.84	-1.72	-	-1.38	-1.68	-0.63	-	-0.49	-0.66	8	0.13	16.38
5842	-	-1.33	-	-1.08	-0.96	-0.69	-0.85	-0.54	-0.53	0.24	0.74	6	0.07	15.31
6028	-	-1.62	-1.52	-1.43	-1.34	-1.21	-1.25	-1.21	-3	-0.02	0.30	3	0.02	13.65
6077	-	-1.51	-1.33	-1.18	-1.05	-	-0.94	-	-	-	-	3	0	17.45

Table 6.4: Parameters of the observed spiral galaxy sample. *(a)* U: NED archive; *(b)* BVRIHK: de Jong & van der Kruit (1994); *(c)* IRAS 12, 25, 60, 100 μm: Saunders (1997); *(d)* T: De Jong 1996b; *(e)* A_B: De Jong 1996b; *(f)* D(Mpc): De Jong 1996b.

Ned	U[a]	B[b]	V[b]	R[b]	I[b]	H[b]	K[b]	12μm[c]	25μm[c]	60μm[c]	100μm[c]	T[d]	A_B^e	D[f]
6123	-	-	-	-	-	-0.41	-0.54	-	-	-	-	3	0	9.85
6277	-	-1.08	-	-0.81	-0.63	-0.45	-0.51	-	-	-	-	5	0	15.19
6445	-	-1.40	-1.21	-1.06	-0.86	-	-0.80	-0.72	-	-0.11	0.48	4	0	16.02
6453	-	-1.35	-1.06	-	-0.95	-	-0.84	-0.52	-0.47	0.41	0.87	4	0	15.31
6460	-	-1.11	-	-0.84	-	-	-0.62	-0.33	-0.27	0.64	1.05	4	0.02	15.19
6536	-	-	-	-	-	-	-1.13	-	-	-	-	3	0	71.69
6746	-2.26	-1.71	-1.45	-1.26	-	-0.85	-0.93	-1.89	-0.54	-0.46	0.11	0	0	71.10
6754	-2.15	-1.74	-	-1.35	-	-	-1.01	-1.27	-0.26	-0.38	-0.09	3	0	71.93
7169	-1.73	-1.39	-1.30	-1.14	-	-	-1.02	-0.43	-0.26	0.65	0.97	5	0.06	24.81
7315	-	-1.37	-1.16	-0.97	-0.78	-	-0.62	-0.41	-0.10	0.46	0.97	4	0.05	12.34
7450	-0.71	-0.41	-0.24	-0.10	-0.01	-	0.24	0.42	0.52	1.38	1.83	4	0.06	19.82
7523	-1.49	-1.08	-0.86	-0.72	-0.53	-	-0.40	-0.32	-0.35	0.12	0.65	3	0.03	12.23
7594	-	-0.57	-	-0.20	-	-	0.06	-0.75	-0.66	0.26	0.90	2	0.03	23.03
7901	-	-0.94	-0.75	-0.61	-0.46	-0.19	-0.33	-0.27	-0.03	0.77	1.21	5	0.03	6.17
8289	-	-1.30	-	-1.06	-0.92	-0.73	-0.85	-0.68	-0.24	0.74	1.03	4	0.01	35.97
8865	-	-1.42	-	-1.06	-0.95	-0.61	-0.76	-1.41	-1.96	-0.39	0.28	2	0	27.42
9024	-	-2.32	-	-	-2.08	-1.89	-2.09	-0.75	-	-1.14	-0.91	8	0.03	26.47
9061	-1.77	-1.19	-	-0.88	-0.63	-	-0.35	-0.94	-0.43	-0.12	0.39	4	0	56.62
9481	-	-1.69	-	-1.40	-1.29	-1.02	-1.17	-0.76	-0.56	-0.16	0.39	4	0	40.48
9915	-	-	-1.30	-	-1	-0.76	-0.90	-0.94	-0.66	-0.07	0.42	3	0.11	21.25
9926	-1.49	-1.20	-1.01	-	-	-	-0.55	-0.10	0.05	0.97	1.34	5	0.10	22.79
9943	-1.63	-1.26	-1.06	-0.92	-0.76	-0.53	-0.64	-0.46	-0.39	0.50	1	5	0.07	22.55
10083	-1.75	-1.27	-1.17	-1.04	-0.96	-0.63	-0.84	-0.55	-0.83	0.21	0.62	2	0.11	21.60
10437	-	-2.12	-2.07	-1.92	-1.78	-	-	-0.88	-1.46	-0.55	-0.35	7	0	29.67
10445	-	-1.59	-1.60	-1.54	-1.34	-1.34	-1.49	-1.68	-	-0.19	0.15	6	0.05	13.06
10584	-	-1.61	-1.43	-1.34	-1.13	-	-1.19	-0.67	-0.87	0.11	0.53	5	0	56.15
11628	-1.89	-1.34	-1.03	-0.91	-0.87	-	-0.57	-0.54	-0.76	-0.37	0.46	2	0.39	43.09
11708	-	-1.62	-1.42	-1.24	-1.10	-	-	-0.83	-0.58	-0.08	0.37	5.50	0.28	42.61
11872	-1.49	-1.08	-0.81	-0.68	-0.50	-	-0.41	-	-	-	-	3	0.25	13.77
12151	-	-2.06	-1.90	-1.96	-1.75	-	-1.69	-	-	-	-	10	0.21	18.64
12379	-	-1.67	-1.42	-1.20	-1.04	-	-0.93	-	-1	-0.36	0.11	4	0.31	63.98
12511	-1.99	-1.85	-1.62	-1.40	-1.23	-	-1.40	-1.26	-2.10	-0.08	0.30	6	0.12	36.56
12614	-	-1.38	-1.15	-1.04	-0.92	-	-0.82	-0.28	0	0.85	1.18	5	0.12	36.44
12654	-	-1.79	-1.55	-1.46	-1.33	-	-1.28	-0.62	-0.55	-0.18	0.34	4	0.09	41.78
12732	-	-2.19	-1.65	-1.31	-1.57	-	-	-	-1.55	-0.92	0.03	9	0.18	9.85
12754	-1.33	-1.06	-0.91	-0.79	-0.73	-	-	-0.54	-0.27	0.54	0.93	6	0.15	9.97

Table 6.4: *Continued*

Conclusions

The ongoing debate about the epoch, if any, of galaxy formation and evolution is beeing tackled in these last years from the cold side of the spectral region. The reason is the recognition that small solid particles, dust grains, formed by the aggregation of heavy elements ejected from stars into the interstellar medium, are able to set the energy balance of galaxies. The UV-optical stellar output is shifted into the IR-submm spectral range, this effect increasing with the strength of star formation in galaxies. In fact the study of the IR universe is unvealing most part of the star formation activity taking place in high-z to nearby galaxies.

This framework provides the starting point for the topics covered in this thesis: in order to investigate the properties of galaxies from their spectral energy distributions, we have developed a spectrophotometric model for galaxies based on detailed computations of dust effects on starlight. This has then been applied in different contexts to retrieve information on galaxies.

The main topics and results of this thesis are summarized below:

(1) We have developed a spectro-photometric self-consistent model for galaxies. The computation includes: (a) 3 different dusty environments (molecular clouds, diffuse ISM, AGB envelopes); (b) a dust model comprehensive of normal big grains, small fluctuating grains, PAH; (c) a realistic geometric distribution for stars and dust in the galaxy model, possibly with both a bulge and a disk component; (d) the radiative transfer of starlight through the different dusty media. The output, the UV to submm spectrum of galaxies, is further extended to the radio wavelegths, computed as a function of the supernova rate. The nebular emission is introduced at a preliminary stage

This model is suited to simulate galaxies of different types and in different evolutionary stages. Indeed, despite the many parameters and uncertainties introduced by the presence of dust, the constraints set by the impressive amount of data available for a number of nearby galaxies, allow to obtain fully consistent physical models describing the radiative outputs linked to star formation and evolution in galaxies. By reproducing the global SED of these nearby galaxies, we are able to provide estimates of star formation rates, masses in dust and stars and supernova rates in keeping with independent estimates coming from other observables. The high quality of the results obtained for local galaxies validates the use of our modelling to describe the evolution of high-z galaxies.

(2) We have applied our model to analyse a sample of K-selected bright early-type

galaxies in the HDF. From the fit to the available UV to near-IR stellar SED of these objects, we estimate the age of the bulk of their stars ($\sim$ 1.5 to 3 Gyrs) and the galactic masses ($\sim 10^9 - 10^{11}\ M_\odot$ already at $z \simeq 1$). We interpret the absence of objects at $z > 1.3$, that should be detectable during the star formation phase expected at these redshifts, as due to dust enshrouded starbursts occurring during the first few Gyrs of the galaxy lifetime. The contribution of these field early-type galaxies to the cosmic star formation rate is predicted: it exceeds the the global amount inferred from high-z dropouts, suggesting that for $z \gtrsim 1.5$ the direct estimate based on optical-UV measurements misses some light, if a subpopulation alone already exceeds the global estimated amount. This may be taken as an evidence that dust indeed played a role in significantly obscuring the active phase of star formation. If moderately true for the average gas-rich spirals, this might have been particularly relevant during the starburst events bringing to the formation of early-type galaxies. Indeed the prediction is close to the value estimated according to the metal abundance in the intracluster medium.

(3) A similar analysis, still at a preliminary stage, has been performed for a K-selected sample of late-type galaxies in the HDF. We find a strong degeneracy between the values of the star formation rate and of extinction based on the fit of the UV to near-IR SED alone. As expected, IR data points are necessary in order to set constraints able to break this degenaracy, always present whenever dust plays a role.

Despite the uncertainty in the spectral fits, we tried to infer the contribution of this population to the cosmic star formation history, as provided by the two most extreme solutions we find for each object. It seems that the total baryonic mass converted into stars is better constrained than the istantaneous star formation, since the two solutions give comparable results. The integrated star formation from this population appears to dominate over that from early-types below $z \sim 1$, due to their protracted SFR, while providing a comparable contribution at higher redshifts.

If this is the case, then the two populations of galaxies should contribute almost equally to the integrated background light, although in different bands. These issues have not been investigated yet.

(4) We have analysed the properties of local galaxies of different morphological type within the framework of the semi-analytic modelling technique, in which galaxies are formed from the hierarchical merging of subunits. The galaxy catalogues are provided by the GALFORM code and then GRASIL is run on them in order to compute the corresponding spectra. We find an overall good agreement when comparing normal and burst galaxy models with different observations: SEDs, extinctions and luminosity functions.

The preliminary results we obtained for high redshit synthetic galaxy catalogues have been presented. By comparing with number counts and integrated background in different bands we find an interesting problem in the deficiency, by a factor $\gtrsim 10$, of the 850μm model counts. This factor can be reduced at maximum by a factor ~ 3 with a shallower slope of the dust absorption efficiency in the submm. It seems therefore the cause is the lack of bright high-z IR galaxies, i.e. part of the star formation should be shifted from the too abundant low luminosity subunits into larger starforming objects.

(5) An interesting outcome of the above analysis for local galaxies is concerned with

the extinction properties of galaxies. Indeed we find that, in our model galaxies, the shallower slope towards the UV and the disappearance of the 2175 Å graphite feature in the attenuation law at increasing star formation rates, as compared to the galactic extinction curve, is the result of the complex and wavelength dependent geometry of our models.

Indeed, in the models, the global attenuation law in the UV is strongly contributed by the component in molecular clouds. The light from the UV emitting stars embedded within them is completely unseen due to the large optical depths, so that the behaviour of the feature in the attenuation law has little to do with the optical properties of grains. Moreover, the shorter the wavelength, the greater is the fraction of starlight coming from younger generations with a larger fraction inside MCs, determining a shallower slope. The additional attenuation of older stars arising in the cirrus component can imprint a weak 2175 Å feature, but this is not the case for starbursting objects, where the primary stellar light is dominated by very young populations.

(6) We have considered the best studied object among the so called extremely red objects, HR10, at z=1.44. From the fit to the available observations for this object, we infer a SFR $\sim 240 M_{\odot}$/yr. The value inferred by other authors, based on fits of the submm data of single temperature grey bodies with a dust efficiency slope of typically 1.5, is $\sim 10^3 M_{\odot}$/yr.

Our estimated value rests on the necessity of reproducing both a very strong UV-optical extinction, as required by the spectral shape in that region, and the submm data. Instead, for the FIR, where most of the reprocessed energy is emitted, only upper limits are available. It would be hard to hide much higher SFRs in the UV-optical and, moreover, to keep below the IR upper limits.

(7) A final comment concerns the outcomes of this thesis as far as the two opposite scenarii for galaxy formation, i.e. monolithic and hierarchical merging, are concerned. As discussed in the introduction, in the 'classical' picture for the formation of early-type galaxies, a relatively short hig-z epoch should exist, that should be observable in the IR due to dust reprocessing in strong starbursts. On the contrary no high-z big object is usually present in bottom-up theories.

At variance with what has been found by different authors for cluster early-type galaxies, we do not find a strictly coeval event of star formation for field early-type galaxies, even if the bulk of the stars in these galaxies is found to be already assembled by $z \sim 1$. We argue a set of dust-enshrouded merging-driven stabursts during the main star formation phase or assembly may hide the detection of higher redshift objects.

We suggest the strong decrease of the comoving mass density claimed by some authors for early-type field galaxies may be due to a misleading color classification, since we find rather blue colors for these galaxies, at variance with those expected for old and strictly coeval ellipticals.

By predicting local galaxies within the framework of hierarchical clustering with the semi-analytical technique, we are able to find a good agreement in all global observed properties of galaxies.

On the other hand, the predictions for high-z galaxies within this framework seem to require a substantial revision of the prescriptions for the dynamical assembly of stars,

in order to have some massive star-forming objects at high-z.

Therefore, the two extreme scenarii recalled above appear to be complementary but not exclusive each other. The reproduction of different available observations seems to require adjustements by both sides, that should make them converge. In fact this is expected, since, whatever is the approach used, it is tuned to converge to the same observations.

Strong improvements in our understanding of galaxies are coming from a better and deeper knowledge of the nearby and the high-z universe through the ISO shallow (ELAIS) and deep surveys and from SCUBA surveys with the related optical identifications. Further extraordinary improvements will be provided by planned missions such as SIRTF, FIRST and NGST. They are expected to detect high-z galaxies, respectively from their far-IR emission, if star-forming, and from their near-IR redshifted starlight. The large ground-based arrays like MMA will reach unprecedented sensitivities and angular resolution in the mm band. All these instruments, together with the ground based 10 meter class telescopes, are complementary to cast light on the problem of galaxy formation.

Appendix A

Details of model computations

A.1 Method to compute $P(T)$

We summarize the method adopted to compute the temperature distribution function $P(T)$ for small fluctuating grains, based on the papers by Guhathakurta & Draine (1989) and Siebenmorgen et al. (1992).

The time variable energy content of small grains is represented through a steady state temperature distribution function $P(T)$, with $\int P(T)dT = 1$, so that $P(T)dT$ is the probability that a grain is in the temperature interval T, $T + dT$. For large grains $P(T)$ approaches $\delta(T_{eq})$, the delta–function at the equilibrium temperature, while for small grains it can be very large.

$P(T)$ is computed as follows: when a grain absorbs or emits photons a transition from an intial state i to a finale f of the grain enthalpy $U(T)$ occurs. Let P_i be the probability to find a grain in the ith enthalpy (or temperature) bin and A_{fi} the transition probability per unit time from state i to $f \neq i$; the condition of statistical equilibrium yields:

$$\frac{dP_f}{dt} = \sum_{i \neq f} A_{fi} P_i - P_f \sum_{g \neq f} A_{gf} = \sum_i A_{fi} P_i = 0 \tag{A.1}$$

with the definition $A_{ff} \equiv -\sum_{g \neq f} A_{gf}$. The equilibrium distribution is thus obtained by solving the following linear system:

$$\begin{cases} \sum_i A_{fi} P_i = 0 \\ \sum_i P_i = 1 \end{cases} \tag{A.2}$$

for each f. The normalization condition of the probability is needed to univocally solve the system.

The matrix elements A_{fi} are computed as follows:

- $i < f$, absorption:

$$A_{fi} = \frac{4\pi J_{\nu_{fi}}}{\Delta U_{fi}} \pi a^2 Q_{abs}(\nu_{fi}, a) \frac{\Delta U_f}{h}$$

- $i > f$, emission:

$$A_{fi} = \frac{4\pi B_{\nu_{fi}}(T_i)}{\Delta U_{fi}} \pi a^2 Q_{abs}(\nu_{fi}, a) \frac{\Delta U_i}{h}$$

in this case when $f = i - 1$ the following term must be added to the above expression for A_{fi}:

$$-\left(\frac{dU}{dt}\right)_i \frac{1}{U_i - U_f}$$

that keeps into account the transitions implying emission (and absorption) of photons of frequency lower than the minimum one, ν_{fi}, allowed by the discretization of the energy states,

where:

$$\Delta U_{fi} = |U_f - U_i|$$
$$\nu_{fi} = \frac{\Delta U_{fi}}{h}$$
$J_{\nu_{fi}}[erg/(cm^2\, s\, hz\, st)]$
is the radiation field at frequency ν_{fi}
ΔU_k is the width of the kth energy state

and the net cooling rate is given by the following equation:

$$\left(\frac{dU}{dt}\right)_i = \left(-\int_{\nu_{min}}^{\frac{U_i - U_{i-1}}{h}} B_\nu(T_i) Q_{abs}(\nu, a) d\nu + \int_{\nu_{min}}^{\frac{U_{i+1} - U_i}{h}} J_\nu Q_{abs}(\nu, a) d\nu\right) 4\pi^2 a^2 \quad \text{(A.3)}$$

where the two terms on the rhs, respectively for cooling and heating, keep into account those transitions between neighbouring states implying photon energies lower than the minimum ones provided by the array of energy states. A net cooling rate is considered since the two terms are similar.

In case of emission, Guhathakurta & Draine (1989) introduced a numerical simplification to speed up the computation, setting $A_{fi} = 0$ for $i > f + 1$, and $A_{f,f+1} = -(\frac{dU}{dt})_i \frac{1}{U_i - U_f}$ for $i = f + 1$, i.e. they assume emission occurs only between neghbouring states, but with a probability that is the sum over all possible downward transitions. Indeed in this case the upper limit of integration for the cooling term in $(dU/dt)_i$ (Eq. A.3) is fixed to a high value (in the UV). This considerably speeds the computation, since the A_{fi} matrix elements above the main diagonal are all zero except those just above it. Siebenmorgen et al. (1992) find that with this approximation the sub–mm emission from small grains is underestimated. Anyway the sub–mm emission in a galaxy is dominated by normal grains, that reach much lower temperatures. Therefore we generally performed the computations according to this faster scheme.

A.2 Emission features from PAH

We describe the equations we used to compute the emission features from PAH. The central wavelenths, bandwidths and band absorption cross sections of the PAH features are from Léger et al. (1989), reported in the Table below:

λ_i μm	$\Delta\lambda_i$ μm	σ_i $10^{-21} cm^2$
3.3	0.04	$35.N_H$
6.2	0.17	$4.1N_C$
7.7	0.7	$2.9N_C$
8.6	0.4	$3.0N_H$
11.3	0.3	$47.N_H$

We gather here the following relations, already presented in Sec. 2.4.2:

$$a = 0.9\sqrt{N_C}\,\text{Å}\ ,\ N_H = x_H\, N_{s,H}\ ,\ N_{s,H} = \sqrt{6\,N_C}\ ,\ \frac{dn}{dN_C} \propto N_C^{-2.25}$$

where a is the radius of a catacondensed PAH with N_C carbon atoms (the most stable configuration, Omont 1986), x_H is the hydrogenation of the molecules, i.e. the ratio between the number of H atoms and the available sites for H (it determines the band ratios due to C-C and C-H bonds), and dn/dN_C is the adopted PAH distribution from $N_C = 20$ to $N_C = 280$.

From the above we get:

$$\begin{aligned} &N_C(a) = nc\, a^2 \quad ,\quad nc = 1.23\,10^{16}\ cm^{-2} \\ &N_H(a) = x_H\, nh\, a \quad ,\quad nh = 2.72\,10^{8}\ cm^{-1} \\ &\frac{dn}{da} = X\, a^{-3.5}\ cm^{-1} \quad ,\quad a_{min} = 4\text{Å}\ ,\ a_{max} = 15\text{Å}\ . \end{aligned}$$

The emission from PAH within band i per H–atom is given by:

$$4\pi\,\epsilon_{PAH}(\nu_i) = 2\int_0^{\infty}\int_{a_{min}}^{a_{max}} S(\nu,\nu_i,a)\,\frac{4\pi J_\nu}{h\,\nu}\,2\,\sigma_{PAH}(\nu,a)\frac{dn}{da}d\nu\,da\ \ \frac{erg}{s\,hz\,H} \qquad \text{(A.4)}$$

where:

$$S(\nu,\nu_i,a) = \sigma_i(a)\int_{T_{min}}^{T_{max}(\nu,a)} \frac{B_{\nu_i}(T)\,C(T,a)}{F(T,a)}\,dT\ \ \frac{erg}{hz}$$

is the energy inside band i from PAH a;

$$F(T,a) = \sum_j B_{\nu_j}(T)\,\Delta\nu_j\,\sigma_j(a)\ \ \frac{erg}{s}$$

is the power emitted by a molecule at temperature T;
$C(T,a)$ is the specific heat, see Eq. 2.17;
$T_{max}(\nu,a)$ is given by

$$h\nu = \int_{T_{min}}^{T_{max}(\nu,a)} C(T,a)\,dT\ ;$$

$\sigma_{PAH}(\nu,a) = \sigma_{PAH}(\nu)\,N_C(a)$, where $\sigma_{PAH}(\nu)$ is the absorption cross section per C atom in Fig. 2.2.
We set $T_{min} = 5K$, but the result is almost independent on it. The factors 2 in Eq. A.4 keep into account isotropic absorption and emission from the two sides of PAH molecules. We find a good fit to the bands ratios and energy in the Galactic cirrus with $x_H = 0.2$ and $X = 3.03\,10^{-25}$ cm$^{2.5}$/H. X fixes the abundance of PAH, the corresponding number of C atoms locked in PAH is $\int N_C(a)(dn/da)\,da = 18$ ppM.

A.3 Setting the grids

A.3.1 r grid

The dimension nr of the radial array is properly set for exponential disks: it is fixed by the ratio of the galaxy radius to the disk scale lengths R_d and z_d. For spheroids it is set to a constant value. In any case a value less than ~ 60 yields a grid fine enough to assure energy balance.

The array is then built imposing ρ_i/ρ_{i+1} =constant. For disks this condition corresponds to an equispaced grid with step R_{gal}/nr. For King profiles it yields:

$$\frac{r_i}{r_c} = \sqrt{\left(1+\left(\frac{R_{gal}}{r_c}\right)^2\right)^{\frac{i}{nr}} - 1} \tag{A.5}$$

For composite systems we merge the two grids, the inner part being for spheroids, the outer for disks, since the King profile is more centrally concentrated than the exponential.

A.3.2 θ grid

For spherically simmetric profiles, the array for the polar angle θ is equispaced.

For disks, and composite systems, we optimize both the array dimension and values, in order to have a finer grid toward the equatorial plane with a reasonable number of mesh points. How much fine and how many points is described in the following: (1) we want $n\theta$ elements with $\theta_1 = 0$ and $\theta_{n\theta} = \pi$. $n\theta$ is odd, so that the number of angles within the first quadrant is $(n\theta - 1)/2$; (2) the angular distance α_1 between the equatorial array element and the one just above it is set so that at R_{gal} it subtends a fraction $f \lesssim 1$ of the disk scale–height z_d, i.e. $\alpha_1 = \arcsin(f\, z_d/R_{gal})$; (3) we impose constant logarithmic angular steps $\Delta \log\theta = (\frac{2}{n\theta-3})\, \log(\frac{\pi}{2\alpha_1})$; (4) we impose a further condition to define $n\theta$, that the second array element closest to the equatorial plane is $g\,\alpha_1$, $g \lesssim 3$, which implies $n\theta = \frac{2\,\log(\pi/2\alpha_1)}{\log g} + 3$.

A.3.3 ϕ grid

Because of the azimuthal simmetry, we compute the local radiation field in each volume element V_i with coordinates $(r, \theta, \phi = 0)$ due to the contribution from all the other elements V_k with $(r, \theta, \phi > 0)$. Therefore we set the ϕ grid with a finer spacing near $\phi = 0$ so that nearby volume elements are smaller. In this way having point like energy sources in the centers of volume elements is a good approximation as far as the energy balance is concerned. This is also helped since we compute a volume–averaged distance between volume elements, described below.

A.4 Volume–averaged distance between volume elements

The volume average of the square of the distance between V_i and all the points within V_k (see Eq. 2.23), $r^2(i,k)$, is given by:

$$
\begin{aligned}
r^2(i,k) &= \frac{\int_{\Delta r_k}\int_{\Delta\phi_k}\int_{\Delta\theta_k} r^2 sen\theta\, d^2(i,k) d\theta\, d\phi\, dr}{V_k} \\
d^2(i,k) &= (r_i sen\theta_i - r sen\theta cos\phi)^2 + (r sen\theta sen\phi)^2 + (r_i cos\theta_i - r cos\theta)^2 \\
V_k &= \int_{\Delta r_k}\int_{\Delta\phi_k}\int_{\Delta\theta_k} r^2 sen\theta\, d\theta\, d\phi\, dr
\end{aligned}
\tag{A.6}
$$

A.5 Method to speed up computation

In order to generate the model galaxy catalogue discussed in Chap. 6 we had to find out a way to speed up the code. Most of the CPU time ($\sim 70-80\%$) is spent by the code in computing the line integral of diffuse gas between the volume elements $V_i(r,\theta,\phi=0)$ and $V_K(r,\theta,\phi>0)$, i.e.

$$\int_k^i \rho^c(s)\, ds$$

where s denotes the path along the way from k to i. In this way we find the optical depth between the two elements, and thus the radiation field heating the dust in V_i due to all the other V_k.

This bottleneck has been eliminated by computing the above integral just one time for sets of self-similar models characterized by the same ratio of the galaxy radius to the dust scalelength.

More precisely, a set of galaxy models must satisfy the following conditions in order to be self-similar:

1 same geometry, i.e. composite bulge+disk, or only bulge or only disk;

2 same value of $R_{gal}/(dust - scalelength)$. This is the main condition, that sets a range of validity to safely apply this faster method (see below). Since in our composite models dust is always in the disk, this means that R_{gal}/R_d^c and R_{gal}/z_d^c must have the same values;

3 same dimensions $(nr, n\theta, n\phi)$ of spatial arrays; same values of angular arrays (θ,ϕ) and ratio of radial array r to dust scale radius. As shown above (App. A.3), both array dimensions and values are functions of the ratio $R_{gal}/scale-radius$, therefore these conditions are automatically satisfied if the scale-radius is set to R_d^c or z_d^c for disks. For radial array of bulges we set r_c in Eq. A.5 equal to a fraction of R_d^c (the median value of r_c/R_d^c for the considered models).

The condition of point 2 implies that R_{gal} must be set proportional to the dust scalelength, i.e. R_d^c, since gas is in the disk. But this value may not be suited for the bulge, whose density could be over or underestimated if R_{gal} is much lower or higher than the tidal radius (see Sec. 2.5.1). This introduces a range of values of the ratio R_d^c/r_c^* to apply safely this fast computation. Specifically, for $R_d^c/r_c^* = 5-50$ the error

in the bulge density is kept within 25% as compared to what it would be inside the tidal radius. This is sufficiently accurate, also keeping into account that bulge stars are surely less affected by dust than those in the disk as far as the integrated SED is concerned.

Of course the stored values of the density integrals are normalized (to $\rho^c(0)\, R_{gal}$) in order to eliminate the absolute values of gas mass and dust scalelength.

Appendix B

Late-type galaxies in the HDF

We have extended the analysis of early-type galaxies in the HDF, presented in Chap. 5, to a complete sample of K-selected late-type galaxies in the same field. The sample consists of 52 objects with K< 20.47. The sample definition is presented, that basically follows the same procedure as in Chap. 5. Then the first results of the analysis with our code GRASIL of the optical-NIR SEDs of the sample galaxies are discussed. As expected, we find that the presence of dust in these galaxies introduces a strong degeneracy in the estimate of age and SFR, due to the scarce information provided by the available SED. However we try to estimate the contribution of field late-type galaxies to the cosmic star formation history. To this aim we consider the two extreme solutions (i.e. youngest, most extincted and oldest, less extincted) we found from fitting the SED of each object in the sample. We find that, despite the large uncertainties on the single objects, the overall result is better constrained, i.e. the total baryonic mass converted into stars is less uncertain than the istantaneous SFR.

B.1 Sample selection and photometry

Dickinson et al. (1997) observed the HDF–North in the near-IR with the IRIM camera, mounted at the KPNO 4 m telescope. The camera employs a 256 × 256 NICMOS-3 array with 0".16 pixel^{-1}, but the released images were geometrically transformed and rebinned into a 1024 × 1024 format. IRIM has observed the same area in the J, H and K filters, for a total of 12, 11.5 and 23 hours, respectively. Formal 5 σ limiting magnitudes for the HDF/IRIM images, computed from the measured sky noise within a 2" diameter circular aperture, are 23.45 mag at J, 22.29 mag at H, and 21.92 mag at K, whereas the image quality is $\sim$ 1".0 FWHM.

Our galaxy sample has been extracted from the HDF/IRIM K-band image through a preliminary selection based on the automatic photometry provided by SExtractor (Bertin & Arnouts 1996). It is flux limited in th K band and it includes only late–type galaxies.

B.1.1 Tests of completeness

To determine the limit of completeness in the K band (hereafter K_L) for inclusion in our sample, we followed the same procedure described in Franceschini et al. (1998)

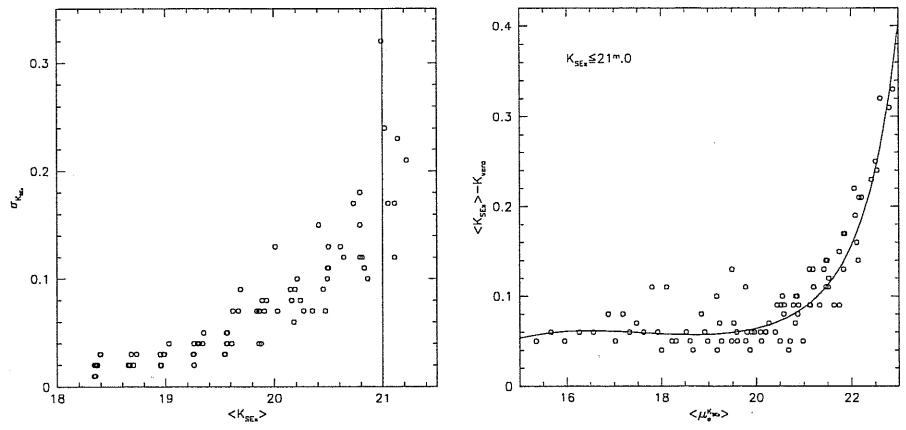

Figure B.1: *Left:* Standard deviation of the SExtractor magnitude estimates as a function of the average magnitude for galaxies in the simulated images: the standard deviation is very small for $< K_{SEx} > \leq 21^m.0$. *Right:* Difference between true flux and the SExtractor flux as a function of the average surface brightness for the subsample of simulated galaxies with $< K_{SEx} > \leq 21^m.0$.

(Chap. 5).

In particular, using the MKOBJECTS tool included in the IRAF package, we produced a synthetic 1024 × 1024 frame, containing a 10 × 10 grid of toy galaxies with exponential luminosity profiles, total K magnitudes ranging from 18.3 to 21 and effective radii r_e ranging from 0".1 to 1".2 (typical values of the HDF late–types). After convolution of this frame with the PSF derived from the few stars in the IRIM K band image, a bootstrapping procedure was carried out to produce 20 different frames mimicking the 'true' image noise. We ran SExtractor on these frames and, for each of the 100 toy galaxies, we produced the detection probability, the average value $< K_{SEx} >$ of the estimated magnitude (to be compared with the input magnitudes K_{true}) and the corresponding standard deviaton $\sigma_{K_{SEx}}$. From the average estimated magnitudes and given the 'true' values of the effective radii (which in the real case can be estimated from the HST images), we also derived the average surface brightness $< \mu_e^K(SEx) >$. These quantities allowed us to check the performances of SExtractor in this particular case.

From the left panel of Fig. B.1, we see that, for $< K_{SEx} > \leq 21.0$ mag (K_{lim} hereafter), the standard deviation of the SExtractor magnitude estimates turns out to be less than 0.18 mag (σ_{max} hereafter). The right panel of the same figure reports $\Delta K = < K_{SEx} > - K_{true}$ as a function of $< \mu_e^K(SEx) >$ for the subsample of toy galaxies with $< K_{SEx} > \leq K_{lim}$. It shows that ΔK systematically increases with $< \mu_e^K(SEx) >$, approaching the maximum value $\Delta K_{max} \sim 0.35$ mag for $< \mu_e^K(SEx) > \simeq 23.0$ mag. The solid line represents the following polynomial fit to the data:

$$\log \Delta K = -1.059 + 0.188 < \mu_*^K > +0.061 < \mu_*^K >^2 +0.006 < \mu_*^K >^3 \ , \qquad \text{(B.1)}$$

where $< \mu_*^K > = < \mu_e^K(SEx) > -21$. This relation provides reliable statistical correc-

tions to the total K magnitudes given by SExtractor.

By analogy with Franceschini et al. (1998), the two previous plots suggest that the strategy to be used in order to obtain a complete flux–limited sample of late–type galaxies from the IRIM K band image consists of the following steps: (1) produce a catalog of objects with $K_{SEx} \leq K_{lim} = 21.0$ mag; (2) evaluate the morphology of each object on the WFPC2/HST frames, removing stars and early-type galaxies from the sample; (3) compute the effective radii of galaxies from high resolution frames in the I_{814} or V_{606} bands, and use these values to derive $< \mu_e^K >$; (4) apply to the K_{SEx} magnitudes the statistical corrections given by Eq. B.1, $K_{corr} = K_{SEx} - \Delta K$; (5) include in the final sample only galaxies with corrected magnitudes less than or equal to $K_L = K_{lim} - \Delta K_{max} - \sigma_{max} = 20.47$ mag.

A total of 176 objects with $K_{SEx} \leq 21$ mag were detected by SExtractor in the IRIM K-band image. After careful inspection of the high resolution HST images, we rejected all elliptical and S0 galaxies (including the 35 early-type objects identified in Franceschini et al. (1998)) and some stars. A few objects were also rejected from the sample due to their position in the frame (at the edges of the image the noise is higher and the magnitude estimate is likely to be uncertain). We then produced a first preliminary, incomplete sample of late–type galaxies (steps 1 and 2 in the previous selection scheme).

The effective radii r_e were estimated running SExtractor on the WFPC2 V_{606} frame (step 3) and using the parameter $FLUX\_RADIUS$, which gives the radius containing half of the total flux emitted by the identified source. The surface brightness $< \mu_e^K(SEx) >$ was evaluated for each galaxy and the statistical corrections ΔK were computed using Eq. B.1.

The final complete sample of late-type galaxies with $K_{corr} < 20.47$ consists of 52 objects over the HDF area of 5.7 square arcmin.

A procedure analogous to that outlined for the K band was used to derive, for each object of the selected sample, the corrected magnitudes in the J and H bands. The corresponding equations are the following:

$$\log \Delta J = -1.471 + 0.094 < \mu_*^J > +0.026 < \mu_*^J >^2 +0.002 < \mu_*^J >^3 \qquad \text{(B.2)}$$

$$\log \Delta H = -1.439 + 0.188 < \mu_*^H > +0.161 < \mu_*^H >^2 +0.031 < \mu_*^H >^3, \qquad \text{(B.3)}$$

where $< \mu_*^J >=< \mu_e^J(SEx) > -20$ and $< \mu_*^H >=< \mu_e^H(SEx) > -20$.

As we did for NIR magnitudes J, H and K, we computed optical magnitudes U, B, V and I from HST frames (see Table B.1). SExtractor analysed F300W, F450W, F606W and F814W WFPC2 images. In this case no corrections have been applied to magnitudes.

Optical magnitudes are in the AB system, defined by the relation (Oke & Gunn 1983):

$$AB = -2.5 \log F_\nu - 48.60 \qquad \text{(B.4)}$$

where F_ν is the flux in $erg\ cm^{-2}\ s^{-1}\ Hz^{-1}$, and the constant is chosen so that $AB = V$ for an object with flat spectrum. Basic data on the sample are listed in Table B.1.

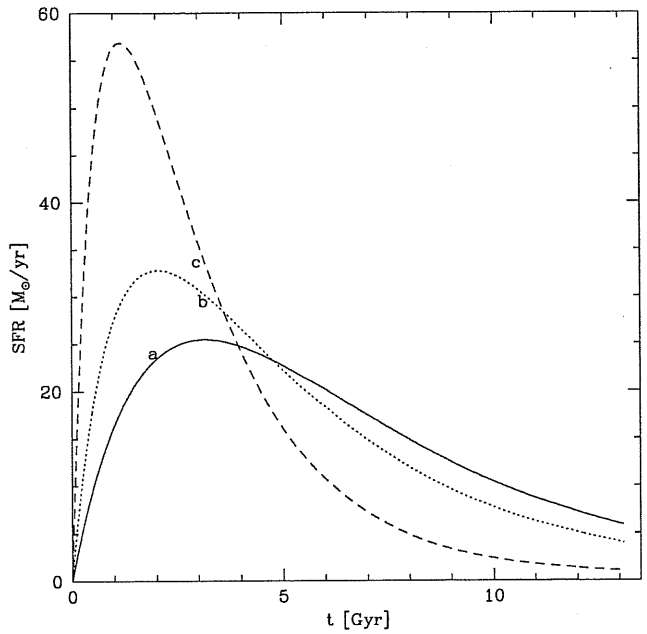

Figure B.2: The three different hystories of star formation.

B.2 Modelling the observed SEDs with GRASIL

As we did for the early-type sample in the HDF (Franceschini et al. 1998, Chap. 5), we performed the analysis of the UV-optical-NIR SEDs of our sample objects using our code GRASIL (Silva et al. 1998, Chap. 2).

The SFR and metallicity histories, that must be provided as inputs to GRASIL, are computed with our chemical evolution code (Sec. 2.2). We have generated 3 different $SFR(t)$ reported in Fig. B.2. They are thought to span a reasonable range of possible evolutions: for curves (a), (b) and (c), the peak occurs at $\sim$ 1, 2 and 3 Gyr respectively, while becoming broader and broader. As a result, half of the final (i.e. at 13 Gyr) mass of star M is assembled at 2, 3.7 and 4.7 Gyr respectively.

We then compute the SED evolution corresponding to these SF histories. In the GRASIL model there are several parameters affecting the overall modifications imprinted by dust on the SED (see Table 2.2). However, if we consider only the UV to NIR extinction of stellar radiation, we can obtain most of the possible behaviors by adjusting just two quantities: the escape timescale from MCs t_o and the total mass of dust. Indeed t_o rules the fraction of light of the youngest stellar generations embedded inside MCs and converted to IR photons, since the MCs optical thickness is very high below $\sim 1\mu$m (cfr. Chap. 4). On the other hand, the effects of the diffuse dust (cirrus) depend on several quantities: the radial and vertical scalelengths for stars and dust R_d and z_d, the residual gas of the galaxy M_g, the dust to gas ratio δ and the fraction of gas which is in the MCs component f_{mc}. However we found that most, if not all, the possible attenuation laws of the diffuse dust, arising from different choices of these quantities,

can be closely mimicked by simply adjusting the amount of gas, while fixing the other quantities to the following 'typical' values: $R_d = 3.5(M/10^{11}M_\odot)^{1/3}$ Kpc, $z_d = 0.1\,R_d$, $\delta = 0.01$ and $f_{mc} = 0.5$. It is worth noticing that while different choices of M_g, R_d, z_d, δ and f_{mc} can yield similar attenuation laws, the shapes of the corresponding IR continuum can be rather different.

Note also that strictly speaking the residual gas M_g is not a parameter, in the sense that it is given at each epoch by the chemical evolution code (trough the Schmidt law relating the SFR to M_g). However we force M_g to different values, in order to arrange in a monoparametric sequence the space of parameters affecting the cirrus extinction. We use the conservative criterion of considering acceptable values from 0.2 to 5 times the 'true' M_g, in the sense that we have tested that, within this range, similar effects on the extinction can be obtained leaving M_g as given by the chemical evolution, and adjusting for instance δ and/or R_d and/or f_{mc} to still plausible values. Moreover, this larger 'freedom' we reclaim on M_g is intended to take into account that the Schmidt law should not be taken too seriously, as a strict relationship between the total gas content and the SFR in the system.

For each of the 3 histories SFR(t) we have generated two grids of models: one with $t_o = 5$ Myr and another with $t_o = 30$ Myr. We found (see Chap. 4) the former is the typical value for normal spirals while the latter is more suited for starbursting systems. Each of these grids consists of 1400 models computed with ages t_G ranging from 0.2 to 10 Gyr in steps of 0.2 Gyr and M_g from 0 to 1 (in units of the final mass of stars) in 28 logarithmic steps. In total we have therefore $1400 \times 2 \times 3 = 8400$ models with different age, gas content, MCs escape timescale, and $SFR(t)$ which we compared with the observed SEDs of the sample, allowing for the obvious scaling in luminosity. In addition we considered one more couple of grids to see how our observed SEDs compare to those expected for spheroidal systems: for these we used the $SFR(t)$ (c) in Fig. B.2, but truncated at 3 Gyr to simulate the onset of galactic wind. In this case the adopted geometry is the King profile of Eq. 2.20 with $r_c = 0.15(M/10^{11}M_\odot)^{1/3}$ Kpc.

Typical results of this χ^2 analysis are shown in Figs. B.3 and B.4. It is immediately apparent that, even within a single grid, a large degeneration exists between the age and the gas content of the object, and that rather different star formation histories can lead to equally good fits (Fig. B.3). Moreover Fig. B.4 illustrates that often it is possible to match quite well the observed SEDs with models differing in the current SFR by factors up to 5–10. This is a dramatic demonstration of a sometimes still undervalued fact: a large amount of SF activity can be easily hidden at wavelengths below a few μm. Only a good coverage of the IR SED, say between a few tenths up to a few hundreds μm, where often actively star forming galaxies emit most of the energy, would improve the situation.

B.3 The star formation hystory of late-type field galaxies

For the sample of early-type galaxies analyzed in Chap. 5, we used our spectral synthesis results to estimate the contribution of this population of field galaxies to the cosmic history of star formation (see Sec. 5.6 and Fig. 5.16). In that case we were remarkably successful in putting tight constraints, thanks to the fact that those systems are observed

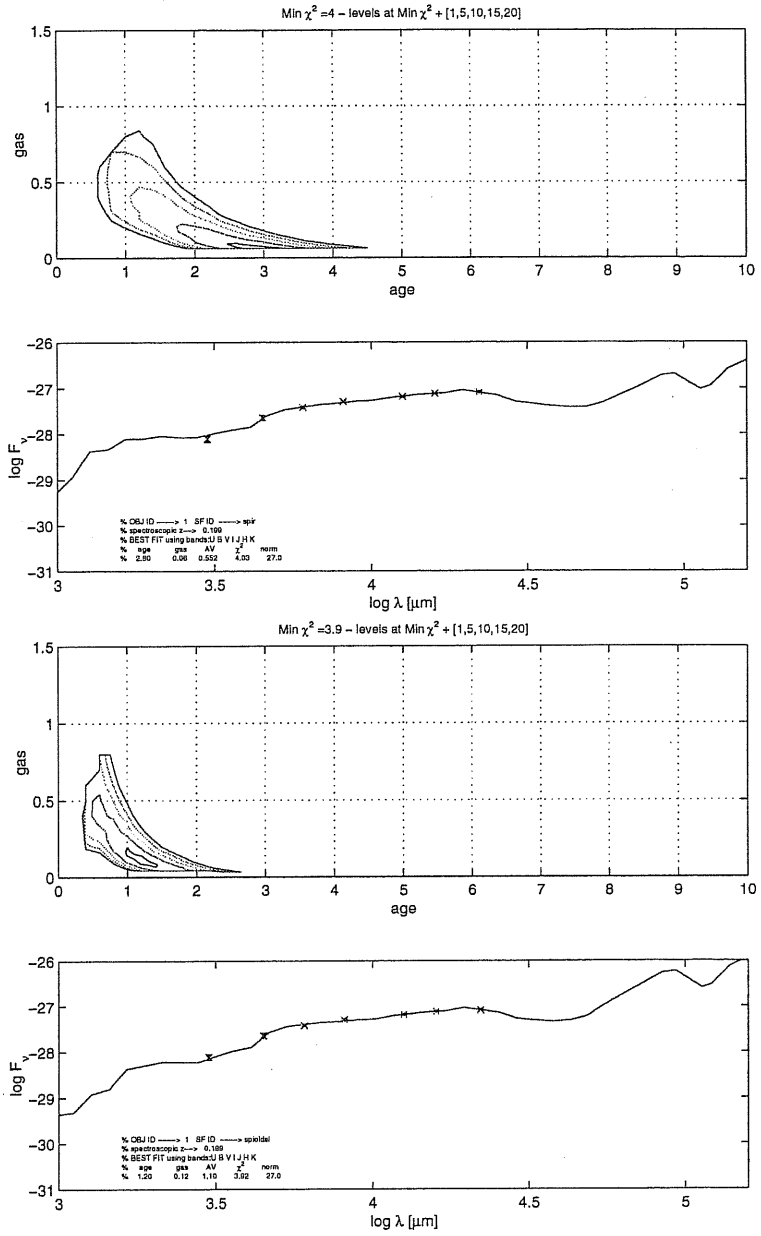

Figure B.3: χ^2 contour and best fits obtained for object number 1 with two grids. The top two panels refer to the age-gas grid corresponding to curve (a) of Fig. B.2 and $t_o = 5$ Myr, while the lower two are for curve (c) and $t_o = 30$ Myr. The contours correspond to a χ^2 increment of 1, 5, 10, 15 and 20 with respect to the best fit in the grid. Therefore the second innermost contour contains solutions with more than 90% confidence level.

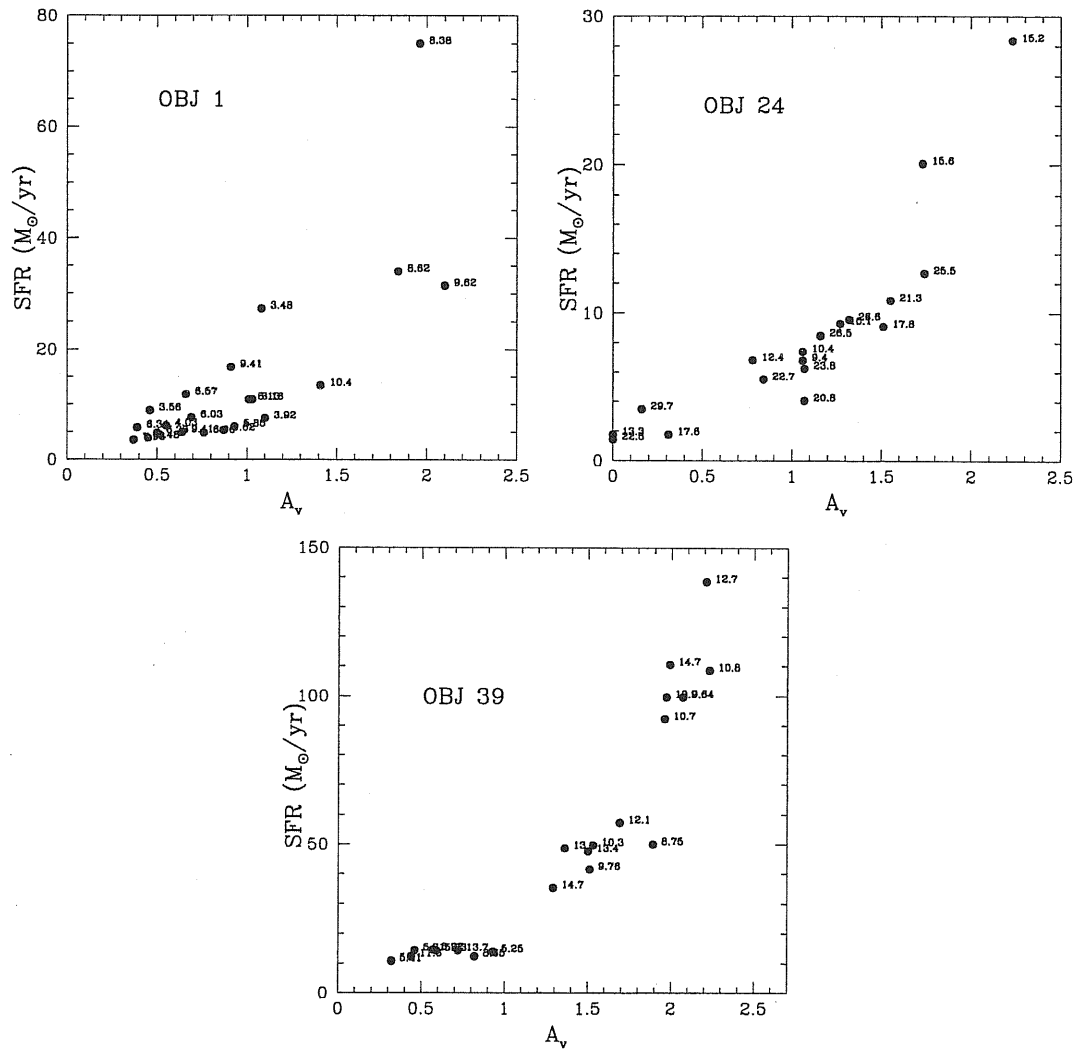

Figure B.4: For three sample objects, the SFR is plotted against the V–band effective extinction. For each grid, we plot the best fit model and two more models: the youngest and the oldest one with $\chi^2 = \chi^2_{best} + 5$. The labels near the points are the corresponding χ^2 values. Since the best solutions (considering all the grids) have $\chi^2 = 3.5$, 9.4 and 5.2 for obj 1, 24 and 39 respectively, there are alternative models, which cannot be rejected on a statistical basis, having SFR which differ by factors up to 10.

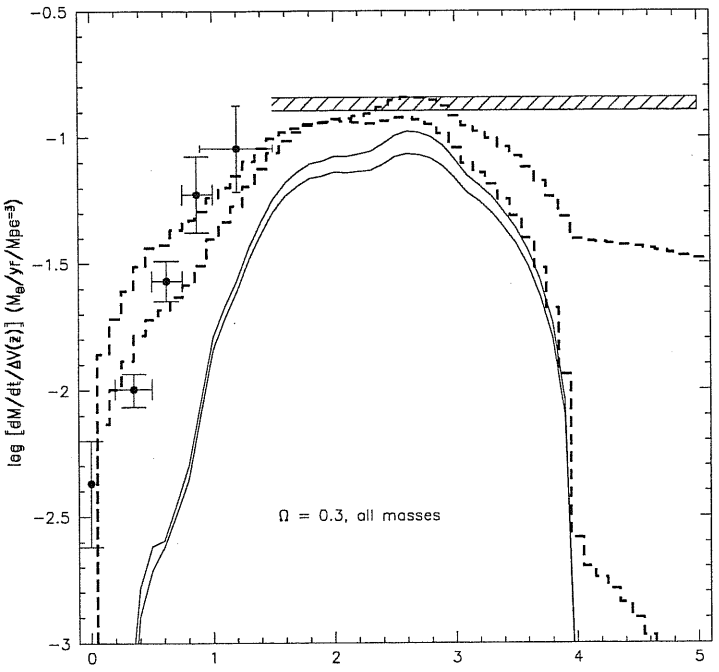

Figure B.5: The contribution to the cosmic SF history from field populations in the HDF: solid lines are for early–type, dashed for late–type. See text for details.

essentially free from dust, and the ensuing uncertainties on their past SF history are relatively moderate. Moreover they are believed to passively evolve at later epochs, without significant SF activity. Here the problem is much worse: as we have seen the presence of dust introduces large uncertainties on the SF history of each object before and at the time it is observed, and moreover it is expected that the SF remains important even at lower redshifts. With these caveats in mind we tried however to perform a similar exercise for the present sample. The result is shown in Fig. B.5. The solid lines are the extreme solutions for the early-type field galaxies (see Fig. 5.16), whilst the two dashed lines refer to the present sample. These were obtained considering for each object the two extreme accetable (i.e. within 90% confidence limit) fits we get, the most extincted and youngest fit (yielding the curve higher at $z < 1.8$ and lower at $z > 1.8$), and the oldest–less extincted one. As expected, the disk–dominated or irregular galaxies display a behaviour very different from that of bulge–dominated objects.

It is somewhat surprising that, despite the large uncertainties on the single objects, the overall result is better constrained. This is due to a sort of compensation in the adopted solutions: the youngest and most extincted ones tend to have a more intense SF activity but less protracted in the past. In other words, the baryonic mass converted into stars is less uncertain than the instantaneous SFR. In any case, it is hopeless to get more stringent constraints on the obscured SF activity based on UV to NIR data alone.

n	α		δ		$r_e(")$	U_{AB}	B_{AB}	V_{AB}	I_{AB}	J_{SEx}	H_{SEx}	K_{SEx}	z
	m	s	$'$	$''$									
0	36	56.65	12	45.60	1.21	24.91	22.49	21.09	20.05	18.26	17.48	16.79	0.517
1	36	51.08	13	20.73	1.12	21.69	20.52	19.95	19.63	18.4	17.87	17.3	0.199
2	36	46.15	11	42.05	0.34	23.4	22.9	22.4	20.8	19.17	18.38	17.37	1.012
3	36	53.90	12	54.05	0.6	23.74	22.8	21.89	20.88	19.12	18.3	17.47	0.642
4	36	43.96	12	50.13	0.31	23.9	22.87	21.83	21.01	19.27	18.46	17.59	(0.55)
5	36	44.58	13	4.66	0.54	25.24	23.63	22.23	21.24	19.29	18.4	17.67	(0.68)
6	36	51.78	13	53.73	0.49	23.92	22.97	21.97	21.09	19.42	18.51	17.7	0.557
7	36	42.91	12	16.26	0.52	22.86	22.22	21.32	20.74	19.2	18.53	17.9	0.454
8	36	49.75	13	13.09	0.63	24.99	23.54	22.29	21.49	19.07	18.56	18.0	0.478
9	36	50.25	12	39.72	0.49	22.59	22.08	21.25	20.69	19.3	18.67	18.0	0.474
10	36	41.95	12	5.41	0.47	23.34	22.6	21.67	21.03	19.42	18.78	18.04	0.432
11	36	45.85	13	25.81	0.85	23.23	22.3	21.45	20.95	19.45	18.86	18.13	(0.4)
12	36	43.18	11	48.05	0.47	26.05	24.95	23.91	22.45	20.14	19.29	18.23	(1.06)
13	36	51.72	12	20.18	0.34	24.85	23.34	22.24	21.55	19.87	19.12	18.31	0.299
14	36	42.72	13	7.26	0.33	25.61	24.58	23.22	22.19	20	19.21	18.32	(0.737)
15	36	47.04	12	34.96	0.4	22.84	22.19	21.46	21.03	19.66	19.05	18.34	0.321
16	36	49.51	14	6.77	0.34	24.17	23.58	22.82	21.83	20.17	19.23	18.41	0.752
17	36	49.51	12	20.11	0.61	25.58	25.16	24.04	22.46	20.34	19.4	18.53	0.961
18	36	41.42	11	42.89	0.33	26.18	25.13	24.81	24.16	20.69	19.66	18.6	1.32
19	36	58.76	12	52.35	0.85	23.18	22.52	21.72	21.31	19.92	19.34	18.77	0.32
20	36	55.58	12	45.43	0.47	24.18	23.63	22.97	21.97	20.35	19.65	18.86	0.79
21	36	50.47	13	16.16	0.64	25.46	24.62	23.74	22.6	20.68	19.95	18.9	(0.88)
22	36	57.33	12	59.63	0.44	22.83	22.53	21.82	21.38	20.1	19.42	18.93	0.473
23	36	41.31	11	40.87	0.33	27.02	24.7	23.61	22.47	20.57	19.73	19.01	0.585
24	36	38.44	12	31.35	0.59	26.76	25.15	23.74	22.67	20.85	20.03	19.17	(0.7)
25	36	49.24	11	48.38	0.32	25.46	24.93	24.16	22.96	20.67	19.98	19.18	0.961

Table B.1: Photometric data of the sample. Col. 1: FOCAS objects identification; Col. 2: our identification; Cols. 3-6: coordinates α and δ (at J2000); Col. 7: effective radius in arcsec derived from HST images; Col. 8-11: U, B, V, I magnitudes in the AB system (see text); Cols. 12-14: J, H, K magnitudes in the standard system; Col. 15: redshift. Values in brackets are photometric redshifts, while the other are spectroscopic (Cohen et al. 1996, Cowie et al. 1996, Soto et al. 1996).

n	α		δ		$r_e(")$	U_{AB}	B_{AB}	V_{AB}	I_{AB}	J_{SEx}	H_{SEx}	K_{SEx}	z
	m	s	$'$	$''$									
26	36	48.62	12	15.81	0.47	26.7	26.2	25.2	23.6	21.23	20.23	19.21	(1.35)
27	36	49.45	13	16.58	0.28	25.41	24.44	24.02	23.27	21.18	20.22	19.22	(1.006)
28	36	48.12	12	14.90	0.88	24.26	23.83	23.54	22.64	20.53	20.02	19.36	0.961
29	36	54.10	13	54.35	0.45	24.35	23.84	23.37	22.43	21.01	20.17	19.41	0.894
30	36	52.70	13	55.49	0.27	23.96	23.22	23.06	22.71	20.64	20.08	19.41	1.355
31	36	38.99	12	19.63	0.45	24.14	23.67	22.95	22.22	20.81	20.17	19.57	(0.77)
32	36	44.19	12	47.90	0.39	22.99	22.65	22.13	21.65	20.5	19.91	19.58	0.558
33	36	49.01	12	20.86	0.18	23.87	23.54	23.23	22.44	20.89	20.53	19.68	0.953
34	36	39.56	12	13.83	0.44	28.2	26.49	25.15	23.79	21.62	20.53	19.69	(1.22)
35	36	48.27	13	13.8	0.29	26.53	25.9	25.3	24.07	21.51	20.36	19.75	(1.165)
36	36	53.45	12	34.52	0.34	24.97	24.25	23.5	22.81	21.47	20.83	19.8	0.559
37	36	55.53	13	53.48	0.7	24.04	23.49	23.23	22.65	21.27	20.48	19.8	1.148
38	36	49.58	14	14.63	0.48	25.4	24	23.8	22.7	21.37	20.75	19.94	(0.92)
39	36	57.67	13	15.32	0.39	24.43	23.94	23.57	22.82	21.29	20.71	19.97	0.952
40	36	55.50	14	2.71	0.55	26.06	24.87	23.87	22.99	21.48	20.75	20.01	0.559
41	36	48.79	13	18.35	0.68	24.27	23.93	23.5	22.76	21.32	20.27	19.66	0.749
42	36	47.19	14	14.18	0.22	26.7	25.74	24.59	23.53	21.84	20.63	20.02	0.609
43	36	57.21	12	25.83	0.51	24.17	24.02	23.91	22.45	21.34	20.6	20.05	0.561
44	36	48.34	14	16.63	0.16	25.86	23.97	23.73	23.43	21.64	20.53	20.11	2.008
45	36	47.78	12	32.93	0.28	25.21	24.73	24.27	23.34	21.47	21.12	20.12	(1.04)
46	36	52.87	14	5.11	0.29	25.7	24.84	24.06	23.25	21.38	20.89	20.21	0.498
47	36	52.02	14	0.91	0.33	25.25	24.55	23.72	23.02	21.48	20.74	20.22	0.557
48	36	48.58	13	28.35	0.47	25.33	24.3	23.95	23	21.22	21.08	20.24	0.958
49	36	44.64	12	27.39	0.24	25.79	24.28	24.11	23.73	21.63	20.89	20.29	(1.58)
50	36	44.45	11	41.82	0.62	24.43	24.46	24.52	23.88	21.05	21.25	20.42	1.02
51	36	56.13	13	29.74	0.39	24.38	24.13	23.97	23.34	21.38	21.3	20.45	(1.2)

Table B.1: *Continued*

Bibliography

J. A. Acosta-Pulido, U. Klaas, R. J. Laureijs, B. Schulz, U. Kinkel, P. Abraham, H. O. Castaneda, L. Cornwall, C. Gabriel, I. Heinrichsen, U. Herbstmeier, H. Krueger, and G. Pelz. *A&A*, 315:L121–L124, Nov. 1996.

N. I. Agladze, A. J. Sievers, S. A. Jones, J. M. Burlitch, and S. V. W. Beckwith. *ApJ*, 462:1026+, May 1996.

O. Almaini, A. Lawrence, and B. J. Boyle. *MNRAS*, 305:L59–L63, May 1999.

P. Andreani, A. Franceschini, and G. L. Granato. Far-ir and mm properties of quasars. In *The Far Infrared and Submillimetre Universe. Edited by A. Wilson. Noordwijk, The Netherlands : ESA, 1997., p.133*, pages 133+, 1997.

N. Arimoto. Stellar population synthesis models for elliptical galaxies. In C. Leitherer, U. Fritze-von Alvensleben, and H. J., editors, *ASP Conf. Ser. 98: From Stars to Galaxies: the Impact of Stellar Physics on Galaxy Evolution*, pages 287+, 1996.

L. Armus, T. M. Heckman, and G. K. Miley. *ApJ*, 364:471–495, Dec. 1990.

H. Aussel, C. J. Cesarsky, D. Elbaz, and J. L. Starck. *A&A*, 342:313–336, Feb. 1999.

V. A. Balzano. *ApJ*, 268:602–627, May 1983.

J. E. Barnes and L. Hernquist. *ApJ*, 471:115+, Nov. 1996.

C. M. Baugh, A. J. Benson, S. Cole, C. S. Frenk, and C. G. Lacey. *MNRAS*, 305: L21–L25, May 1999.

C. M. Baugh, S. Cole, and C. S. Frenk. *MNRAS*, 282:L27–L32, Sept. 1996.

C. M. Baugh, S. Cole, C. S. Frenk, and C. G. Lacey. *ApJ*, 498:504+, May 1998.

J. E. Beckman, R. F. Peletier, J. H. Knapen, R. L. M. Corradi, and L. J. Gentet. *ApJ*, 467:175+, Aug. 1996.

P. J. Bedijn. *A&A*, 186:136–152, Nov. 1987.

R. Bender, B. Ziegler, and G. Bruzual. *ApJL*, 463:L51–+, June 1996.

G. Bertelli, A. Bressan, C. Chiosi, F. Fagotto, and E. Nasi. *A&AS*, 106:275–302, Aug. 1994.

E. Bertin, M. Dennefeld, and M. Moshir. *A&A*, 323:685–696, July 1997.

M. S. Bessell, P. R. Wood, J. M. Brett, and M. Scholz. *A&AS*, 89:335–366, Aug. 1991.

S. Bianchi, A. Ferrara, and C. Giovanardi. *ApJ*, 465:127+, July 1996.

B. Binggeli, A. Sandage, and M. Tarenghi. *AJ*, 89:64–82, Jan. 1984.

T. Bloecker. *A&A*, 297:727+, May 1995a.

T. Bloecker. *A&A*, 299:755+, July 1995b.

F. Boulanger, P. Boissel, D. Cesarsky, and C. Ryter. *A&A*, 339:194–200, Nov. 1998.

F. Boulanger and F. Viallefond. *A&A*, 266:37–56, Dec. 1992.

G. H. Bowen and L. A. Willson. *ApJL*, 375:L53–L56, July 1991.

A. Bressan, C. Chiosi, and F. Fagotto. *ApJS*, 94:63–115, Aug. 1994.

A. Bressan, F. Fagotto, G. Bertelli, and C. Chiosi. *A&AS*, 100:647–664, Sept. 1993.

A. Bressan, G. L. Granato, and L. Silva. *A&A*, 332:135–148, 1998.

G. Bruzual and S. Charlot. *in preparation*, 1999.

G. Bruzual A. and S. Charlot. *ApJ*, 405:538–553, Mar. 1993.

G. Bruzual A., G. Magris, and N. Calvet. *ApJ*, 333:673–688, Oct. 1988.

V. Buat, J. M. Deharveng, and J. Donas. *A&A*, 223:42–46, Oct. 1989.

V. Buat and C. Xu. *A&A*, 306:61+, Feb. 1996.

C. Burigana, L. Danese, G. De Zotti, A. Franceschini, P. Mazzei, and L. Toffolatti. *MNRAS*, 287:L17–L20, May 1997.

D. Calzetti. *AJ*, 113:162–184, Jan. 1997.

D. Calzetti, A. L. Kinney, and T. Storchi-Bergmann. *ApJ*, 429:582–601, July 1994.

D. Calzetti, A. L. Kinney, and T. Storchi-Bergmann. *ApJ*, 458:132+, Feb. 1996.

E. Cappellaro, M. Turatto, D. Y. Tsvetkov, O. S. Bartunov, C. Pollas, R. Evans, and M. Hamuy. *A&A*, 322:431–441, June 1997.

J. A. Cardelli, G. C. Clayton, and J. S. Mathis. *ApJ*, 345:245–256, Oct. 1989.

J. A. Cardelli, D. M. Meyer, M. Jura, and B. D. Savage. *ApJ*, 467:334+, Aug. 1996.

D. P. Carico, D. B. Sanders, B. T. Soifer, J. H. Elias, K. Matthews, and G. Neugebauer. *AJ*, 95:356–373, Feb. 1988.

D. P. Carico, D. B. Sanders, B. T. Soifer, K. Matthews, and G. Neugebauer. *AJ*, 100: 70–83, July 1990.

C. M. Carollo and I. j. Danziger. *MNRAS*, 270:523+, Oct. 1994.

J. I. Castor, D. C. Abbott, and R. I. Klein. *ApJ*, 195:157–174, Jan. 1975.

S. Charlot, G. Worthey, and A. Bressan. *ApJ*, 457:625+, Feb. 1996.

C. Chiosi, G. Bertelli, and A. Bressan. *A&A*, 196:84–108, May 1988.

A. Cimatti, P. Andreani, H. Rottgering, and R. Tilanus. *Nature*, 392:895–897, 1998.

A. Cimatti, S. Bianchi, A. Ferrara, and C. Giovanardi. *MNRAS*, 290:L43–L49, Sept. 1997.

A. D. Code and G. A. Welch. *ApJ*, 256:1–12, May 1982.

J. G. Cohen, L. L. Cowie, D. W. Hogg, A. Songaila, R. Blandford, E. M. Hu, and P. Shopbell. *ApJL*, 471:L5–+, Nov. 1996.

M. Cohen and K. Volk. *AJ*, 98:1563–1571, Nov. 1989.

S. Cole, A. Aragon-Salamanca, C. S. Frenk, J. F. b. . Navarro, and S. E. Zepf. *MNRAS*, 271:781+, Dec. 1994.

S. Cole, C. G. Lacey, A. J. Baugh, and C. S. Frenk. *submitted to MNRAS*, 1999.

A. J. Collison and J. D. Fix. *ApJ*, 368:545–557, Feb. 1991.

J. J. Condon. *ARA&A*, 30:575–611, 1992.

J. J. Condon and Q. F. Yin. *ApJ*, 357:97–104, July 1990.

A. J. Connolly, A. S. Szalay, M. Dickinson, M. U. Subbarao, and R. J. Brunner. *ApJL*, 486:L11–+, Sept. 1997.

S. Considere and E. Athanassoula. *Astronomy and Astrophysics Supplement Series*, 76: 365–0138, Dec. 1988.

R. S. De Jong. *A&AS*, 118:557–573, Sept. 1996a.

R. S. De Jong. *A&A*, 313:45–64, Sept. 1996b.

R. S. De Jong. *A&A*, 313:377–395, Sept. 1996c.

R. S. De Jong and P. C. Van Der Kruit. *Astronomy and Astrophysics Supplement Series*, 106:451–504, Sept. 1994.

G. De Vaucouleurs, A. De Vaucouleurs, J. Corwin, H. G., R. J. Buta, G. Paturel, and P. Fouque. *Third Reference Catalogue of Bright Galaxies.* Volume 1-3, XII, 2069 pp. 7 figs.. Springer-Verlag Berlin Heidelberg New York, 1991.

F. X. Desert, F. Boulanger, and J. L. Puget. *A&A*, 237:215–236, Oct. 1990.

F. X. Desert and et al. *A&A*, 342:363–377, Feb. 1999.

N. A. Devereux, R. Price, L. A. Wells, and N. Duric. *AJ*, 108:1667–1673, Nov. 1994.

N. A. Devereux and J. S. Young. *ApJ*, 359:42–56, Aug. 1990.

N. A. Devereux and J. S. Young. *AJ*, 103:1536–1544, May 1992.

N. A. Devereux and J. S. Young. *AJ*, 106:948+, Sept. 1993.

J. E. G. Devriendt, B. Guiderdoni, and R. Sadat. *astro-ph/9906332*, 1999.

A. Dey, J. R. Graham, R. J. Ivison, I. Smail, G. S. Wright, and M. C. Liu. *ApJ*, 519: 610–621, July 1999.

S. Djorgovski and D. J. Thompson. Searches for primeval galaxies. In *IAU Symposia*, volume 149, pages 337+, 1992.

J. S. Doane and W. G. Mathews. *ApJ*, 419:573+, Dec. 1993.

J. Donas, J. M. Deharveng, M. Laget, B. Milliard, and D. Huguenin. *A&A*, 180:12–26, June 1987.

J. Dorschner and T. Henning. *A&A Rev.*, 6:271+, 1995.

B. T. Draine and N. Anderson. *ApJ*, 292:494–499, May 1985.

B. T. Draine and H. M. Lee. *ApJ*, 285:89, 1984.

B. T. Draine and S. Malhotra. *ApJ*, 414:632–645, Sept. 1993.

S. P. Driver, A. Fernandez-Soto, W. J. Couch, S. C. Odewahn, R. A. Windhorst, S. Phillips, K. Lanzetta, and A. Yahil. *ApJL*, 496:L93–+, Apr. 1998.

E. Dwek. *ApJ*, 501:643+, July 1998.

E. Dwek, R. G. Arendt, D. J. Fixsen, T. J. Sodroski, N. Odegard, J. L. Weiland, W. T. Reach, M. G. Hauser, T. Kelsall, S. H. Moseley, R. F. Silverberg, R. A. Shafer, J. Ballester, D. Bazell, and R. Isaacman. *ApJ*, 475:565+, Feb. 1997.

E. Dwek, R. G. Arendt, M. G. Hauser, D. Fixsen, T. Kelsall, D. Leisawitz, Y. C. Pei, E. L. Wright, J. C. Mather, S. H. Moseley, N. Odegard, R. Shafer, R. F. Silverberg,

and J. L. Weiland. *ApJ*, 508:106–122, Nov. 1998.

D. Elbaz, H. Aussel, C. J. Cesarsky, F. X. Desert, D. Fadda, A. Franceschini, M. Harwit, J. L. Puget, and J. L. Starck. *astro-ph/9902229*, 1999.

M. Elitzur, P. Goldreich, and N. Scoville. *ApJ*, 205:384–396, Apr. 1976.

G. Engargiola. *ApJS*, 76:875–910, July 1991.

R. Evans. The far infrared/stellar energy balance. In J. I. Davies and D. Burstein, editors, *"The opacity of Spiral Disks"*, page 281. Kluwer Academic Publisher, 1995.

F. Fagotto, A. Bressan, G. Bertelli, and C. Chiosi. *A&AS*, 104:365–376, Apr. 1994 a.

F. Fagotto, A. Bressan, G. Bertelli, and C. Chiosi. *A&AS*, 105:29–38, May 1994 b.

G. Fasano, S. Cristiani, S. Arnouts, and M. Filippi. *AJ*, 115:1400–1411, Apr. 1998.

G. Fasano, R. Falomo, and R. Scarpa. *MNRAS*, 282:40–66, Sept. 1996.

G. Fasano and M. Filippi. *A&AS*, 129:583–591, May 1998.

A. Ferrara, S. Bianchi, A. Cimatti, and C. Giovanardi. *astro-ph/9903078*, 1999.

M. Fioc and B. Rocca-Volmerange. *A&A*, 326:950–962, Oct. 1997.

D. J. Fixsen, E. Dwek, J. C. Mather, C. L. Bennett, and R. A. Shafer. *ApJ*, 508: 123–128, Nov. 1998.

M. A. Fluks, B. Plez, P. S. The, D. De Winter, B. E. Westerlund, and H. C. Steenman. *A&AS*, 105:311–336, June 1994.

A. Franceschini, L. Danese, L. Toffolatti, and G. De Zotti. *MNRAS*, 233:157–174, July 1988.

A. Franceschini, G. De Zotti, L. Toffolatti, P. Mazzei, and L. Danese. *Astronomy and Astrophysics Supplement Series*, 89:285–310, Aug. 1991.

A. Franceschini, P. Mazzei, G. De Zotti, and L. Danese. *ApJ*, 427:140–154, May 1994.

A. Franceschini, L. Silva, G. Fasano, G. L. Granato, A. Bressan, S. Arnouts, and L. Danese. *ApJ*, 506:600–620, Oct. 1998.

W. L. Freedman. *AJ*, 104:1349–1359, Oct. 1992.

H. E. Froehlich. *Astronomische Nachrichten*, 303:97–103, 1982.

F. Fusi-Pecci and A. Renzini. *A&A*, 46:447–454, Feb. 1976.

J. P. Gardner, R. M. Sharples, C. S. Frenk, and B. E. Carrasco. *ApJL*, 480:L99–+, May 1997.

R. Genzel, D. Lutz, E. Sturm, E. Egami, D. Kunze, A. F. M. Moorwood, D. Rigopoulou, H. W. W. Spoon, A. Sternberg, L. E. Tacconi-Garman, L. Tacconi, and N. Thatte. *ApJ*, 498:579+, May 1998.

M. Giavalisco, C. C. Steidel, and F. D. Macchetto. *ApJ*, 470:189+, Oct. 1996.

D. R. Gies and D. L. Lambert. *ApJ*, 387:673–700, Mar. 1992.

R. Giovanelli, M. P. Haynes, J. J. Salzer, G. Wegner, L. N. Da Costa, and W. Freudling. *AJ*, 110:1059+, Sept. 1995.

P. Goldreich and N. Scoville. *ApJ*, 205:144–154, Apr. 1976.

P. Goldschmidt, S. J. Oliver, S. B. G. Serjeant, A. Baker, N. Eaton, A. Efstathiou, C. Gruppioni, R. G. Mann, B. Mobasher, M. Rowan-Robinson, T. J. Sumner,

L. Danese, D. Elbaz, A. Franceschini, E. Egami, M. Kontizas, A. Lawrence, R. McMahon, H. U. Norgaard-Nielsen, I. Perez-Fournon, and J. I. Gonzalez-Serrano. *MNRAS*, 289:465–470, Aug. 1997.

K. D. Gordon, D. Calzetti, and A. N. Witt. *ApJ*, 487:625+, Oct. 1997.

J. R. Graham and A. Dey. *ApJ*, 471:720+, Nov. 1996.

G. L. Granato and L. Danese. *MNRAS*, 268:235–252, 1994.

G. L. Granato, L. Danese, and A. Franceschini. *ApJ*, 486:147+, Sept. 1997.

G. L. Granato, G. C. Lacey, L. Silva, A. Bressan, C. M. Baugh, S. Cole, and C. S. Frenk. *in preparation*, 1999.

C. J. Grillmair, T. R. Lauer, G. Worthey, S. M. Faber, W. L. Freedman, B. F. Madore, E. A. Ajhar, W. A. Baum, J. A. Holtzman, C. R. Lynds, P. B. O'Neil, E. J. J. S., and P. B. . . . *AJ*, 112:1975+, Nov. 1996.

M. A. T. Groenewegen and T. De Jong. *A&A*, 288:782–790, Aug. 1994.

M. A. T. Groenewegen, C. H. Smith, P. R. Wood, A. Omont, and T. Fujiyoshi. *ApJL*, 449:L119–+, Aug. 1995.

P. Guhathakurta and B. T. Draine. *ApJ*, 345:230–244, Oct. 1989.

B. Guiderdoni, E. Hivon, F. R. Bouchet, and B. Maffei. *MNRAS*, 295:877–898, Apr. 1998.

B. Guiderdoni and B. Rocca-Volmerange. *A&A*, 186:1–2, Nov. 1987.

H. J. Habing. *A&A Rev.*, 7:97–207, 1996.

H. J. Habing, J. Tignon, and A. G. G. M. Tielens. *A&A*, 286:523–534, June 1994.

M. G. Hauser, R. G. Arendt, T. Kelsall, E. Dwek, N. Odegard, J. L. Weiland, H. T. Freudenreich, W. T. Reach, R. F. Silverberg, S. H. Moseley, Y. C. Pei, P. Lubin, J. C. Mather, R. A. Shafer, G. F. Smoot, R. Weiss, D. T. Wilkinson, and E. L. Wright. *ApJ*, 508:25–43, Nov. 1998.

M. G. Hauser, T. Kelsall, R. G. Arendt, J. L. Weiland, H. T. Freudenreich, N. Odegard, E. Dwek, S. H. Moseley, R. F. Silverberg, and Y. C. Pei. The cobe diffuse infrared background experiment search for the cosmic infrared background: I. limits and possible detections. In *American Astronomical Society Meeting*, volume 191, pages 9101+, Dec. 1997.

T. M. Heckman, C. Robert, C. Leitherer, D. R. Garnett, and F. Van Der Rydt. *ApJ*, 503:646+, Aug. 1998.

C. Helling, U. G. Jorgensen, B. Plez, and H. R. Johnson. *A&A*, 315:194–203, Nov. 1996.

G. Helou, I. R. Khan, L. Malek, and L. Boehmer. *ApJS*, 68:151–172, Oct. 1988.

H. Hippelein, D. Lemke, R. J. Tuffs, M. Haas, H. J. Voelk, U. Klaas, U. Kinkel, C. M. Telesco, and C. Xu. *A&A*, 315:L79–L81, Nov. 1996.

D. W. Hogg, J. G. Cohen, R. Blandford, S. D. J. Gwyn, F. D. A. Hartwick, B. Mobasher, P. Mazzei, M. Sawicki, H. Lin, H. K. C. Yee, A. J. Connolly, R. J. Brunner, I. Csabai, M. Dickinson, M. U. Subbarao, A. S. Szalay, A. Fernandez-Soto, K. M. Lanzetta, and A. Yahil. *AJ*, 115:1418–1422, Apr. 1998.

E. M. Hu and S. E. Ridgway. *AJ*, 107:1303–1306, Apr. 1994.

D. H. Hughes, S. Serjeant, J. Dunlop, M. Rowan-Robinson, A. Blain, R. G. Mann, R. Ivison, J. Peacock, A. Efstathiou, W. Gear, S. Oliver, A. Lawrence, M. Longair, P. Goldschmidt, and T. Jenness. *Nature*, 394:241–247, 1998.

J. Iben, I. *ApJ*, 277:333–354, Feb. 1984.

T. Ichikawa, W. Van Driel, T. Aoki, T. Soyano, K. Tarusawa, and S. Yoshida. *ApJ*, 433:645–647, Oct. 1994.

T. Ichikawa, K. Yanagisawa, N. Itoh, K. Tarusawa, W. Van Driel, and M. Ueno. *AJ*, 109:2038+, May 1995.

M. Im, S. Casertano, R. E. Griffiths, K. U. Ratnatunga, and J. A. Tyson. *ApJ*, 441: 494–504, Mar. 1995.

M. Im, R. E. Griffiths, K. U. Ratnatunga, and V. L. Sarajedini. *ApJL*, 461:L79–+, Apr. 1996.

C. D. Impey, C. G. Wynn-Williams, and E. E. Becklin. *ApJ*, 309:572–592, Oct. 1986.

Z. Ivezic and M. Elitzur. *ApJ*, 445:415–432, May 1995.

R. J. Ivison, I. Smail, J. F. Le Borgne, A. W. Blain, J. P. Kneib, J. Bezecourt, T. H. Kerr, and J. K. Davies. *MNRAS*, 298:583–593, Aug. 1998.

I. Jorgensen, M. Franx, and P. Kjaergaard. *MNRAS*, 276:1341–1364, Oct. 1995.

K. Justtanont and A. G. G. M. Tielens. *ApJ*, 389:400–412, Apr. 1992.

G. Kauffmann. *MNRAS*, 281:475–486, July 1996.

G. Kauffmann and S. Charlot. *MNRAS*, 294:705+, Mar. 1998.

G. Kauffmann, S. Charlot, and S. D. M. White. *MNRAS*, 283:L117–L122, Dec. 1996.

G. Kauffmann, J. M. Colberg, A. Diaferio, and S. D. M. White. *MNRAS*, 303:188–206, Feb. 1999.

G. Kauffmann, A. Nusser, and M. Steinmetz. *MNRAS*, 286:795–811, Apr. 1997.

G. Kauffmann, S. D. M. White, and B. Guiderdoni. *MNRAS*, 264:201+, Sept. 1993.

K. Kawara, Y. Sato, H. Matsuhara, Y. Taniguchi, H. Okuda, Y. Sofue, T. Matsumoto, K. Wakamatsu, H. Karoji, S. Okamura, K. C. Chambers, L. L. Cowie, R. D. Joseph, and D. B. Sanders. *A&A*, 336:L9–L12, Aug. 1998.

J. Kennicutt, R. C. *ApJ*, 272:54–67, Sept. 1983.

J. Kennicutt, R. C. *ApJ*, 498:541+, May 1998a.

J. Kennicutt, R. C. *ARA&A*, 36:189–232, 1998b.

J. Kennicutt, Robert C., P. Tamblyn, and C. E. Congdon. *ApJ*, 435:22–36, Nov. 1994.

D. C. H. Kim and D. B. Sanders. *ApJS*, 119:41–58, Nov. 1998.

S. H. Kim and P. G. Martin. *ApJ*, 462:296+, May 1996.

A. L. Kinney, R. C. Bohlin, D. Calzetti, N. Panagia, and R. F. G. Wyse. *ApJS*, 86: 5–93, May 1993.

U. Klaas, M. Haas, I. Heinrichsen, and B. Schulz. *A&A*, 325:L21–L24, Sept. 1997.

U. Klein, R. Wielebinski, and H. W. Morsi. *A&A*, 190:41–46, Jan. 1988.

J. H. Knapen, J. Cepa, J. E. Beckman, M. Soledad Del Rio, and A. Pedlar. *ApJ*, 416: 563+, Oct. 1993.

G. R. Knapp, G. Helou, and A. A. Stark. *AJ*, 94:54–60, July 1987.

E. Krugel and R. Siebenmorgen. *A&A*, 282:407–417, Feb. 1994.

R. L. Kurucz. Model atmospheres for population synthesis. In *IAU Symposia*, volume 149, pages 225+, 1992.

N. D. Kylafis and J. N. Bahcall. *ApJ*, 317:637–645, June 1987.

C. Lacey, B. Guiderdoni, B. Rocca-Volmerange, and J. Silk. *ApJ*, 402:15–41, Jan. 1993.

C. Lacey and J. Silk. *ApJ*, 381:14–32, Nov. 1991.

P. O. Lagage, A. Claret, J. Ballet, F. Boulanger, C. J. Cesarsky, D. Cesarsky, C. Fransson, and A. Pollock. *A&A*, 315:L273–L276, Nov. 1996.

A. Lançon and B. Rocca-Volmerange. *A&AS*, 96:593–612, Dec. 1992.

A. Lancon and B. Rocca-Volmerange. *New Astronomy, vol. 1, no. 3, p. 215-234.*, 1: 215–234, Nov. 1996.

A. Laor and B. T. Draine. *ApJ*, 402:441, 1993.

R. B. Larson. *MNRAS*, 169:229–246, Nov. 1974.

A. Leger, L. D'Hendecourt, and D. Defourneau. *A&A*, 216:148–164, June 1989a.

A. Leger, L. Verstraete, L. D'Hendecourt, O. Dutuit, W. Schmidt, and J. Lauer. The pah hypotesis and the extinction curve. In L. J. Allamandola and A. G. G. M. Tielens, editors, *"IAU Symposium No 135 - Interstellar Dust"*, page 173. Kluwer Academic Publisher, 1989b.

C. Leitherer and T. M. Heckman. *ApJS*, 96:9–38, Jan. 1995.

C. Leitherer, D. Schaerer, J. D. Goldader, R. M. G. Delgado, C. Robert, D. F. Kune, D. F. De Mello, D. Devost, and T. M. Heckman. *ApJS*, 123:3–40, July 1999.

S. J. Lilly, S. A. Eales, W. K. P. Gear, F. Hammer, O. Le Fevre, D. Crampton, J. R. Bond, and L. Dunne. *ApJ*, 518:641–655, June 1999.

S. J. Lilly, O. Le Fevre, F. Hammer, and D. Crampton. *ApJL*, 460:L1–+, Mar. 1996.

S. J. Lilly, L. Tresse, F. Hammer, D. Crampton, and O. Le Fevre. *ApJ*, 455:108+, Dec. 1995.

K. Y. Lo, K. W. Cheung, C. R. Masson, T. G. Phillips, S. L. Scott, and D. P. Woody. *ApJ*, 312:574–591, Jan. 1987.

D. Lutz, H. W. W. Spoon, D. Rigopoulou, A. F. M. Moorwood, and R. Genzel. *ApJL*, 505:L103–L107, Oct. 1998.

P. Madau, H. C. Ferguson, M. E. Dickinson, M. Giavalisco, C. C. Steidel, and A. Fruchter. *MNRAS*, 283:1388–1404, Dec. 1996.

P. Madau, L. Pozzetti, and M. Dickinson. *ApJ*, 498:106+, May 1998.

S. Malhotra, G. Helou, D. Van Buren, M. Kong, C. A. Beichman, H. Dinerstein, D. J. Hollenbach, D. A. Hunter, K. Y. Lo, S. D. Lord, N. Y. Lu, R. H. Rubin, G. J. Stacey, J. Thronson, H. A., and M. W. Werner. *A&A*, 315:L161–L164, Nov. 1996.

R. G. Mann, S. J. Oliver, S. B. G. Serjeant, M. Rowan-Robinson, A. Baker, N. Eaton, A. Efstathiou, P. Goldschmidt, B. Mobasher, T. J. Sumner, L. Danese, D. Elbaz, A. Franceschini, E. Egami, M. Kontizas, A. Lawrence, R. McMahon, H. U. Norgaard-Nielsen, I. Perez-Fournon, and J. I. Gonzalez-Serrano. *MNRAS*, 289:482–489, Aug.

1997.

D. Maoz. *ApJL*, 490:L135–+, Dec. 1997.

M. Marengo, G. Canil, G. Silvestro, L. Origlia, M. Busso, and P. Persi. *A&A*, 322: 924–932, June 1997.

P. Marigo, A. Bressan, and C. Chiosi. *A&A*, 313:545–564, Sept. 1996.

P. Marigo, A. Bressan, and C. Chiosi. *A&A*, 331:564–580, Mar. 1998.

J. S. Mathis. *ARA&A*, 28:37–70, 1990.

J. S. Mathis. *ApJ*, 472:643+, Dec. 1996.

J. S. Mathis. *ApJ*, 497:824+, Apr. 1998.

J. S. Mathis, P. G. Mezger, and N. Panagia. *A&A*, 128:212–229, Nov. 1983.

J. S. Mathis and G. Whiffen. *ApJ*, 341:808–822, June 1989.

F. Matteucci. *Fundamentals of Cosmic Physics*, 17:283–396, 1996.

K. Mattila, D. Lemke, L. K. Haikala, R. J. Laureijs, A. Leger, K. Lehtinen, C. Leinert, and P. G. Mezger. *A&A*, 315:L353–L356, Nov. 1996.

P. Mazzei, G. De Zotti, and C. Xu. *ApJ*, 422:81–91, Feb. 1994.

P. Mazzei, C. Xu, and G. De Zotti. *A&A*, 256:45–55, Mar. 1992.

K. K. McLeod, G. H. Rieke, M. J. Rieke, and D. M. Kelly. *ApJ*, 412:111–126, July 1993.

A. Men'shchikov and T. Henning. 2d radiative transfer models of the embedded ysos hl tau and l1551 irs 5: What is inside? In H. U. Kaufl and R. Siebenmorgen, editors, *"ESO Astrophysics Symposia - The Role of Dust in the Formation of Stars"*, page 351. Springer-Verlag, 1996.

G. R. Meurer, T. M. Heckman, M. D. Lehnert, C. Leitherer, and J. Lowenthal. *AJ*, 114:54–68, July 1997.

G. R. Meurer, T. M. Heckman, C. Leitherer, A. Kinney, C. Robert, and D. R. Garnett. *AJ*, 110:2665+, Dec. 1995.

K. Mihara and F. Takahara. *PASJ*, 46:447–460, Oct. 1994.

R. F. Mushotzky and M. Loewenstein. *ApJL*, 481:L63–+, June 1997.

N. Netzer and M. Elitzur. *ApJ*, 410:701–713, June 1993.

A. Noels and N. Grevesse. *Origin and Evolution of the Elements.* Cambridge University Press, —c1993, edited by Prantzos, N.; Vangioni-Flam, E.; Cassé, M., 1993.

S. J. Oliver, P. Goldschmidt, A. Franceschini, S. B. G. Serjeant, A. Efstathiou, A. Verma, C. Gruppioni, N. Eaton, R. G. Mann, B. Mobasher, C. P. Pearson, M. Rowan-Robinson, T. J. Sumner, L. Danese, D. Elbaz, E. Egami, M. Kontizas, A. Lawrence, R. McMahon, H. U. Norgaard-Nielsen, I. Perez-Fournon, and J. I. Gonzalez-Serrano. *MNRAS*, 289:471–481, Aug. 1997.

A. Omont. *A&A*, 164:159–178, Aug. 1986.

A. Omont, R. G. McMahon, P. Cox, E. Kreysa, J. Bergeron, F. Pajot, and L. J. Storrie-Lombardi. *A&A*, 315:1–10, Nov. 1996.

B. Paczynski. *Acta Astronomica*, 21:417–435, 1971.

M. A. Pahre and S. G. Djorgovski. *ApJL*, 449:L1–+, Aug. 1995.

P. Panuzzo and et al. *in preparation*, 1999.

M. Pettini, M. Kellogg, C. C. Steidel, M. Dickinson, K. L. Adelberger, and M. Giavalisco. *ApJ*, 508:539–550, Dec. 1998.

M. Pettini, D. L. King, L. J. Smith, and R. W. Hunstead. *ApJ*, 478:536+, Mar. 1997.

L. Portinari, C. Chiosi, and A. Bressan. *A&A*, 334:505–539, June 1998.

W. H. Press and P. Schechter. *ApJ*, 187:425–438, Feb. 1974.

J. L. Puget, A. Abergel, J. P. Bernard, F. Boulanger, W. B. Burton, F. X. Desert, and D. Hartmann. *A&A*, 308:L5–+, Apr. 1996.

J. L. Puget, G. Lagache, D. L. Clements, W. T. Reach, H. Aussel, F. R. Bouchet, C. Cesarsky, F. X. Desert, H. Dole, D. Elbaz, A. Franceschini, B. Guiderdoni, and A. F. M. Moorwood. *A&A*, 345:29–35, May 1999.

J. L. Puget and A. Leger. *ARA&A*, 27:161–198, 1989.

J. L. Puget, A. Leger, and F. Boulanger. *A&A*, 142:L19, 1985.

R. J. Rand, S. R. Kulkarni, and W. Rice. *ApJ*, 390:66–78, May 1992.

A. Renzini and A. Buzzoni. Global properties of stellar populations and the spectral evolution of galaxies. In *Spectral Evolution of Galaxies*, pages 195–231, 1986.

W. Rice, C. J. Lonsdale, B. T. Soifer, G. Neugebauer, E. L. Koplan, L. A. Lloyd, T. De Jong, and H. J. Habing. *ApJS*, 68:91–127, Oct. 1988.

A. Rifatto, G. Longo, and M. Capaccioli. *Astronomy and Astrophysics Supplement Series*, 114:527+, Dec. 1995.

D. Rigopoulou, A. Lawrence, and M. Rowan-Robinson. *MNRAS*, 278:1049–1068, Feb. 1996.

M. Rowan-Robinson. *ApJ*, 234:111–128, Nov. 1979.

M. Rowan-Robinson. *MNRAS*, 219:737–749, Apr. 1986.

M. Rowan-Robinson. *MNRAS*, 258:787–799, Oct. 1992.

M. Rowan-Robinson. Infrared luminous galaxies and agn. In *ASP Conf. Ser. 133: Science With The NGST*, pages 119+, 1998.

M. Rowan-Robinson, R. G. Mann, S. J. Oliver, A. Efstathiou, N. Eaton, P. Goldschmidt, B. Mobasher, S. B. G. Serjeant, T. J. Sumner, L. Danese, D. Elbaz, A. Franceschini, E. Egami, M. Kontizas, A. Lawrence, R. McMahon, H. U. Norgaard-Nielsen, I. Perez-Fournon, and J. I. Gonzalez-Serrano. *MNRAS*, 289:490+, Aug. 1997.

G. B. Rybicky and A. P. Lightman. *Radiative Processes in Astrophysics*. John Wiley & Sons, 1979.

E. E. Salpeter. *ApJ*, 121:161+, Jan. 1955.

E. E. Salpeter. *ApJ*, 193:579–584, Nov. 1974 a.

E. E. Salpeter. *ApJ*, 193:585–592, Nov. 1974 b.

A. Sandage and G. A. Tammann. *ApJ*, 196:313–328, Mar. 1975.

D. B. Sanders and I. F. Mirabel. *ARA&A*, 34:749+, 1996.

D. B. Sanders, B. T. Soifer, J. H. Elias, B. F. Madore, K. Matthews, G. Neugebauer,

and N. Z. Scoville. *ApJ*, 325:74–91, Feb. 1988.

J. Santos, J. F. C. and J. A. Frogel. *ApJ*, 479:764+, Apr. 1997.

W. Saunders, M. Rowan-Robinson, A. Lawrence, G. Efstathiou, N. Kaiser, R. S. Ellis, and C. S. Frenk. *MNRAS*, 242:318–337, Jan. 1990.

M. Sauvage, J. Blommaert, F. Boulanger, C. J. Cesarsky, D. A. Cesarsky, F. X. Desert, D. Elbaz, P. Gallais, G. Joncas, L. Metcalfe, K. Okumura, S. Ott, R. Siebenmorgen, J. L. Starck, D. Tran, and L. Vigroux. *A&A*, 315:L89–L92, Nov. 1996.

M. J. Sawicki, H. Lin, and H. K. C. Yee. *AJ*, 113:1–12, Jan. 1997.

D. J. Schlegel, D. P. Finkbeiner, and M. Davis. *ApJ*, 500:525+, June 1998.

D. Schoenberner. *A&A*, 103:119–130, Nov. 1981.

N. Scoville and J. S. Young. *ApJ*, 265:148+, Feb. 1983.

N. Z. Scoville, M. S. Yun, and P. M. Bryant. *ApJ*, 484:702+, July 1997.

R. Siebenmorgen, E. Krügel, and J. S. Mathis. *A&A*, 266:501–512, Dec. 1992.

L. Silva. *Degree Thesis*, Univ. Padova:IT, 1995.

L. Silva, G. L. Granato, A. Bressan, and L. Danese. *ApJ*, 509:103–117, Dec. 1998.

I. Smail, R. Ivison, A. Blain, J. P. Kneib, F. Owen, A. Franceschini, M. Harwit, J. L. Puget, and J. L. Starck. *astro-ph/9906196*, 1999.

I. Smail, R. J. Ivison, and A. W. Blain. *ApJL*, 490:L5–+, Nov. 1997.

C. H. Smith, D. K. Aitken, and P. F. Roche. *MNRAS*, 241:425–431, Dec. 1989.

J. Smith. *ApJ*, 261:463–472, Oct. 1982.

T. P. Snow and A. N. Witt. *Science*, 270:1455+, Dec. 1995.

T. P. Snow and A. N. Witt. *ApJL*, 468:L65–+, Sept. 1996.

U. J. Sofia, J. A. Cardelli, and B. D. Savage. *ApJ*, 430:650–666, Aug. 1994.

B. T. Soifer, L. Boehmer, G. Neugebauer, and D. B. Sanders. *AJ*, 98:766–797, Sept. 1989.

B. T. Soifer and G. Neugebauer. *AJ*, 101:354–361, Feb. 1991.

B. T. Soifer, D. B. Sanders, B. F. Madore, G. Neugebauer, G. E. Danielson, J. H. Elias, C. J. Lonsdale, and W. L. Rice. *ApJ*, 320:238–257, Sept. 1987.

A. Solinger, P. Morrison, and T. Markert. *ApJ*, 211:707–717, Feb. 1977.

P. M. Solomon, D. Downes, S. J. E. Radford, and J. W. Barrett. *ApJ*, 478:144+, Mar. 1997.

S. A. Stanford, P. R. Eisenhardt, and M. Dickinson. *ApJ*, 492:461+, Jan. 1998.

A. A. Stark, J. A. Davidson, S. Platt, D. A. Harper, R. Pernic, R. Loewenstein, G. Engargiola, and S. Casey. *ApJ*, 337:650–657, Feb. 1989.

C. C. Steidel, K. L. Adelberger, M. Giavalisco, M. Dickinson, and M. Pettini. *ApJ*, 519: 1–17, July 1999.

V. Straizys and Z. Sviderskiene. *A&A*, 17:312+, Mar. 1972.

E. Sturm, D. Lutz, R. Genzel, A. Sternberg, E. Egami, D. Kunze, D. Rigopoulou, O. H. Bauer, H. Feuchtgruber, A. F. M. Moorwood, and T. De Graauw. *A&A*, 315: L133–L136, Nov. 1996.

L. J. Tacconi and J. S. Young. *ApJ*, 308:600–610, Sept. 1986.

G. A. Tammann. Supernova statistics and related problems. In *Supernovae: A Survey of Current Research*, pages 371–403, Nov. 1982.

G. A. Tammann, W. Loeffler, and A. Schroeder. *ApJS*, 92:487–493, June 1994.

R. Tantalo, C. Chiosi, A. Bressan, and F. Fagotto. *A&A*, 311:361–383, July 1996.

M. A. Treyer, R. S. Ellis, B. Milliard, J. Donas, and T. J. Bridges. *MNRAS*, 300: 303–314, Oct. 1998.

J. C. Tsai and W. G. Mathews. *ApJ*, 468:571+, Sept. 1996.

R. J. Tuffs, D. Lemke, C. Xu, J. I. Davies, C. Gabriel, I. Heinrichsen, G. Helou, H. Hippelein, N. Y. Lu, and D. Skaley. *A&A*, 315:L149–L152, Nov. 1996.

R. B. Tully. *Journal of the American Association of Variable star observers*, 27:437–448, 1974.

R. B. Tully, M. J. Pierce, J. S. Huang, W. Saunders, M. A. W. Verheijen, and P. L. Witchalls. *AJ*, 115:2264–2272, June 1998.

W. E. C. J. Van Der Veen and H. J. Habing. *A&A*, 194:125–134, Apr. 1988.

W. Van Driel, T. De Graauw, T. De Jong, and P. R. Wesselius. *Astronomy and Astrophysics Supplement Series*, 101:207+, Oct. 1993.

E. Vassiliadis and P. R. Wood. *ApJ*, 413:641–657, Aug. 1993.

B. Wang and T. M. Heckman. *ApJ*, 457:645+, Feb. 1996.

D. Ward-Thompson and E. I. Robson. *MNRAS*, 244:458–464, June 1990.

V. Weidemann. *A&A*, 188:74–84, Dec. 1987.

S. D. M. White and C. S. Frenk. *ApJ*, 379:52–79, Sept. 1991.

P. Whitelock, J. Menzies, M. Feast, R. Catchpole, F. Marang, and B. Carter. *MNRAS*, 276:219–254, Sept. 1995.

P. Whitelock, J. Menzies, M. Feast, F. Marang, B. Carter, G. Roberts, R. Catchpole, and J. Chapman. *MNRAS*, 267:711+, Apr. 1994.

W. Wild, A. I. Harris, A. Eckart, R. Genzel, U. U. Graf, J. M. Jackson, A. P. G. Russell, and J. Stutzki. *A&A*, 265:447–464, Nov. 1992.

R. E. Williams, B. Blacker, M. Dickinson, W. V. D. Dixon, H. C. Ferguson, A. S. Fruchter, M. Giavalisco, R. L. Gilliland, I. Heyer, R. Katsanis, Z. Levay, R. A. Lucas, D. B. McElroy, L. Petro, M. Postman, H. M. Adorf, and R. Hook. *AJ*, 112:1335+, Oct. 1996.

M. W. Wise and D. R. Silva. *ApJ*, 461:155+, Apr. 1996.

A. N. Witt, J. Thronson, Harley A., and J. Capuano, John M. *ApJ*, 393:611–630, July 1992.

P. R. Wood, J. B. Whiteoak, S. M. G. Hughes, M. S. Bessell, F. F. Gardner, and A. R. Hyland. *ApJ*, 397:552–569, Oct. 1992.

G. Worthey, S. M. Faber, J. J. Gonzalez, and D. Burstein. *ApJS*, 94:687–722, Oct. 1994.

C. G. Wynn-Williams and E. E. Becklin. *ApJ*, 412:535–540, Aug. 1993.

C. Xu and V. Buat. *A&A*, 293:L65–L68, Jan. 1995.

C. Xu and G. De Zotti. *A&A*, 225:12–26, Nov. 1989.

J. S. Young, S. Xie, J. D. P. Kenney, and W. L. Rice. *ApJS*, 70:699–722, Aug. 1989.

S. E. Zepf. *Nature*, 390:377+, Nov. 1997.

E. Zucca, G. Zamorani, G. Vettolani, A. Cappi, R. Merighi, M. Mignoli, G. M. Stirpe, H. Macgillivray, C. Collins, C. Balkowski, V. Cayatte, S. Maurogordato, D. Proust, G. Chincarini, L. Guzzo, D. Maccagni, R. Scaramella, A. Blanchard, and M. Ramella. *A&A*, 326:477–488, Oct. 1997.